

Experimental Study of Initial State Radiative Events at HERA and a Measurement of the Proton Longitudinal Structure Function

Jason Schwartz

Department of Physics

McGill University

Montreal, Quebec

May, 2011

A thesis submitted to McGill University in partial fulfillment of the requirements of
the degree of Doctor of Philosophy

©Jason Schwartz, 2011

DEDICATION

To my fiancée Marisa.

ACKNOWLEDGEMENTS

I would like first to thank the McGill University Department of Physics for providing me the opportunity to pursue my degree and to the ZEUS/Canada group for providing me funding throughout my graduate career. I would especially like to thank Professor François Corriveau for his supervision and guidance.

The work presented in this thesis would not have been possible if it were not for the dedication of the entire ZEUS collaboration. Special mention goes to Professors Halina Abramowicz, Aharon Levy, Allen Caldwell, Iris Abt, Kunihiro Nagano, Tobias Haas, John Martin and Sampa Bhadra. My gratitude is also extended to the members of the F_L working group, including: Burkard Reiser, Tim Namsou, Jolanta Sztuk-Dambietz, Bill Schmidke, Daniel Kollar, Julia Grebenyuk and Prabhdeep Kaur.

Living and studying in Hamburg, Germany was a unique experience which I am thankful for. My time in Germany would not have been the same were it not for the friends I had made, including: Trevor Stewart, Michel Sauter, Amir Stern, Tom Danielson, Eric Brownson, Michele Rosin, Tim Gosau, Dan Nicholass, Katie Oliver to name a few.

McGill University was a great university to grow intellectually and socially. I feel fortunate to have shared an office and many stimulating lunch break with Nazim Hussain, Bertrand Chapleau, Marc-Andre Dufor, Miika Klemetti, Pete Watson and Changyi Zhou. All the friends I have made in the McGill physics department have had a profound impact on me, for which I am thankful.

For spiritual guidance during my student years, I sincerely thank Rabbis Weiss, Hundert and Fishberg.

I thank my parents for their love, support and for and for always believing in me, they taught me how to think for myself and provided me with the tools I needed to succeed. Special mentions go to my twin brother Jordan, for whom together we master the sciences. My sisters Jessica and Jaclyn are two truly creative people from whom I draw inspiration.

Lastly, I would like to thank my beautiful fiancée Marisa, to whom this thesis is dedicated. Her patience, love and support has given me the strength and confidence I needed to pursue my studies.

ABSTRACT

A first measurement of the radiative contribution to deep inelastic electron-proton scattering has been performed with the ZEUS detector at HERA. Results show consistency with predictions made by the HERACLES Monte Carlo program. New calibration and simulation of the far luminosity measurement system, including a photon calorimeter and two aerogel Cherenkov detectors, have been implemented. Both calibration and simulation were applied to tag photons produced in the initial state radiative process. These tagged events were used to perform measurements of the deep inelastic ep scattering reduced cross section down to momentum transfer squared, $Q^2 = 3.0 \text{ GeV}^2$, a region normally inaccessible to ZEUS. A determination of the radiative contribution to deep inelastic scattering has aided in the measurement of the structure functions F_2 and F_L , which were simultaneously extracted in the kinematic region $8.0 \text{ GeV}^2 < Q^2 < 130 \text{ GeV}^2$ and $2.5 \times 10^{-4} < x < 0.005$, where x is associated with the fraction of momentum carried by the interacting quark, using collision data at three centre-of-mass energies, 318 GeV, 251 GeV and 225 GeV.

RÉSUMÉ

La contribution radiative à la diffusion inélastique profonde électron-proton a été mesurée pour la première fois avec le détecteur ZEUS à HERA. Les résultats démontrent un accord avec les prédictions faites par le programme Monte-Carlo HERACLES. De nouvelles calibration et simulation du système éloigné de mesure de la luminosité, incluant un calorimètre à photons et deux détecteurs Cherenkov en aérogel, ont été effectuées. Ces calibration et simulation ont été toutes deux utilisées pour identifier les photons produits dans le processus de radiation de l'état initial. Les événements ainsi choisis ont permis de mesurer la section efficace réduite de diffusion inélastique profonde ep à des valeurs du carré du transfert de quantité de mouvement aussi basses que $Q^2 = 3.0 \text{ GeV}^2$, une région cinématique normalement non-accessible à ZEUS. Une détermination de la contribution radiative à la diffusion inélastique profonde a aidé les mesures des fonctions de structure F_2 et F_L , qui ont été extraites simultanément dans la région cinématique $8.0 \text{ GeV}^2 < Q^2 < 130 \text{ GeV}^2$ et $2.5 \times 10^{-4} < x < 0.005$, où x peut être associé la fraction de la quantité de mouvement du proton participant à la réaction, et ce en exploitant les données de collisions prises à trois énergies du centre de masse, 318 GeV, 251 GeV et 225 GeV.

TABLE OF CONTENTS

DEDICATION	i
ACKNOWLEDGEMENTS	ii
ABSTRACT	iv
RÉSUMÉ	v
1	Introduction	1
	1.1 Introduction	1
2	Physics Overview	4
	2.1 Introduction	4
	2.2 Historical Introduction	5
	2.2.1 Early Developments	5
	2.2.2 Ernest Rutherford and the Development of the Atom	6
	2.3 The Standard Model of Particle Physics	6
	2.3.1 The Quark Model	9
	2.3.2 Quantum Chromodynamics	10
	2.3.3 Asymptotic Freedom and Colour Confinement	10
	2.4 Deep Inelastic Scattering in the QPM	11
	2.4.1 Kinematics	12
	2.4.2 DIS Cross Section	14
	2.4.3 Bjorken Scaling	20
	2.5 Deep Inelastic Scattering in QCD	20
	2.5.1 Factorization Theorem	20
	2.5.2 DGLAP	21
	2.5.3 The Longitudinal Structure Function F_L	25
	2.6 Relevant Physics Processes	26
	2.6.1 DIS	27
	2.6.2 Photoproduction	27
	2.6.3 Diffractive DIS	28
	2.7 Initial State Radiation	29
3	HERA and ZEUS	32
	3.1 The HERA Collider	32

3.2	The ZEUS Detector	36
3.2.1	Tracking Detectors	37
3.2.2	The Uranium-scintillator Calorimeter	40
3.2.3	Small Angle Rear Tracking Detector and the Hadron- Electron Separator	43
3.2.4	Trigger and Data Acquisition	44
3.2.5	First Level Trigger	46
3.2.6	Second Level Trigger	46
3.2.7	Third Level Trigger	46
3.3	The Luminosity System	47
3.3.1	6-Meter Tagger	47
3.3.2	Luminosity Spectrometer	48
3.3.3	Photon Calorimeter and Cherenkov Detectors	49
4	Monte Carlo	52
4.1	Introduction	52
4.2	Physics Simulation	53
4.2.1	QED Initial and Final State Radiation	54
4.2.2	Hard Scattering and QCD Radiation	56
4.2.3	Hadronization and Decay	58
4.3	ZEUS Detector Simulation	58
4.4	Simulation of the Luminosity System	60
4.4.1	Geometric Acceptance	60
4.4.2	Aperture Determination	61
4.4.3	Photon Calorimeter and Aerogel Detectors	62
4.4.4	Inclusion of Beam Related Background	64
4.4.5	Comparisons with Data	66
5	Event Reconstruction and Selection	67
5.1	Event Reconstruction	67
5.1.1	Electron Reconstruction	68
5.1.2	Hadronic Reconstruction	68
5.1.3	Hadronic Quantities	70
5.1.4	Vertex Reconstruction	72
5.1.5	Z vertex Reweighting	72
5.2	Event Reconstruction Methods	76
5.2.1	Electron Method	77
5.2.2	Jacquet-Blondel Method	77
5.2.3	Sigma Method	78
5.2.4	Double Angle Method	79
5.3	Kinematic Reconstruction with ISR	79
5.3.1	Electron Method with ISR	80

5.3.2	Jacquet-Blondel Method with ISR	80
5.3.3	Double Angle Method with ISR	80
5.4	The Kinematic Peak	81
5.5	Calibration of the Photon Calorimeter	82
5.6	Calibration of the PCAL+AERO System	84
5.6.1	Calibration Results	86
5.7	Backgrounds	87
5.7.1	Photoproduction	88
5.7.2	QED Compton events	89
5.8	Event Sample and Selection	89
5.8.1	Event Sample	89
5.8.2	The F_L Trigger Definitions: SPP15 and SPP16	90
5.8.3	The ISR Trigger Definition: SPP11	91
5.9	Event Selection	91
5.9.1	Neutral Current DIS Event Selection	92
5.9.2	Satellite Vertex Selection	95
5.9.3	ISR-Enriched Selection	96
5.9.4	Tagged Photon Samples	97
5.10	Summary of Event Samples	98
6	Experimental Verification of Radiative Corrections to DIS	99
6.1	Introduction	99
6.2	Measurement Technique	101
6.2.1	Photon Energies in bins of $\mathbf{E} - \mathbf{p}_z$	103
6.2.2	ISR Signal Extraction	103
6.2.3	First Measurement of the ISR Cross Section	106
6.3	Measuring the ISR Cross Section	111
6.3.1	Bin Selection	112
6.3.2	Cross Section Unfolding Technique	116
6.3.3	Uncertainties	117
6.3.4	The $\mathbf{E} - \mathbf{p}_z$ Method	120
6.3.5	The PCAL Method	121
6.4	Comparing Methods	124
7	Probing the Protons Structure with ISR	129
7.1	Introduction	129
7.2	Techniques	130
7.2.1	Measurement Concept	130
7.2.2	ISR Photon Tagging	131
7.2.3	Event Reconstruction	133
7.2.4	Bin Selection and Systematics	133
7.2.5	Cross Section Unfolding	135

7.3	Results	136
8	Measurement of the DIS Cross Section and the Longitudinal Structure Function F_L	139
8.1	Introduction	139
8.2	Experimental Procedure	142
	8.2.1 Datasets	142
	8.2.2 Measurement Technique	142
	8.2.3 Improvements to Previous Measurement	144
	8.2.4 Cross Section Extraction	144
8.3	Results	146
	8.3.1 Reduced Cross Sections	146
	8.3.2 F_L Measurement	149
9	Discussions	154
9.1	Radiative Events	154
	9.1.1 Verification of the Radiative Correction	154
	9.1.2 Discussion of Results	156
	9.1.3 Measurement of the DIS reduced Cross section using Tagged-ISR Events	158
	9.1.4 The Longitudinal Structure Function with ISR	159
	9.1.5 Opportunities for New Studies	160
9.2	F_L	162
10	Conclusions	163
	Appendix	
A	Control Distributions	164
	A.1 Control Distributions	164
B	Radiative Events	174
	B.1 Values for the ISR Cross Section	174
	B.1.1 ISR Cross Section Measurement with the $E - p_z$ Method	174
	B.1.2 ISR Cross Section Measurement with the PCAL Method	176
	B.2 Cross Sections for the ISR-Tagged Sample	177
	B.2.1 Systematics	179
	B.2.2 Purities, Efficiencies and Acceptances in bins of y and Q^2	190
C	F_L Measurement	192
	C.1 F_L Measurement	192
	C.1.1 Purities, Efficiencies and Acceptances	197

C.2	Rosenbluth Plots	202
C.2.1	Combined Nominal and Satellite Vertex	202
D	Glossary of Abbreviations	205
	References	206

CHAPTER 1

Introduction

1.1 Introduction

Particle physics is a scientific discipline that aims to understand, observe and classify the most basic constituents of matter and their interactions. Whereas the philosophy behind particle physics can be traced to the era of the ancient Greeks, the science of particle physics has evolved alongside the major scientific discoveries of the 19th and 20th centuries. Particle physics is therefore a branch of modern physics where theoretical advances can motivate discovery and discovery can in-turn motivate theoretical advancements. Experimentalists use particle collisions as a means to probe deep into the core of matter. The questions that this field aims to answer have intrigued people for millennia and answering them requires some of the largest and most intricate machines ever built.

The HERA particle accelerator, which was part of the DESY accelerator complex in Hamburg, Germany, had unparalleled success in observing the proton structure. It collided high energy protons and electrons (or positrons). These highly energetic collisions were observed by the H1 and ZEUS experiments and they allowed physicists to study the distribution of quarks and gluons inside the proton.

Immediately before an interaction at HERA, the incoming electron can radiate a photon, causing the collision to actually occur at a reduced centre-of-mass energy.

This phenomenon severely affects the topology and reconstruction of the event. According to theoretical predictions, energy corrections from this electromagnetic initial state radiation (ISR) can be larger than 50 %. The theoretical foundations of ISR in high-energy ep scattering are well established. Nevertheless, a correction this large must be experimentally verified. This thesis marks ZEUS's first measurement of the radiative correction.

The theoretical basis for this thesis is derived from the Standard Model of particle physics. Chapter 2 is devoted to the relevant theoretical framework to describe Deep Inelastic electron-proton Scattering (DIS). The cross section for DIS is parameterized by three empirical proton structure functions. When studied within the context of the Quark Parton Model (QPM), DIS is described through the interaction of three spin- $\frac{1}{2}$ valence quarks. Quantum Chromodynamics (QCD) revises this theory to include the spin-1 gluons. It is in this theory that contributions from the third proton structure function, called the longitudinal structure function, become significant.

The ZEUS detector observed particle collisions produced by the HERA accelerator. The experimental components relevant to this thesis are described in chapter 3. Collision rates measured in the ZEUS detector are compared to theoretical predictions via Monte Carlo (MC) simulations. MC programs simulate the ZEUS detector and the full physics of an event. Techniques used to perform the event simulations are discussed in chapter 4. The event samples and the reconstruction techniques used to analyze them are outlined in chapter 5.

In chapter 6, measurements of the contribution from initial state electromagnetic radiation to the neutral current positron-proton deep inelastic scattering cross section and their comparisons to theoretical predictions are presented. In chapter 7, the reduction of the collision centre-of-mass energy, resulting from the emission of

electromagnetic initial state radiation, is used to extend the accessible kinematic range, for structure function measurements, to lower virtualities than previously available. Photon measurements are performed using the photon detectors located 107 m downstream from the interaction point. In particular, the calibration of the photon detectors is outlined in section 5.6, while a full simulation of the geometry and detector response is developed in section 4.4.

Gluons carry a large fraction of the protons momentum. The size of this contribution is directly related to the protons longitudinal structure function. The accuracy on a measurement of this structure function depends on the ability to understand events at high inelasticities, where radiative corrections are at their largest. A firm understanding of radiative corrections is necessary for measurements of the longitudinal structure function. Chapter 8 outlines the efforts to measure the longitudinal structure function in wider regions of phase space than previously achieved.

A discussion of all the results presented in this thesis is given in chapter 9 and conclusions are presented in chapter 10.

CHAPTER 2

Physics Overview

2.1 Introduction

Scattering experiments are the primary source of information on the Standard Model of particle physics. Beams of high energy particles are made to collide at a single point and a detector is used to measure the configuration of the final state particles. There are three categories of scattering experiments: elastic, inelastic and deep inelastic. In elastic scattering, both particles involved bounce off each other, conserving kinetic energy and all quantum states. In inelastic scattering, the kinetic energy is not conserved and energy is used to change the quantum states of the outgoing particles. In Deep Inelastic Scattering (DIS), the initial state particles collide, resulting in a large phase space for particle creation. The DIS process occurs at very high momentum transfers and allows one to probe deep inside the proton to reveal its internal structure. This chapter motivates the theory behind DIS and will lay the foundations needed to understand the experimental results presented in this thesis.

This chapter begins with a brief introduction to the history of particle physics, in section 2.2. This is followed by a qualitative discussion of the Standard Model of particle physics in section 2.3. Sections 2.4 and 2.5 develop the theoretical basis for DIS within the Quark Parton Model (QPM) and motivate the theory of the strong interaction, Quantum Chromodynamics (QCD). In these sections, the proton

structure functions are introduced and the parton evolution equations are defined. Section 2.6 gives a general overview of the different physics processes, including background processes, which are present in an electron-proton physics environment. The final section in this chapter, section 2.7, develops a theoretical description of initial state radiation.

2.2 Historical Introduction

2.2.1 Early Developments

Everything tangible in the universe is comprised of matter, but what is matter comprised of? This question has intrigued people for many millennia. The history of particle physics can be traced back to the late 4th century BCE. Ancient greek philosophers, Leucippus and Democritus, proposed that everything seen in nature is composed of discrete fundamental building blocks which they called *atomos* ($\alpha\tau\omicron\mu\omicron\varsigma$). Atoms, as we know them today, were first confirmed by 18th century chemists attempting to explain chemical reactions. It was not long after the discovery of the atom that scientists questioned whether atoms themselves are divisible. With the discovery of the electron in 1897, J.J. Thomson confirmed the divisibility of the atom. He concluded that electrons are electrically charged because they can be deflected in an electric field. He also noticed that atoms are electrically neutral, seemingly a contradiction. Thomson's vision of the atom is much different than ours today. He hypothesized that negatively charged electrons were embedded within a positively charged sea. This "plum pudding" model of the atom was superseded by the current model which was proposed and verified by Ernest Rutherford in 1909 and later extended by Neils Bohr in 1913 [1].

2.2.2 Ernest Rutherford and the Development of the Atom

Ernest Rutherford was a prolific scientist whose pioneering work changed the way we understand matter. While a professor at McGill University(1898-1907), Rutherford proved that radioactive decay was caused by the mutation of one element into another. He later discovered the atomic nucleus. His famous gold foil experiment is considered one of the first particle scattering experiments. In this experiment, a radium source undergoes alpha decay and alpha particles are directed into a gold foil. In Thomson's "plum pudding" model, the positively charged alpha particle should be lightly deflected by the uniform charge distribution. Instead, some of the alpha particles were observed to recoil from the gold foil. This result implies that there is a dense positively charged target within the atom. This experiment confirmed the existence of a hard core, called the nucleus, in the atom. Later it was shown that the nucleus is comprised of positively charged protons and neutral neutrons bound together by the strong nuclear force. The constituents of the proton are, in turn, the concern of this thesis.

2.3 The Standard Model of Particle Physics

The Standard Model of particle physics is a theory that describes the behaviour of all known fundamental particles and most of the forces that exist in nature. At the time of this thesis, we know of two classes of fundamental particles, the fermions and the bosons. Fermions are the particles of matter and bosons are the force carriers. In nature there are four fundamental forces. Gravity is the weakest of all forces but the most commonly recognizable because it holds us to the ground ¹. Electric and magnetic forces are unified into the electromagnetic force. The weak nuclear

¹ The Standard Model does not provide a theory of gravity.

force is responsible for the spontaneous decay of nuclei. Weak and electromagnetic forces are further unified in the theory of the electroweak interactions. The strong nuclear force is responsible for keeping the constituents of the proton and neutron bound together and keeping the latter bound to each other in the nucleus, despite the overall positive charge. Each of these forces is mediated by a force carrying particle. Listed in table 2.1 are the Standard Model vector bosons and their properties.

Boson	Mass (GeV)	Charge	Spin	Force
γ (Photon)	0	0	1	Electromagnetic
W^\pm	80.4	± 1	1	Weak
Z^0	91.2	0	1	Weak
g (Gluon)	0	0	1	Strong

Table 2.1: The basic properties of the force carrying vector bosons in the Standard Model.

A noticeable omission from this table is the yet undiscovered Higgs Boson. The Higgs Boson is a hypothetical scalar boson that gives mass to the W^\pm and Z^0 particles through *electroweak symmetry breaking*. According to theoretical predictions, the HERA accelerator was not expected to observe the Higgs boson and no such discovery has been made.

Fermions are spin- $\frac{1}{2}$ particles and as such obey the Pauli exclusion principle. There are 12 different fermions, each with its own anti-particle. Fermions can be further subdivided into two classes: leptons and quarks. Charged leptons and quarks both interact with the electromagnetic force and as such carry some sort of electromagnetic charge. Leptons have an integer charge (0, ± 1) while quarks have a fractional charge ($\pm \frac{1}{3}$ or $\pm \frac{2}{3}$). Quarks also have an integer colour charge. Colour charge is the charge carried by the strong nuclear force. The fermions in the Standard Model are listed in table 2.2.

Leptons			Quarks		
Flavour	Mass (GeV)	Charge	Flavour	Mass (GeV)	Charge
ν_e	$< 10^{-8}$	0	u (up)	0.003	+
e	0.000511	-1	d (down)	0.006	-
ν_μ	< 0.0002	0	c (charm)	1.3	+
μ	0.106	-1	s (strange)	0.1	-
ν_τ	< 0.02	0	t (top)	175	+
τ	1.7771	-1	b (bottom)	4.3	-

Table 2.2: Properties of the three generations of fermions displaying their masses (or mass upper limits) and electric charges.

There exist six flavours of quarks, and they are grouped into three different generations. The six flavours are u (up), d (down), s (strange), c (charm), t (top) and b (bottom). The three generations differ from each other only by the mass of the quarks. These masses are purely empirical quantities and the reason for their values remains one of the mysteries of nature. Quarks are never observed independently, they are always bound into hadrons. This is because quarks carry a colour charge and are subject to a phenomenon called *colour confinement*. Hadrons come in two known types, quark anti-quark bound states called mesons or three quark bound states called baryons.¹ The proton is an example of a hadron, it contains two u quarks and one d quark.

Leptons do not carry a colour charge and can therefore be found as free particles. Like quarks, leptons also have six flavours and are arranged into three generations according to their masses. Each generation consists of a charged-uncharged pair, the six flavours of leptons are the electron, e , the electron neutrino, ν_e , the muon, μ , the muon neutrino, ν_μ , the tau, τ , and the tau neutrino, ν_τ . The anti-particle of the

¹ Bound states of higher orders are not forbidden by the Standard Model, but have not yet been observed.

electron is called the positron, e^+ . In this thesis, the terms electron and positron will be used interchangeably and will refer to the positron unless otherwise stated.

The Standard Model is a quantum field theory, whereby particle interactions occur not directly at a singular point in space, but through dynamical fields. The theory itself is a unification of several other theories. Quantum Electrodynamics (QED) is a U(1) invariant gauge theory and possesses a single gauge boson, the photon. The W^\pm and Z^0 bosons of the weak interaction form the SU(2) weak interaction. The combination of QED and weak interaction theory form the U(1) \times SU(2) electroweak theory. The gluon comes in eight different varieties which are superpositions of red, anti-red, blue, anti-blue, green and anti-green coloured states. These states correspond to the generators of the SU(3) gauge group. The Standard Model is a SU(3) \times SU(2) \times U(1) gauge theory.

2.3.1 The Quark Model

The early inelastic particle scattering experiments discovered a zoo of new hadrons. Hadrons were given names like pions and kaons and were described by newly discovered discrete internal symmetries like isospin I , hypercharge Y , baryon number \mathcal{B} , strangeness S , charm C , bottomness B and topness T . These symmetries are related to the electromagnetic charge, Q , of a hadron via the Gell-Mann-Nishijima formula

$$Q = I_z + \frac{1}{2}Y \quad (2.1)$$

where there I_z is the z projection of the isospin and the hypercharge Y is given by $Y = \mathcal{B} + S + C + B + T$. These properties allowed physicists to classify and even predict new hadrons. A graphical representation of the light spin-0 mesons is displayed in figure 2.1, as an example. The quark model, although excellent for

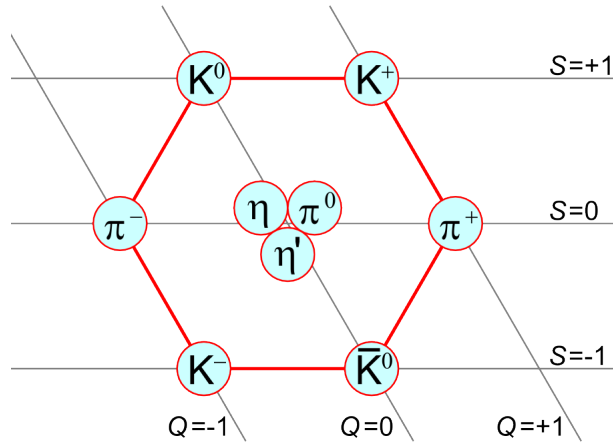


Figure 2.1: The nine spin zero mesons containing only u , d and s quarks arranged in a nonet [2].

classifying and predicting the existence of new hadrons, does not explain the force that binds them together.

2.3.2 Quantum Chromodynamics

Quantum Chromodynamics (QCD) describes the strong nuclear force and is the $SU(3)$ component of the Standard Model. QCD is best understood in the language of quantum field theory. The non-abelian nature of QCD leads to gluon self interactions, this consequently gives rise to the concepts of *colour confinement* and *asymptotic freedom*.

2.3.3 Asymptotic Freedom and Colour Confinement

Unlike the photon (the QED analogue to the gluon), the gluon can self-interact which leads to an effect called *colour confinement*. Colour confinement stipulates that quarks can never be found as free particles and must be bound into hadrons [3]. Another peculiar property of QCD called *asymptotic freedom*. When studied with a high energy probe, quarks inside of hadrons are essentially free. This is demonstrated by the running nature of the strong coupling constant, α_s . This is shown in figure 2.2.

At the energy scales studied in this thesis, QCD is considered to be weakly coupled and calculations using perturbation theory are possible.

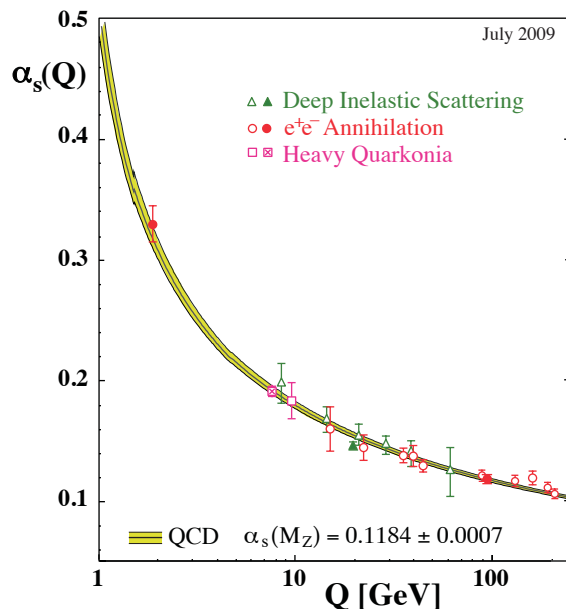


Figure 2.2: The running of the strong coupling constant, α_s . When hadrons are probed with a high energy probe, it is observed that they are not strongly bound together. On the contrary when a weak probe is used, the strong force appears to be very strong [4].

2.4 Deep Inelastic Scattering in the QPM

The lepton-proton DIS process, $lp \rightarrow l'X$, is an invaluable tool for uncovering the partonic nature of the proton. In the Quark Parton Model (QPM), a hadron is described as a configuration of spin- $\frac{1}{2}$ partons. Each parton in the hadron carries a fraction of the total hadronic momentum. Within the QPM, DIS is described as the interaction between a lepton and a quark. The quark is carrying a momentum fraction, x , of the total hadron's momentum. The QPM is a simplified model, but it gives a profound insight into DIS. This section aims to develop an understanding of DIS within the context of the QPM.

2.4.1 Kinematics

Particle interactions in the QPM are understood to be the incoherent sum of point-like scattering of spin-1/2 particles. Of primary interest to this thesis is the electron-proton scattering process $l(k)p(p) \rightarrow l'(k')X(P_X)$, where k , p , k' and P_x are the 4-momenta vectors of their respective states. A schematic Feynman diagram for this process is displayed in figure 2.3. Several Lorentz invariant variables are introduced to

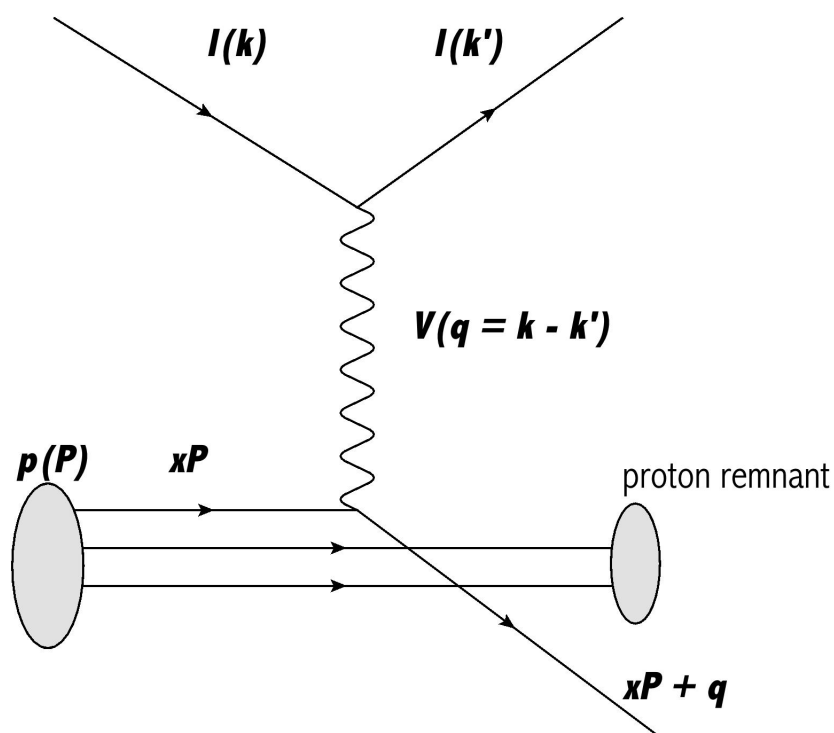


Figure 2.3: A Schematic diagram demonstrating the DIS process $lp \rightarrow l'X$.

describe DIS. In DIS, a lepton and proton interact via the exchange of a virtual vector boson V . The 4-momentum of this vector boson is simply given by the difference between the incoming and outgoing lepton's 4-momenta

$$q = k - k'. \quad (2.2)$$

The depth of the probe, or the virtuality, of the exchange boson can be represented as the inverse square of the exchange boson 4-momentum

$$Q^2 = -q^2. \quad (2.3)$$

The momentum of the hadronic final state is the 4-momentum sum of the incoming proton and the 4-momentum transfer

$$P_X = p + q. \quad (2.4)$$

The centre-of-mass energy squared of the collision is given by the 4-momentum sum of the two initial state particles squared

$$s = (k + p)^2. \quad (2.5)$$

One of the principles behind the QPM is that the partons carry the momentum of the proton and interactions occur with a single parton within the proton, rather than the proton as a whole. If the proton is carrying the momentum p , then it is clear that any given parton will be carrying some fraction xp of the total momentum. This factor x is called the Bjorken scaling variable and is expressed as

$$x = \frac{Q^2}{2p \cdot q}. \quad (2.6)$$

Furthermore, the incoming lepton imparts a fraction of its total energy into the collision. This fraction is called the inelasticity and is related to the lepton scattering angle in the positron-quark centre-of-mass frame

$$y = \frac{p \cdot q}{p \cdot k}. \quad (2.7)$$

The kinematic variables, x , y , Q^2 and s are related to one another via the equation:

$$Q^2 = sxy. \quad (2.8)$$

Because the centre-of-mass energy is typically given a-priori, only two of the variables are independent. Therefore, the whole kinematic space can be described by two of the variables. In addition, the variables are bound by physics restrictions:

$$0 < Q^2 < s$$

$$0 < x < 1$$

$$0 < y < 1$$

The plane spanned by these variables is referred to as the kinematic plane. The (x, Q^2) plane where measurements have been made at the HERA and several fixed target experiments is shown in figure 2.4.

2.4.2 DIS Cross Section

Particle interactions are described in the language of the differential cross section, $d\sigma$, which is the probability of observing a particle at a specific solid angle.

$$\frac{d\sigma}{d\Omega} = \frac{\text{scattered flux/unit of solid angle}}{\text{incident flux/unit of surface}} \quad (2.9)$$

A basic particle physics experimental apparatus consists of a beam of particles with a flux F colliding with a target. At some scattering angle θ , a detector with a solid angle, $d\Omega$, is placed. This detector will measure the flux of scattered particles. An illustration of this concept of a cross section is given in figure 2.5. The total cross section is proportional to the number of events that are measured in every solid angle. This can be obtained by integrating over the measured cross section over all

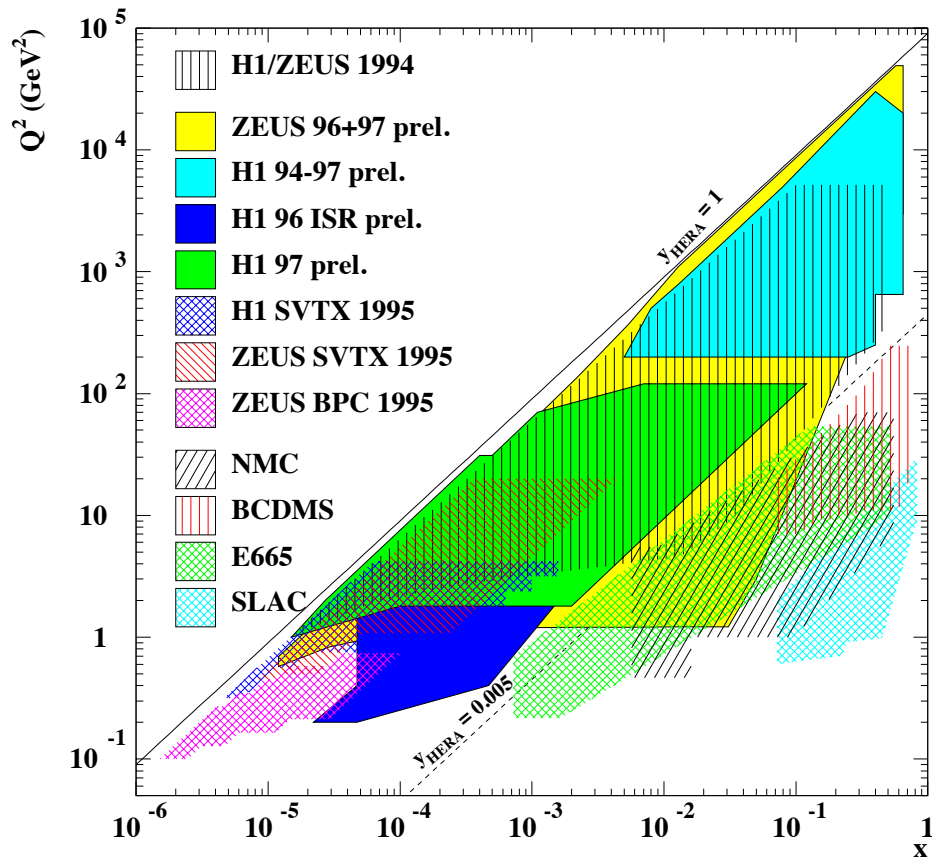


Figure 2.4: The kinematic plane accessible to the HERA experiment and fixed target experiments. Diagonal lines represent regions of constant y . Also shown here is how the HERA kinematic range can be extended with Initial State Radiation (H1 96 ISR) and by events with a shifted vertex (H1/ZEUS SVTX 1995). [5]

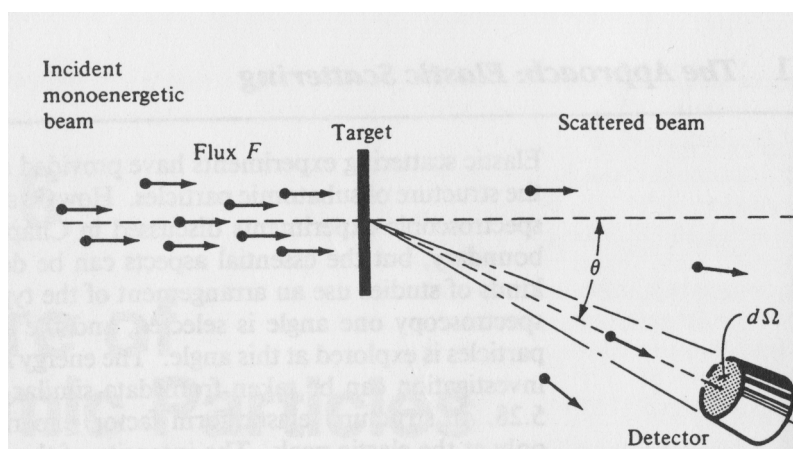


Figure 2.5: A beam of particles is incident on a target. The probability for particles to scatter into a specific solid angle $d\Omega$ is the differential cross section [6]

solid angles $d\Omega$.

$$\sigma_{tot} = \int d\Omega \frac{d\sigma}{d\Omega} \quad (2.10)$$

Cross sections provide a link between experimental results and theoretical predictions. Fermi's golden rule for scattering provides a prescription for mathematically determining a cross section. This rule states that the cross section, σ , is proportional to the amplitude \mathcal{M} . \mathcal{M} can be determined by following a series of Feynman rules [7, 8].

Before examining the DIS cross section, a simpler case will be studied and extended. Electron-muon scattering (Feynman diagram shown in figure 2.6) is an inelastic process where an electron and muon interact via the exchange of a virtual photon. Fermi's golden rule of particle interactions allows one to write the cross section as being proportional to the spin-summed average of the amplitude squared

$$d\sigma \sim \frac{1}{4} \sum_{\text{spins}} |\mathcal{M}|^2 = \frac{e^2 e'^2}{q^4} L_{\mu\nu}^e L_{\mu\nu}^{\mu\text{on}} \quad (2.11)$$

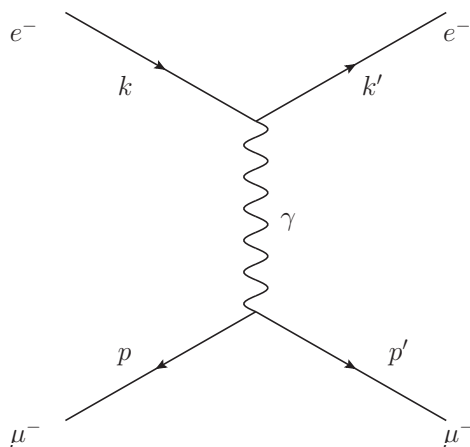


Figure 2.6: A Feynman Diagram for electron muon scattering.

where $L_{\text{muon}}^{\mu\nu}$ is the muon tensor and $L_{\mu\nu}^e$ is the electron tensor. $L_{\mu\nu}^e$ is determined to be

$$L_{\mu\nu}^e = 2(k'_\mu k_\nu + k'_\nu k_\mu - (k' \cdot k)g_{\mu\nu}) \quad (2.12)$$

where k and k' are the 4-momenta of the initial and final state electrons and $g_{\mu\nu}$ is the metric tensor for the space.

The muon tensor is very similar to the electron tensor, replacing the incoming and outgoing electron 4-momentum vectors with those from the muon. This example illustrates that it is possible to define the electron and a muon components of the interaction separately. The cross section is proportional to the tensor multiplication of the two quantities. The same holds true for DIS where the leptonic system interacts with the hadronic system via the exchange of a virtual boson.

It can be inferred from this example that the cross section for DIS should be the contraction of a leptonic tensor with a hadronic one

$$d\sigma \sim L_{\mu\nu}^e W^{\mu\nu}. \quad (2.13)$$

The leptonic tensor, $L_{\mu\nu}^e$, is simply the one found in the electron-muon scattering example, as in equation 2.12. The hadronic tensor, $W^{\mu\nu}$, parameterises our knowledge of the hadronic system. A complete derivation can be found in references [9, 10].

The hadronic tensor simplifies to

$$W^{\mu\nu} = W_1(-g^{\mu\nu} + \frac{q^\mu q^\nu}{q^2}) + \frac{W_2}{M^2}(p^\mu - \frac{p \cdot q}{q^2}q^\mu)(p^\nu - \frac{p \cdot q}{q^2}q^\nu), \quad (2.14)$$

where W_1 and W_2 are scalar functions called structure functions and M is the proton mass. Redefining the structure functions to

$$F_1(x, Q^2) = MW_1(x, Q^2) \quad (2.15)$$

$$F_2(x, Q^2) = \frac{p \cdot q}{M}W_2(x, Q^2), \quad (2.16)$$

and expressing the cross section in terms of the previously defined Lorentz invariant variables x , y and Q^2 , one obtains

$$\frac{d^2\sigma}{dx dQ^2} = \frac{2\pi\alpha^2}{xQ^4} [Y_+ F_2(x, Q^2) - y^2 F_L(x, Q^2)], \quad (2.17)$$

where α is the QED coupling constant, $Y_+ = 1 + (1 - y)^2$ is a kinematical factor and a new structure function, F_L , has been introduced. Referred to as the *longitudinal structure function*, F_L is proportional to the cross section for probing the proton with a longitudinally polarized photon and is related to the other structure functions by

$$F_L(x, Q^2) = F_2(x, Q^2) - 2xF_1(x, Q^2). \quad (2.18)$$

This relationship is known as the Callan-Gross relation.

A third structure function F_3 has been neglected. This structure function is only relevant at higher Q^2 and arises from parity violation in the weak interaction. This

thesis deals with events at lower Q^2 , where W^\pm and Z^0 boson exchanges are negligible.

By dividing out all the kinematical factors, the F_2 structure function can be directly accessed. The reduced cross section is defined to be:

$$\sigma_r(x, Q^2, y) \equiv \frac{xQ^4}{2\pi\alpha^2 Y_+} \left[\frac{d^2\sigma}{dx dQ^2} \right] = F_2(x, Q^2) - \frac{y^2}{Y_+} F_L(x, Q^2) \quad (2.19)$$

In this equation, F_L is suppressed by a factor of $\frac{y^2}{Y_+}$, which means that for small values of y (i.e. $y < 0.5$), the contribution from F_L is negligible. By construct σ_r is dimensionless.

In the QPM, structure functions can be expressed in terms of parton distribution functions (PDFs). Within the context of DIS, PDFs describe the momentum distributions of the partons in the hadron. PDFs cannot be calculated from first principles and must be extracted through structure function measurements. In the QPM they are related to the structure functions by:

$$F_1(x, Q^2) = \sum_i \frac{1}{2} e_i^2 f_i(x) \quad (2.20)$$

$$F_2(x, Q^2) = \sum_i x e_i^2 f_i(x) \quad (2.21)$$

where $f_i(x)$ is the PDF for the quark i , and e is the charge of that quark. By referring to the Callan-Gross relation stated in equation 2.18, it is clear that the longitudinal structure function F_L is zero in the QPM. It is also important to note that these equations don't have any dependence on the interaction scale Q^2 . This property is known as Bjorken scaling. The QPM works very well to describe many phenomena in DIS, but its success is limited by its failure to predict violations in Bjorken scale invariance.

2.4.3 Bjorken Scaling

Bjorken scaling invariance states that, because the proton consists of three point-like spin- $\frac{1}{2}$ fermions, it should look the same at any probe depth. In the QPM, only the spin- $\frac{1}{2}$ fermions are considered to carry momentum. However, it was experimentally verified that gluons actually carry about half of the proton momentum. The contribution from radiative spin-1 gluons and $q\bar{q}$ pair production in the proton gives rise to violations in Bjorken scale invariance. To fully understand the proton, it is important to improve the parton model by introducing the theory of the strong interaction, Quantum Chromodynamics (QCD).

2.5 Deep Inelastic Scattering in QCD

QCD provides a detailed description of DIS and the structure functions. A critical difference between DIS in QCD versus the QPM is the introduction of gluon radiation and $q\bar{q}$ pair production. At DIS energy scales, spin- $\frac{1}{2}$ partons are asymptotically free, allowing for DIS to be studied perturbatively. A consequence of this manifests itself in the factorization theorem and the parton evolution equations. These concepts will be discussed in this section.

2.5.1 Factorization Theorem

Factorization theorem states that the DIS cross section can be factorized into a convolution of two terms: a hard scattering term, which can be exactly calculated using perturbative QCD and a non-perturbative PDF [10, 3]. This is represented by

$$F_2(x, Q^2) = f_i \otimes \hat{\sigma}^i = \int_x^1 \frac{d\xi}{\xi} \sum_i f_i(\xi, \mu) \hat{\sigma}^i\left(\frac{x}{\xi}, \frac{Q^2}{\mu}, \alpha_s\right) \quad (2.22)$$

where $\hat{\sigma}$ is the cross section, f_i is the PDF of any given quark and μ is the *factorization* scale. This equation also has an explicit dependence on Q^2 , which implies violations in Bjorken scaling.

When the factorization scale is sufficiently large, which is the case for DIS, QCD is considered to be weakly coupled. This allows $\hat{\sigma}$ to be calculated order-by-order using a perturbation expansion. The PDFs from equation 2.22 can be extracted by measurements of the structure functions. Furthermore, using perturbative QCD, it is possible to describe the evolution of the PDFs.

2.5.2 DGLAP

Although parton distribution functions are an empirical quantity, a theoretical formalism to describe their evolution was developed by Dokshitzer, Gribov, Lipatov, Altarelli and Parisi, known commonly as DGLAP [11, 12, 13, 14]. These equations describe the way gluon and quark momentum distributions (PDFs) evolve with Bjorken- x and the interaction scale Q^2 :

$$\frac{\partial q(x, Q^2)}{\partial \ln Q^2} = \frac{\alpha_s(Q^2)}{2\pi} \int_x^1 \frac{d\xi}{\xi} \left(P_{q,q}\left(\frac{x}{\xi}\right)q(\xi, Q^2) + P_{qg}\left(\frac{x}{\xi}\right)g(z, Q^2) \right) \quad (2.23)$$

$$\frac{\partial g(x, Q^2)}{\partial \ln Q^2} = \frac{\alpha_s(Q^2)}{2\pi} \int_x^1 \frac{d\xi}{\xi} \left(P_{g,g}\left(\frac{x}{\xi}\right)g(\xi, Q^2) + P_{gq}\left(\frac{x}{\xi}\right)q(z, Q^2) \right) \quad (2.24)$$

where $q(x, Q^2)$ is a quark PDF, $g(x, Q^2)$ the gluon PDF and $P(\frac{x}{\xi})$ is a splitting function. There are four splitting functions, each representing the probability of a specific QCD radiative process. The leading order diagrams representing each of the four splitting functions are displayed in figure 2.7, where z ranges between 0 and 1. These diagrams represent the first order in a perturbation expansion and are defined

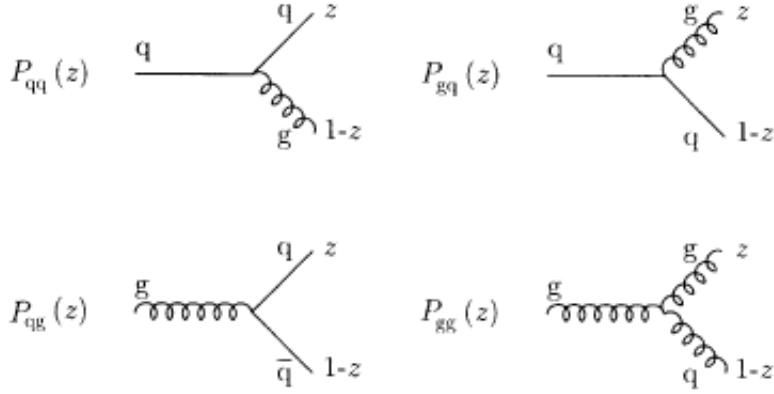


Figure 2.7: The four leading order splitting functions[10]

mathematically as:

$$P_{qq}(z) = \frac{4}{3} \left[\frac{1+z^2}{1-z} \right] \quad (2.25)$$

$$P_{gq}(z) = \frac{4}{3} \left[\frac{1+(1-z^2)}{z} \right] \quad (2.26)$$

$$P_{qg}(z) = \frac{1}{2} [z^2 + (1-z^2)] \quad (2.27)$$

$$P_{gg}(z) = 6 \left[\frac{1-z}{z} + \frac{z}{1-z} + z(1-z) \right] \quad (2.28)$$

Figure 2.8 shows how the PDFs for the up quark, down quark, gluon and the partonic sea, evolve with Bjorken- x for a fixed Q^2 . These PDFs were extracted by the HERAPDF working group [15] and use only structure function measurements from HERA. The ZEUS experiment also has its own PDF sets known as ZEUS-JETS [16] and these use only ZEUS measurements. Other groups produce more global PDF sets, including CTEQ [17] and MSTW [18]. CTEQ and ZEUS-JETS PDF sets will be used throughout this thesis. PDFs are implemented into the PDFLIB program [19], which can be easily integrated into Monte Carlo (MC) simulations.

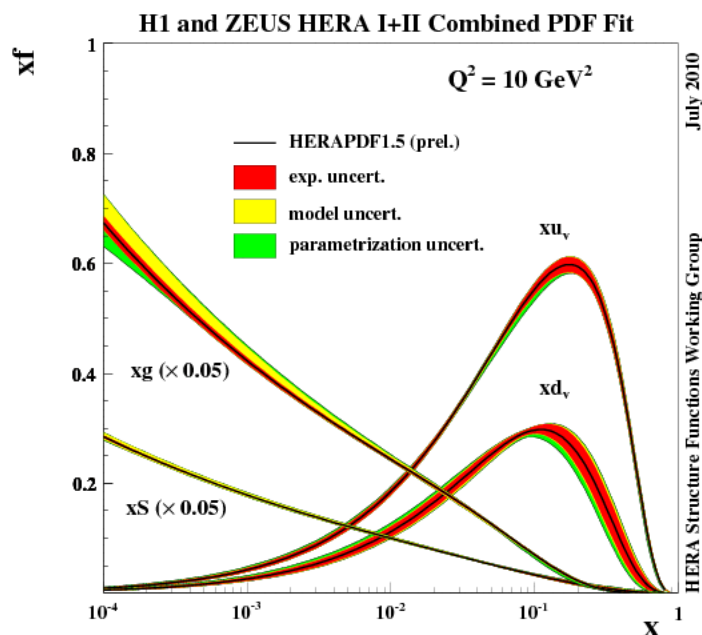


Figure 2.8: An example of PDFs extracted from HERA structure function measurements. The u , d sea and gluon contributions are shown.

As seen from equation 2.22, PDFs are related to the structure functions. PDFs are commonly extracted from DIS via reduced cross section and structure function measurements. The H1 and ZEUS experiments had unparalleled success at measuring DIS. A summary of measurements is given in figure 2.9. These results are compared with the HERAPDF1.0 PDF set.

At low- Q^2 and high- x the valence quarks carry the largest contribution of the proton momentum. As Q^2 increases, the distance scales being probed decreases giving rise to more quantum fluctuations within the proton and hence larger contributions from the $q\bar{q}$ sea. At high- Q^2 and low Bjorken- x , the $q\bar{q}$ sea and gluon dynamics dominate and contribute to scaling violations. This gluon dominated region is where contributions from the longitudinal structure function F_L become non-negligible.

H1 and ZEUS

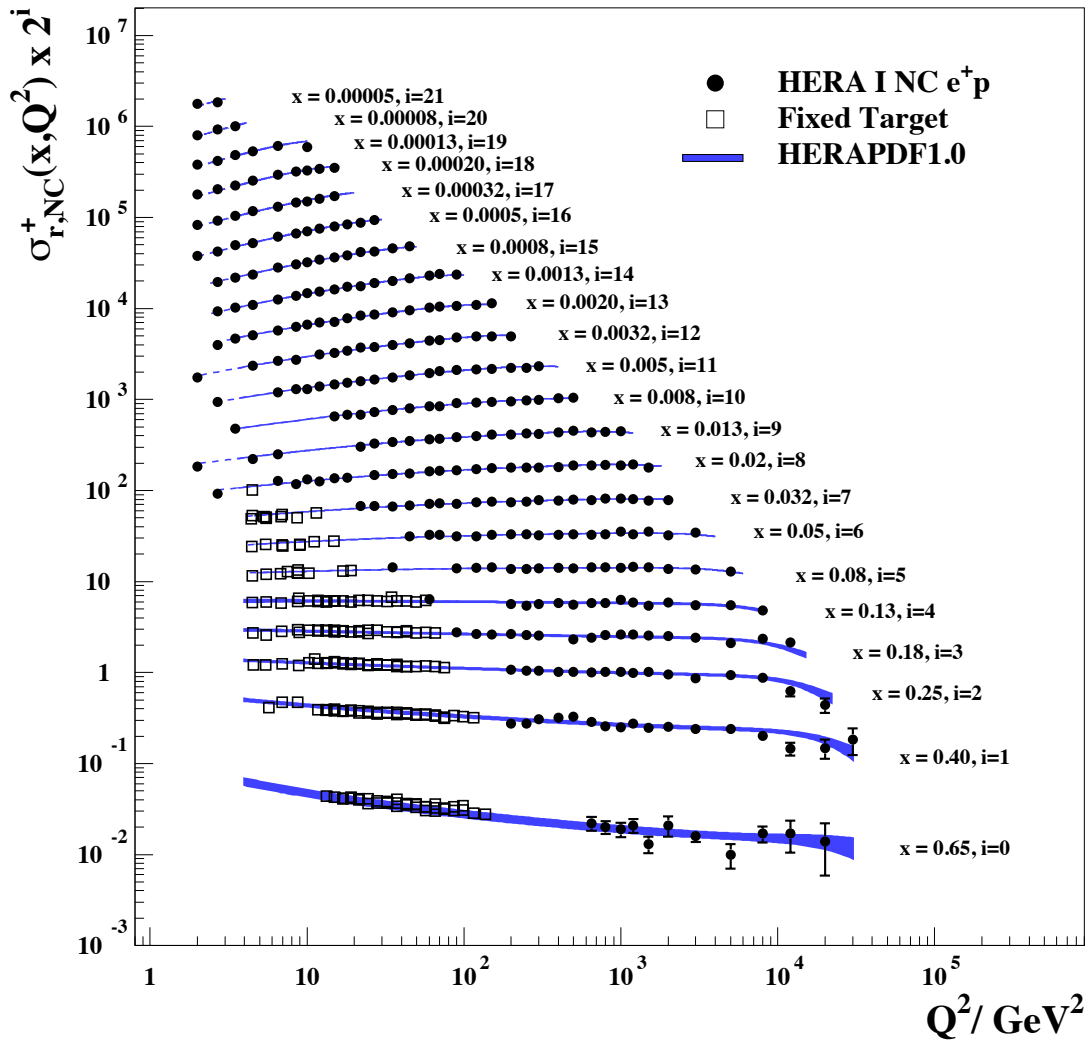


Figure 2.9: Measurement of the DIS reduced cross section for a large range of x and Q^2 . Measurements were made with the ZEUS and H1 experiments and combined into a common measurement.

2.5.3 The Longitudinal Structure Function F_L

The Callan-Gross relationship, equation 2.18, $F_L(x, Q^2) = F_2(x, Q^2) - 2xF_1(x, Q^2)$, demonstrates the association between the longitudinal structure function, F_L , and the other structure functions, F_1 and F_2 . F_L obtains its name because it is proportional to the cross section for probing the proton with a longitudinally polarized photon.

Using the Callan-Gross relationship, we can determine F_L from the F_1 structure function, which is proportional to the cross section for transversely polarized photons

$$F_1 = \frac{Q^2}{8x\pi^2\alpha} \sigma_T \quad (2.29)$$

and F_2 which is a superposition of the longitudinal and the transverse cross sections

$$F_2 = \frac{Q^2}{4\pi^2\alpha} (\sigma_T + \sigma_L). \quad (2.30)$$

Real photons are transversely polarized, implying that $\sigma_L = 0$, although this does not have to be true for virtual photons. However, longitudinally polarized virtual photons cannot probe spin- $\frac{1}{2}$ particles because it violates helicity. This concept is demonstrated in figure 2.10(a). This implies that in the QPM, where the gluon is disregarded, $F_L = 0$. In QCD this does not need to be the case since the helicity can be balanced by the introduction of gluon radiation. This is shown in figure 2.10(b). In the DGLAP formalism, at low- x , the F_2 structure function is dominated by contributions from the $q\bar{q}$ sea. The low- x region also contains a sizeable contribution from the gluon, which manifests itself in scaling violations in the F_2 structure function. Using the DGLAP equations 2.23 and 2.24, the F_2 structure function can be inferred as a convolution of the quark-gluon splitting function P_{qg} , with the gluon

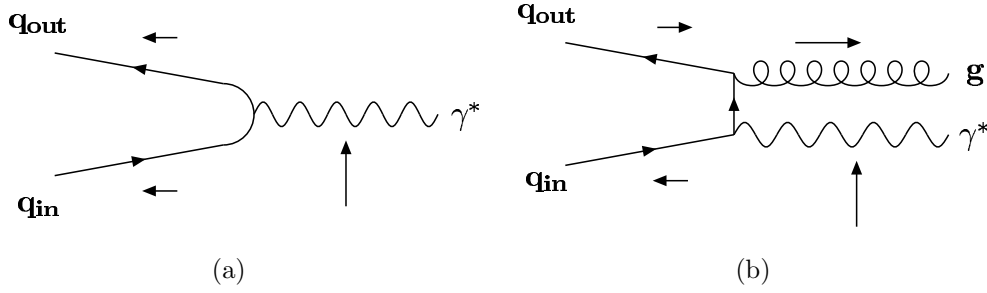


Figure 2.10: (a) In the Breit Frame a quark interacts with a longitudinally polarized virtual photon and subsequently flips its helicity. This violates helicity conservation. (b) Introducing a gluon balances the helicity [20].

parton distribution function g :

$$\frac{\partial F_2(x, Q^2)}{\partial \ln Q^2} = \frac{\alpha_s(Q^2)}{2\pi} \left[P_{qq} \otimes F_2 + 2 \sum_i^{n_f} e_i^2 P_{qg} \otimes xg \right] \quad (2.31)$$

where α_s is the strong coupling constant, the P 's are the splitting functions and g is the gluon PDF. Measuring the gluon PDF is complicated by this convolution. Fortunately, the longitudinal structure function provides direct access to the gluon PDF. Following from the Callan-Gross relationship, $F_L = F_2 - 2xF_1$, it can be derived that

$$F_L(x, Q^2) = \frac{\alpha_s}{2\pi} \int_x^1 \frac{d\xi}{\xi} \left[\frac{8}{3} \left(\frac{x}{\xi} \right)^2 F_2(\xi, Q^2) + 4 \sum_i^{n_f} e_i^2 \left(\frac{x}{\xi} \right)^2 \left(1 - \frac{x}{\xi} \right) \xi g(\xi, Q^2) \right] \quad (2.32)$$

This equation shows a direct relationship between F_L and the gluon parton distribution function, $g(x)$. The determination of the longitudinal structure function is one of the achievements outlined in this thesis.

2.6 Relevant Physics Processes

DIS, mediated by a neutral current (γ or Z^0), is the main physics process of interest for this thesis. However, several other physics processes occur in a high energy

electron-proton environment, some of which could potentially be misidentified. This section describes the event topologies for processes which occur in an ep environment.

2.6.1 DIS

DIS events are events with high virtualities where the exchange boson can probe deep into the proton to reveal its internal structure. The diagram representing this process was displayed in figure 2.3. In a neutral current DIS event, the hadronic energy flow, from the scattered parton, is balanced by the scattered electron. For the case of charged current DIS, a neutrino will escape detection and the system will look unbalanced. Moreover, in a DIS event, the proton will be broken up and its remnant will continue to travel in the forward direction. Partons being ejected from the proton result in the creation of hadronic jets. These jets give insight into the partonic nature of the proton.

2.6.2 Photoproduction

Photoproduction occurs in the kinematic regime where $Q^2 \sim 0$. An almost real photon is emitted from the incoming electron, resulting in it being only slightly deflected. Because of the low virtuality of the event, the photon is unable to probe the internal partonic structure. Instead, partons within the proton can, in turn, probe the photon for its internal partonic structure. A parton in the proton and a parton in the photon have a large momentum exchange resulting in high transverse energy (E_T) jets. At leading order there are two types of photoproduction processes, direct and resolved. The Feynman diagrams for the two leading order processes are shown in figure 2.11. In direct photoproduction the photon interacts as a whole with the quarks within the proton. In the resolved process quantum fluctuations within

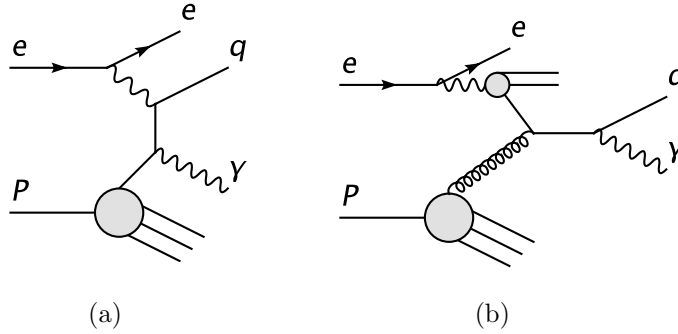


Figure 2.11: The two leading order diagrams for direct photoproduction (a) and resolved photoproduction (b)

the photon can create a hadronic state and partons within the proton can interact with it.

Photoproduction occurs in copious amounts resulting from the $\frac{1}{Q^4}$ suppression of the DIS cross section (see equation 2.17). For this thesis, photoproduction is a background process. It interferes with DIS because the topology makes it possible for it to fake higher- Q^2 event. This is especially likely when high- E_T jets are produced and when the photon is scattered at a large polar angle at the same time.

2.6.3 Diffractive DIS

About 10% of all DIS events seen at HERA are categorized as being diffractive events. These events are characterized by the proton being unbroken and only slightly deflected, while hadronic jets are created and measured with a large gap, separating the jets from the proton remnant. There are two classes of diffractive events: single dissociative, where the proton is left completely intact, and double-dissociative, where the proton is broken up. The large gap in rapidity is caused by the transfer of a colourless object called a Pomeron.

Understanding the diffractive portion of DIS is key to understanding the overall hadronic energy flow in the system for all events.

2.7 Initial State Radiation

Initial State Radiation (ISR) is the emission of a hard photon, from the electron, prior to a DIS interaction. By effectively reducing the energy of the incoming electron, E_e , and hence the collision centre-of-mass energy, ISR modifies the reconstruction of the event kinematics [21]. A Feynman diagram representing a DIS interaction with the emission of ISR is shown in figure 2.12.

The collision centre-of-mass energy of the radiative DIS event is $\sqrt{s} = \sqrt{4E_p(E_e - E_\gamma)}$. Denoting the 4-momenta of the ISR photon as k_γ , the gauge invariant kinematic variables become:

$$Q^2 = -q^2 = -(k - k' - k_\gamma)^2 \quad (2.33)$$

$$x = \frac{Q^2}{2p \cdot q} \quad (2.34)$$

$$y = \frac{q \cdot p}{(k - k_\gamma) \cdot p} \quad (2.35)$$

In measurements, the way that ISR modifies the kinematic reconstruction is also dependent on the reconstruction method. This will be discussed in more detail in section 5.3.

DIS with ISR is described by the triply differential cross section [22]:

$$\frac{d^3\sigma}{dx dQ^2 dz} = \alpha^3 P(z) \frac{1 + (1 - Q^2/xzS)^2}{xQ^4} \left\{ F_2(x, Q^2) - \frac{y^2}{Y_+} F_L(x, Q^2) \right\} \quad (2.36)$$

where z is the fraction of the beam energy lost to the ISR photon. This is defined as:

$$z = \frac{E_e - E_\gamma}{E_e} \quad (2.37)$$

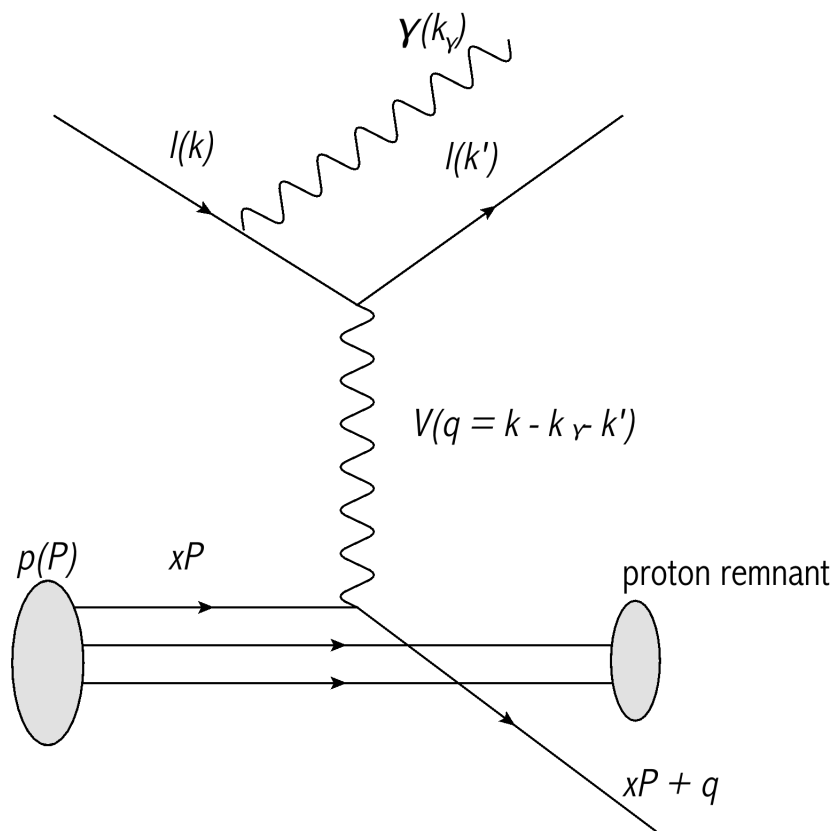


Figure 2.12: A Feynman diagram depicting DIS in the presence of Initial State Radiation.

$P(z)$ is the QED splitting function, which represents the probability of emitting a photon with a specific energy, E_γ . This is defined by

$$P(z) = \frac{1 + z^2}{1 - z} \ln \frac{E_e^2 \theta_0^2}{m_e^2} - \frac{z}{1 - z} \quad (2.38)$$

where θ_0 is the photon polar angle with respect to the electron beam line. Photons emitted in ISR are essentially co-linear, hence θ_0 is typically less than 0.25 mrad [23].

ISR can be thought of as an electroweak correction to the DIS cross section and can contribute significantly to the overall DIS cross section. The $\frac{1}{Q^4}$ suppression of the DIS cross section implies many more events will be observed at low- Q^2 than at

high- Q^2 . It also implies that ISR events that are generated below a certain threshold will migrate into regions of higher Q^2 . At really high- y values, migrations from ISR can be higher than 50%. In addition to the measurement of the protons longitudinal structure function, understanding the contributions from ISR to DIS is one of the primary studies outlined in this thesis.

CHAPTER 3

HERA and ZEUS

3.1 The HERA Collider

The Hadron-Electron Ring Accelerator (HERA)[24] accelerated and collided electrons (or positrons¹) and protons with asymmetric beam energies. HERA was located at the Deutsches Elektronen Synchrotron (DESY) facility in Hamburg, Germany. Built by an international collaboration, it began operating in 1992 and was decommissioned in the summer of 2007.

HERA consisted of a main storage ring being fed protons and electrons from the pre-accelerator, PETRA. The circumference of the main storage ring was 6.3 km and it ran 15-20 meters under the western outskirts of the city of Hamburg. Electrons of $E_e = 27.5$ GeV and protons of $E_p = 920$ GeV were accelerated separately in opposite directions and collided at two interaction points. HERA hosted two colliding beam experiments, H1 and ZEUS, and two fixed target experiments; HERA-B and HERMES. The HERA beam line is outlined in the figure 3.1.

HERA initially collided protons of $E_p = 820$ GeV with electrons of $E_e = 27.5$ GeV. The proton beam was upgraded in 1998 to $E_p = 920$ GeV and the electron beam

¹ the term electron will be used interchangeably to describe both electrons and positrons. When the distinction is required a special note of it will be made (see page 9).

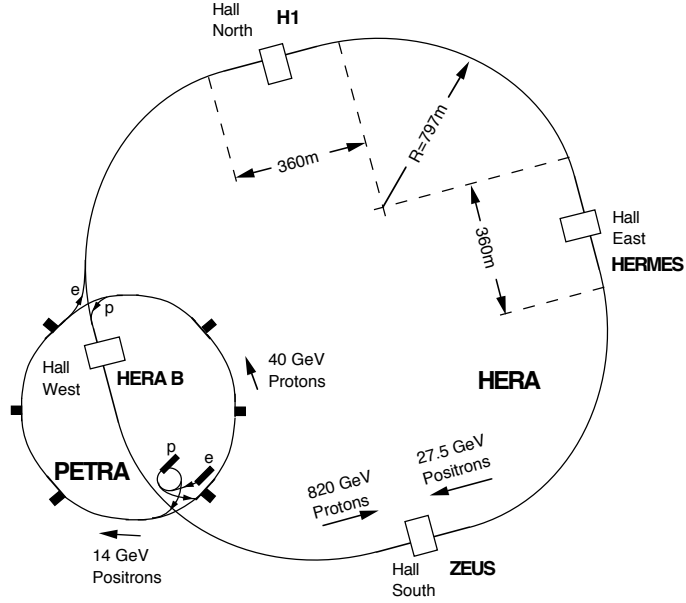


Figure 3.1: The HERA Accelerator and the location of experimental halls

energy was left unchanged. Throughout its lifetime HERA delivered about half an inverse femtobarn of luminosity to each of the colliding beam experiments. The evolution of the luminosity with time is outlined in figure 3.2. In the last six months of data taking, HERA lowered the proton beam energy twice to facilitate a measurement of the longitudinal structure function. The various beam energies and luminosities collected and relevant to this thesis are displayed in table 3.1.

	E_e [GeV]	E_p [GeV]	\sqrt{s} [GeV]	\mathcal{L} [pb^{-1}] Delivered	\mathcal{L} [pb^{-1}] ZEUS Measured
HER	27.5	920	318.2	180.54	145.90
MER	27.5	575	251.5	9.36	7.77
LER	27.5	460	224.9	15.69	13.18

Table 3.1: Beam energies and luminosity delivered by HERA and measured by ZEUS for the 2006 and 2007 e^+ running period. HER, MER and LER refer to High, Medium and Low energy running periods respectively.

The rate of collisions at HERA is defined by the equation:

$$R = \sigma L \quad (3.1)$$

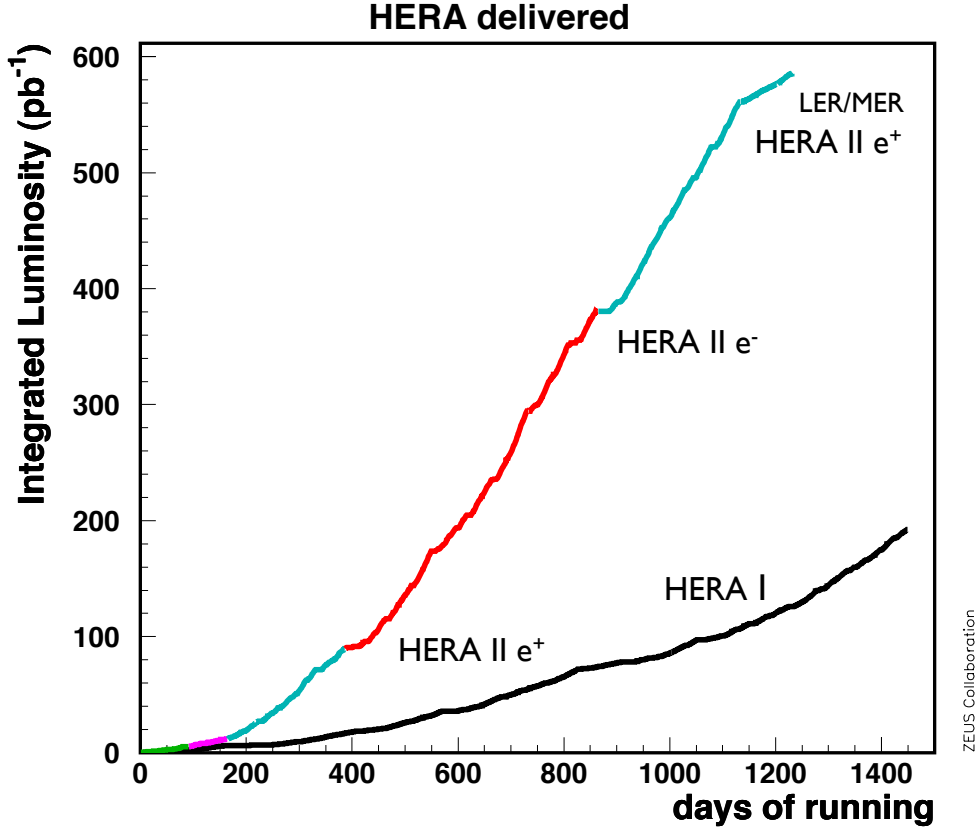


Figure 3.2: The total luminosity delivered by the HERA Accelerator as a function of time. Both running periods are displayed separately.

where σ is the cross section and L is the instantaneous luminosity which can be written as:

$$L = fn \frac{N_e N_p}{4\pi\sigma_x\sigma_y} \quad (3.2)$$

where n is the number of bunches in each beam, f is the frequency of revolutions, N_e and N_p are the number of particles per bunch and σ_x and σ_y are the height and width of the beam. L is the instantaneous luminosity in units of collisions per area and is not to be confused with \mathcal{L} which is the luminosity integrated over time. When the term luminosity is used throughout this thesis, it is to refer to the integrated luminosity, which is defined as $\mathcal{L} = \int L dt$.

In the year 2000, HERA underwent a significant upgrade designed to increase the

luminosity. Modest increases to the beam currents were implemented and the beam widths were reduced. The period before the upgrade is commonly referred to as HERA–I and the period post upgrade as HERA–II. Table 3.2 outlines HERA’s design parameters, the analysis outlined in this thesis uses data from HERA–II exclusively. HERA–I properties are just included for historical perspective.

Parameter	HERA–I		HERA–II	
	electrons	protons	electrons	protons
Energy [GeV]	27.5	820 / 920	27.5	920
Beam current [mA]	50	100	58	140
Number of bunches	200		220	
Particles per bunch	$3.5 \cdot 10^{10}$	$7.3 \cdot 10^{10}$	$4.0 \cdot 10^{10}$	$10.3 \cdot 10^{10}$
Bunches in beam	189	180	189	140
Colliding bunches	174		180	
Bunch spacing [ns]	96		96	
Beam width (σ_x) [μm]	187	187	112	112
Beam height (σ_y) [μm]	50	50	30	30
Luminosity (L) [$\text{cm}^{-2}\text{s}^{-1}$]	$1.78 \cdot 10^{31}$		$7.57 \cdot 10^{31}$	

Table 3.2: HERA design parameters [25]

HERA–II was capable of storing 220 bunches separated by 96ns. Since not all bunches were populated, four possible scenarios could occur for each bunch crossing:

- The electron bunch and the proton bunch will cross at the interaction point.
- The electron bunch will pass through the interaction point with no matching proton bunch.
- The proton bunch will pass through the interaction point with no matching electron bunch.
- Both electron and proton bunches are empty.

The filled bunches with no partner are referred to as pilot bunches and play an important role in understanding the luminosity and calibrating detector components in the luminosity system.

3.2 The ZEUS Detector

The ZEUS detector[26] is a general purpose detector designed to measure all physics processes occurring at HERA. ZEUS was an asymmetric hermitic detector covering the entire solid angle, except around the beam pipe. An asymmetric design is desired to account for the energy imbalance of the ep collision. The hadronic energy mostly flows in the forward direction. A cartesian right-handed coordinate system is used for describing the detector geometry. The geometry was defined for a proton travelling in the positive z -direction to collide with an electron at $z = 0$. The y -direction is defined so that positive y points upwards. x is defined as pointing horizontally into the centre of the HERA ring. The coordinate $(x, y, z) = (0, 0, 0)$ occurs at the interaction point. A visual representation of the coordinate system is displayed in figure 3.3.

The innermost component surrounding the interaction point is the silicon-based Micro Vertex Detector (MVD) [27]. Traveling outward from the IP is the Central Tracking Detector (CTD). There exists tracking detectors in the forward region including the Forward Tracking Detector (FTD) and the Straw-Tube Tracker (STT) as well as a small tracking detector in the rear (SRTD). Just beyond the tracking detectors is a solenoid providing a 1.43 T magnetic field. As a result of the magnetic field, charged tracks will bend in the tracking detectors allowing for a momentum measurement. Surrounding the solenoid and the tracking detectors are three separate calorimeters; the Forward Calorimeter (FCAL), Barrel Calorimeter (BCAL) and the Rear Calorimeter (RCAL). The calorimeter is separated into electromagnetic and

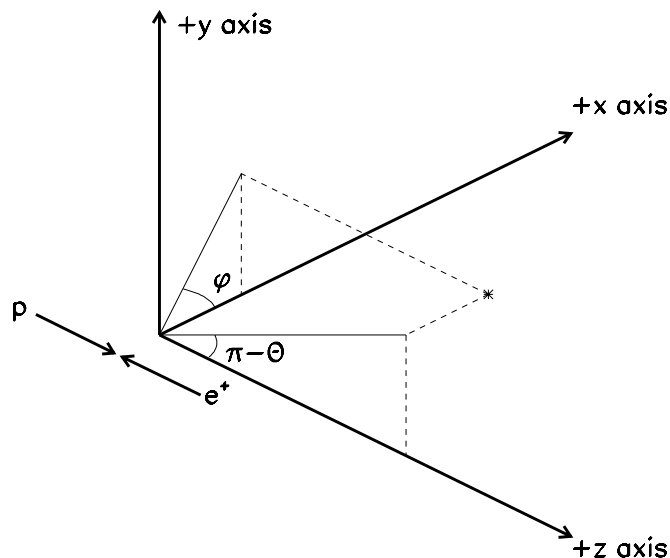


Figure 3.3: The ZEUS Coordinate System

hadronic components. The Rear Hadron-Electron Separator (RHES) is a layer of silicon pad detectors and is located within the electromagnetic calorimeter. On the outer layer of the ZEUS detector are the muon spectrometers (FMUON, BMUON and RMUON) which measure high energy muons.

A cartoon depiction of the ZEUS detector is shown in figure 3.4 and the components most relevant to this thesis will be discussed in further detail below.

3.2.1 Tracking Detectors

The charge, momentum and vertex information of charged particles are determined by the ZEUS tracking system. This system contains two main components, the MVD [28, 29] and the CTD [30, 31]. Both are located inside the superconducting solenoid which supplies a 1.43 T magnetic field.

Installed during the HERA luminosity upgrade, the MVD is a silicon strip tracking detector. The detector was comprised of two components, the forward MVD (FMVD)

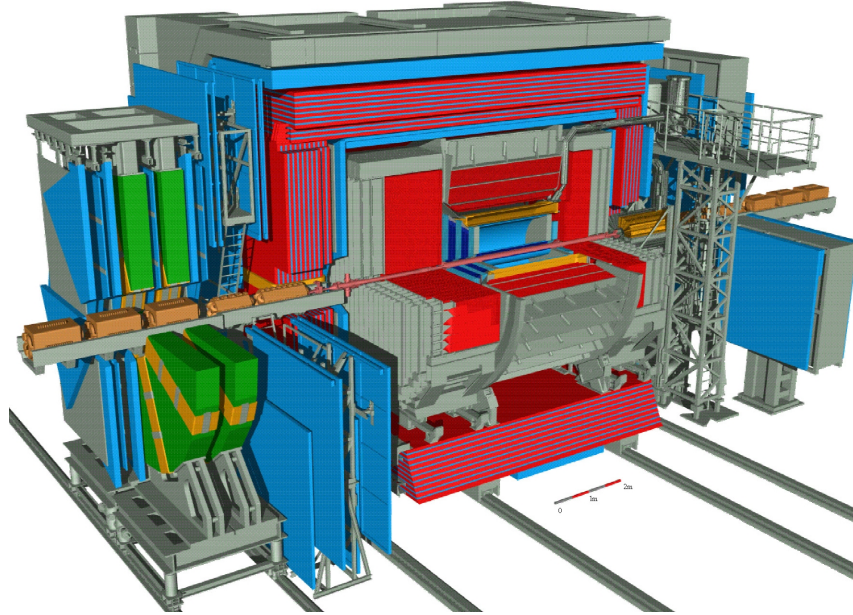


Figure 3.4: Cartoon depicting the ZEUS Detector

and the barrel MVD (BMVD), and covers the polar region $7^\circ < \theta < 150^\circ$. A transverse slice of the MVD is shown in figure 3.5.

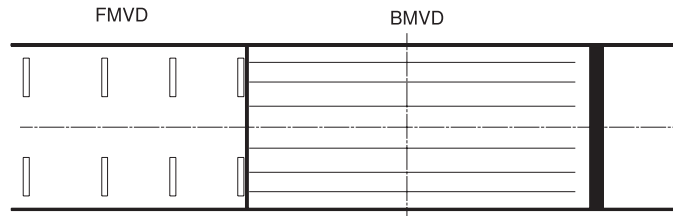


Figure 3.5: A longitudinal cut of the MVD depicting its two components, BMVD and FMVD.

The BMVD contains 600 silicon strip detectors mounted on 30 support structures. The strip detectors are square and measure 6.15 x 6.15 cm in size. The arrangement of strips is shown in figure 3.6(a). The FMVD is composed of 480 silicon readout strips arranged in a circular wheel around the beam pipe, with the beam coming in perpendicularly to the detector face. From figure 3.6(b) we see two different sizes of trapezoidal strips used, they measure roughly about 7x7.5 cm in size. Since the

beam pipe is elliptical the two different shapes of the wedges are used to maximize coverage. Because of the proximity to the IP, the MVD is subject to very high levels

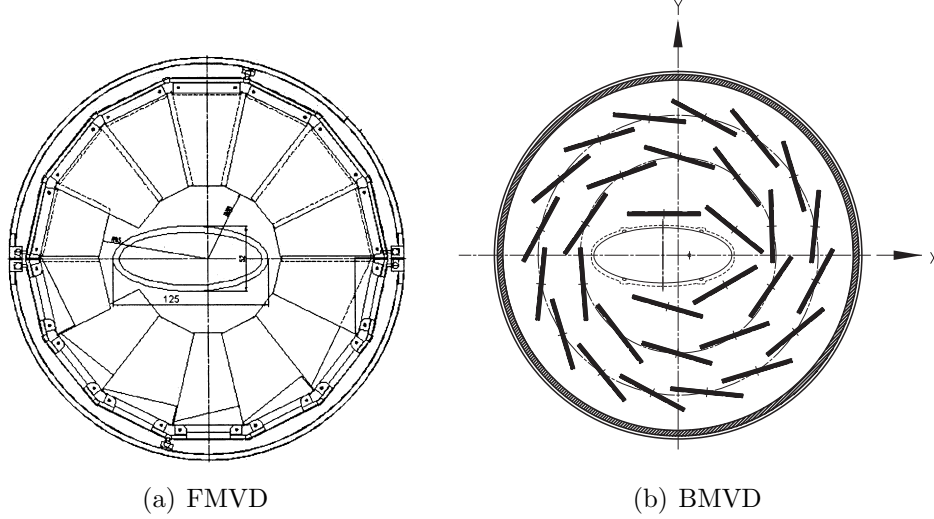


Figure 3.6: A transverse view of the ZEUS MVD components.

of radiation. Regardless of this, hit efficiencies are around 98%.

The CTD [30, 31] was the preferred component for measuring the charge and momentum of charged particles. The CTD was a wire drift chamber filled with a $\text{Ar}:\text{CO}_2:\text{C}_2\text{H}_6$ gas mixture. It had a 205 cm active length and operated within the polar region $15^\circ < \theta < 164^\circ$. The CTD is organized into 9 concentric superlayers, which are comprised of 32 (inner most) to 96 (outermost) drift chambers, see figure 3.7. In total the CTD consists of 4068 sense wires.

Tracks which traverse at least three superlayers and for $p_T > 150$ MeV have a transverse momentum resolution of $\sigma(p_T)/p_T = 0.0058p_T \oplus 0.0065 \oplus 0.0014/p_T$. For tracks that pass through all superlayers the position resolution in the $r - \phi$ plane is $180 \mu\text{m}$ and 2 mm in the z -direction. The combined resolution of the CTD and MVD system is $\sigma(p_T)/p_T = 0.0026p_T \oplus 0.0104 \oplus 0.0019/p_T$ [32].

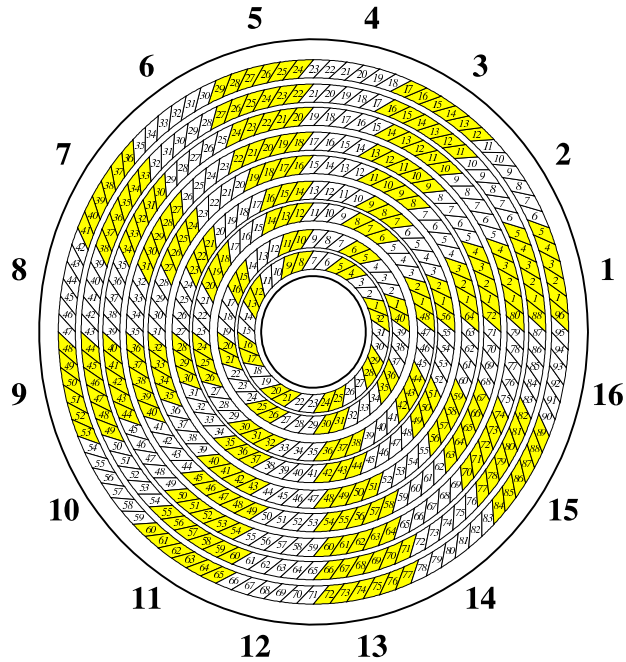


Figure 3.7: The x-y profile of the ZEUS CTD. The 9 superlayers and 16 sectors are visually represented.

3.2.2 The Uranium-scintillator Calorimeter

The ZEUS calorimeter [33] is a high-resolution uranium²-scintillator sampling compensating calorimeter. It is roughly hermetic and surrounds the solenoid and the tracking systems. It is segmented into three areas: the Forward Calorimeter (FCAL), Barrel Calorimeter (BCAL) and Rear Calorimeter (RCAL). A general schematic view of the detector is shown in figure 3.8. The calorimeter is subdivided into different units, the smallest of which is called a cell. Cells are combined together to form towers. The BCAL and FCAL towers are made up of one layer of electromagnetic (EMC) cells and two hadronic (HAC) cells, while the RCAL tower consists of just one electromagnetic and one hadronic cell. An example of a BCAL tower is shown

² depleted U: U²³⁸(98.1%) Nb(1.7%)+U²³⁵(0.2%)

in figure 3.9. A set of towers forms a module within the FCAL, BCAL or RCAL.

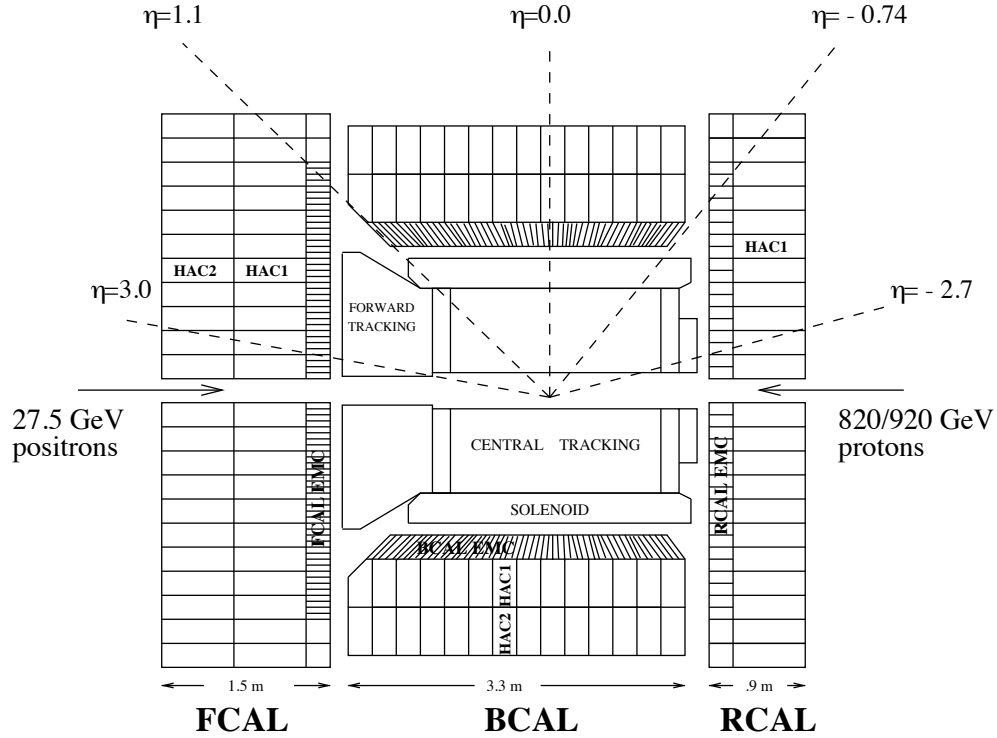


Figure 3.8: A schematic of the ZEUS Calorimeter with components labelled and where η is the pseudorapidity defined by $\eta = -\ln \tan \frac{\theta}{2}$.

The calorimeter covers an angular region between $2.2^\circ < \theta < 176.5^\circ$ and varies between 24.3 and 25.9 radiation lengths deep.

Each calorimeter cell is read out by two photomultiplier tubes (PMT). The benefit of having a double readout, is that when one PMT fails, one can still make an energy measurement. Both PMTs failing at the same time would create a “hole” in the detector and the energy deposit information would be lost. For this reason, bad channels were constantly monitored and repaired throughout the lifetime of the experiment. For most the HERA-II running period bad channels were kept below 2.5% and holes were consistently less than five out of 6000 [34]. Having a redundant

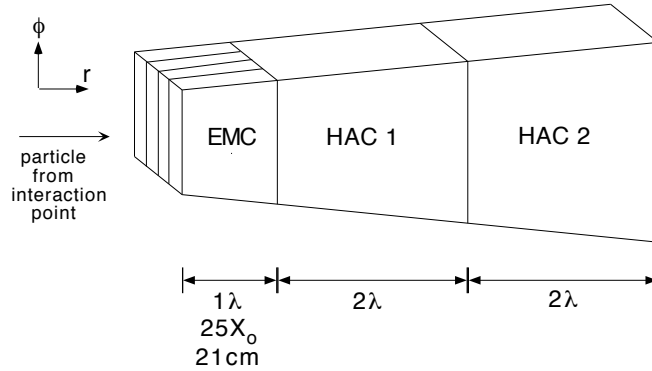


Figure 3.9: A diagram of a BCAL Tower. Four EMC cells are stacked horizontally and two HAC are stacked on on top.

readout also makes it possible to measure the position of a particle by using the energy imbalance in one PMT versus the energy in the other:

$$I = \frac{E_{left} - E_{right}}{E_{left} + E_{right}} \quad (3.3)$$

This is proportional to the position of the particle within the cell.

The choice of uranium as an absorber leads to an effect called compensating calorimetry. Electrons and hadrons deposit energy in calorimeters differently. Electrons and photons travelling through a material will undergo an electromagnetic showering process, quickly succumbing to bremsstrahlung and e^+e^- pair production. Hadronic showers also have an electromagnetic component through $\pi^0 \rightarrow \gamma\gamma$, but they also lose energy to *single particle interactions*. In a non-compensating calorimeter an electron will deposit more energy in the calorimeter than a pion of the same energy. In a compensating calorimeter particles will hard scatter off uranium atoms causing the release of slow moving neutrons. The slow moving neutrons collide with the protons in the scintillator, producing a signal which is measured by the PMTs. With compensation, the ratio of energy deposited by electrons or hadrons of the same

energy, e/h , is equal to 1. This effect is the motivating factor behind the choice of uranium rather than a more commonly used material like lead, iron or tungsten. Compensation in ZEUS is achieved with an absorber plate thickness of one radiation length ($1X_0$ or 3.3 mm) layered in-between 2.6 mm sheets of scintillator.

Another benefit from using uranium is that it acts as a consistent low level signal for detector calibration. By monitoring the readout from the PMTs over time one can adjust the energy calibration or determine if a channel should be marked as bad.

Using a test beam of electrons the electromagnetic energy resolution was found to be $\sigma(E)/E = 18\%/\sqrt{E [\text{GeV}]}$. The hadronic energy resolution was determined using a pion beam to be $\sigma(E)/E = 35\%/\sqrt{E [\text{GeV}]}$ [35].

The light yield from the scintillator was observed by PMT's via two wavelength shifting optical guides (WLS). The signals from the PMTs go to the front end electronics, which were mounted on the calorimeter [33]. From the front end electronics the processed signals are sent to the Calorimeter First Level Trigger (CFLT) which uses them for the decision to accept or reject the event.

3.2.3 Small Angle Rear Tracking Detector and the Hadron-Electron Separator

The Small Angle Rear Tracking detector (SRTD) [36] was mounted on the face of the RCAL and surrounded the beam pipe. It consisted of two layers of scintillator strip arrays arranged into horizontal and vertical strips. The SRTD provided a better position resolution than the calorimeter, especially at lower electron angles. The SRTD covered the angular range $163^\circ < \theta < 176^\circ$ and had a position resolution of ~ 3 mm.

The Hadron-Electron Separators (HES) [37, 38] were shower maximum detectors embedded in the RCAL (RHES) and FCAL (FHES) at the location of the shower maximum ($\sim 3X_0$). A plane of $20\text{ cm} \times 20\text{ cm}$ silicon diode panels comprised the HES. The HES was segmented more finely than the CAL and provided a more accurate position measurement and helped in the identification of electrons.

3.2.4 Trigger and Data Acquisition

HERA has a beam crossing every 96 ns which corresponds to an interaction rate of 10.4 MHz. But we are only interested in specific classes of events, the rest are considered backgrounds. The main source of background comes from low- Q^2 (soft) interactions. However the background can come from many sources, including beam-gas interactions, halo muons, cosmic rays and synchrotron radiation of the electron beam. The desirable physics processes are produced at a much smaller rate than the background. The purpose of the ZEUS trigger system is to reject events which are not wanted and to reduce the event sample to a manageable size.

The ZEUS data acquisition (DAQ) system is capable of working with an input rate of ~ 10 Hz. The trigger must work within the means of the DAQ system and reduce the rate from 10.4 MHz to 10 Hz. ZEUS uses a three level trigger system. Raw energies from the detector components are used as input into the First Level Trigger (FLT). The FLT outputs good events to the Second Level Trigger (SLT). In the SLT the event rate is further reduced before being reconstructed in the event builder. The event builder sends events at a rate of ~ 80 Hz to the Third Level Trigger (TLT) which selects good events and sends them to the computing facilities for storage and easy access for analysis. For archival purposes and redundancy a copy is stored on tape. A diagram of the three level trigger system designed for ZEUS is shown in Figure 3.10.

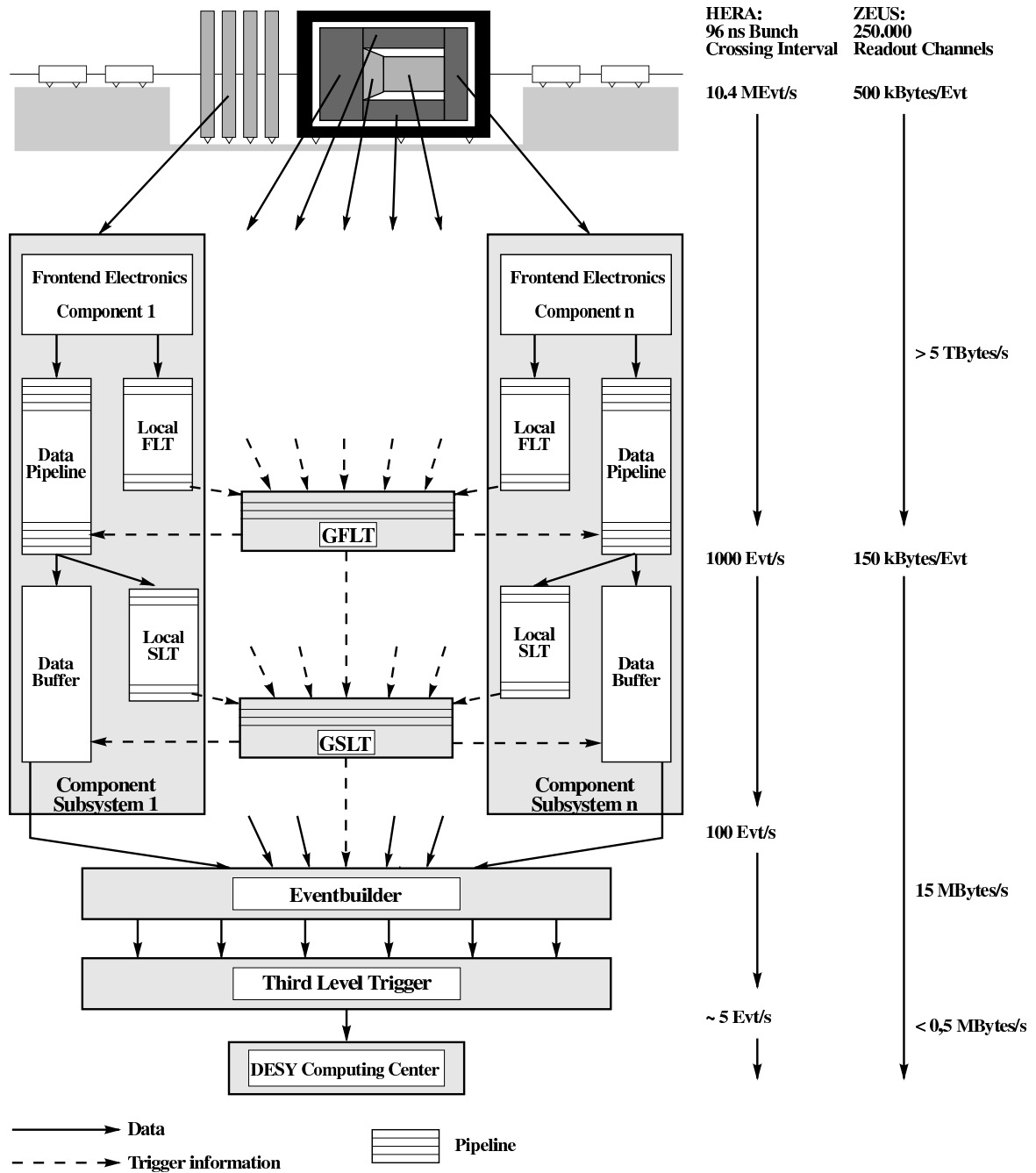


Figure 3.10: The ZEUS trigger and DAQ system [39]

3.2.5 First Level Trigger

The First Level Trigger (FLT) must suppress the background and reduce the signal from 10.4 MHz to about 1 kHz. Each main detector component has its own FLT processor and the trigger information is combined into the Global First Level Trigger (GFLT). The GFLT minimally reconstructs an event and can make a decision whether to accept or reject. The time between bunch crossings (96 ns) is too short to make a trigger decision. Because of this the event information is stored in a pipeline and processed about $4.4\mu\text{sec}$ after the crossing. If the event passes the GFLT criteria it is sent to the second level of processing [40].

3.2.6 Second Level Trigger

The rate of events at the Second Level Trigger (SLT) is around 1 kHz, giving the SLT more time to reconstruct the event. The local SLT component information is combined into the Global SLT (GSLT). In 10 ms the SLT can make some semi-complicated event reconstruction. For example, calorimeter information is used to determine the event $E - p_z$ by summing over all the energy deposits and subtracting off the longitudinal component. The information from the CTD is used to reconstruct the primary interaction vertex. The event rate is further reduced to 30 - 85 Hz before the next level of reconstruction.

3.2.7 Third Level Trigger

Before an event makes it to the Third Level Trigger (TLT) it must be reconstructed in the Event Builder. The event builder combines the information from the SLT and all other components making it possible to identify tracks, electrons and jets. Combing all the component information gives a more complete picture to the TLT which further reduces the event rate to ~ 10 Hz.

3.3 The Luminosity System

To measure the luminosity, all that is needed is the measured rate of a specific process dN_{proc}/dt , once corrected for detector acceptance and efficiencies, and the theoretical cross section for the production of this process, σ_{proc} :

$$\mathcal{L} = \frac{dN_{\text{proc}}/dt}{\sigma_{\text{proc}}} \quad (3.4)$$

At ZEUS, luminosity is measured by counting the rate of $ep \rightarrow e\gamma p$ bremsstrahlung photons emitted by the incoming electrons. The rate of bremsstrahlung is measured by counting the number of events in two independent detectors. The differential cross section as a function of photon energy of bremsstrahlung events is described by the Bethe-Heitler formula[41]:

$$\frac{d\sigma}{dk_\gamma} = 4\alpha r_e^2 \frac{E'_e}{k_\gamma E_e} \left(\frac{E_e}{E'_e} + \frac{E'_e}{E_e} - \frac{2}{3} \right) \left(\ln \frac{4E_p E_e E'_e}{m_e m_p k_\gamma} - \frac{1}{2} \right) \quad (3.5)$$

All the luminosity measuring equipment is located in the rear direction. The layout relative to the ZEUS central detector is shown in figure 3.11 The luminosity measuring system consisted of three components; the Photon Calorimeter (PCAL), the Photon Spectrometer (SPEC) and the 6-meter tagger (TAG6). The luminosity measurements are made with the PCAL and the SPEC, located at $Z < -92$ m downstream from the interaction point. The TAG6 measures lightly deflected electrons 6 meters from the interaction point.

3.3.1 6-Meter Tagger

The 6-Meter tagger (TAG6) is tungsten-scintillator spaghetti calorimeter segmented into a 14 by 5 cell array in the X - Y plane. Located at approximately $Z = -6$ m downstream from the central detector, the TAG6 was originally designed as part of luminosity system. HERA quadruple magnets deflect slightly off-momentum electrons

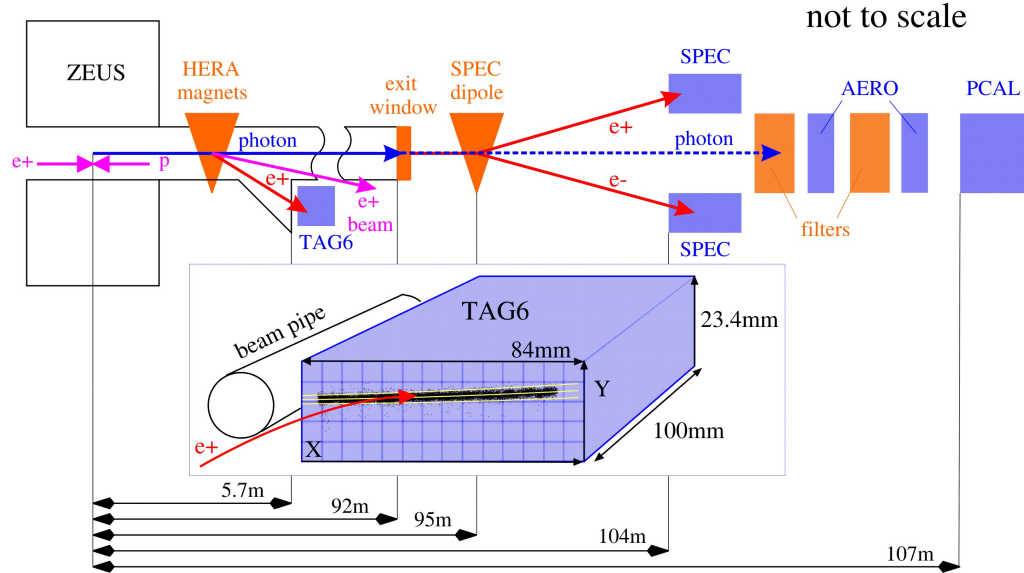


Figure 3.11: A schematic view of the ZEUS luminosity system. [42]

into the tagger. The TAG6 exhibits near perfect acceptance for electrons deflected during the bremsstrahlung process, but only within a narrow energy range. Electrons with energy between 3.8 GeV and 7.1 GeV are very likely to be observed while outside that range the kinematics of the event make them impossible to observe. The TAG6 can be used to measure coincidences between electrons and bremsstrahlung photons and the other luminosity measuring components, thus aiding in the luminosity determination.

3.3.2 Luminosity Spectrometer

At $Z = -92$ m, roughly co-linear photons will leave the HERA vacuum system via an exit window. Upon exiting the vacuum approximately 9% of photons will convert into e^+e^- pairs. At $Z = -95$ m the converted pairs are separated using a dipole magnet and measured by a pair of tungsten-scintillator sandwich calorimeters located at $Z = -104$ m [43]. Two calorimeters, one up and the other down, are segmented into horizontal and vertical strips, which facilitate a measurement of both energy

and position. This system is known as the luminosity spectrometer (SPEC) and measures e^+e^- pairs created by photons with an energy range between 15 – 25 GeV. The energy of the incident photon is the sum of the energy deposited in the up and down calorimeters ($E_\gamma = E_{\text{up}} + E_{\text{down}}$), while the position of the photon on the exit window is determined as follows.

The $x - y$ position of the electrons on the face of each calorimeter were calculated using the linear energy-weighted means of the deposited energy. For example, the x -position in the upper calorimeter was obtained from

$$x_e^{up} = \frac{\sum_{i=0}^{N_{\text{strips}}} X_i \epsilon_i^x S_i}{\sum_{i=0}^{N_{\text{strips}}} \epsilon_i^x S_i} \quad (3.6)$$

where X_i is the position of the i^{th} strip and $\epsilon_i^x S_i$ is the energy deposited in the strip. The y -coordinate, y_e^{up} , is calculated using a similar approach. From the positions of the e^+e^- pairs one can calculate the position of the incident photon.

$$x_\gamma = \frac{1}{2}[x_{\text{up}} + x_{\text{down}}] \quad (3.7)$$

and the y position can be calculated using:

$$y_\gamma = \frac{E_{\text{up}} y_{\text{up}} + E_{\text{down}} y_{\text{dn}}}{E_{\text{up}} + E_{\text{down}}} \quad (3.8)$$

3.3.3 Photon Calorimeter and Cherenkov Detectors

The Photon Calorimeter (PCAL) is used in one of the two luminosity measurements at ZEUS. Installed during the HERA-II upgrade, the PCAL is heavily shielded by $4.2X_0$ to survive in a very high radiation environment. The calorimeter is a lead-scintillator sampling calorimeter consisting of 48 layers and read out by two PMTs. Wedged inside the PCAL is a position detector, segmented into 17 vertical and 14 horizontal scintillator strips. The shielding causes a non-linear energy response and

poor position and energy resolution. To linearize the photon energy resolution, two Aerogel Cherenkov detectors (AERO) were placed before the PCAL. The setup of the far luminosity system is shown in figure 3.12.

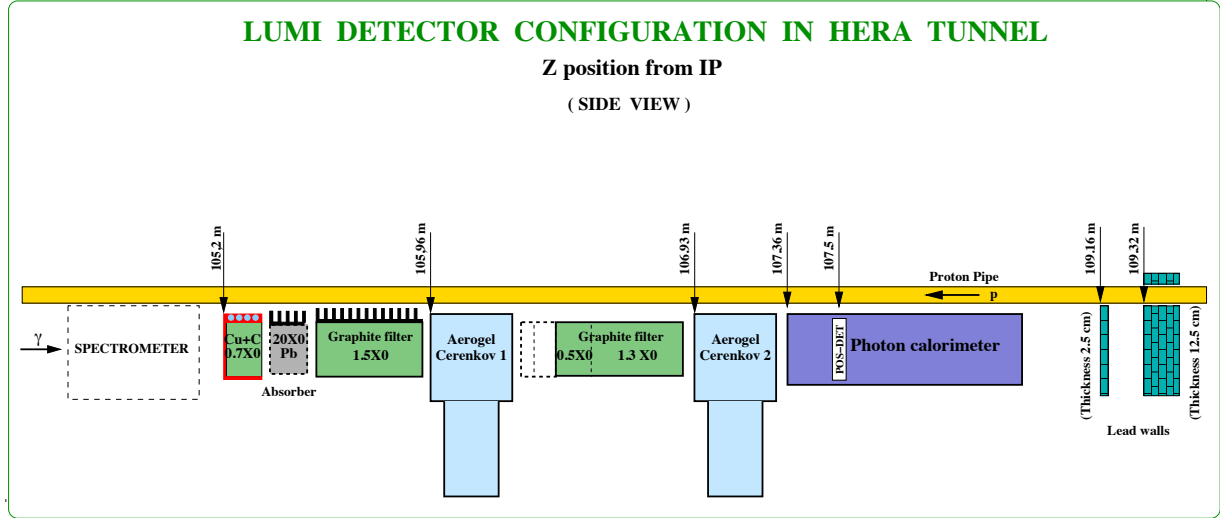


Figure 3.12: A schematic view of the Photon Calorimeter showing the active and inactive components.

Two graphite filters were installed before the PCAL each with a depth of $1.5 X_0$ and $1.8 X_0$. A silica Aerogel Cherenkov detector is placed after each graphite filter. The silica used had an index of refraction of 1.030. Photon showering in the graphite filters will produce electrons which emit Cherenkov light while traversing the AERO. Cherenkov light is detected by a PMT so long as the electron is above the 1.62 MeV threshold energy [44]. Higher energy bremsstrahlung events are well above the threshold energy and do produce a signal in the AERO detectors. An optical system, consisting of a mirror and a Fresnel lens, guide the Cherenkov light to the PMTs where results are read out.

By sampling the shower energy it is possible to combine the three active components (PCAL and the two aerogel detectors) to improve the energy measurement of the

incident photon. A combined energy measurement can be made with

$$E_\gamma = a_1 E_1^{AERO} + a_2 E_2^{AERO} + a_3 E_\gamma^{PCAL} \quad (3.9)$$

where E_1^{AERO} and E_2^{AERO} are the raw ADC values measured in the aerogel detectors and E_γ^{PCAL} is the scintillator energy deposited in the PCAL. The constants a_1 , a_2 and a_3 can be determined by either a MC simulation or by using a sample of events with a known energy. The method of calibrating the PCAL+AERO system is further discussed in section 5.6.

CHAPTER 4

Monte Carlo

4.1 Introduction

Particle physics detectors are not perfect. Their efficiency for detecting particles is less than 100%. Furthermore, effects like energy leakage and backplash can make some event topologies difficult to reconstruct. To measure a cross section, the imperfect efficiency must be appropriately treated. Monte Carlo (MC) is the ideal tool to determine the detector efficiency and for calculating its acceptance. This is done by simulating all of the underlying physics event topologies that can contribute in the measurement and passing them through a full detector simulation. Fully reconstructed MC events can be directly compared to data. Such a MC simulation for HERA consists of two steps:

- Simulation of the ep interaction onto the parton level including fragmentation and next to leading order radiative effects.
- Simulation of the entire detector including active and inactive materials.

DJANGO 1.6 [45], HERWIG [46] and PYTHIA [47] are examples of MC event generators that simulate ep interactions. At the ZEUS experiment, the detector simulation is handled by a program called MOZART [48] developed using the GEANT 3.21 [49] framework. This chapter gives a basic description of physics simulations with an emphasis on radiative corrections and detector simulations. It will also outline a

standalone simulation of the luminosity system which has been developed and used exclusively in this analysis.

4.2 Physics Simulation

MC programs such as DJANGO [45] randomly generate events according to the cross section:

$$\frac{d^2\sigma}{dx dQ^2} = \frac{2\pi\alpha^2}{xQ^4} [Y_+ F_2^{\text{PDF}}(x, Q^2) - y^2 F_L^{\text{PDF}}(x, Q^2) - Y_- x F_3^{\text{PDF}}(x, Q^2)] (1 + \delta_r(x, Q^2)) \quad (4.1)$$

where the structure functions F_2^{PDF} , F_L^{PDF} and F_3^{PDF} are the result of a set of parton distribution functions. The analyses outlined in this thesis all use either the CTEQ5D [17] or ZEUS-JETS [16] PDF parameterisations. HERACLES 4.6 [45], incorporated in DJANGO, is used to calculate electroweak corrections, of the order $\mathcal{O}(\alpha^2)$ to the DIS cross section, $\delta_r(x, Q^2)$. The hard scattering process is calculated by the ARIADNE [50] program which is based on the colour dipole model [51]. The JETSET [52] program for calculating hadronisation, fragmentation and decay is implemented within ARIADNE. The flow of the physics portion of a MC simulation at the ZEUS experiment is displayed in figure 4.1. In summary, a MC simulation of a DIS event contains the following components:

- A simulation of initial and final state QED radiation.
- A simulation of initial and final state QCD radiation
- Calculation of the hard scattering interaction.
- A simulation of the hadronization, fragmentation and particle decays.

Components relevant to this thesis will be discussed in greater detail.

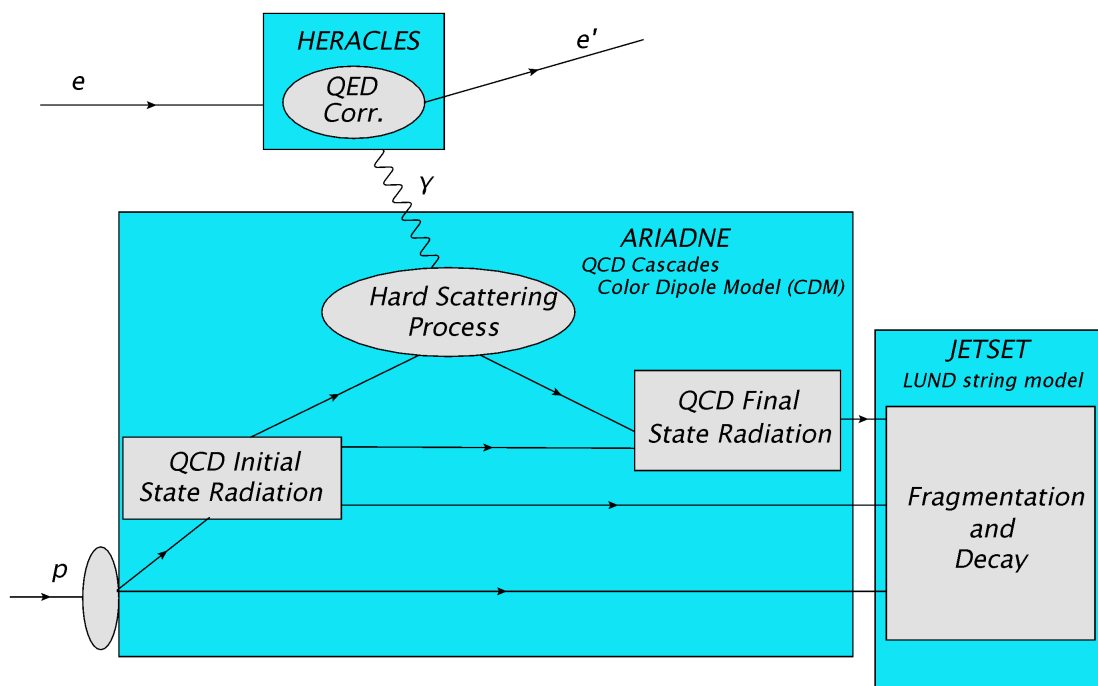


Figure 4.1: Schematic diagram of an inclusive ep generator such as DJANGO [45]

4.2.1 QED Initial and Final State Radiation

Understanding the effects of QED radiation on the Born level cross section is not trivial. In this analysis, simulation of electroweak radiative effects is handled by the HERACLES portion of the DJANGO MC event generator [45]. The Feynman diagrams for the QED next to leading order physics processes, which are treated by HERACLES, are displayed in figure 4.2. These processes can result in large corrections to the measured overall cross section. As discussed in section 2.7, Initial State Radiation (ISR) reduces the effective centre-of-mass energy and hence, modifies the kinematics of an event. Properly simulating ISR has been a challenge dating back to the early days of HERA [53]. Studies, performed for this thesis, based on the HERACLES program show that, at very high inelasticities, ISR corrections can be greater than 250% of the overall DIS cross section. The results of one such study that was performed for this thesis, using a standalone version of HERACLES, are shown in figure 4.3. In

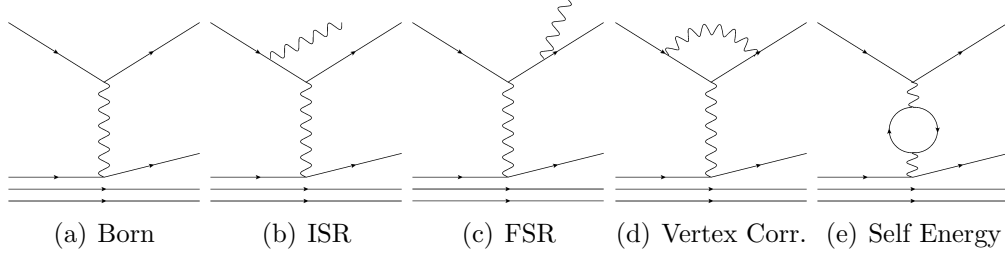


Figure 4.2: Feynman diagrams for QED Radiation. (a) is the Born level cross section without any radiative effects. (b) and (c) are the diagrams for Initial and Final State Radiation. (d) and (e) represent diagrams that are higher order QED effects.

this figure, $\sigma^{Physical}$ is the physical cross section which includes electroweak radiative corrections and σ^{Born} is the Born level cross section for DIS.

Figure 4.3 shows the radiative correction for events, which need not satisfy any selection criteria. In a typical DIS analysis, requirements would be placed on the event topology with the intention of reducing contributions from radiative correction as well as other backgrounds. The example is a set of selection criteria that would typically be found in a DIS analysis:

- An electron is required with $E'_e > 6$ GeV
- $E - p_z > 42$ GeV this requirement states that the event is well contained. This requirement is equivalent to a cut of $E_\gamma < 6.5$ GeV on the ISR photon.

Figure 4.4 displays the same ratio of cross sections as figure 4.3, but with the above selection criteria applied. This figure does not exhibit the rapid rise at high- y and is relatively flat. The dashed vertical line at $y \sim 0.8$ is the result of the electron energy requirement. The electron and $E - p_z$ requirement result in the radiative correction being no larger than 30% for the regions of interest. Also displayed in Figure 4.4, is the contribution from Final State Radiation (FSR). FSR events are tagged and the reconstruction of the kinematic variables are corrected to include this process. The

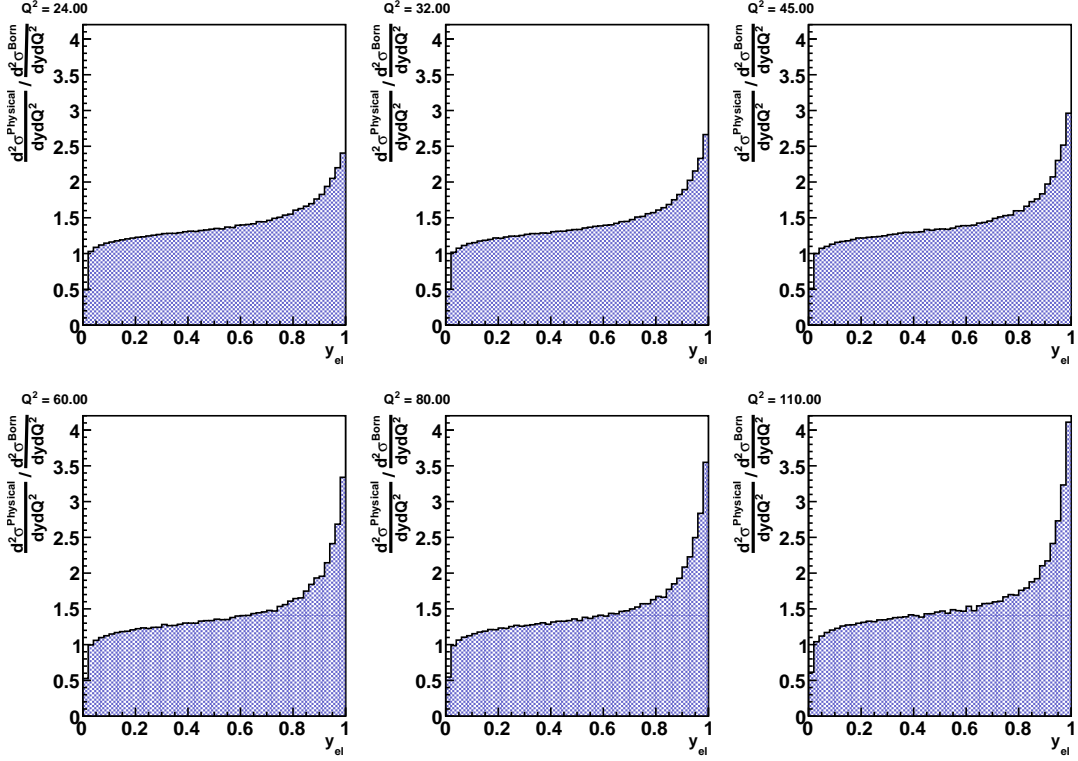


Figure 4.3: Size of the radiative correction as a function of inelasticity, y , for six Q^2 bins in the range $24 \text{ GeV}^2 < Q^2 < 110 \text{ GeV}^2$.

contribution due to FSR is typically small in the lower Q^2 regime. This is because, at low Q^2 the photon is emitted co-linear to the electron and is measured in the same energy cluster. At higher Q^2 , where the electron is measured in the BCAL and is more likely to have been deflected by the ZEUS magnetic field, FSR becomes a large source of uncertainty.

4.2.2 Hard Scattering and QCD Radiation

QCD radiation is analogous to QED radiation with the caveat that gluons carry colour charge. There are two methods which generators use to incorporate QCD radiation into a physics event. The first method is the matrix element (ME) approach, which calculates the matrix elements beginning with leading order. This method is limited by the complexity in calculating higher order diagrams. When this limit is

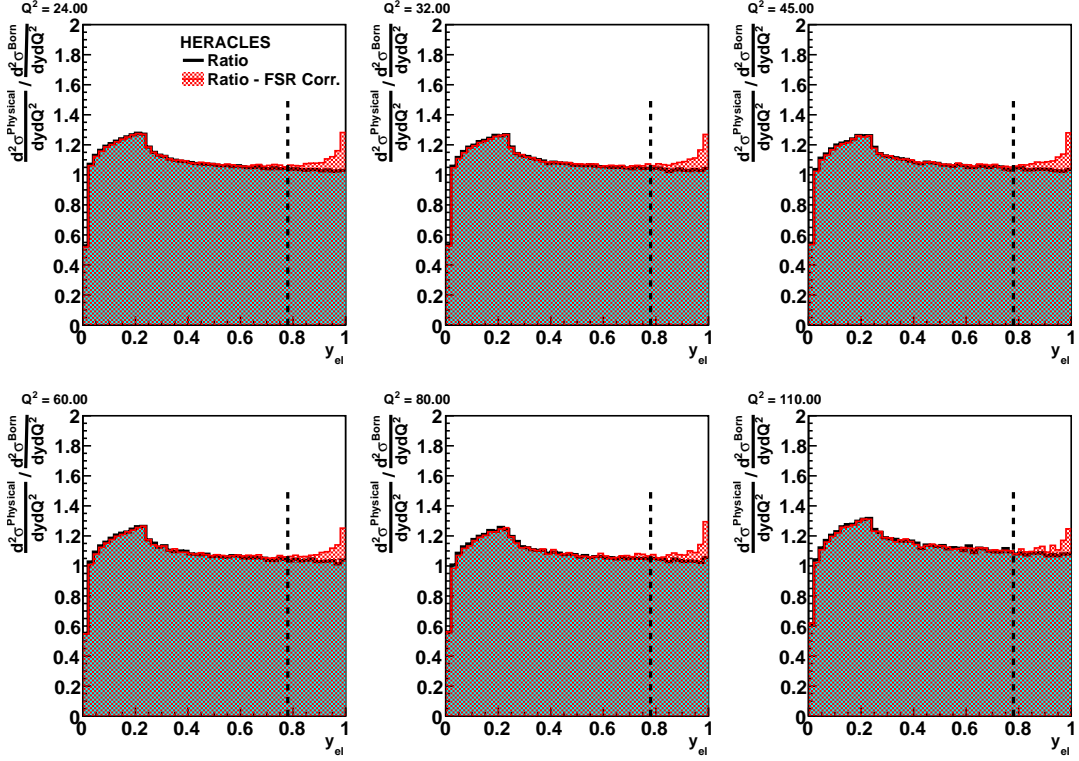


Figure 4.4: Size of the radiative correction as a function of inelasticity, y , for six Q^2 bins in the range $24 \text{ GeV}^2 < Q^2 < 110 \text{ GeV}^2$, when a basic DIS event selection criteria is applied. Also shown is the contribution from events with FSR. When FSR is present, the electron and photon clusters are added together before the event is reconstructed. Vertical hashed lines mark the maximum expected y value corresponding to a 6 GeV electron cut.

reached, one would use a parton shower (PS) approach, where each term contribution is approximated. These two approaches are commonly combined to form the MEPS approach, which is used in ARIADNE. ARIADNE is based on the Colour Dipole Model (CDM) [51] for simulating parton cascades. In the CDM, gluon emission from a $q\bar{q}$ can be treated as radiation from the colour dipole between the partons q and \bar{q} . Emission of a second softer gluon is treated as the emission of radiation from two independent dipoles [50].

4.2.3 Hadronization and Decay

As a result of QCD confinement (see section 2.3.2), only colourless hadrons are observed in the final state. Hadronization is the process that binds quarks together to create colour neutral states. For this analysis the hadronization and particle decay processes are handled by DJANGO [45], linked to the JETSET [52] program. JETSET uses the Lund string model [54] to describe the hadronization process. In the Lund string model, the colour field between a $q\bar{q}$ pair is represented by a one-dimensional string. As partons separate the potential energy stored in the string becomes sufficient to create a new $q\bar{q}$ pair. Hadronization, as described by the Lund string model, is illustrated visually in figure 4.5.

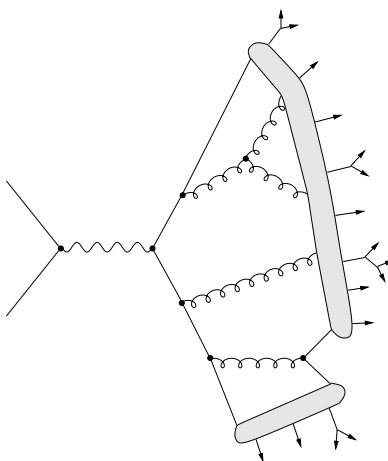


Figure 4.5: Schematic diagram of hadronization as described by the Lund string model

4.3 ZEUS Detector Simulation

A MC output consists of a lists of 4-vectors and particle codes for all final state particles. A framework is required to propagate the particle 4-vectors through the ZEUS detector and to properly model the detector response. For this purpose the

ZEUS collaboration developed the MOZART¹ program. This program was developed using the GEANT [49] package.

To simulate the ZEUS trigger the CZAR² package is used. This package is a combination of two programs: ZGANA³ and TLT_ZGANA. After the MC event is processed through the detector and trigger simulations, it can then be reconstructed in the same manner as data. For this task, the ZEPHYR⁴ program is used. The output from

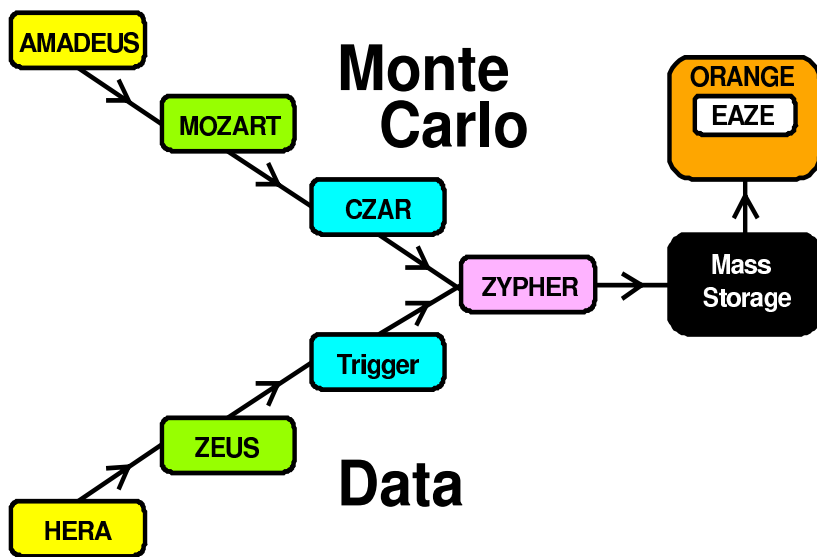


Figure 4.6: Flow diagram showing the chain of programs that process MC and Data events. Where ZYPHER is referring to ZEPHYR.

ZEPHYR is stored on hard disks in the DESY computing centre and can be retrieved for offline analysis. A flow chart illustrating the way that MC and data are processed is shown in figure 4.6.

¹ **MO**nte Carlo for **ZE**US Analysis **R**econstruction and **T**racking

² **C**omplete **Z**GANA Analysis **R**outines

³ **ZE**US **GE**ANT **AN**alysis

⁴ **ZE**US **PH**ysics **R**econstruction

4.4 Simulation of the Luminosity System

Due to lack of manpower, a proper simulation of the ZEUS luminosity system, which was described in section 3.3, was never pursued. For the analysis presented in this thesis, a standalone simulation of the luminosity system has been developed. This simulation can be incorporated into any offline ROOT [55] analysis.

Conditions in the luminosity system vary from run to run. An advantage of a standalone simulation is that it can be developed and tuned to the parameters specific to each running period. The tuneable parameters are:

- The position, width and tilt of the beam of photons on the face of the luminosity system.
- The magnet geometry that block photons in certain areas of the detector. This defines an *aperture*.
- The rate of accidental Bethe-Heitler (BH) overlays.

The simulation and with aforementioned parameters is described in greater detail below.

4.4.1 Geometric Acceptance

MC generators such as DJANGO [45] output the 4-vectors of initial and final state particles. A simulation determines if a photon is within the acceptance region. Photons generated at the ZEUS interaction point are projected into the luminosity system,

$$X_{proj} = Z_{SPEC} \cos \phi \tan \theta \quad (4.2)$$

$$Y_{proj} = Z_{SPEC} \sin \phi \tan \theta \quad (4.3)$$

where Z_{SPEC} is the Z position of the front of the Photon Spectrometer (SPEC), θ is the polar angle of the generated photon with respect to the Z -axis and ϕ is the photon's azimuthal angle.

A sample has been obtained that selects on *pilot bunches*. In a pilot bunch configuration, the electron (proton) is unaccompanied by a proton (electron). This configuration is free of DIS events and provides an ideal environment to study BH events.

The position resolution of the SPEC is superior to that of the PCAL and is used to measure the photon position. The measured distribution in the X - Y plane forms a slightly rotated ellipse, the area of which is known as the beam spot. The angle of rotation of the beam spot, with respect to the X -axis is known as the beam tilt.

The beam spot, beam spread and beam tilt parameters are determined from a pilot electron bunch sample. The luminosity system has its own coordinate system, with respect to the ZEUS system, therefore a linear shift is applied. Using the pilot bunch sample, the X and Y distributions in the MC can be tuned to match the data. These distributions are shown in figure 4.7.

A single set of input parameters are used to tune the Monte Carlo for run ranges used in this thesis. The stability of the beam has been studied over time and no large fluctuations were observed during the 2006/2007 e^+ running period.

4.4.2 Aperture Determination

A photographic foil, sensitive to synchrotron radiation, was placed directly in front of the SPEC for a short period during the 2006 e^+ running period. The HERA magnets act as an aperture, blocking some photons from reaching the luminosity system. Light and dark bands visible in figure 4.8 represent regions of high and

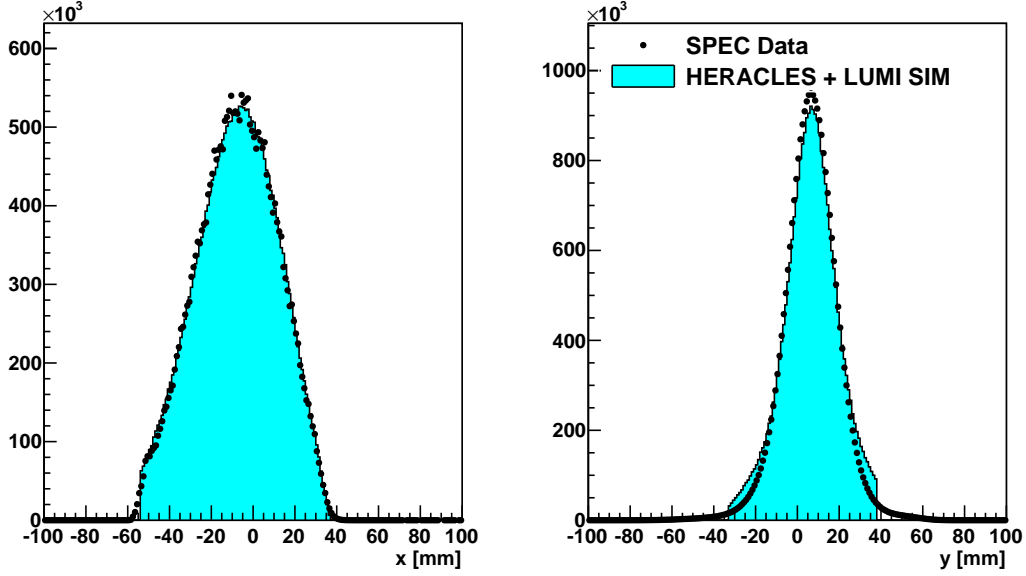


Figure 4.7: Comparisons of the data and MC distributions for both the X (left) and Y (right) positions.

low flux, respectively. From the irradiated foil, the boundaries of the geometric acceptance region were measured using a ruler.

To account for e^+e^- conversions in the luminosity system exit window, 8.8% of the events are randomly rejected. This value was precisely measured by the ZEUS Luminosity working group [56].

4.4.3 Photon Calorimeter and Aerogel Detectors

Using the Aerogel detectors (AERO) in conjunction with the photon calorimeter (PCAL) improves the energy resolution and the linearity of the detector response. The combination of the two components will be referred to as PCAL+AERO. Two graphite filters were placed before the PCAL and each filter was followed by an AERO detector (see figure 3.11). The AERO detectors measure the showers starting in the filters and result in an improved measurement of photon energy. To reproduce the calibrated energy in the data (see section 5.6), the photon energy is both offset

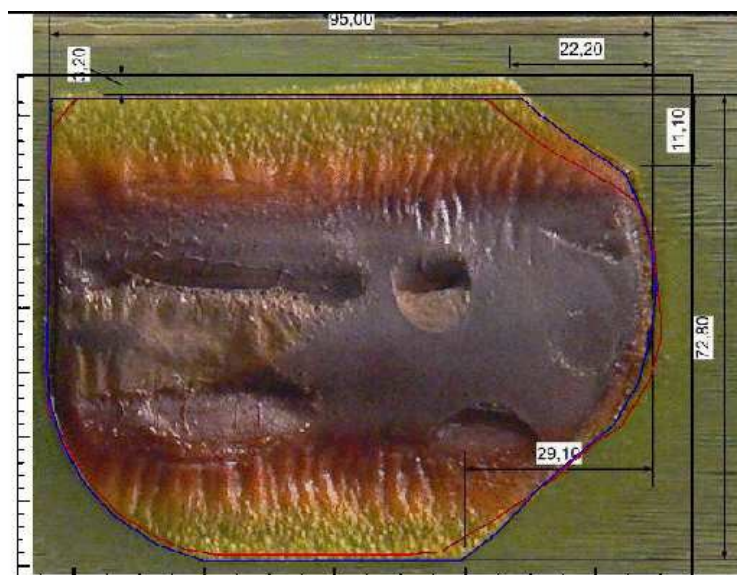


Figure 4.8: A photograph of a foil placed after the luminosity system exit window. The reference scales are in units of centimetres.

and smeared,

$$E_\gamma = (E_\gamma^{\text{Gen}} - E_\gamma^{\text{Offset}}) \otimes \Upsilon_{\text{res}} \quad (4.4)$$

where,

- E_γ^{Gen} is the true energy from the MC generator.
- E_γ^{Offset} is the offset. By studying tagged-ISR events this parameter was found to be 0.98 GeV.
- Υ_{res} is the amount of smearing required to reproduce the data. This parameter is determined on an event-by-event basis by applying a gaussian smearing, where the gaussian has a mean $(E_\gamma^{\text{Gen}} - E_\gamma^{\text{Offset}})$ and a width σ_γ .

Pilot bunch samples were used to determine the parameter σ_γ in the following way.

The 6-meter tagger (TAG6) has a near perfect acceptance for bremsstrahlung electrons within the energy range 3.8 - 7.1 GeV [57]. From these electrons, the energy

of the bremsstrahlung photon can be estimated,

$$E_\gamma = E_e^{beam} - E_e^{TAG6}. \quad (4.5)$$

where E_e^{beam} is the beam energy and E_e^{TAG6} is the energy measured in the TAG6. Using a sample of bremsstrahlung events in the above energy range, the resolution, σ_γ , was determined to be $\sigma_\gamma = 0.65\sqrt{E_\gamma^{Gen}}$.

4.4.4 Inclusion of Beam Related Background

BH events dominate the signal in the PCAL+AERO system. The contribution from BH is a function of the instantaneous luminosity, but for the datasets used in this thesis we expect on average ~ 2.5 photons with a threshold energy $E_\gamma > 200$ MeV per event. Consequently, there is a high probability that BH events can accompany an ISR event. These pileup events must be convoluted with the energy of a photon in the simulation. To perform the convolution it is necessary to obtain a BH enriched sample. This sample must come from the data obtained during the same running period that we wish to analyze.

By selecting DIS events that are within the kinematic peak (see section 5.4), we can obtain a sample with minimal or no ISR. Events were selected if,

- They satisfied one of the inclusive DIS triggers SPP11 or SPP15 or SPP16 (see section 5.8.2 or section 5.8.3).
- An electron with $E'_e > 8$ GeV was measured in the RCAL or BCAL.
- The vertex was well reconstructed.
- They satisfy the requirement for a kinematic peak event.

An example of a BH spectrum that corresponds to this event selection is shown in figure 4.9. The pedestal region, which is around 0 GeV and the “knee” around

$E_{\gamma}^{PCAL+AERO} > 27.5$ GeV are features worth highlighting. Events in the pedestal correspond to events where very little, or no photon energy was deposited. This region provides an excellent signal to normalize different data sets because it is a constant background. Below the knee region, the photon has more energy than the incoming electron, $E_{\gamma} > E_e$, implying that events in this region contain multiple photons. Therefore, all events in the knee region are a convolution of multiple BH events or BH convoluted with ISR.

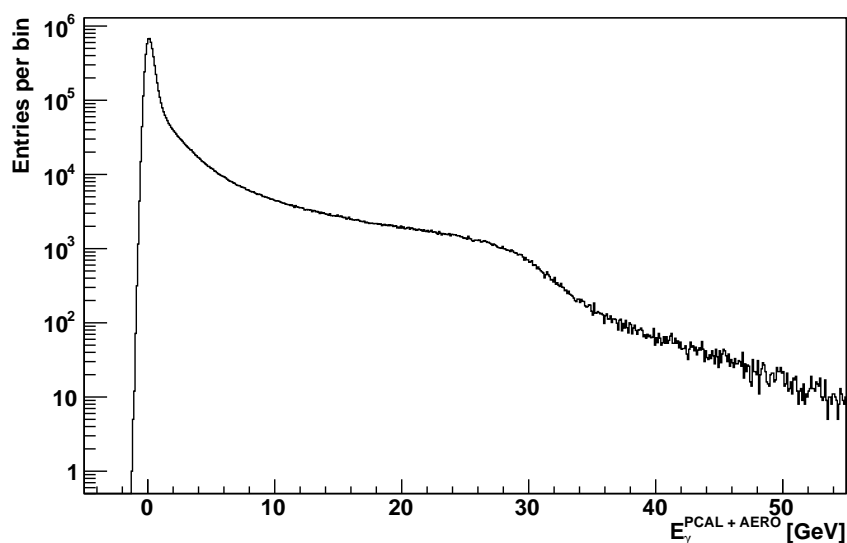


Figure 4.9: The $E_{\gamma}^{PCAL+AERO}$ spectrum for DIS, no-ISR, candidates.

BH events overlay real physics events. When a photon is detected in the luminosity system it can come from any of the following processes:

- ISR
- ISR + BH
- BH
- ISR + multiple BH
- multiple BH

Figure 4.9 contains $N \geq 0$ BH events. A random sampling procedure assigns a value from the above spectrum to every event. When an ISR photon falls within the aperture, the BH energy and the reconstructed ISR energy (see equation 4.4) are added.

4.4.5 Comparisons with Data

A key test of the validity of the luminosity system simulation is to compare the simulation to real data. One such quality control test comes from data-MC comparisons for the PCAL+AERO distribution. Figure 4.10 shows this comparison for

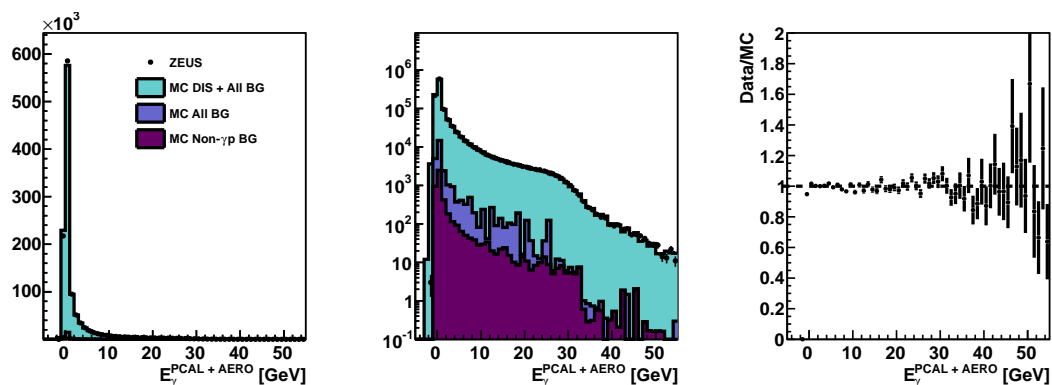


Figure 4.10: Photon Energy as measured in the PCAL+AERO system, shown on both linear (left) and log (middle) scales. The ratio of data to MC is also shown (right).

DIS events where the datasets are normalized to luminosity. An excellent agreement between data and MC is observed.

CHAPTER 5

Event Reconstruction and Selection

To make a decision on whether an event contributes to the signal, it must be fully reconstructed. This chapter outlines several techniques that are used to reconstruct the physics of an event. To perform the analyses outlined in this thesis, the Photon Calorimeter (PCAL) and the two aerogel Cherenkov counters (AERO) must first be calibrated. Two calibrations have been performed, the PCAL-only calibration, described in section 5.5 and the improved PCAL+AERO calibration described in section 5.6. Once an event is reconstructed, background can be suppressed by applying an event selection criterion.

5.1 Event Reconstruction

Neutral current DIS events can be split up into two separate parts: the scattered electron and the hadronic system. To describe the physics of the event each of these systems must be reconstructed. DIS events are categorized by their location in the (x, Q^2) kinematic plane (see figure 2.4). To determine the location on the kinematic plane that an event lies, it is necessary to reconstruct the kinematic variables of the event.

A collision event in the ZEUS detector is displayed in figure 5.1. In the X - Y view, we see a single track balancing the hadronic energy flow. This is characteristic of a neutral current DIS event. The energy deposit, which is also displayed in the side view at the top of the BCAL, is likely from an electron. Only a single parton, the one

seen as the hadronic jet, partakes in the interaction, the rest of the proton, the so called remnant, continues travelling in the positive Z -direction and is partly detected in the FCAL surrounding the beam pipe.

Before the kinematic variables of this event can be measured, all of the energy deposits need to be classified and the location of the interaction vertex must be reconstructed. This section will introduce the methods used to reconstruct the electron, the hadronic system and the vertex position.

5.1.1 Electron Reconstruction

Neutral Current DIS is characterized by a scattered electron in the final state. Dedicated algorithms are applied to identify electrons in the ZEUS calorimeter. The ZEUS calorimeter has some small areas of inactive material and energy can leak between the different sections. A neural network program called **SINISTRA** [58] is used to identify and classify electron candidates. **SINISTRA** combines calorimeter and central tracking information to match charged tracks to energy deposits. The program works by forming hit calorimeter cells into islands. Islands which trace back through the CTD are checked for corresponding tracks. If a match is found, or the island is out of the CTD range, the island is referred to as an electron candidate. The neural network, trained on MC electrons, assigns a probability to each candidate. Often **SINISTRA** will identify multiple candidates for a single event. The analyses outlined in this thesis, always use the candidate with the highest probability.

5.1.2 Hadronic Reconstruction

Hadrons have a deeper shower profile than electrons in the calorimeter, helping **SINISTRA** distinguish between the two. The hadronic energy is reconstructed by studying ZEUS Unified Flow Objects (ZUFO) [59] which are essentially Energy Flow

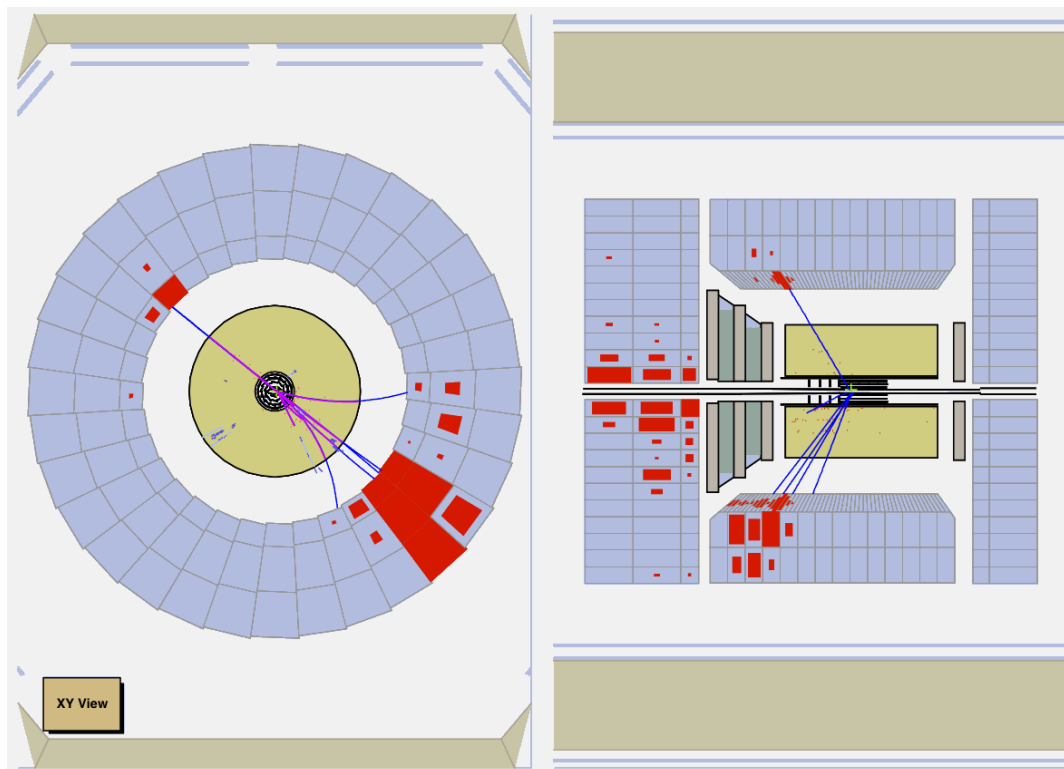


Figure 5.1: An example of a high- Q^2 Neutral Current DIS event. In the YZ view (right), the electron candidate is seen in the upper BCAL and the hadronic system is seen lower in the BCAL. The proton remnant is partly observed scattered around the beam pipe in the FCAL. In the XY view (left), the electron candidate balances the hadronic system, implying this event has no missing transverse energy.

Objects (EFOs). ZUFOS are formed by clustering calorimeter cell deposits into islands. The formation of ZUFOS is illustrated in figure 5.2. Detector backplash, via the albedo effect on the face of the calorimeter, can potentially lead to poor ZUFOS reconstruction. A technique called CorAndCut [60] has been developed that cuts away the backplash deposits and corrects for energy losses inside dead materials. The CorAndCut technique will be used for hadronic energy reconstruction throughout this thesis.

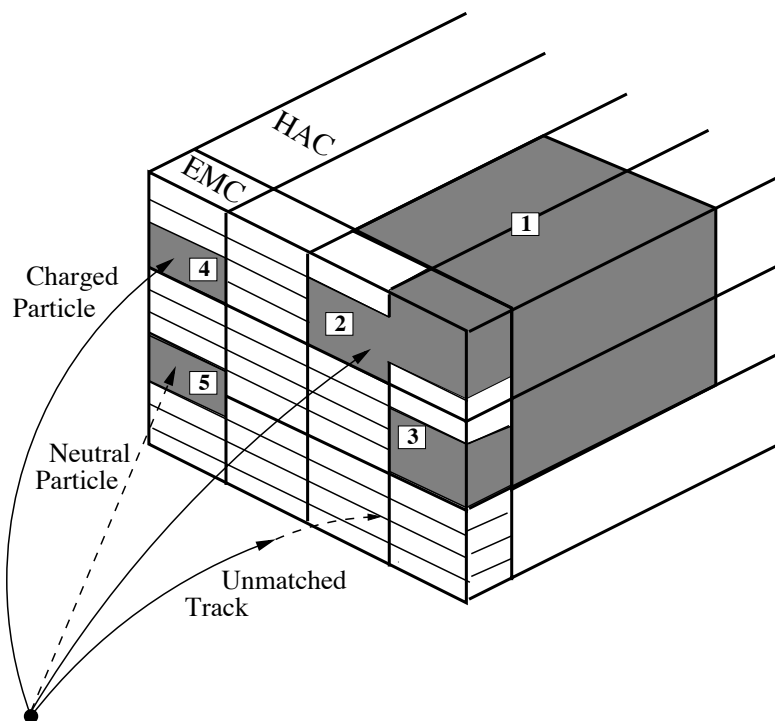


Figure 5.2: Schematic diagram demonstrating the formation of ZUFOs from calorimeter islands. Neighbouring EMC cells of regions (2) and (3) combine to form cell islands. They are merged with the HAC deposit (1) to form a tower island. Regions (4) and (5) could possibly correspond to electron and photon candidates.

5.1.3 Hadronic Quantities

An important variable characterizing events in the ZEUS detector is $E - p_z$, the sum over the energies of all islands, subtracted by the longitudinal projection of their energies. This is represented by the equation:

$$\delta = E - p_z \equiv \sum_i E_i (1 - \cos \theta_i) \quad (5.1)$$

where E_i is the energy measured in a deposit i and θ_i is the measured polar angle of the deposit. The equation sums over both the scattered electron and hadronic deposits. Re-representing the previous equation in terms of the electron and hadronic

components gives:

$$\delta = \sum_h [E_h - p_z]_h + [E_e - p_z]_e \quad (5.2)$$

where the subscript h refers to the hadronic quantities and e refers to the electron. This sum, δ , is a particularly interesting quantity, is a conserved quantity, meaning that it should be the same before and after an event. Before an event, the incoming proton is travelling along the z -axis with $E_p = 920$ GeV and the electron travelling in the opposite direction with $E_e = 27.5$ GeV. Plugging these values into equation 5.2 gives: $\delta = (920 - 920) + (27.5 + 27.5) = 55$ GeV. After a collision, δ is mostly unaffected as large parts of the proton beam remnant escape detection at very small angles down the beam pipe. If an event is fully contained it is also expected that $\delta = 2E_e$. In the case of an ISR event, the photon travels down the beam pipe and the event is no longer fully contained. The energy of an ISR photon can be introduced into equation 5.2 by defining the total δ_{tot}

$$\delta_{tot} = \delta + 2E_\gamma = 2E_e \quad (5.3)$$

where δ is the measured value and E_γ is the energy of the ISR photon. The energy of the photon can be indirectly measured by rearranging equation 5.3 into

$$E_\gamma = (2E_e - \delta)/2. \quad (5.4)$$

Photoproduction, as described in section 2.6.2, can also lower the $E - p_z$ value because the electron escapes down the rear through the beam pipe. Either a photon or a hadron may then fake an electron in the RCAL. This process is a possible source for background.

Another interesting hadronic quantity, which can intuitively be understood as the polar angle of the struck quark which partook in the interaction, is the hadronic

angle γ_h . This angle is defined to be:

$$\cos \gamma_h = \frac{p_{T,h}^2 - \delta_h^2}{p_{T,h}^2 + \delta_h^2} \quad (5.5)$$

where δ_h is the sum of the hadronic $E - p_z$.

5.1.4 Vertex Reconstruction

Tracking information from the MVD and the CTD are combined to reconstruct the (X, Y, Z) coordinates of the ep interaction. The primary interaction vertex, and any secondary vertices, are reconstructed offline using the VCTRACK [61] program.

5.1.5 Z vertex Reweighting

The Z vertex (Z_{vtx}) is a quantity that is dependent on the ZEUS and HERA running conditions, thus the MC Z_{vtx} distribution must be modelled for each running period. For the running periods used in this analysis, the MC was not initially generated with the correct vertex distribution. The procedure outlined in this section is based on an unpublished internal ZEUS note [62] and highlights the specific procedure used to correct the distribution for the ISR dataset. The Z_{vtx} distribution in the MC sample has to be reweighted to reflect the current conditions.

To demonstrate the necessity for a reweighting procedure, a Z_{vtx} distribution without a reweighting procedure is shown in figure 5.3

The first step in the reweighting process is to generate a reconstructed MC event sample where the Z_{vtx} is unbiased by the selection criteria. Such a sample would result in the Z_{vtx} reconstruction efficiency being flat. In general the reconstruction efficiency is defined as

$$\text{Efficiency} = \frac{(\# \text{events measured in a bin})_{\text{after selection}}}{(\# \text{events generated in a bin})_{\text{before selection}}} \quad (5.6)$$

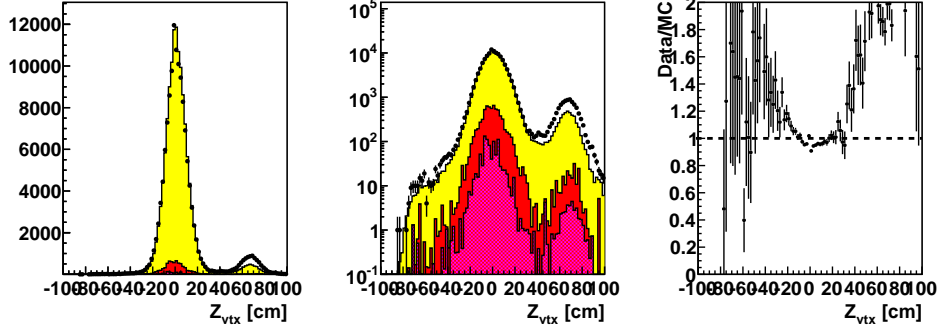


Figure 5.3: The Z_{vtx} distribution for data (points) and MC plotted on a linear and log scale. The contributions from photoproduction and QEDC are represented in the inner histograms. Also shown is the ratio between data and MC.

The following event selection was used to obtain a sample that does not bias the Z_{vtx} :

- The event must meet the trigger requirements of the ISR trigger (to be defined in section 5.8.3).
- A Sinistra candidate is found where the energy of the highest probability candidate is $E'_e > 8$ GeV.
- The highest probability, P_e of the Sinistra candidate satisfies the requirement that

$$P_e > \max\left(0.8, 0.95 - 1.5e^{-E'_e/2.5}\right). \quad (5.7)$$

This requirement was shown in a MC study to have the highest efficiency for electron tagging [63].

- The electron is measured with a polar angle in the range $40^\circ < \theta'_e < 160^\circ$
- $E - p_z$ must be in the range 15 GeV and 65 GeV.
- At least 3 tracks have been used to reconstruct the vertex position.

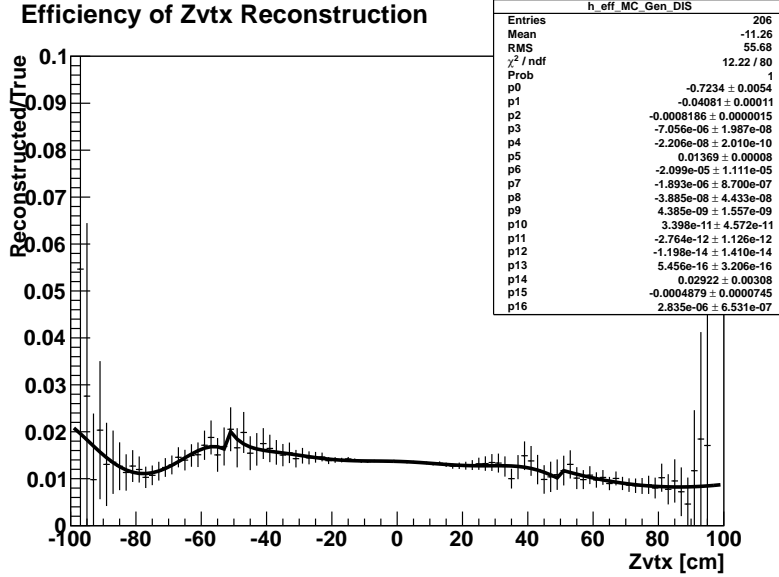


Figure 5.4: The efficiency of the Z_{vtx} reconstruction. This distribution is parameterized by three different polynomials each describing a different region in the detector.

Ideally, the Z_{vtx} efficiency should be parameterized by a flat line. Because the selection could not produce a completely unbiased sample, the efficiency will be parameterized using different polynomials to describe three different regions. The results of the parameterisation of the efficiency are displayed in figure 5.4. Slight discontinuities exist on the boundaries of the different polynomials, but this has a negligible effect on the analyses presented in this thesis, which restrict measurements to the continuous region $30 \text{ cm} < Z_{vtx} < -30 \text{ cm}$. The data can be scaled onto the generated level by dividing the data Z_{vtx} distribution by the efficiency. Once this is achieved the Z_{vtx} distribution is parameterized.

In an ideal environment the Z_{vtx} distribution would be a single gaussian centred around the interaction point. As demonstrated in figure 5.3, this is not actually the case. HERA delivers particles in bunches and each bunch contains a main bunch and satellite bunches, which both precede and follow the main bunch. Interactions between the proton satellite bunch and the main electron, or interactions between

the satellite electrons, and the main protons bunches are known to occur. This gives the Z_{vtx} its unique features. The proton and electron can interact based on these five scenarios:

- Interaction between proton in main bunch and electron in main bunch.
- Interaction between early proton satellite and electron in main bunch.
- Interaction between late proton satellite and electron in main bunch.
- Interaction between proton in main bunch and electron in early satellite.
- Interaction between proton in main bunch and electron in late satellite.

The Z_{vtx} can be modelled by the convolution of five gaussians. Each gaussian represents one of the five scenarios. The fitted Z_{vtx} distribution is displayed in figure 5.5. The fit was simplified by applying the following constraints to the fit pa-

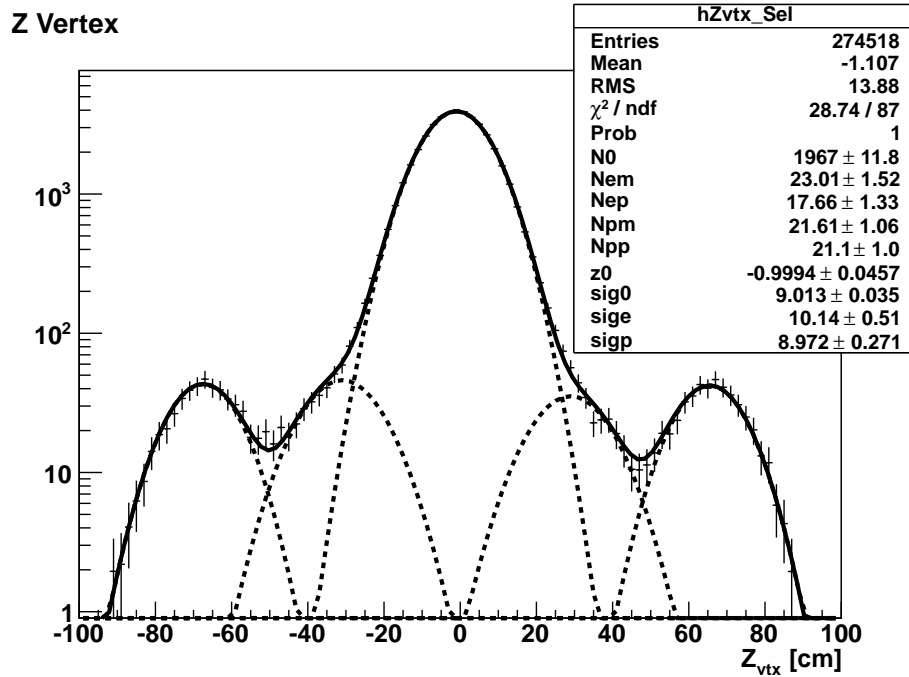


Figure 5.5: The data Z_{vtx} distribution unfolded onto the generator level. This distribution is parameterized by a convolution of five gaussians.

rameters:

- Because the position resolution is uniform throughout the detector, each of the five gaussians is assumed to have a similar width.
- Symmetric satellite vertices are equidistant from the main interaction point.

Weights based on the fitted distribution are assigned on an event-by-event basis. An example of a resulting Z_{vtx} distribution is given in figure 5.6.

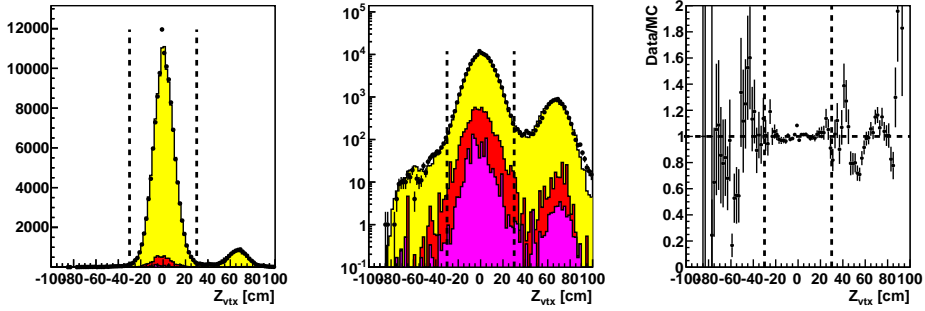


Figure 5.6: The Z_{vtx} distribution for data (points) and MC (yellow histogram) plotted on a linear and log scale. The contributions from photoproduction and QEDC are represented in the inner histograms. Also shown is the ratio between data and MC.

5.2 Event Reconstruction Methods

A DIS event is categorized by its location in the (x, Q^2) plane. Using the measured electron and hadronic system, these variables can be determined. Several methods have been developed to accurately measure the kinematic variables, x , y and Q^2 . The kinematic variables can be determined using two or more of the following independent variables:

- E'_e , the energy of the scattered electron.
- θ'_e , the polar angle of the scattered electron.
- $[E - p_z]_h$, the hadronic component of the $E - p_z$.

- $p_{T,h}$, the transverse momentum of the hadronic system.

Furthermore, because the center-of-mass energy, \sqrt{s} , of an event is known from the HERA accelerator, only two of the kinematic variables need to be determined. This is demonstrated by the relation:

$$Q^2 = sxy \quad (5.8)$$

Several event reconstruction methods exist. Each method has its advantages and disadvantages and regions where they work particularly well. For example, each reconstruction method handles ISR differently. This section will review four of the commonly used event reconstruction methods. In the next section each method will be slightly modified to account for ISR.

5.2.1 Electron Method

The electron method is ideal to reconstruct neutral current DIS events when an electron can be accurately measured. The entire kinematics of the event can be reconstructed using the electron energy E'_e and its scattered angle θ'_e . The equations that define this method are:

$$y_e = 1 - \frac{E'_e}{2E_e} (1 - \cos\theta'_e) \quad (5.9)$$

$$Q_e^2 = 2E_e E'_e (1 + \cos\theta'_e) \quad (5.10)$$

In the high- y region, the electron can be very accurately measured because it traverses both the CTD and the CAL. Because the electron method is the most accurate in the high- y region, it will be the method of choice for this analysis.

5.2.2 Jacquet-Blondel Method

The hadron method, commonly referred to as the Jacquet-Blondel method [64], uses only the hadronic information. This method is the only method available when

studying charged current events, where a neutrino escapes detection in the final state. The equations that define this method are:

$$y_{JB} = \frac{[E - p_z]_h}{2E_e} \quad (5.11)$$

$$Q_{JB}^2 = \frac{p_{T,h}^2}{1 - y_{JB}} \quad (5.12)$$

In the electron method, limitations arise from the quality of the electron reconstruction. In the Jacquet-Blondel method, the quality of the hadronic system is key. The Q_{JB}^2 reconstruction relies on the assumption that very little hadronic energy escapes down the beam pipe. This method gives a good description of y , it is particularly accurate in the low y region.

5.2.3 Sigma Method

The sigma method combines both hadronic and electron informations and makes use of the fact that for a hermetic detector (see equation 5.2):

$$\delta = \delta_h + \delta_e = 2E_e \quad (5.13)$$

The equations that define this method are:

$$y_\Sigma = \frac{\delta_h}{\delta} \quad (5.14)$$

$$Q_\Sigma^2 = \frac{E'_e \sin^2 \theta'_e}{1 - y_\Sigma} \quad (5.15)$$

The emission of an ISR photon does not affect the event reconstruction when using the sigma method. Both y_Σ and Q_Σ^2 depend on δ in such a way, that they are automatically adjusted in the event of ISR. This method is not used in this thesis, but is shown for completeness.

5.2.4 Double Angle Method

The double angle method uses the angles for both the electron and the hadronic system (θ'_e, γ_h) .

$$y_{DA} = \frac{(1 - \cos \gamma_h) \sin \theta'_e}{\sin \gamma_h + \sin \theta'_e - \sin(\theta'_e + \gamma_h)} \quad (5.16)$$

$$Q_{DA}^2 = 4E_e^2 \frac{\sin \gamma_h (1 + \cos \theta'_e)}{\sin \gamma_h + \sin \theta'_e - \sin(\theta'_e + \gamma_h)} \quad (5.17)$$

This method works best for high- Q^2 and for low- y . This thesis is interested in low- Q^2 events where the electron method provides the best description.

5.3 Kinematic Reconstruction with ISR

In the ISR process, a photon is emitted from the electron before a DIS interaction. ISR leads to substantial shifts in the reconstructed variables [21]. By measuring the energy of the ISR photon, it is possible to reconstruct the true kinematics of an event.

The fraction of energy carried away by the ISR photon is defined to be:

$$f_\gamma = E_\gamma / E_e \quad (5.18)$$

where E_γ is the energy of the ISR photon and E_e is the energy of the incoming electron beam. ISR acts to lower the effective centre-of-mass energy of the event:

$$s_{true} = (1 - f_\gamma) s_{nominal} \quad (5.19)$$

The relation $Q^2 = sxy$ still holds, except that one must be careful to use s_{true} and not $s_{nominal}$ when determining x from the other two equations.

The following subsections will state the necessary corrections to the event kinematic reconstruction variables.

5.3.1 Electron Method with ISR

The electron method, originally described in section 5.2.1, is particularly sensitive to ISR especially at high- y . This can be seen from the equations:

$$y_{true} = \frac{y_e - f_\gamma}{1 - f_\gamma} \quad (5.20)$$

$$Q_{true}^2 = Q_e^2(1 - f_\gamma) \quad (5.21)$$

ISR affects the Q_e^2 reconstruction by shifting it to larger values. In a low Q_e^2 analysis such as the one described in this thesis, this can lead to the pollution of events from a Q_e^2 that is below a selection threshold. When correcting for the kinematics using equation 5.21, it is possible to gain access to lower Q_e^2 events than otherwise accessible. The measured y_e will also be larger than y_{true} .

5.3.2 Jacquet-Blondel Method with ISR

The y_{JB} method is affected in the following way:

$$y_{true} = y_{JB} \frac{1}{1 - f_\gamma} \quad (5.22)$$

$$Q_{true}^2 = Q_{JB}^2 \left(\frac{1 - y_{JB}}{1 - (y_{JB}/(1 - f_\gamma))} \right) \quad (5.23)$$

5.3.3 Double Angle Method with ISR

In the double angle method, the y_{DA} variable is not sensitive to ISR while Q_{DA}^2 is heavily affected. In the presence of ISR, Q_{DA}^2 will be shifted to much higher values.

$$y_{true} = y_{DA} \quad (5.24)$$

$$Q_{true}^2 = Q_{DA}^2(1 - f_\gamma)^2 \quad (5.25)$$

5.4 The Kinematic Peak

The *kinematic peak* is a term used to describe events where the event is kinematically well contained in the detector. In principle, the kinematic peak is free from ISR and photoproduction. The kinematic peak is most commonly defined as all events that satisfy the condition $\delta \approx 2E_e$. This thesis uses a similar definition, but will introduce a new notation.

A relationship between ISR photon energy, E_γ and δ has been shown to exist (see section 5.1.3). This relationship predicts that energy lost from the incoming electron can be attributed to ISR. An indirect but more accurate approach of predicting the ISR energy is to exploit the reconstruction methods to infer the energy. For example, in a well contained event with no ISR, we would expect the electron method and the Jacquet-Blondel method to give the same value for y . Therefore,

$$y_{JB} = y_{el} = 1 - \frac{E'_e}{2E_e} (1 - \cos\theta_e) \quad (5.26)$$

where this equation can be rearranged, allowing the scattered electron energy, E'_e , to be defined by

$$E_e^y = E'_e = \frac{2E_e(1 - y_{JB})}{1 - \cos\theta'_e} \quad (5.27)$$

where E_e^y is a new variable defined as the predicted scattered electron energy. This equation facilitates a new approach to define the kinematic peak.

An event is considered to be in the kinematic peak if the difference between the predicted and measured electron energy is zero: $E_e^y - E'_e \sim 0$. If the difference is large, it means that part of the event has evaded detection by the central detector, which is likely the result of ISR. In this thesis, an event is defined to be within the kinematic peak if it falls within the range $-5 \text{ GeV} < E_e^y - E'_e < 2 \text{ GeV}$.

Using the parameter E_e^y it is possible to make a prediction for how much energy such an ISR photon has. This is represented by the equation

$$E_\gamma^{Exp} = \frac{1 - \cos \theta'_e}{2(1 - y_{JB})} (E_e^y - E'_e) \quad (5.28)$$

where E_γ^{Exp} is the expected photon energy. This equation provides an expectation for the photon energy, which can be compared with the energy measured in the luminosity system.

5.5 Calibration of the Photon Calorimeter

Photons can be measured by the ZEUS Luminosity detector, specifically by the Photon Calorimeter (PCAL) located at $Z = -107\text{m}$. The PCAL is one of four active components in the far luminosity system. The other active components are the two aerogel detectors and the photon spectrometer (SPEC). $4X_0$ of dead material shielded the PCAL from radiation damage. The luminosity system was only sensitive to photons that were emitted collinearly to the HERA beam line ($\theta_\gamma < 0.3$ mrad) and not every photon incident on the luminosity system was detected by all. In principle, most of these collinear photons will reach the PCAL with the exception of $8.8 \pm 0.6\%$ which will convert into e^+e^- pairs in the exit window. Some of the e^+e^- pairs will subsequently be deflected by the dipole magnets into the SPEC, where they are measured.

A GEANT [49] simulation has been developed that describes energy deposition and the composition of inactive materials protecting the PCAL. From the GEANT simulation, one can determine the relationship between incident photon energy and raw scintillator energy. 10 million Bethe-Heitler (BH) MC events have been generated and were passed through this detector simulation. The BH photons were generated with energy between $0 < E_\gamma < 27.56$ GeV, emulating the electron beam at HERA.

This simulation does not account for pileup effects which could result in more than 27.56 GeV energy being measured in the PCAL. The results of the simulation are shown in figure 5.7.

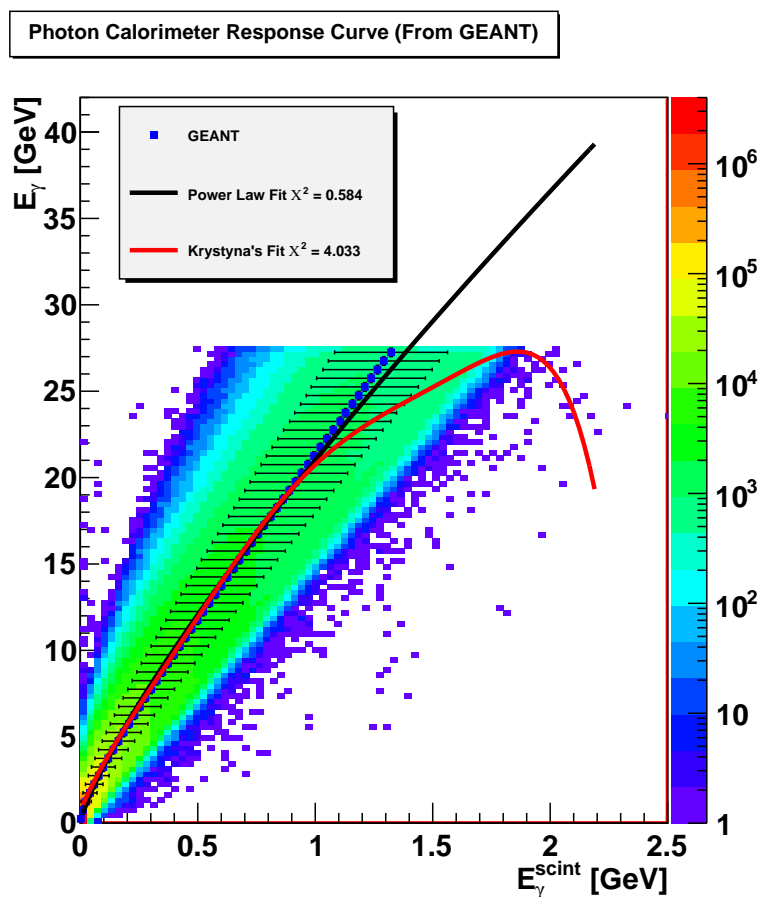


Figure 5.7: The response function of the PCAL. The old calibration is compared to the new. The x -axis represents the uncalibrated energy that was measured into the calorimeter.

A previous calibration of the PCAL fitted an 8th order polynomial to the energy response distribution. This parameterisation failed, because it exhibited unphysical behaviours beyond the restricted ranges where it was defined. A new response function has been developed which more accurately describes the PCAL energy response. This is parameterized by the equation:

$$E_\gamma = \begin{cases} a(E_\gamma^{scint})^p & E_\gamma^{scint} \geq E_\gamma^{scint, cut} \\ \frac{a(E_\gamma^{scint, cut})^p}{E_\gamma^{scint, cut}} E_\gamma^{scint} & E_\gamma^{scint} < E_\gamma^{scint, cut} \end{cases} \quad (5.29)$$

where E_γ^{scint} is the uncalibrated energy measured in the PCAL, a and p are constants which were determined to be $a = 21.8$ and $p = 0.8$ by finding the values which minimized the χ^2 of the fit and $E_\gamma^{scint, cut} = 0.02$ GeV.

5.6 Calibration of the PCAL+AERO System

As mentioned in section 5.5, the far part of the luminosity system contains four active components: the PCAL, SPEC and two aerogel detectors. The aerogel detectors are placed in front of the PCAL and can be used in conjunction with the PCAL to obtain an improved energy resolution. For this calibration, a proper GEANT simulation is not available and the manpower did not exist to develop one. In this situation a data-based calibration is necessary. The form of the energy response was assumed to follow:

$$E_\gamma = a_1 E_1^{AERO} + a_2 E_2^{AERO} + a_3 E_\gamma^{PCAL} \quad (5.30)$$

Where E_{AERO1} and E_{AERO2} are the raw ADC counts from the aerogel detectors, E_{scint} is the uncalibrated energy deposited in the PCAL and a_1 , a_2 and a_3 constants that need to be determined. A χ^2 minimization procedure has been developed to constrain these constants. The same TAG6 DQM runs, which trigger on pilot electron bunches, and were used to determine the resolution of the PCAL+AERO for the MC simulation (see section 4.4.3), are used for this procedure. A pure BH sample is obtained from these runs by requiring a hit in the TAG6. Also it is essential to only calibrate using events which traverse the PCAL and both aerogel detectors. Correlation distributions, which show the relationship between the PCAL and the two aerogel detectors are shown in figure 5.8. Only events between the solid lines in

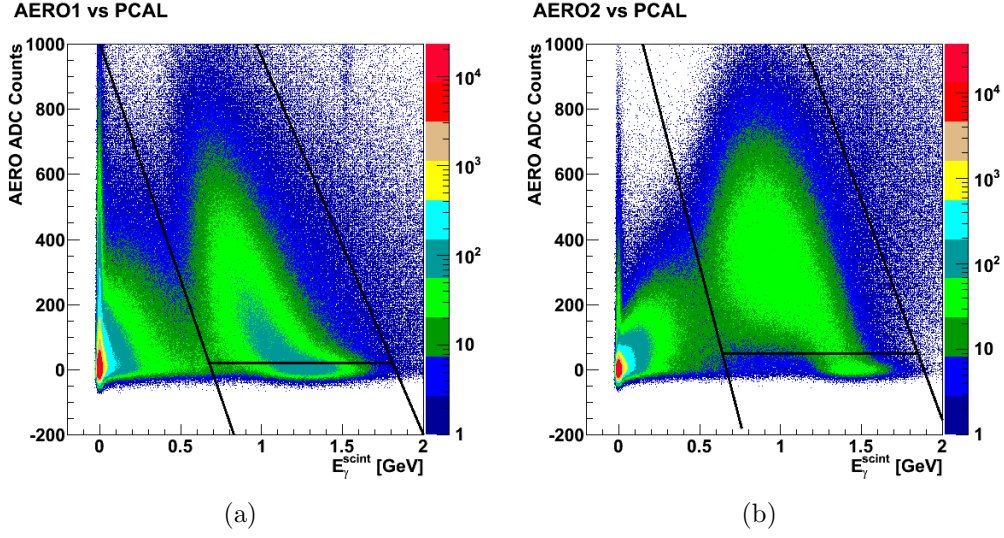


Figure 5.8: Raw aerogel energy plotted against raw scintillator energy for both (a) AERO1 and (b) AERO2. Only events within the solid lines are used in the calibration.

the image are selected. The TAG6 energy can be related to the BH photon energy by the relation

$$E_\gamma = E_e - E_{TAG6} \quad (5.31)$$

where E_e is the electron beam energy. The constants in equation 5.30 are then extracted by determining the values which return the lowest χ^2 .

$$\chi^2 = \sum_{i=1}^N \frac{(\sum_{j=1}^3 a_j e_j - E_{\gamma,i})^2}{\sigma_i^2} \quad (5.32)$$

where the outer sum runs over every one of the N BH events with a hit in the TAG6, $\sum_{j=1}^3 a_j e_j$ is simply restating 5.30 and σ is the combined resolution of E_γ and the inner sum. For this situation, all events are given equal weights such that, $\sigma = 1$.

Differentiating equation 5.32 using $\frac{\partial \chi^2}{\partial a_k} = 0$ yields:

$$\sum_{i=1}^N \frac{E_{\gamma,i}}{\sigma_i^2} e_k = \sum_{j=1}^3 a_j \sum_{i=0}^N \frac{e_j e_k}{\sigma_i^2} \quad (5.33)$$

Equation 5.33 can be expressed as:

$$\beta_k = \alpha_j V_{jk} \quad (5.34)$$

where α_j is a vector of constants. Rearranging the above equation gives an expression for the constants: $\alpha = V^{-1}b$. From this method the constants were found to be: $a_1 = 0.0069$, $a_2 = 0.0106$ and $a_3 = 17.047$.

5.6.1 Calibration Results

The result of the calibration is displayed in figure 5.9. The energy distribution from the new PCAL+AERO calibration has a narrower width and is more symmetric. The non-symmetric nature of the PCAL-only calibration arises from the $4X_0$ inactive material, where an electromagnetic shower may escape detection. Using the aerogel allows us to sample the shower profile as it traverses the passive material, hence allowing for a better measurement. This new calibration is very successful and has already been used in one publication [42] and is slated for two more.

Since this calibration is also implemented in the MC simulation of the luminosity system, the energy resolution can be examined. One approach is to use the expected photon energy from the calorimeter, E_γ^{Exp} , defined in section 5.4. The relative photon energy bias is defined as:

$$\Delta_\gamma = \frac{E_\gamma^{Exp} - E_\gamma^{Mea}}{E_\gamma^{Exp}} \quad (5.35)$$

where E_γ^{Mea} is the measured photon energy in the PCAL+AERO. Due to the large background contribution from uncorrelated BH overlays, it is best to observe this parameter by making bins in E_γ^{Exp} . This is shown in figure 5.10 where 7 bins are displayed. The kinematic peak region, where no high energy photons are expected to be observed, is contained within the first bin.

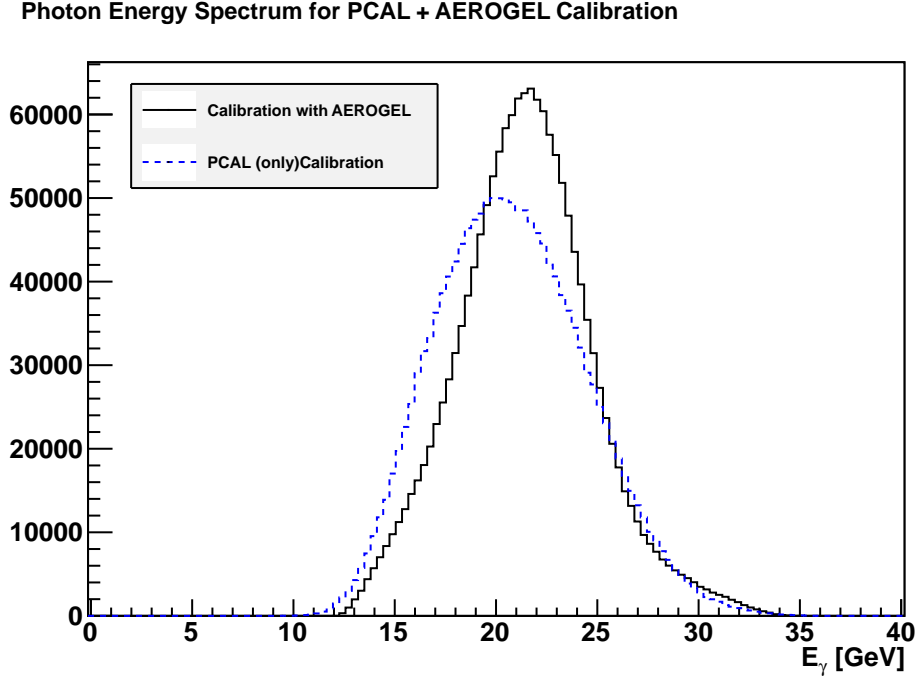


Figure 5.9: Energy of BH photons for both the PCAL calibration and the PCAL+AERO calibration.

Data and Monte Carlo show a good agreement for most of the bins. The important feature of these distributions, which is most apparent in the latter bins, is the ISR peak located at $\Delta_\gamma \approx 0$. The highest peak located $\Delta_\gamma \approx 1$ corresponds to events where no energy is measured in the PCAL+AERO. In the region where $\Delta_\gamma < 0$, a photon is measured with a higher energy than is predicted. This is possible if there is an uncorrelated BH photon or an ISR along with a BH overlay.

5.7 Backgrounds

The analyses outlined in this thesis use a series of selection criteria to obtain a Neutral Current (NC) DIS sample that is relatively free of background. A NC DIS event is characterized by the measurement of a scattered electron. Many backgrounds can fake this signal, including photoproduction and QED Compton events. In this chapter, the main sources of NC DIS background will be introduced and discussed.

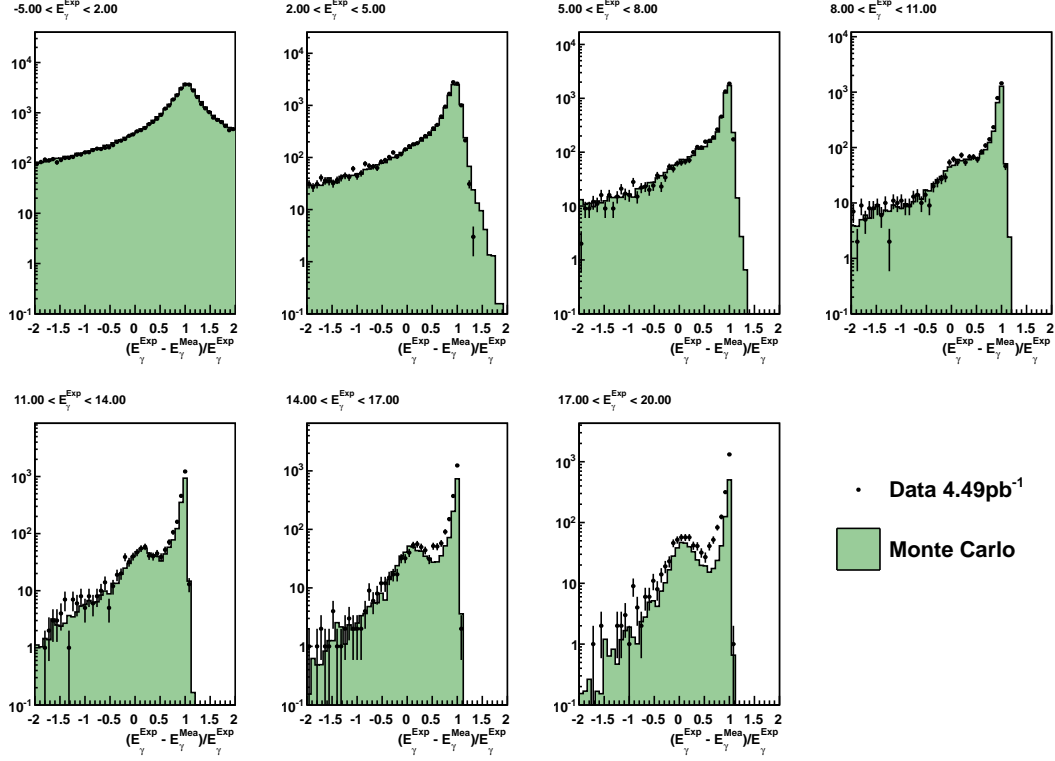


Figure 5.10: Photon Energy Bias, Δ_γ , is shown for 7 variably sized bins of E_γ^{Exp} . This plot compares Data using the new PCAL+AERO calibration with results from the simulation.

5.7.1 Photoproduction

The term photoproduction refers to a class of events characterized by the emission of an almost on mass-shell photon. These events have $Q^2 \sim 0 \text{ GeV}^2$ and occur several orders of magnitude more often than DIS events. Because the electron is only lightly deflected and continues to travel down the beam pipe, most photoproduction events are quickly rejected by cutting events with a minimum E'_e . More photoproduction events can also be rejected by applying minimum cut on the variable δ . In section 5.1.3, δ was defined as $\delta = \sum_h (E_h - p_{z,h}) + (E_e - p_{z,e})$ where the two components should add up to $2E_e$. In photoproduction events, the real scattered electron is not detected and as a consequence δ is expected to be less than $2E_e$. Cutting on δ does remove a large fraction of photoproduction events, but still some of them can

be reconstructed with a higher δ and are virtually indistinguishable from DIS. A photoproduction enriched MC sample has been generated using PYTHIA 6.221 [47], this sample is used for estimating the background contribution.

5.7.2 QED Compton events

QED Compton (QEDC) events are a specific type of event characterized by the observation of two electromagnetic objects in the central detector with back-to-back balanced p_T and $E - p_z$ adding up to 55 GeV. These events are unlikely to be associated with a low $E - p_z$ ISR event, but they can contribute in the kinematic peak. For this thesis, a QEDC MC sample has been generated, with the GRAPE-COMPTON [65] generator. It demonstrates that QEDC is not a large contribution to any of the measured cross sections in this thesis.

5.8 Event Sample and Selection

5.8.1 Event Sample

Four different data samples are used in this thesis, three of them correspond to special running conditions which are referred to as the High Energy Running (HER), Low Energy Running (LER) and Medium Energy Running (MER). The fourth one is called the ISR Dataset. Data in the ISR dataset is obtained using a special trigger configuration called SPP11. Table 5.1 is a summary of the data accumulated in each of these running ranges and the total number of events accumulated. All the events measured will be subject to a series of selection criteria which will be detailed below.

A special trigger chain has been implemented for the datasets used in the analyses discussed in this thesis. These trigger definitions will be given below, followed by

Name	Period	E_p [GeV]	\sqrt{s} [GeV]	\mathcal{L} [pb ⁻¹]	Collected	Events
HER	2006/2007 e^+	920	318.2	180.54		22782929
MER	2007 e^+	575	251.5	9.36		4622620
LER	2007 e^+	460	224.9	15.69		8893949
ISR	2007 e^+	920	318.2	4.354		4339137

Table 5.1: The luminosity and number of measured events for the four different data sets.

a detailed list of the event selection used for measuring ISR and the NC DIS cross sections.

5.8.2 The F_L Trigger Definitions: SPP15 and SPP16

SPP15 and SPP16 are trigger chains which make specific event requirements on all three levels of the ZEUS trigger system (for details about the ZEUS trigger, see section 3.2.4). Their purpose is to select NC DIS events, which are used to measure F_2 and F_L . These triggers are multi-purpose and used at all three beam energies, i.e. in HER, MER and LER, without modifications.

The Third Level Trigger (TLT) requirements on SPP15 and SPP16 derive from the following requirements on the Second Level Trigger (SLT):

- $E - p_z > 30$ GeV
- At least 2.5 GeV is measured in the electromagnetic part of the RCAL, BCAL or FCAL.
- The removal of off-momentum positrons is achieved by a timing cut.

SPP15 and SPP16 have further requirements on the TLT. The SPP15 requirement is:

- $30 \text{ GeV} < E - p_z < 80 \text{ GeV}$.

The SPP16 requirements are:

- $E'_e > 2$ GeV
- A 12 cm box cut is placed around the beam pipe on the electron position, $|x| < 12$ cm and $|y| < 12$
- $E - p_z > 30$ GeV

5.8.3 The ISR Trigger Definition: SPP11

SPP11 is a trigger definition designed to extend the measurable range in δ . Maximizing this range increases the measurable energy range of ISR photons. This trigger definition, and the dataset extracted from it, are used exclusively in the work contained in this thesis. The SLT definitions for SPP11 are:

- $E - p_z > 12$ GeV
- $E'_e > 5$ GeV

The TLT definition for SPP11 are:

- $E - p_z > 12$ GeV
- $E'_e > 4$ GeV
- Photoproduction is suppressed by introducing a 18 cm box cut around the beam pipe. This is defined by $|x| < 18$ cm and $|y| < 18$

This trigger was installed during the last part of the 2007 e^+ running period and accumulated 4.49 pb^{-1} in total.

5.9 Event Selection

This thesis contains three complementary analyses. The first analysis to be presented is the experimental verification of the radiative correction to DIS. This analysis benefits from the PCAL+AERO calibration and detector simulation. Also benefiting

from these components is the second analysis, which uses radiative events as a means to probe the proton at lower virtualities than normally accessible. The third analysis uses three different centre-of-mass energies (HER, MER and LER datasets) to extract the F_2 and F_L structure functions.

A Neutral Current (NC) DIS sample is required to perform each of these analyses. Section 5.9.1 outlines the basic NC DIS criteria applied to the datasets to reduce non-DIS background. The NC DIS requirements to be listed will be used as a foundation for all analyses presented in this thesis. To perform each analysis, slight modifications to this criterion are required. To save space, the event selection criteria listed in sections 5.9.2 - 5.9.4, are derived from section 5.9.1 and only changes to the standard NC DIS selection will be shown. Section 5.10 will summarize all the event samples used in this thesis.

5.9.1 Neutral Current DIS Event Selection

A general NC DIS event selection is presented in this section. This selection is used in the measurement of the F_2 and F_L structure function with the HER, MER and LER datasets.

Events were selected if they satisfied the criteria:

- Events triggered either SPP15 or SPP16.
- The highest probability Sinistra electron candidate has $E'_e > 6$ GeV.
- The highest probability electron candidate satisfies the following requirement on the probability of the candidate as function of its energy

$$P_e > \max\left(0.8, 0.95 - 1.5e^{-E'_e/2.5}\right) \quad (5.36)$$

This particular cut was shown to maximize the electron finding efficiency.

- Requiring that $42 \text{ GeV} < \delta < 65 \text{ GeV}$ reduces contributions from non-DIS backgrounds and ISR.
- The reconstructed Vertex position is consistent with being in the central interaction point, $|Z_{vtx}| < 30 \text{ cm}$.
- $y_{el} < 0.95$, removes poorly reconstructed events
- $y_{JB} > 0.05$, removes events where the hadronic system is not well contained.
- The ratio of the transverse momentum of the hadronic system to the transverse momentum of the scattered electron must be balanced. This is represented by the condition $p_{T,h}/p_{T,e} > 0.3$, which removes poorly reconstructed DIS events.
- The event is consistent with the expected HERA topology of two interacting beams crossing. A timing cut on ensures that the event is consistent with a HERA bunch crossing.
- The event topology is inconsistent with that of a QEDC event. Events were rejected if they contained two back-to-back electrons, in the ϕ direction, with equal energy.

An electron backwards tracking utility is used in this thesis. This utility is known as UVF [63] and requires that a calorimeter deposit, which Sinistra defines as coming from an electron candidate, be matched up with a track in the CTD and the MVD (see section 3.2.1 for a description of the tracking system). This utility is highly effective at tagging photoproduction events whereby an electron is faked in the calorimeter. A UVF candidate is considered to be a good electron if it satisfies the conditions that:

- The candidate's projected path passes through the MVD fiducial volume

- The candidate must be related to a track that traversed at least four CTD super layers.
- The energy of the candidate must be measured in the RCAL.
- The electron scattering angle (θ'_e) is determined from the SRTD, or if unavailable from the HES (see section 3.2.3 for a description of these components). If no information is available from either of these two components, events are rejected.

To ensure that the event will be properly reconstructed, various cuts were made on the detector fiducial volume. An event will be rejected if its location is consistent with it being measured in

- a calorimeter cell which has been labeled as a *bad cell* for that specific run.
- the narrow crack between the RCAL and the BCAL.
- an area in the CAL known as the *chimney*. A hole in the CAL allows for a helium cooling pipe to pass through to the inner detector.

After applying all the criteria approximately 97% of the initial sample was rejected and the HER, MER and LER samples contain 823075, 118120, 205773, events respectively. The same selection criteria has been applied to data and reconstructed MC events. Figures A.1, A.2 and A.3 compare data with the fully reconstructed MC for four key detector quantities: electron energy (E'_e), electron scattering angle (θ'_e), $E - p_z$ (δ) and the Z vertex. Each figure corresponds to a dataset from a different running period. Figures demonstrate excellent agreement between these variables for all three datasets.

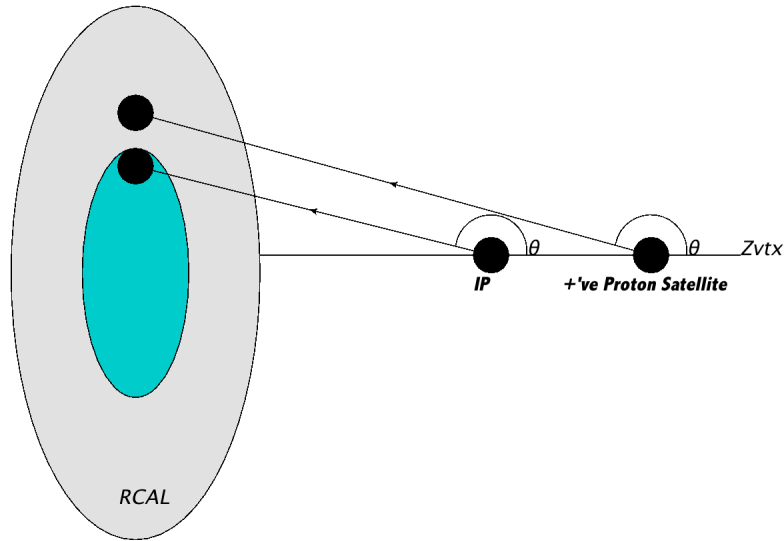


Figure 5.11: A visual representation of the geometry of a satellite vertex event where the darker region represents the lower limits of the ZEUS calorimeter.

5.9.2 Satellite Vertex Selection

It is possible to extend the ZEUS kinematic range to lower momentum transfers, Q^2 , by selecting events that interacted with the positive satellite proton bunch. Figure 5.11 shows the geometry for this class of events. Comparing an event in the nominal interaction point with a satellite vertex event, it is possible to measure events at lower virtualities than normally accessible, as can be seen from figure 5.11.

Shifted vertex samples have been selected for the HER, LER and MER running periods. Events are considered to be within the satellite vertex if the vertex is reconstructed within the range $30 \text{ cm} < Z_{vtx} < 100 \text{ cm}$. The samples use the same event selection as the nominal analysis discussed in section 5.9.1, the only exceptions being that the Z vertex be reconstructed in the positive proton satellite region and the requirement on y_{JB} has been lifted. The y_{JB} cut was removed after studies showed that it was unnecessary for this sample.

For the HER, MER and LER samples 50742, 15781 and 31286 events were measured respectively. Detector control distributions comparing data and MC for various key detector quantities are shown in figures A.4 for HER, A.5 for MER and A.6 for LER. They demonstrate very strong agreements between data and MC throughout the whole measurable range.

5.9.3 ISR-Enriched Selection

A measurement of the radiative correction is important for ZEUS and other DIS experiments. As mentioned previously, ISR lowers the effective energy of the incoming electron and hence reduces the δ measured. Non-radiative DIS events are measured around $\delta \approx 55$ GeV. Events reconstructed with lower δ values are not necessarily ISR events, for example, photoproduction also lowers the δ of an event.

This section contains the prescription to create an ISR-enriched selection. The aim is to reduce the contribution from non-DIS events while minimally affecting the ISR contribution. An ISR-enriched selection is motivated for two different event samples, the ISR sample and the HER sample. Both samples have distinct advantages and disadvantages. The ISR sample uses the SPP11 trigger requirements (see section 5.8.3) and can measure δ values as low as 13 GeV, however the statistical power of the $\mathcal{L} = 4.49pb^{-1}$ sample is limited. The HER sample using the SPP15 or SPP16 trigger definitions, has ten times the luminosity of the ISR sample, but has a SLT cut at $\delta > 30$ GeV. The selection criteria outlined in this section correspond mostly to those of the NC DIS sample outlined in section 5.9.1. Modifications to the NC DIS selection are listed in the following two sections.

ISR-Enriched Selection - HER Sample

- $E - p_z$ must be found within the range $35 \text{ GeV} < \delta < 65 \text{ GeV}$.

- To preserve ISR events, the requirement on y_{JB} have been lifted.

After the event selection, the ISR-enriched sample from the HER dataset contains 1163192, events. The control distributions for this event sample are displayed in figure A.1.

ISR-Enriched Selection - ISR Sample

- Events satisfied the trigger criteria for SPP11.
- $E - p_z$ must be found within the range $15 \text{ GeV} < \delta < 65 \text{ GeV}$.
- To preserve ISR events, the requirement on y_{JB} have been lifted.

After the event selection, the ISR enriched sample from the ISR dataset contains 123986, events. The control distributions for this data sample are shown in figure A.7.

5.9.4 Tagged Photon Samples

An ISR-tagged sample can be obtained by tagging events where the ISR photon is predicted and observed. Photon energy is predicted from equation 5.28. The PCAL+AERO system measures collinear ISR photons at $Z = -107 \text{ m}$. An ISR-tagged sample is a subset of the ISR-enriched samples described in the previous section. To tag photons, additional requirements are applied to the sample. These requirements are:

- $|E_{\gamma}^{Exp} - E_{\gamma}^{Mea}| < 4.5 \text{ GeV}$.
- $E_{\gamma}^{Exp} > 5 \text{ GeV}$.
- $E_{\gamma}^{Mea} > 5 \text{ GeV}$.

These additional criteria require that a photon be predicted using equation 5.28 and observed, in the PCAL+AERO, with a similar energy.

ISR Tagged Selection - HER Sample

Applying the ISR-tagged selection criteria to the HER sample returns 15065 events. The control distributions are shown in figure A.8.

ISR Tagged Selection - ISR Sample

Applying the ISR-tagged selection criteria to the ISR sample returns 2911 events. The control distributions are shown in figure A.8.

5.10 Summary of Event Samples

In total 10 event samples are used in this thesis, they are summarized in table 5.2 for the purpose of clarity.

Sample	\mathcal{L}	# Events
HER Nominal Vertex	44.5 pb ⁻¹	823075
MER Nominal Vertex	7.1 pb ⁻¹	118120
LER Nominal Vertex	13.9 pb ⁻¹	205773
HER Satellite Vertex	44.5 pb ⁻¹	50742
MER Satellite Vertex	7.1 pb ⁻¹	15781
LER Satellite Vertex	13.9 pb ⁻¹	31286
HER Dataset ISR-Enriched	44.5 pb ⁻¹	1163192
ISR Dataset ISR-Enriched	4.49 pb ⁻¹	123986
HER Dataset ISR-Tagged	44.5 pb ⁻¹	15065
ISR Dataset ISR-Tagged	4.49 pb ⁻¹	2911

Table 5.2: Event samples used in this thesis.

CHAPTER 6

Experimental Verification of Radiative Corrections to DIS

6.1 Introduction

The topic of radiative corrections at HERA has garnered much attention over the years [66, 67, 68, 69]. QED Initial State Radiation (ISR) is predicted to be a large correction to the DIS cross section. Monte Carlo (MC) programs such as HERACLES [45] predict the size of the radiative correction for DIS events. Cross section measurements made at HERA are related to the Born level cross section through the equation:

$$\left[\frac{d^2\sigma^{ep}}{dx dQ^2} \right]^{Mea} = \left[\frac{d^2\sigma^{ep}}{dx dQ^2} \right]^{Born} (1 + \delta_{RC}(x, Q^2)) \quad (6.1)$$

where the double differential terms are the measured and Born level cross sections respectively. $\delta_{RC}(x, Q^2)$ is the contribution from radiative corrections. The HERACLES program calculates all QED higher-order corrections to $\mathcal{O}(\alpha^2)$ and is generally accepted to provide the best description of the radiative DIS [70]. Nevertheless, an experimental check of $\delta_{RC}(x, Q^2)$ can further advance our understanding of this correction. This is especially critical when studying the high- y regime where the ISR contribution becomes very large and an understanding of the radiative correction limits our knowledge of proton structure [20].

The first analysis to be presented in this thesis is an experimental verification of the radiative correction. Without a perfect photon detector, it is impossible to measure $\delta_{RC}(x, Q^2)$, however its contribution can be verified by measuring the spectrum for

radiative photons, $\frac{d\sigma^{\text{ISR}}}{dE_\gamma}$. A previous measurement of this cross section has been performed by the H1 Experiment using 1993 data [71] (see figure 6.1). This techni-

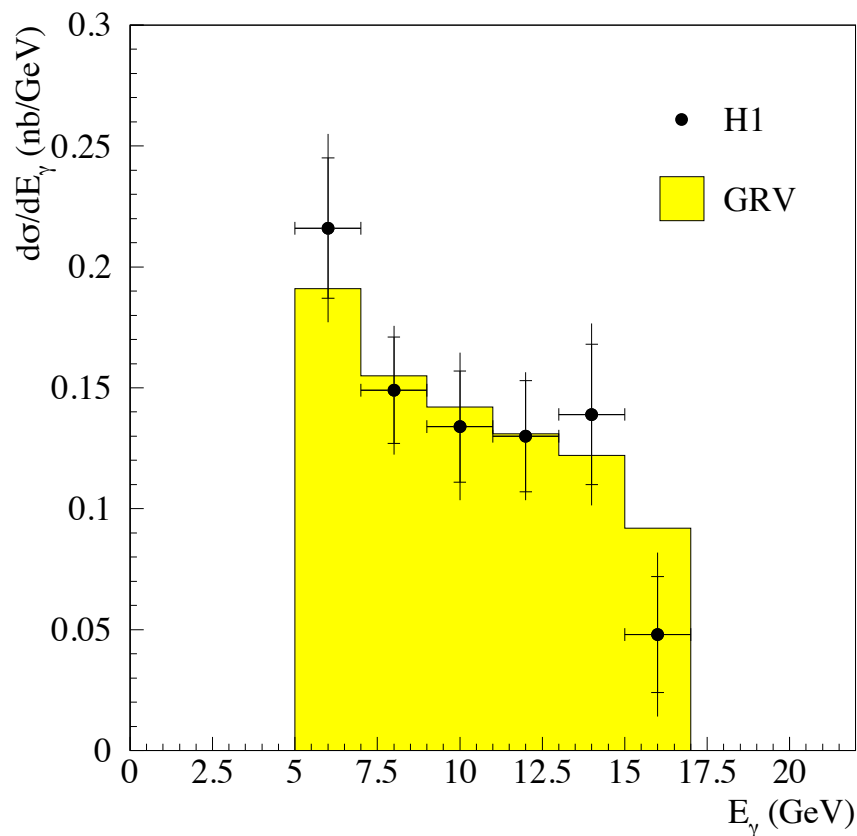


Figure 6.1: The ISR cross section measured by the H1 Experiment in 1993. Results are compared with HERACLES [71].

cally challenging measurement requires a direct measurement of collinear radiative photons.

Section 6.2 outlines the techniques used in the measurement. In section 6.2.2, the ISR signal is extracted and the number of ISR events are counted in bins of $E - p_z$, this number is used to determine $\frac{d\sigma^{\text{ISR}}}{d\delta}$. The chapter concludes with the measurement of the ISR cross section, $\frac{d\sigma^{\text{ISR}}}{dE_\gamma}$, which marks the first time this cross section has been determined from the ZEUS detector.

6.2 Measurement Technique

A collinear ISR photon can be measured using the ZEUS luminosity measuring system (see section 3.3). The photon energy is measured using the photon calorimeter (PCAL) combined with the aerogel Cherenkov detectors (AERO). The calibration for the PCAL+AERO system is outlined in section 5.6. A standalone MC simulation has been developed for this analysis (see section 4.4). This simulation facilitates the comparison between data and theoretical predictions. This analysis uses the ISR-enriched sample introduced in section 5.9.3.

Two independent techniques are used to verify the size of the radiative correction. The first technique relies on the main calorimeter to infer the photon energy, which is then verified by a direct measurement of the photon. This method is complicated by the dominating BH background. The second technique uses only the luminosity system information.

The variable $E - p_z$ has a strong relationship to the ISR photon energy. This is evident in the relationship between $E - p_z$ and E_γ displayed in figure 6.2. Some of the interesting features of this contour plot include:

- **The Kinematic Peak**

Events reconstructed around $E - p_z \approx 55$ GeV are considered to be kinematic peak events. These events are the dominating feature of this plot. The events measured here should not contain any high energy ISR events. All the higher energy photons are expected to arise from BH overlays. The BH background is not correlated to DIS events and is expected to occur at the same rate regardless of $E - p_z$.

- **The ISR Band**

This shallow diagonal band, that begins on the upper left side and moves

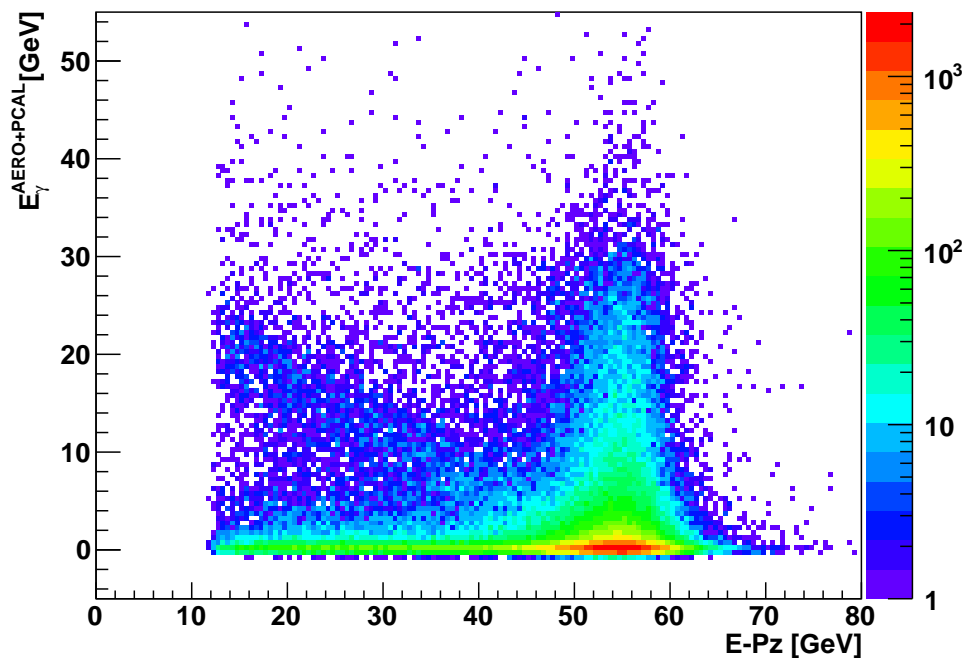


Figure 6.2: Events from the 2007 ISR running period show the correlation between E_γ and $E - p_z$.

downward, is called the ISR band. This region is where we would theoretically predict ISR events to exist.

- **Low $E - p_z$ events**

The luminosity system has a limited acceptance region and accepts about 30% of ISR photons. Background processes, such as photoproduction, have a reduced $E - p_z$ and these background events can contain an overlay photon and interfere with the ISR signal.

Because the PCAL+AERO measurement does not distinguish between BH and ISR events, extracting the number of ISR events from the ISR band is not trivial. A prescription for statistically subtracting the BH overlays from the ISR signal has been developed.

6.2.1 Photon Energies in bins of $E - p_z$

The aim of this section is to count the number of ISR events and to compare that result with predictions from HERACLES. A relationship between the ISR photon and the detector quantity $E - p_z$, is clearly visible in the ISR band in figure 6.2. To exploit this relationship, bins of $E - p_z$ can be defined.

ISR-enriched samples are generated for both the HER and the ISR datasets in section 5.9.3. The HER dataset ($\mathcal{L} = 44.5\text{pb}^{-1}$) has approximately 10 times more statistics than the ISR dataset ($\mathcal{L} = 4.49\text{pb}^{-1}$), but the ISR dataset extends to much lower $E - p_z$ ($E - p_z > 15.0\text{ GeV}$ compared to $E - p_z > 35.0\text{ GeV}$). Due to statistics, ISR dataset was distributed in $E - p_z$ bins of 5 GeV while the HER dataset has 2.5 GeV wide bins. Seven photon energy distributions from the HER dataset, spanning the range $35.0 < E - p_z < 52.5\text{ GeV}$ are shown in figure 6.3. Figure 6.4 displays the equivalent plot for the ISR dataset, but spanning the range $15.0 < E - p_z < 50.0\text{ GeV}$. In all of these figures, the ISR signal is expected to be a peak that is shifting to lower photon energies for increasing values of $E - p_z$. The dotted area represents the predicted contribution of ISR from the MC. The extended tail arises from ISR events being accompanied by a BH overlay, as was described in section 4.4.4.

6.2.2 ISR Signal Extraction

To extract the ISR signal, it is necessary to find a prescription for treating the large BH overlay background. The number of ISR events is given by the relation:

$$N^{ISR} = N_{data} - CN_{BH} \quad (6.2)$$

where C is a normalization constant and N_{BH} is a BH enriched sample. A pure BH sample can be obtained by selecting events in the kinematic peak (See section 5.4).

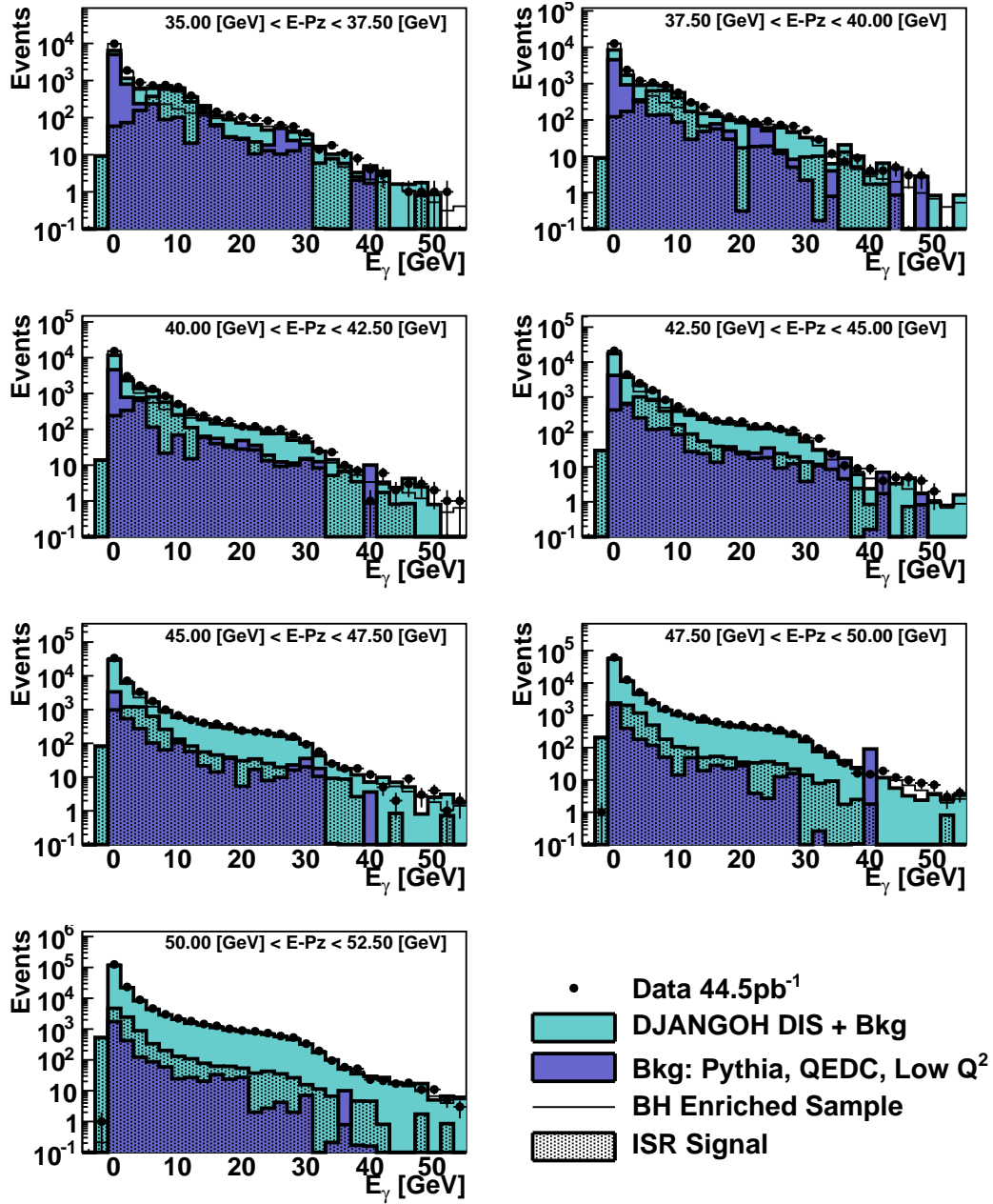


Figure 6.3: Distributions of photon energy in for different bins of $E - p_z$ for the HER dataset. The points represent data and the two histograms represent the MC contributions. The predicted ISR signal is shown by the dotted area. Also shown (thin solid line) is a BH enriched sample distribution, which is normalized to the pedestals, overlaid and superimposed to each distribution.

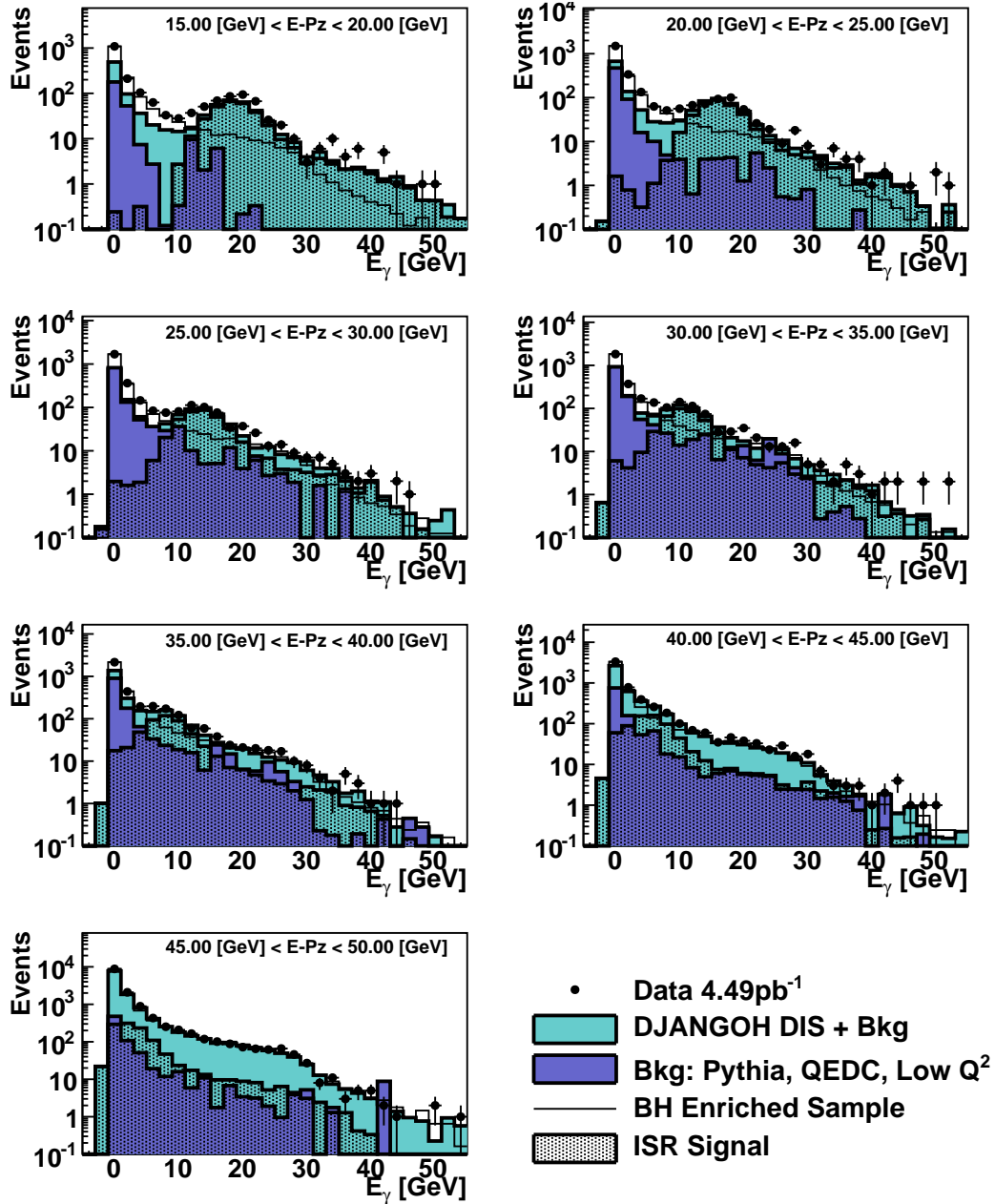


Figure 6.4: Distributions of photon energy in for different bins of $E - p_z$ for the ISR dataset. The points represent data and the two histograms represent the MC contributions. The predicted ISR signal is shown by the dotted area. Also shown (thin solid line) is a BH enriched sample distribution, which is normalized to the pedestals, overlaid and superimposed to each distribution.

The normalization constant is found by fixing the height of the pedestal of the kinematic peak sample to be the height of the pedestal in each $E - p_z$ bin. An example of a kinematic peak sample was shown already in figure 4.9.

The pedestal region is located around $E_\gamma \sim 0$ and is always the maximum. Data and MC are treated in the exact same manner and the normalization constants are determined independently. The BH contribution from each $E - p_z$ bin is subtracted, leaving behind the ISR signal. The resulting distributions are displayed in figure 6.5 for the HER dataset and figure 6.6 for the ISR dataset.

Clearly visible in each distribution is the ISR signal and its tendency to move to lower E_γ for increasing $E - p_z$. In general, very good agreement is demonstrated between data and MC predictions.

The vertical lines in the figures 6.5 and 6.6 represent a $\sim 2.5 \sigma$ range from the mean peak position or down to 1 GeV. Below 1 GeV is considered to be the pedestal region. The number of ISR events, N^{ISR} , in each $E - p_z$ bin is obtained by integrating between the two vertical lines. For the HER dataset this result is shown in figure 6.7 and for the ISR dataset the result is displayed in figure 6.8.

6.2.3 First Measurement of the ISR Cross Section

In principle, once the number of ISR events, $N_{\text{Data}}^{\text{ISR}}$, is measured, the cross section for ISR events in bins of $E - p_z$ can be determined. The cross section for ISR events is given by:

$$\frac{d\sigma^{\text{ISR}}}{d\delta} = \frac{N_{\text{Data}}^{\text{ISR}} N_{\text{Gen}}^{\text{ISR}}}{N_{\text{Rec}}^{\text{ISR}} \mathcal{L} \Delta\delta} \quad (6.3)$$

where \mathcal{L} is the integrated luminosity of the sample and $\Delta\delta$ is the size of the $E - p_z$ bin. This result is displayed in figure 6.9 and shows very good agreement with HERACLES predictions throughout the entire $E - p_z$ region. From this result, it has

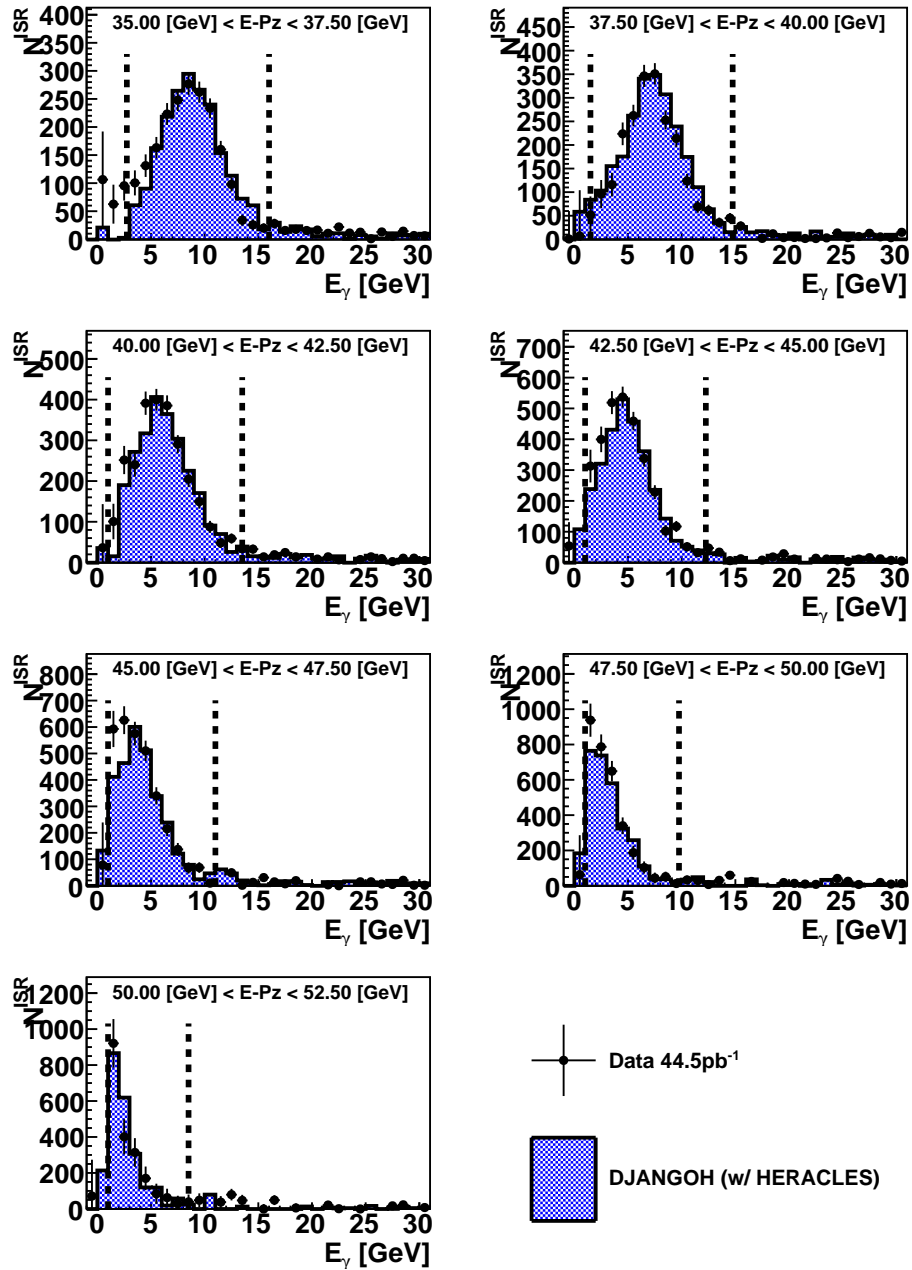


Figure 6.5: Distributions of photon energy for different bins of $E - p_z$. Results for the HER dataset are shown after the BH events have been statistically subtracted.

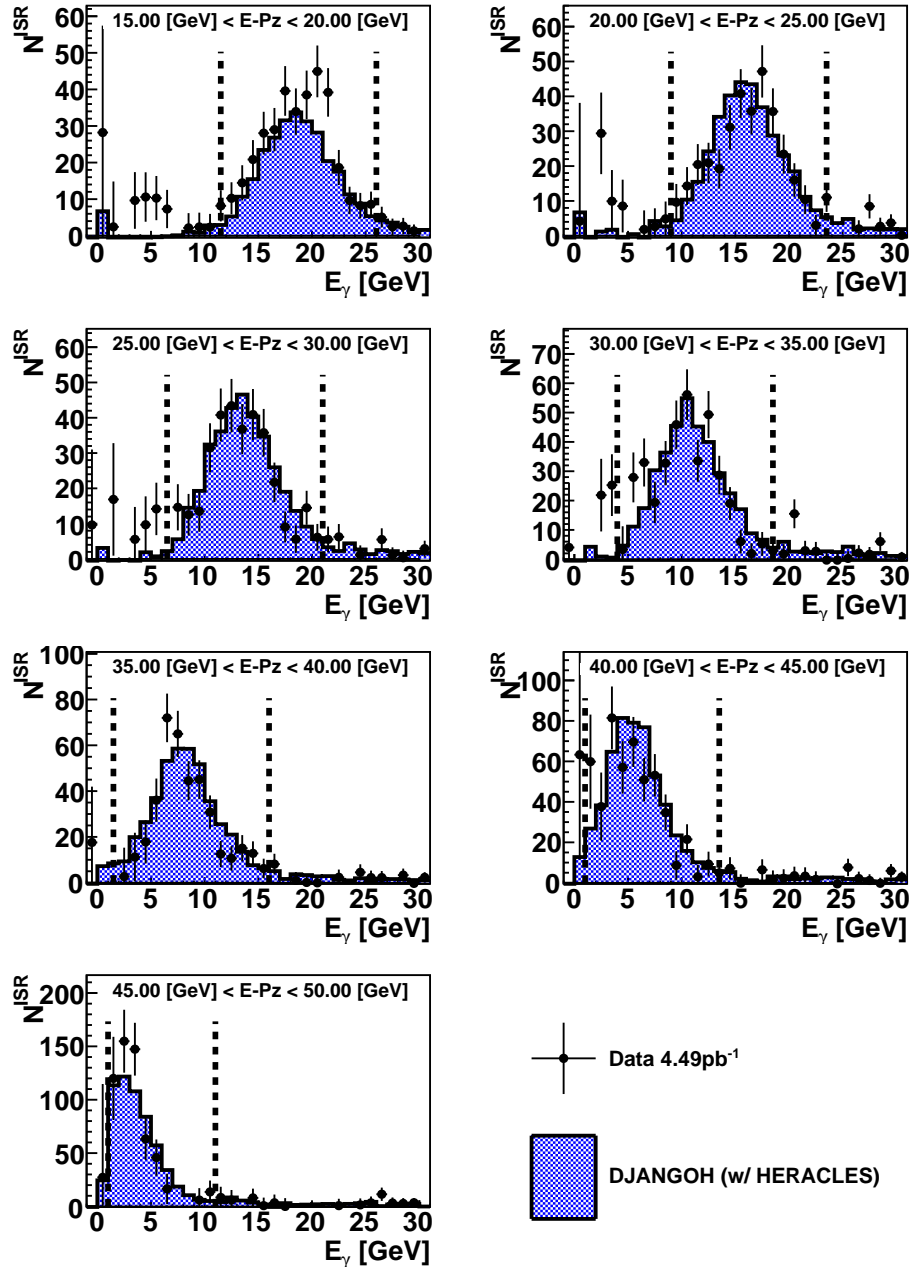


Figure 6.6: Distributions of photon energy for different bins of $E - p_z$. Results for the ISR dataset are shown after the BH events have been statistically subtracted.

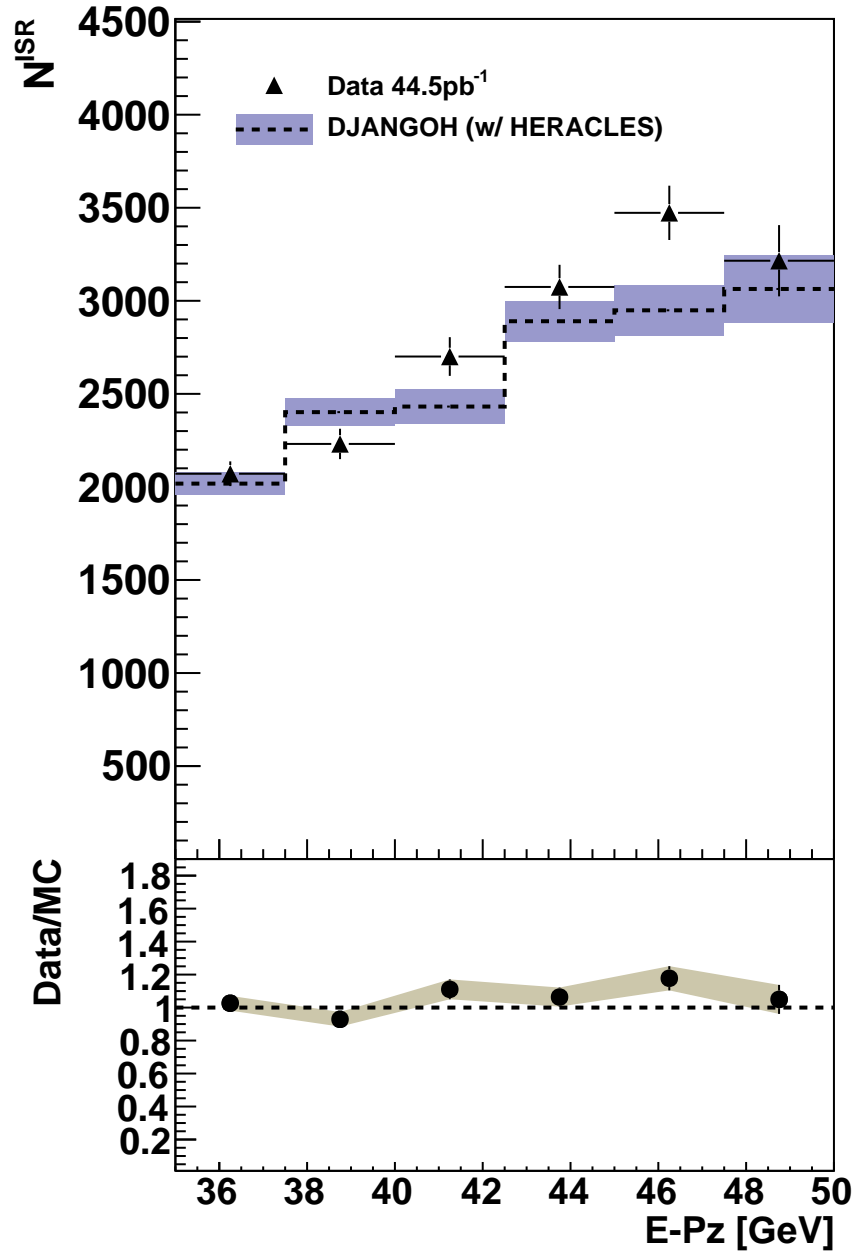


Figure 6.7: The number of ISR events, N_{ISR} , measured in each $E - p_z$ bin for the HER dataset (top). An error-wide band to guide the eye showing the data-MC ratio is also displayed (bottom). Only statistical errors are shown.

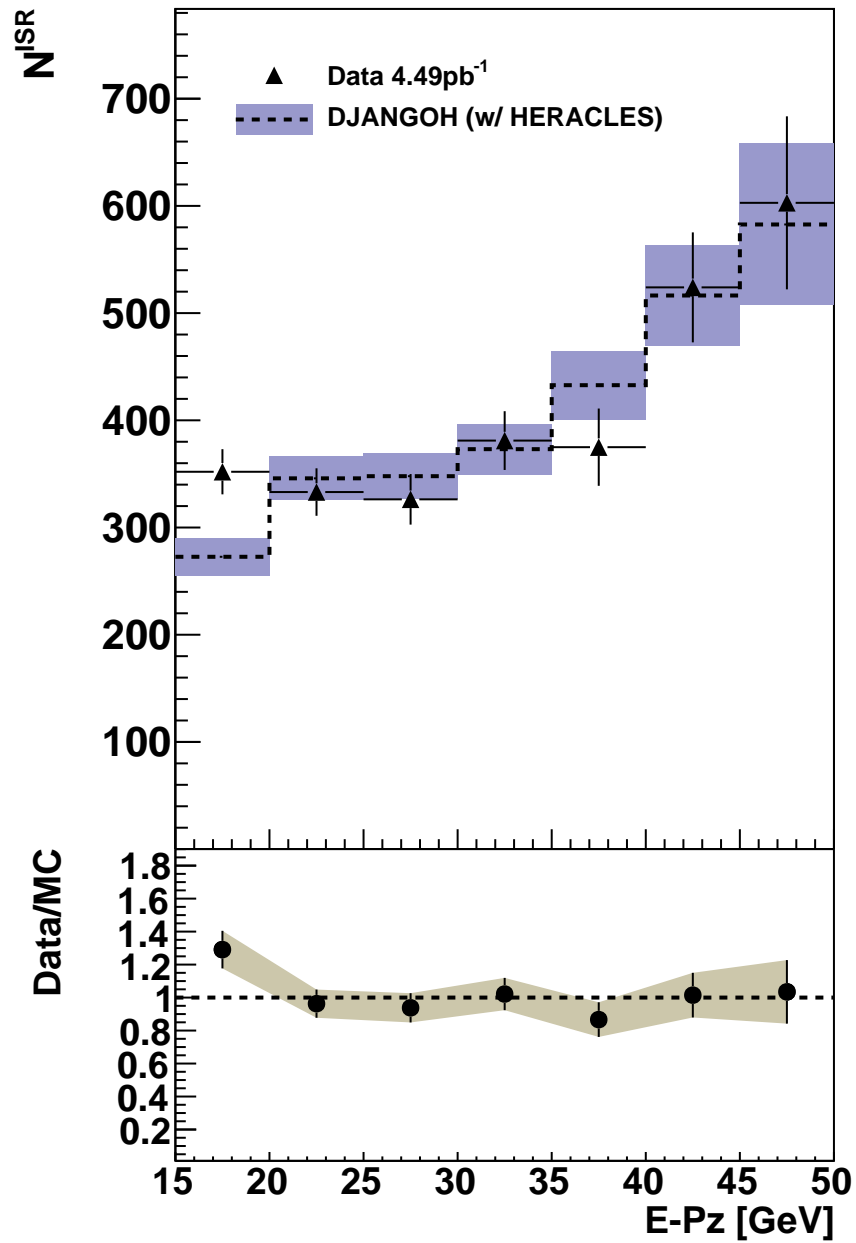


Figure 6.8: The number of ISR events, N_{ISR} , measured in each $E - p_z$ bin for the ISR dataset (top). An error-wide band to guide the eye showing the data-MC ratio is also displayed (bottom). Only statistical errors are shown.

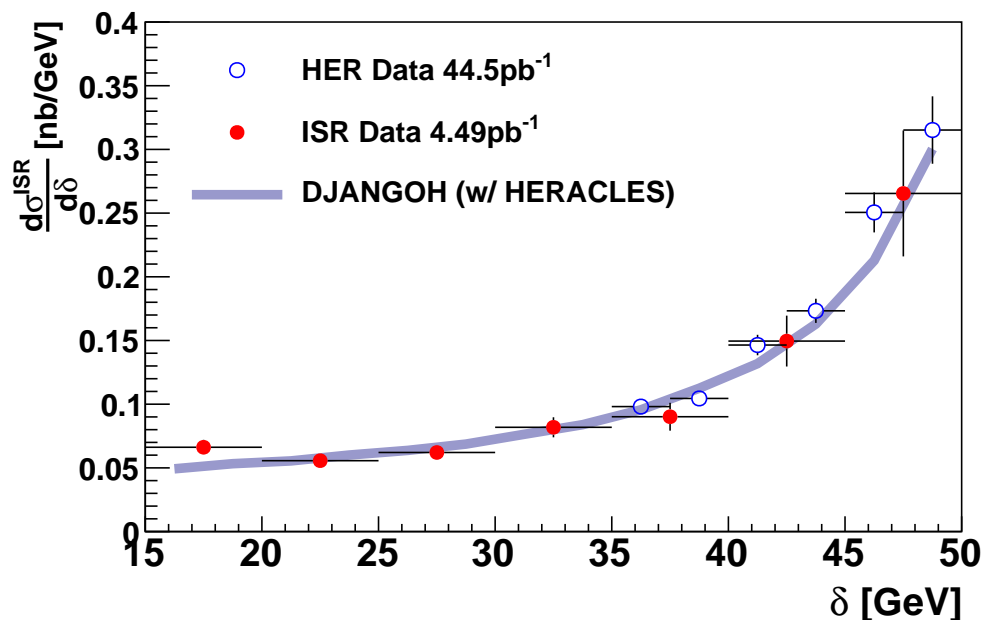


Figure 6.9: The ISR Cross Section $\frac{d\sigma^{\text{ISR}}}{d\delta}$ from the HER and ISR datasets. Comparisons are made with HERACLES predictions. Only statistical errors are shown.

been demonstrated that $E - p_z$ can be exploited to obtain predictions of ISR photon energies.

This result also lays the framework for the measurement of the ISR cross section, $\frac{d\sigma^{\text{ISR}}}{dE_\gamma}$, which will serve as an experimental check of the radiative correction predicted from HERACLES.

6.3 Measuring the ISR Cross Section

The aim of this section is to measure the radiative portion of the DIS cross section, $\frac{d\sigma^{\text{ISR}}}{dE_\gamma}$. This cross section has never before been measured with the ZEUS detector.

This cross section will be measured within the following kinematic boundaries:

- $E'_e > 6$ GeV

- $E_{\gamma}^{Gen} > 5 \text{ GeV}$
- $Q^2 > 11 \text{ GeV}^2$ - A minimum Q^2 removes poorly reconstructed events.
- The photon must be accepted by the ZEUS luminosity system. This is roughly equivalent to the requirement $\theta_{\gamma} < 0.045 \text{ mrad}$

These boundaries are applied at the MC generator level and are intended to match equivalent criteria at the reconstructed level (see section 5.9.3 for full event selection).

Two equally valid experimental approaches are used to perform this measurement. Using two methods is advantageous because one can serve as a cross check of the other. The first technique is built up from the subtraction formalism described in section 6.2; this will be referred to as the $E - p_z$ Method since the signal is first extracted in bins of $E - p_z$. In the second method, the photon is measured by the luminosity system and there are no requirements on the main detector; this method is called the *PCAL Method*. These methods differ in the way the number of ISR events, N^{ISR} , is extracted. Common to both methods is the binning and cross section determination procedure.

6.3.1 Bin Selection

To obtain the maximum amount of information from a cross section, the optimal binning must be chosen. The purity, efficiency and acceptances indicators are used to determine the quality of the data in the bin. These quantities are defined below for selected events:

- The purity is an indicator which we will use to determine whether or not the bin is qualitatively good. It is defined as the ratio between the number of events which are generated and reconstructed in a specific bin to the number

of events reconstructed in that specific bin.

$$\text{Purity} = \frac{\text{\#events generated and reconstructed in bin}}{\text{\#events reconstructed in bin}} \quad (6.4)$$

- The efficiency is a measure of how many events are both measured and generated in a specific bin compared to how many events are generated in that same bin. Otherwise stated:

$$\text{Efficiency} = \frac{\text{\#events generated and reconstructed in bin}}{\text{\#events generated in bin}} \quad (6.5)$$

- The acceptance is defined as how many events are measured in a specific bin compared to the number of events generated in that bin.

$$\text{Acceptance} = \frac{\text{\#events reconstructed in bin}}{\text{\#events generated in bin}} \quad (6.6)$$

The purity, efficiency and acceptance for the HER and ISR datasets are displayed in figure 6.10 and figure 6.11 respectively. The vertical lines represent the regions where measurements are made. Below 5 GeV, it is difficult to deconvolute ISR from the BH background while the upper limit is dictated by the $E - p_z$ requirements on the TLT Trigger definition.

In a typical DIS analysis, one might restrict their study to events where the acceptance and purity are measured above 20% and 30% respectively [20]. Because this thesis uses the luminosity monitors, which are situated in a high-background environment, migrations are much more likely to occur. These migrations result in reduced values for purity, efficiency and acceptance. These indicators are introduced to determine if a bin is qualitatively good, however this thesis does not require any minimum values.

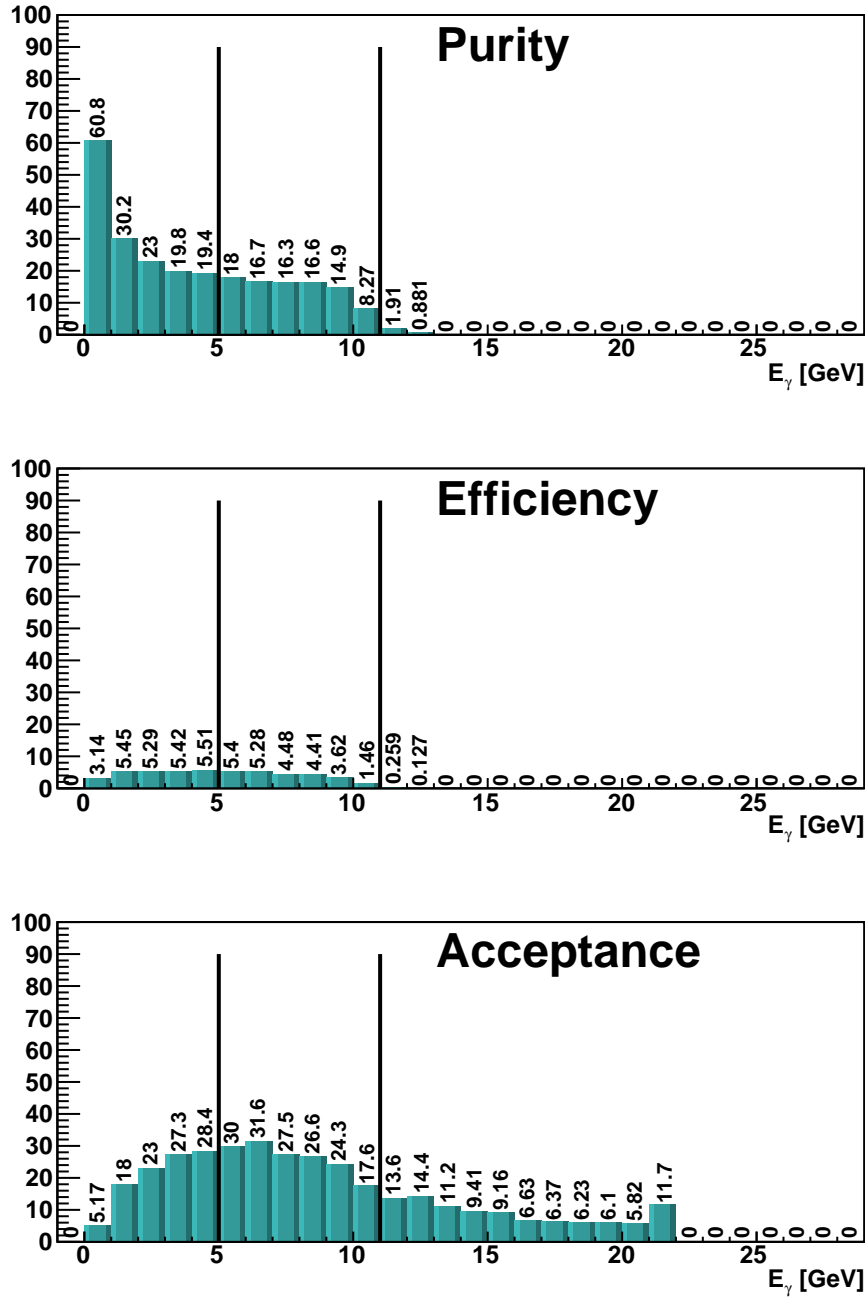


Figure 6.10: The bin purities, efficiencies, and acceptances, given in percent, are shown for the HER Dataset. Measurements are made within the vertical lines.

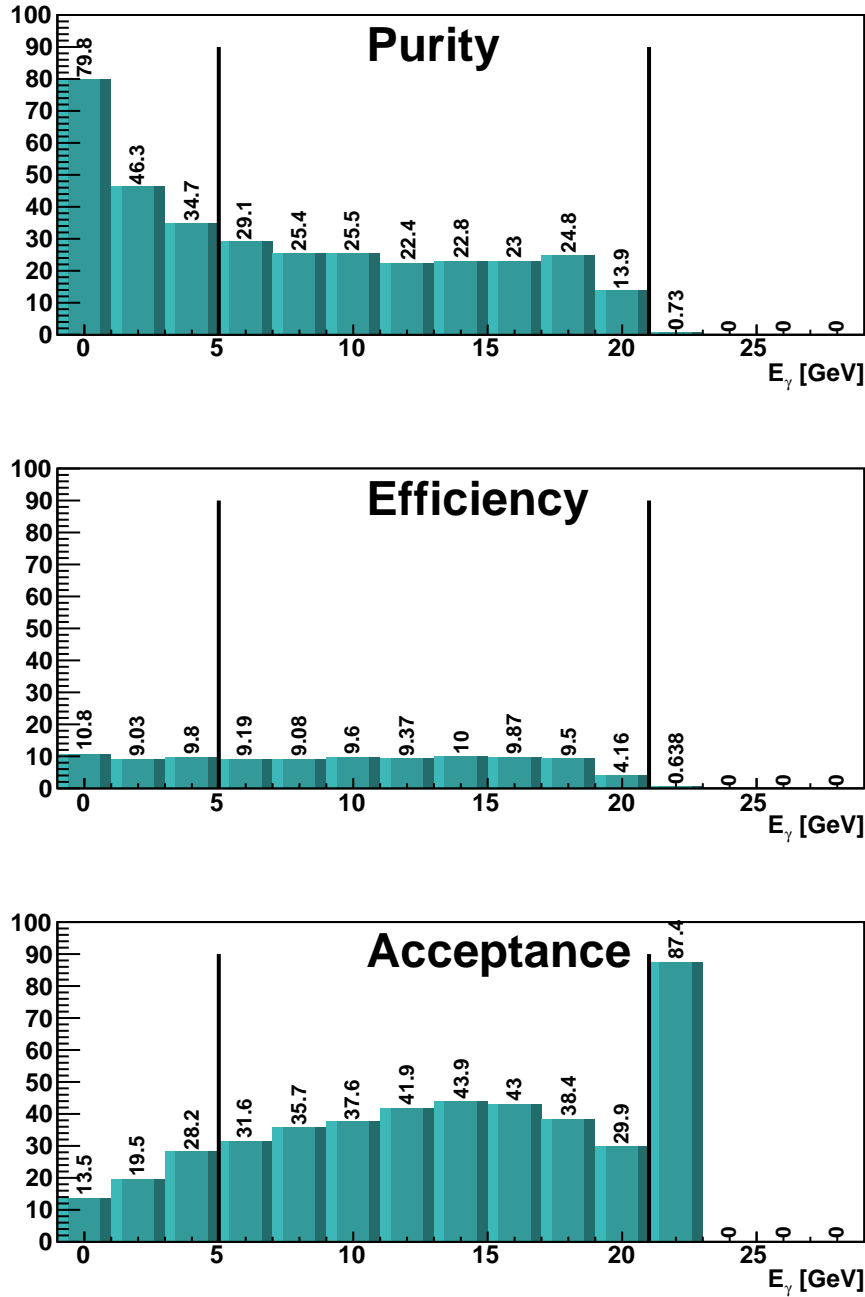


Figure 6.11: The bin purities, efficiencies, and acceptances, given in percent, are shown for the ISR Dataset. Measurements are made within the vertical lines.

6.3.2 Cross Section Unfolding Technique

In an ideal scenario the measured cross section is the number of measured events divided by the integrated luminosity, \mathcal{L} .

$$\sigma = \frac{N^{ISR}}{\mathcal{L}} \quad (6.7)$$

However, no particle detector is perfect and N_{data} can only be accurately measured in certain detector regions. The cross section formula used to determine the number of ISR events for each photon energy is defined by:

$$\frac{d\sigma^{ISR}}{dE_\gamma} = \frac{N^{ISR}}{\mathcal{L}A\Delta E_\gamma} \quad (6.8)$$

Where ΔE_γ is the width of the E_γ bin and A is the acceptance, defined in equation 6.6 to be $A = N_{MC}/N_{True}$. By simplifying equation 6.8 and recognizing that $N_{True}/\mathcal{L}\Delta E_\gamma$ is just the theoretical cross section as predicted by HERACLES, $\frac{d\sigma^{theory}}{dE_\gamma}$, the following cross section can be defined:

$$\frac{d\sigma^{ISR}}{dE_\gamma} = \frac{N_{data} - N_{MC}^{Bkg}}{N_{MC}^{ISR}} \frac{d\sigma^{theory}}{dE_\gamma} \quad (6.9)$$

where $\frac{d\sigma^{theory}}{dE_\gamma}$ is the Standard Model Born level cross section calculation, N_{data} is the number of events observed in the data, N_{MC}^{ISR} is the number of events predicted in the MC and N_{MC}^{Bkg} denotes the number of background events predicted in the MC. There are several sources of background which enter this term. The main source of background is from uncorrected Bethe-Heitler (BH) events. The contributions from photoproduction (see section 5.7.1) and QEDC (see section 5.7.2) are also included in this term, but have a negligible effect. The theoretical cross section calculations are performed in the MC using the CTEQ5D [17] parameterisation of the proton PDF.

6.3.3 Uncertainties

All physical measurements are associated with some sort of uncertainty. Uncertainties, or errors, are typically separated into two classes: statistical and systematic uncertainties. Statistical uncertainties arise from stochastic fluctuations which are inherent to measurements with a finite set of observations. The definition of systematic uncertainties can be much more complicated. These errors parameterise our limited knowledge of the detector, theoretical understandings, reconstruction methods and environmental conditions which can affect the experimental outcome. The treatment of statistical errors will be discussed, followed by a detailed overview of the various systematic uncertainties.

Statistical Uncertainties

Equation 6.9 demonstrates that the ISR cross section is proportional to the number of ISR events measured divided by the number of events predicted,

$$\frac{d\sigma^{\text{ISR}}}{dE_\gamma} \sim \frac{N_{\text{data}} - N_{MC}^{\text{Bkg}}}{N_{MC}^{\text{ISR}}} \quad (6.10)$$

In general, the statistical uncertainty on the number of events measured in a bin is the square root of the that number:

$$\Delta N_{\text{data}} = \sqrt{N_{\text{data}}} \quad (6.11)$$

The statistical uncertainty on the ISR cross section is determined by adding the statistical errors on all measured quantities in quadrature;

$$\delta_{\text{stat}} = \Delta \frac{d\sigma^{\text{ISR}}}{dE_\gamma} / \frac{d\sigma^{\text{ISR}}}{dE_\gamma} = \sqrt{\frac{(\Delta N_{\text{data}})^2 + (\Delta N_{MC}^{\text{Bkg}})^2}{(N_{\text{data}} + N_{MC}^{\text{Bkg}})^2} + \left(\frac{\Delta N_{MC}^{\text{ISR}}}{N_{MC}^{\text{ISR}}}\right)^2} \quad (6.12)$$

This formula is applied for all statistical errors in every bin.

Systematic Uncertainties

The analysis contained in this thesis has several associated systematic uncertainties. Systematic uncertainties arise from a limited understanding of various parts of the measurement and analysis method. The treatment of these uncertainties involves identifying all the possible sources and applying a positive and negative variation, each corresponding to a fluctuation of one standard deviation [72]. The uncertainties are symmetrized by taking the average deviation from the central value. The total systematic uncertainty is determined by taking the squared sum of all identified sources. In total, 15 sources of systematic errors have been identified, they are displayed in table 6.1.

In general, results can be sensitive to choices made when defining parameters. In this analysis additional, systematic cross checks have been performed to study the sensitivity of the results on certain parameters. The systematic checks performed in this analysis include:

- Changing the definition of the kinematic peak from $-5 \text{ GeV} < E_e^y - E_e' < 2 \text{ GeV}$ to $-5 \text{ GeV} < E_e^y - E_e' < 0 \text{ GeV}$ (see section 5.4). This results in a 1.9% variation in the measured cross sections.
- The selection criteria used to obtain a pure BH spectrum was modified (see section 4.4.4) resulting in a 1% variation in the measured cross sections.
- The electron energy cut was varied from $E_e' > 6 \text{ GeV}$ to $E_e' > 8 \text{ GeV}$, resulting in a 0.3% variation in the measured cross sections.

These cross checks demonstrate that the analysis is not particularly sensitive to the choice of parameters.

Number	Systematic Name	Systematic Description
1	γ B-Spot	The position of the mean beam spot on the face of the luminosity system is known to fluctuate by ± 2 mm in x and ± 0.5 mm in y .
2	γ B-Spread	The width of the beam of photons incident on the luminosity system is known within ± 2 mm.
3	γ B-Tilt	The distribution of photons on the face of the luminosity system makes a tilted ellipse. The angle made between the semi-major axis and the x - y plane is referred to as the beam tilt. This angle is known to $\pm 1^\circ$.
4	e^+e^- Convert	The number of events that convert into e^+e^- pairs as they exit the HERA vacuum, before entering the luminosity system, is known to 2%.
5	BH	The normalization of the Bethe-Heitler background was varied by $\pm 2\%$.
6	γ Escale	The photon energy scale is known to within $\pm 2\%$.
7	Lumi App	The size of the aperture has been measured by hand using a ruler. The associated uncertainty corresponding to this measurement is ± 2 mm.
8	Ee Scale	The electron energy scale is understood with $\pm 0.5\%$ precision for $E'_e > 20$ GeV and $\pm 1.9\%$ for $E'_e > 6$ GeV. The systematic is assumed to scale linearly between these two points [73].
9	He Scale	A variation of $\pm 2\%$ on the hadronic energy scale is applied [73].
10	Sin Eff	The uncertainty on the electron finding, using the Sinistra package, is determined by tightening and loosening the criteria on the exponential probability cut defined in 5.8.
11	SRTD +	The SRTD position uncertainty is ± 2 mm in the horizontal direction.
12	SRTD -	The SRTD position uncertainty is ± 2 mm in the vertical direction.
13	HES +	The HES position uncertainty is ± 2 mm in the horizontal direction.
14	HES -	he HES position uncertainty is ± 2 mm in the vertical direction.
15	γP	A $\pm 10\%$ uncertainty is attributed to the uncertainty on the photoproduction cross section

Table 6.1: The systematic uncertainties associated with the analyses presented in this thesis.

6.3.4 The $E - p_z$ Method

Results

The first method used to extract $\frac{d\sigma}{dE_\gamma}^{\text{ISR}}$ is the $E - p_z$ method. This method builds on the work performed in section 6.2.2. Adding all $E - p_z$ bins of figures 6.5 and 6.6 together, the total number of photons observed, N^{ISR} as a function of E_γ for the HER and ISR datasets respectively can be obtained. The cross section can then be determined by applying the cross section formula of equation 6.9.

The results are displayed in figure 6.12 for the HER and ISR datasets. The table

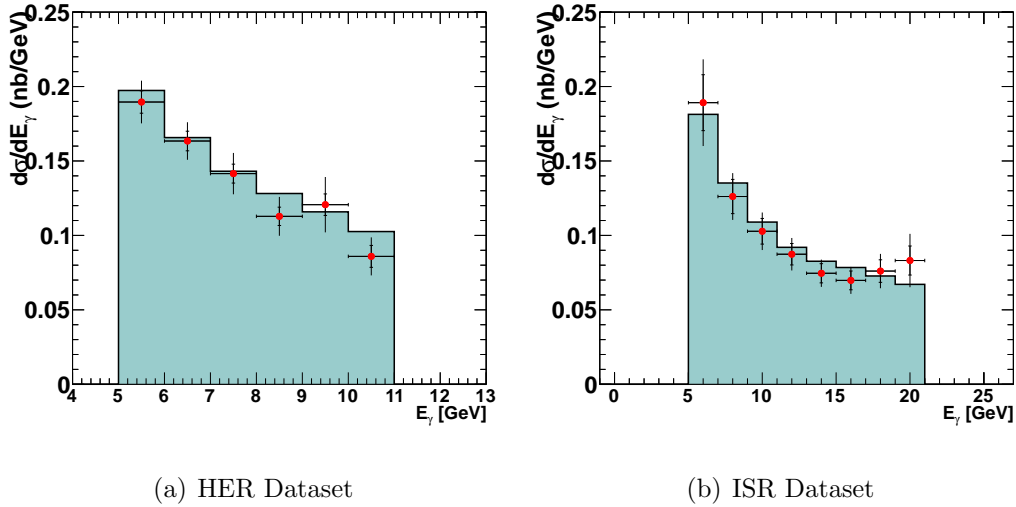


Figure 6.12: The ISR cross section $\frac{d\sigma}{dE_\gamma}^{\text{ISR}}$ measured for the HER dataset (a) and the ISR dataset (b). Results are compared with predictions from HERACLES. Both statistical and systematic errors are shown.

of values corresponding to these measurements is given in tables B.1 and B.2. The error bars in these figures represent the statistical and systematic uncertainties. The systematics studied for this analysis are visually represented in figures 6.13 and 6.14. They display the difference from the nominal value for each systematic uncertainty described in table 6.1.

The photoproduction and QEDC background samples used in this thesis are statistically insufficient and when included produce large fluctuations on the cross sections ($> 15\%$). Because of this, they are not included in these cross sections. A reasonable estimate for the size of this contribution would be 2-3%.

The results presented in this section will be discussed in chapter 9.

6.3.5 The PCAL Method

The ISR cross section, $\frac{d\sigma}{dE_\gamma}^{\text{ISR}}$, can be determined directly from the ZEUS luminosity system without the use of the calorimeter for estimating the photon energy. A standalone MC simulation of the luminosity system has been developed and includes a full prescription for the treatment of BH overlay photons (see section 4.4).

This analysis uses the ISR-enriched sample outlined in section 5.9.3 and is performed for the HER and ISR datasets. The standalone simulation makes a prediction for the size of the BH background contribution. A control distribution for the photon energy distribution is shown in figure 6.15 for the HER and ISR dataset.

These distributions demonstrate that the sums of the ISR process and the BH overlays are in good agreement with the observed data distribution.

The systematic uncertainties studied for this method are shown in table 6.1. The difference from the nominal value for both positive and negative variations for the HER dataset and the ISR dataset are shown in figure 6.16 and figure 6.17 respectively.

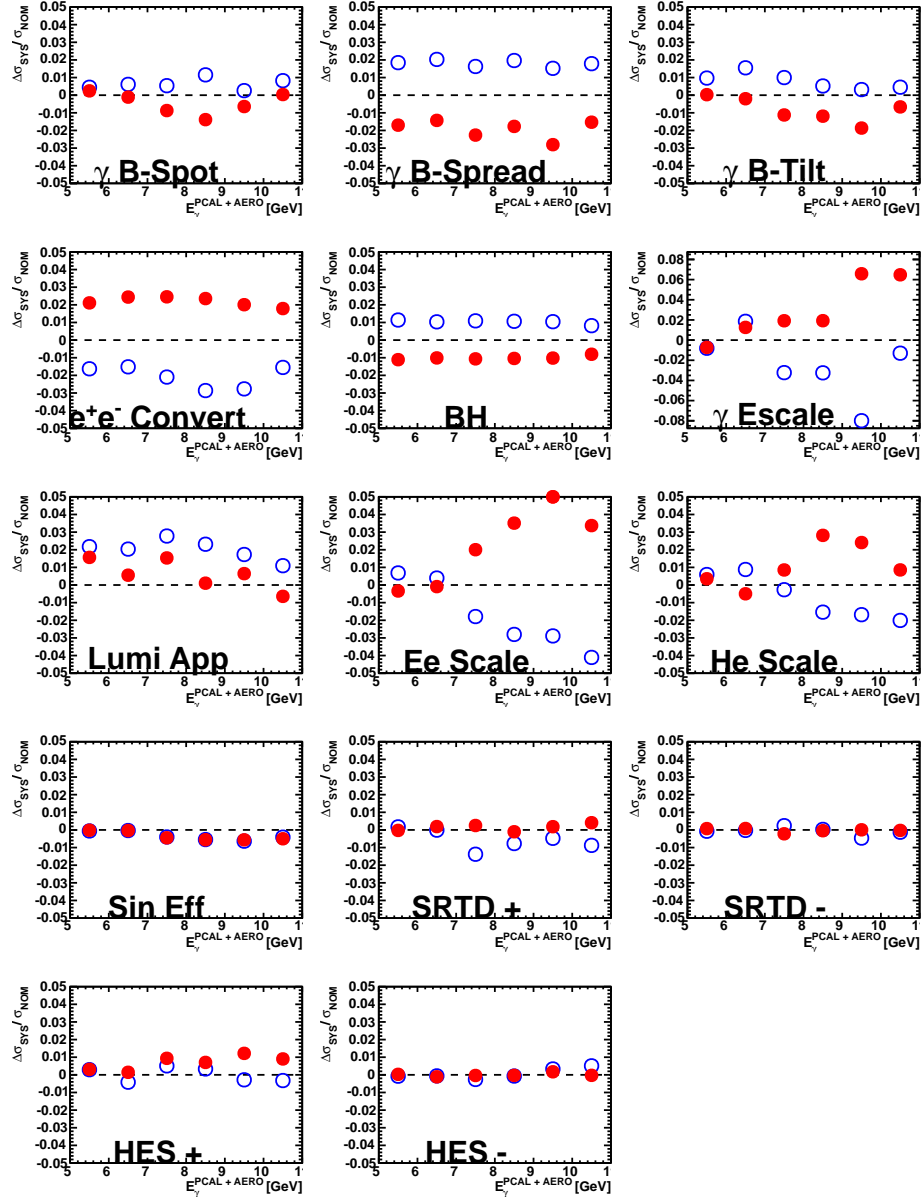


Figure 6.13: Systematic uncertainties associated with the cross section calculated using the $E - p_z$ method from the HER dataset. Positive (open circles) and negative (closed circles) are shown. The labels correspond to table 6.1

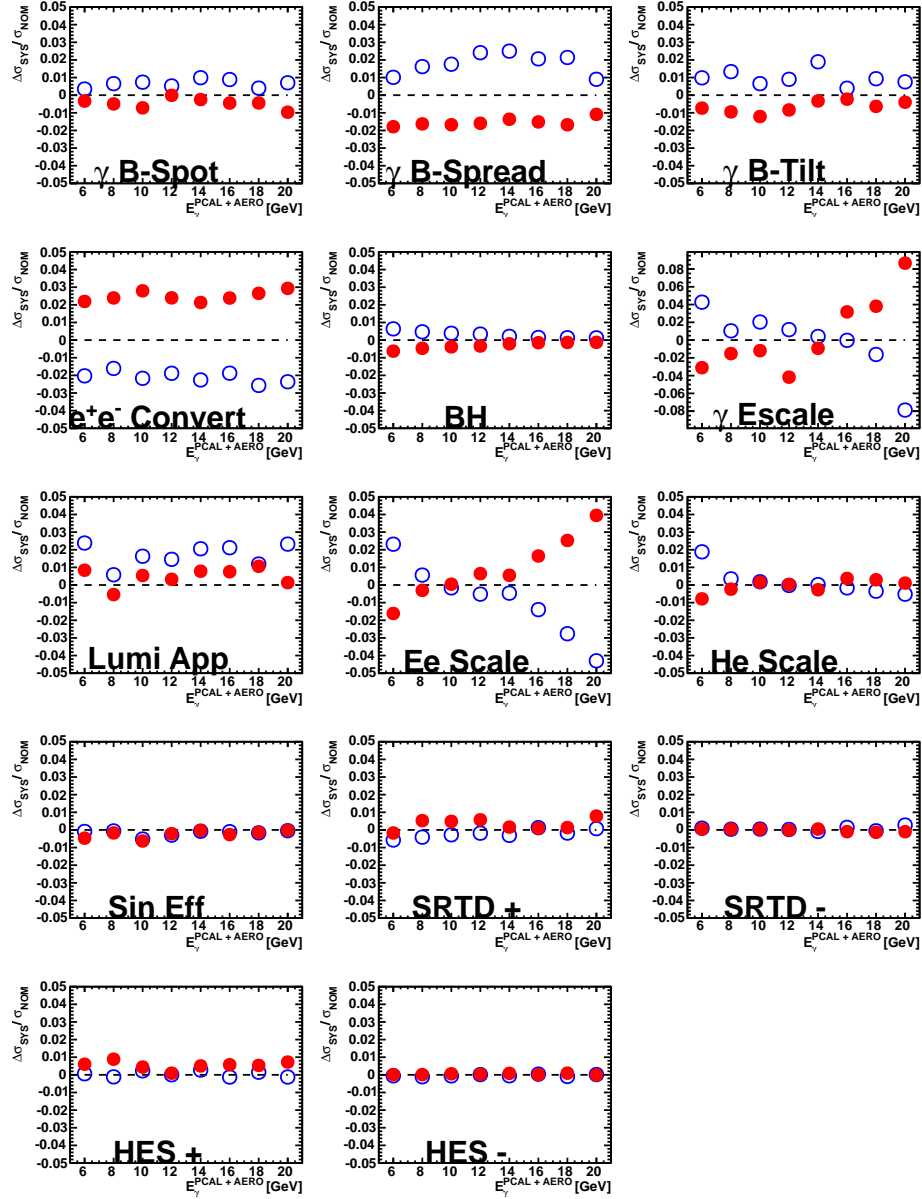


Figure 6.14: Systematic uncertainties associated with the cross section calculated using the $E - p_z$ method from the ISR dataset. Positive (open circles) and negative (closed circles) are shown. The labels correspond to table 6.1

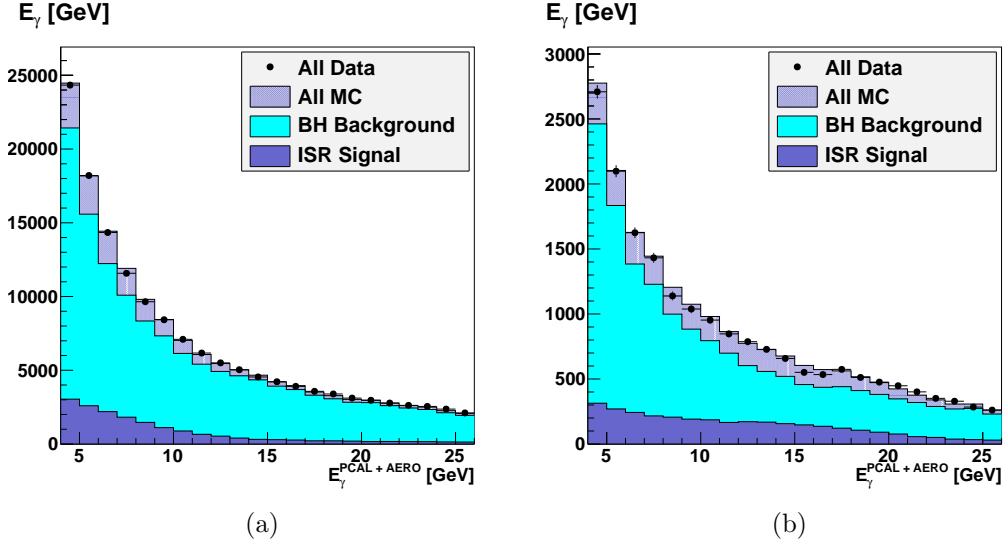


Figure 6.15: A control distribution comparing the PCAL+AERO energy spectrum with the MC simulation for the HER dataset (left) and ISR dataset(right). Contributions from ISR and BH are shown separately and their sum is also displayed.

Results

The number of ISR events can be determined from the cross section of equation 6.9, where the background term N_{MC}^{Bkg} term contains all backgrounds from BH Overlay events, photoproduction and QEDC. The cross sections, extracted using equation 6.12, are shown in figure 6.18 for the HER and ISR samples and show agreement with the MC predictions. Values for this measurement are given in tables B.3 and B.4.

6.4 Comparing Methods

The PCAL method and the $E - p_z$ method are both used to measure the ISR cross section from the HER and ISR datasets. Figure 6.19 represents all the previous measurements of $\frac{d\sigma}{dE_\gamma}^{\text{ISR}}$ on a single plot. In general a very good agreement between data and MC is observed. No large deviations from the predicted values are observed. Most points show consistency within the calculated statistical and systematic errors

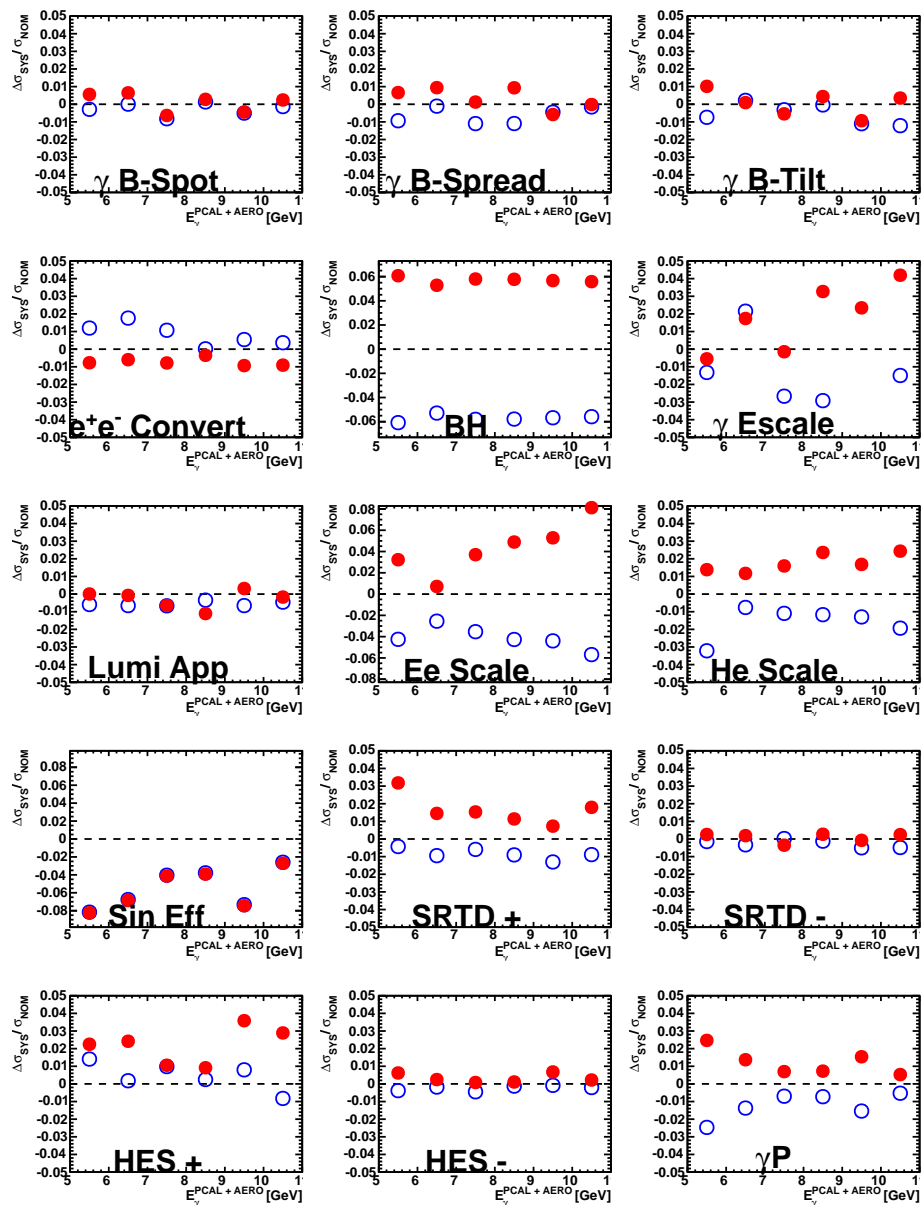


Figure 6.16: Systematic uncertainties associated with the cross section calculated using the PCAL method from the HER dataset. The text in the figure (bottom) corresponds to table 6.1

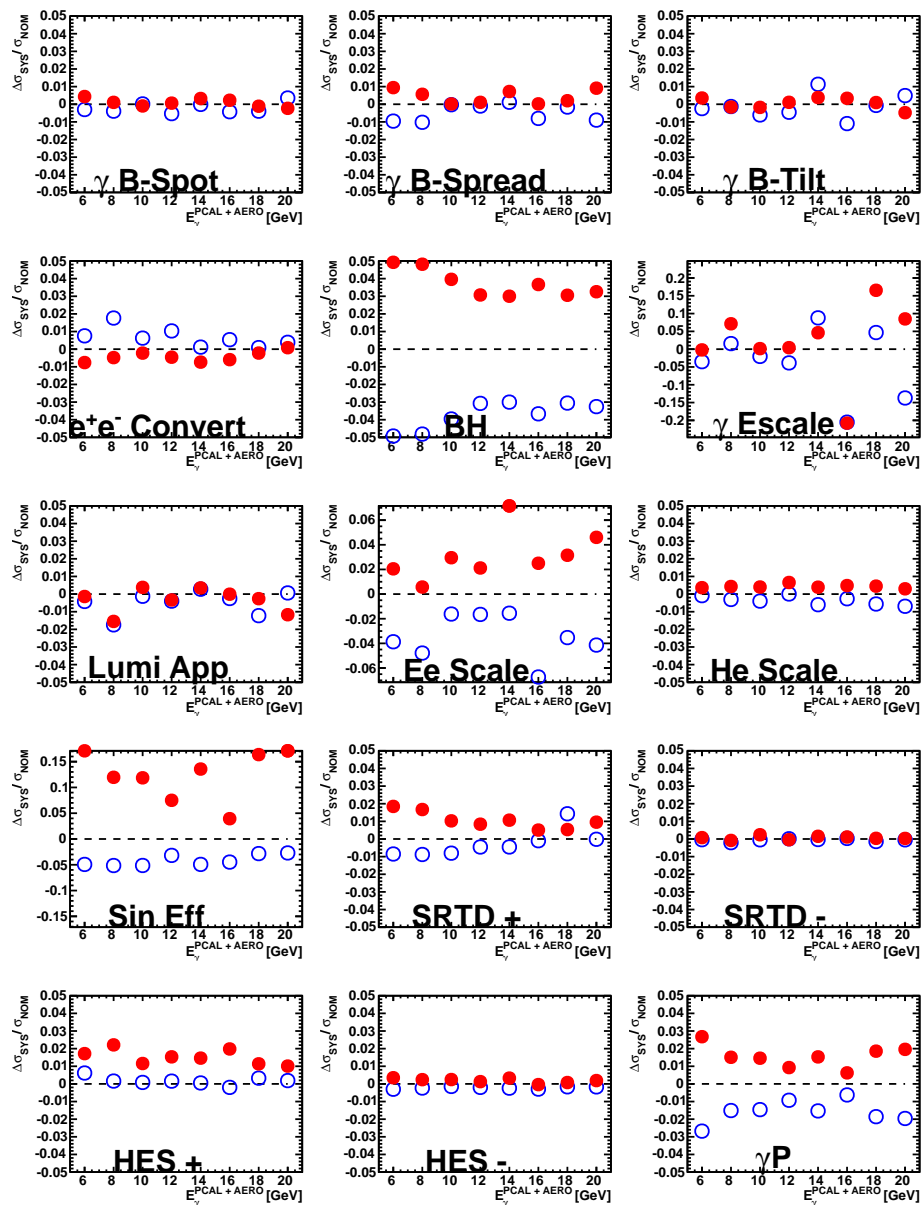


Figure 6.17: Systematic uncertainties associated with the cross section calculated using the PCAL method from the ISR dataset. The text in the figure (bottom) corresponds to table 6.1

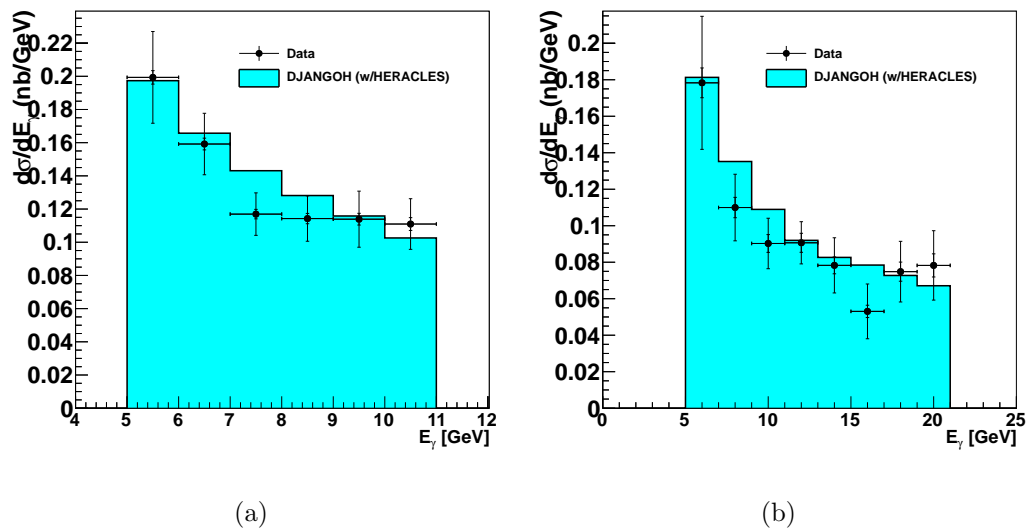


Figure 6.18: The ISR cross section $\frac{d\sigma}{dE_\gamma}^{\text{ISR}}$ measured for the HER dataset (a) and ISR dataset (b) extracted using the PCAL method. Results are compared with HERACLES predictions.

and with the radiative predictions from HERACLES. The cross section appears to be slightly but systematically shifted to lower values for energies less than $E_\gamma < 17$ GeV. This could indicate a theoretical discrepancy, however, deviations are within the uncertainties.

The radiative component of DIS has been successfully measured and compared with MC predictions. This was the first measurement of its kind at ZEUS and the first to use the calibration and simulation of the far luminosity measurement system.

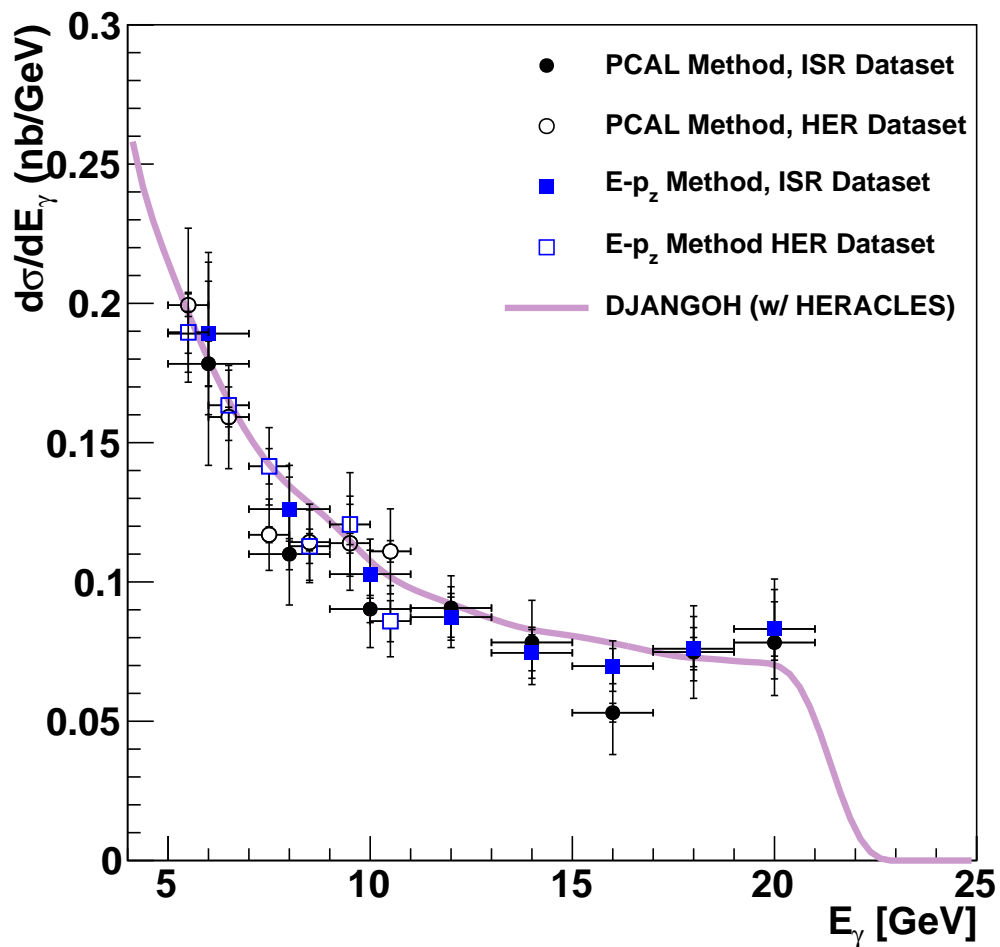


Figure 6.19: The ISR cross section is displayed for the $E - p_z$ method and the PCAL Method for both ISR and HER Datasets. Results are compared with DJANGO MC with HERACLES. Statistical and systematic uncertainties are shown.

CHAPTER 7

Probing the Protons Structure with ISR

7.1 Introduction

A Deep Inelastic Scattering (DIS) event with Initial State Radiation (ISR) can be understood as a non-radiative ep event at a reduced centre-of-mass energy. When such an event is reconstructed taking into account ISR, it is possible to perform measurements at virtualities (Q^2) lower by a factor of two than normally accessible at ZEUS. Furthermore, these low- Q^2 events are typically in the low- y regime. Neither collider or fixed target experiments can kinematically reach this region, resulting in a lack of measurements.

This chapter presents a measurement of the DIS reduced cross section for events with an ISR photon. To perform such a measurement, the kinematics of the event must be corrected to include the ISR photon. Theoretically, it is also possible to measure the longitudinal structure function, F_L , with these events. An independent measurement of the reduced cross section will test the feasibility of an F_L determination with ISR events.

The analysis presented in this chapter is based on a similar published analysis [74], which was performed using ZEUS 1994 data.

7.2 Techniques

7.2.1 Measurement Concept

In the electron method, the virtuality is reconstructed via equation 5.9, which is restated here:

$$Q_e^2 = 2E_e E'_e (1 + \cos\theta_e) \quad (7.1)$$

In a radiative DIS event, the incoming electron radiates a photon, with energy E_γ , resulting in a modification of the effective electron beam energy,

$$E_e = E_e^{beam} - E_\gamma \quad (7.2)$$

where $E_e^{beam} = 27.56$ GeV, which is the nominal electron beam energy.

The SPP11 trigger, defined in section 5.8.3, was designed to extend the $E - p_z$ range to $E - p_z > 12$ GeV. Choosing to measure above the minimum trigger threshold, we are interested in events with $E - p_z > 15$ GeV. Kinematically, this corresponds to photons with energies up to $E_\gamma \sim 20$ GeV. From equation 7.2, a 20 GeV photon effectively reduces the incoming electron beam energy to, $E_e = 7.5$ GeV. The ZEUS detector is, at best, capable measuring virtualities as low as $Q^2 = 11$ GeV². From the equation,

$$Q_{true}^2 = Q_e^2 (1 - E_\gamma / E_e^{beam}) \quad (7.3)$$

we determine that it would be possible, with ISR, to perform structure function measurements down to $Q^2 = 3$ GeV².

In this chapter, the measurement of the ISR photon is exploited to correct the kinematic reconstruction of tagged ISR events. The reduced cross section σ_r (see equation 2.19) is extracted down to virtualities as low as $Q^2 = 3$ GeV², a region which not nominally accessible in the ZEUS detector. In this region $\alpha_s \approx 0.35$, which

keeps this measurement within the perturbative regime. This measurement uses the ISR-tagged data sample defined in section 5.9.4.

The binning of the y and Q^2 plane was selected to maximize statistical precision and to minimize migration between neighbouring bins.

A full study of the systematics of this measurement is used to determine if a bin is quantitatively good. The cross section is unfolded onto the Born level using the CTEQ5D [17] parameterisation of the proton PDF, which is the standard PDF choice for DIS analyses at ZEUS.

7.2.2 ISR Photon Tagging

This analysis is performed using the ISR-tagged selection (see section 5.9.4). The method for ISR-tagging will be examined in further detail.

Backgrounds from BH overlays contaminate every DIS event. Every DIS event (including DIS + ISR events) contains between 0 and N BH overlays. To discriminate between a BH overlay and an ISR event, ZEUS's high resolution uranium calorimeter is exploited. Detector information can be used to make a prediction for the energy of the ISR photon. In the previous chapter, $E - p_z$ was used as a means to estimate the photon energy. In section 5.4, new variables were introduced that, by exploiting differences in the kinematic variable reconstruction methods, can directly predict the energy of the radiative photon. This lead to the definition of equation 5.28 which is re-stated here:

$$E_{\gamma}^{Exp} = \frac{1 - \cos \theta'_e}{2(1 - y_{JB})} (E_e^y - E'_e) \quad (7.4)$$

where $E_e^y = \frac{2E_e(1-y_{JB})}{1-\cos\theta'_e}$. A correlation plot displaying the expected photon energy E_{γ}^{Exp} versus the measured photon energy $E_{\gamma}^{PCAL+AERO}$ is displayed in figure 7.1.

This figure is simply a re-representation of figure 6.2, so all the same features are

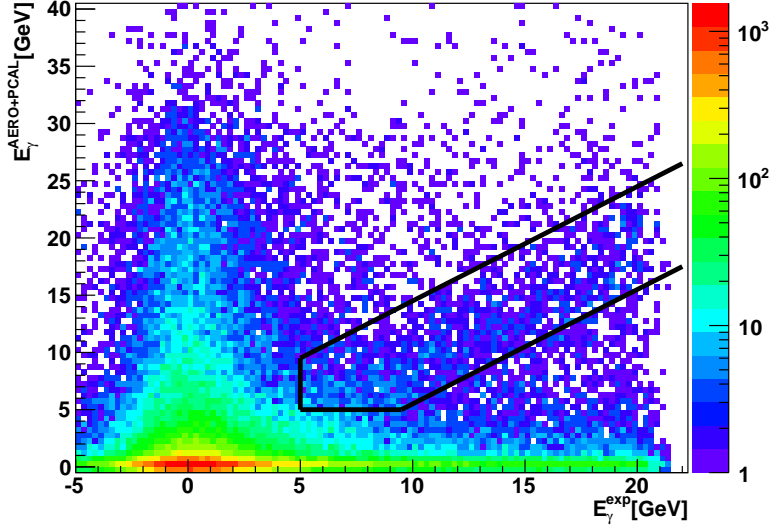


Figure 7.1: Correlation between E_{γ}^{Exp} and $E_{\gamma}^{PCAL+AERO}$ for events in the ISR Dataset. The solid lines represent the area where an ISR photon is expected to show up.

observed, including the diagonal ISR Band. However, in this representation, the slope of the ISR band is 1. The solid lines represent the bounds for the ISR-tagged sample. We will refer to events in this region to be *ISR-tagged* events. These events are selected based on the criteria defined in section 5.9.4 and restated below:

- A photon must have been measured in the luminosity detectors with energy $E_{\gamma}^{Mea} > 5$ GeV.
- The event topology is consistent with observing a photon having energy $E_{\gamma}^{Exp} > 5$ GeV
- The difference in the observed and predicted photon energy is sufficiently small, $|E_{\gamma}^{Exp} - E_{\gamma}^{Mea}| < 4.5$ GeV

This procedure leads to an ISR-tagged sample and should only contain events with an ISR photon. These requirements also greatly reduce the contribution from uncorrelated BH overlays. Figure 7.2 shows the difference between expected and measured photon energies $E_{\gamma}^{Exp} - E_{\gamma}^{Mea}$ for the HER and ISR datasets. A gaussian fit to both

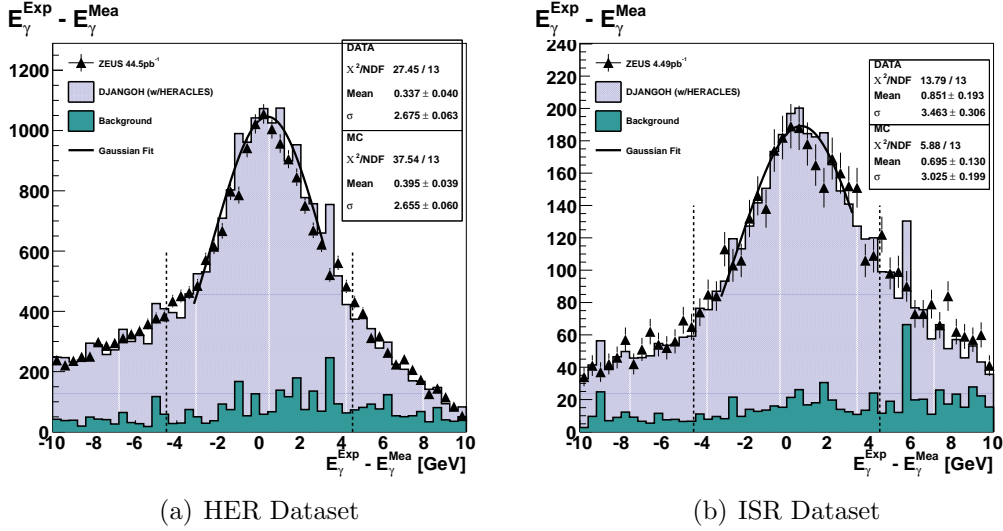


Figure 7.2: The difference between expected photon energy E_{γ}^{Exp} and the energy measured in the PCAL+AERO system E_{γ}^{Mea} for the HER dataset (a) and the ISR dataset (b). Vertical lines represent the positions of the cuts. Results from a gaussian fit to data and MC are also shown.

data and Monte Carlo distribution demonstrate good agreement for both the HER and ISR datasets.

7.2.3 Event Reconstruction

The event kinematics are reconstructed using the electron method and corrected to account for ISR (see section 5.3.1). E_{γ}^{Exp} is used to correct the event kinematics, because the high resolution uranium calorimeter has a better resolution than the PCAL+AERO.

7.2.4 Bin Selection and Systematics

The y and Q^2 binning was made sufficiently large to minimize event migrations. Furthermore, bin sizes were adjusted to give similar statistical precision throughout the kinematic plane. ISR affects the various reconstruction methods differently (see

section 5.3). For the electron method, ISR shifts events to higher- Q^2 and higher- y values.

Bins with systematics fluctuations larger than 25% or statistical uncertainties large than 50% are considered to be bad. The systematics for this analysis are displayed in Appendix B.2.1. These loose selection criteria results in losing about half of the bins. Nevertheless, the bin purity, efficiency and acceptance bin indicators for $y > 0.35$ are mostly less than 10%, indicating issues with data quality in these regions. The bin purity, efficiency and acceptance bin indicators are shown in Appendix B.2.2.

The number of events reconstructed in each y and Q^2 bin is shown for the HER and ISR datasets in figure 7.3.

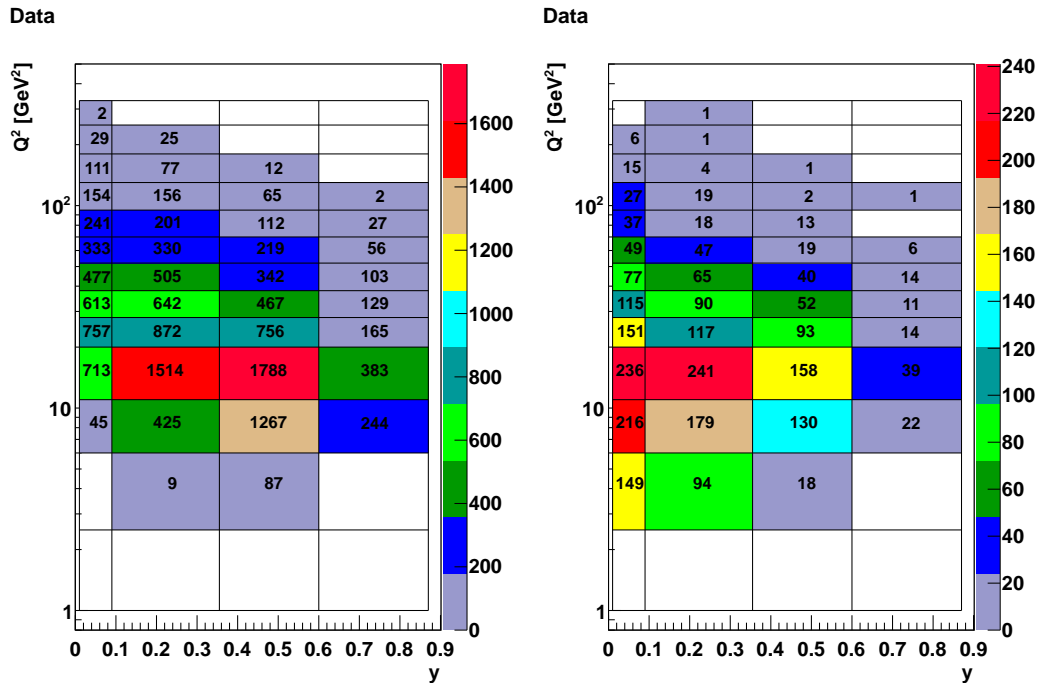


Figure 7.3: The number of events measured in each y and Q^2 bin for the HER dataset (left) and the ISR dataset (right).

7.2.5 Cross Section Unfolding

In a perfect detector the cross section is the number of events measured divided by the luminosity. For each y and Q^2 bin, this becomes

$$\frac{d^2\sigma}{dydQ^2} = \frac{N(y, Q^2)}{\mathcal{L}\Delta y\Delta Q^2}. \quad (7.5)$$

where \mathcal{L} is the luminosity of the sample, Δy and ΔQ^2 are the widths of the bins. However in reality, detectors are not perfect and the acceptance must be taken into consideration. MC studies of the efficiencies, acceptances and bin purities are shown in Appendix B.2.2. The acceptance is related to the bin-by-bin unfolding equation,

$$\frac{d^2d\sigma}{dydQ^2} = \frac{N(y, Q^2)}{A(y, Q^2)} \left[\frac{1}{\mathcal{L}\Delta y\Delta Q^2} \right] \quad (7.6)$$

where $A(y, Q^2)$ is the acceptance which equation 6.6 defined as:

$$A(y, Q^2) = \frac{N_{MC}(y, Q^2)}{N_{Gen}(y, Q^2)}, \quad (7.7)$$

where N_{MC} is the number of MC DIS events that have been reconstructed in a specific bin and N_{Gen} is the number of DIS events that were generated in that same bin. The measurement of the number of events, $N(y, Q^2)$, contains both good DIS events and other backgrounds. The background can be determined from the MC and subtracted off using:

$$N(y, Q^2) = N_{data}(y, Q^2) - N_{MC}^{Bkg}(y, Q^2) \quad (7.8)$$

where $N_{MC}^{Bkg}(y, Q^2)$ contains all the contributions from bremsstrahlung overlays, photoproduction and QED Compton events. This term is below 20% for $y < 0.35$ and increases with increasing y to almost 85% at high- y .

Substituting equations 7.7 and 7.8 into equation 7.6 gives

$$\frac{d^2d\sigma}{dydQ^2} = \frac{N_{data}(y, Q^2) - N_{MC}^{Bkg}(y, Q^2)}{N_{MC}(y, Q^2)} \left[\frac{N_{Gen}}{\mathcal{L}\Delta y\Delta Q^2} \right] \quad (7.9)$$

where $\left[\frac{N_{Gen}}{\mathcal{L}\Delta y\Delta Q^2} \right]$ is the theoretical prediction for the cross section, which is determined from the MC. This equation can be re-written as:

$$\left. \frac{d^2d\sigma}{dydQ^2} \right|^{mea} = \frac{N_{data}(y, Q^2) - N_{MC}^{Bkg}(y, Q^2)}{N_{MC}(y, Q^2)} \left. \frac{d^2d\sigma}{dydQ^2} \right|^{theory} \quad (7.10)$$

where the superscripts *mea* and *theory*, represent the measured and theoretical cross sections, respectively. The double differential cross section can be re-written as a reduced cross section by dividing out the kinematical factors. This technique was introduced in section 2.4.2 and allows direct access to the F_2 structure function. Relating equation 7.10 to the reduced cross section gives

$$\sigma_r^{mea}(y, Q^2) = \frac{N_{data}(y, Q^2) - N_{MC}^{Bkg}(y, Q^2)}{N_{MC}(y, Q^2)} \sigma_r^{theory}(y, Q^2) \quad (7.11)$$

where, in this measurement the cross section is unfolded onto the CTEQ5D PDF parameterisation of the Born cross section, $\sigma_r^{theory}(y, Q^2)$

7.3 Results

The reduced cross section has been measured in the kinematic region defined by $3.0 \text{ GeV}^2 < Q^2 < 52 \text{ GeV}^2$ and $0.01 < y < 0.87$ where the kinematic variables, reconstructed with the electron method, have been corrected to account for ISR. The measured reduced cross sections are displayed in figure 7.4 for the HER Dataset and figure 7.5 for the ISR dataset. Results are compared to the CTEQ5D parameterisation. The table of values for these results are displayed in Appendix B.2.

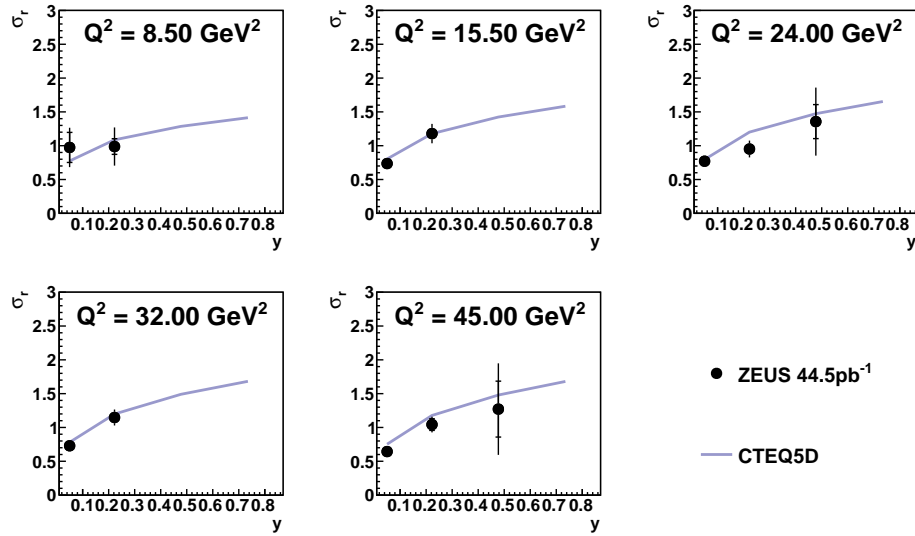


Figure 7.4: The measured reduced cross section for the HER dataset, from events where the kinematics have been reconstructed to include ISR. Results are compared with the CTEQ5D parameterisation.

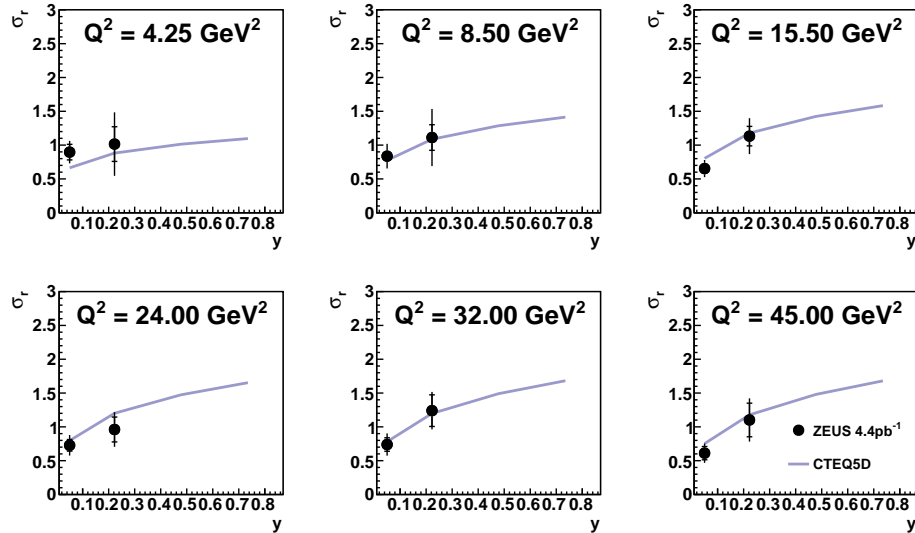


Figure 7.5: The measured reduced cross section for the ISR dataset, from events where the kinematics have been reconstructed to include ISR. Results are compared the theory where the CTEQ5D parameterisation is used.

This analysis was based on a similar published analysis which used 1994 (HERA-I) data [74]. The PCAL+AERO calibration and simulation (introduced for HERA-II) were ideal to perform an ISR measurement. However, the higher luminosity

environment leads to higher rates of uncorrelated BH overlays, which add to the ISR photon. These overlays result in large out-of-bin migrations that affect the bin purities and in turn lead to larger systematic uncertainties.

The results from this chapter demonstrate that because of statistics, migrations and a small accessible range in y , it would not be feasible to measure the longitudinal structure function, F_L , using ISR data in the HERA-II environment. Nevertheless, the results from this measurement show good agreement with CTEQ5D predictions and succeeded in measuring the reduced cross section down to 3.0 GeV^2 .

Another method for calculating the reduced cross section at lower virtualities is to study events which originated from the satellite vertex. This will be presented in the next chapter and will be used to determine the longitudinal structure function F_L .

CHAPTER 8

Measurement of the DIS Cross Section and the Longitudinal Structure Function F_L

8.1 Introduction

At the time of writing, measurements of the F_2 structure function provide the largest constraints on the gluon Parton Distribution Function (PDF), $g(x)$. However, previous measurements of F_2 required assumptions about the contributions from the longitudinal structure function, F_L , or were limited to regions of phase space where contributions from F_L were predicted to be negligible [75]. Furthermore, QCD describes F_2 as a convolution of $g(x)$ and the P_{gg} splitting function, thus any extraction of $g(x)$ from F_2 is model dependent. The longitudinal structure function, F_L , is directly related to $g(x)$, as can be seen from equation 2.32. A measurement of F_L is technically challenging and requires data at multiple centre-of-mass energies.

Before HERA was decommissioned, in July 2007, the proton beam energy was lowered from its nominal energy of 920 GeV (HER) to 460 GeV (LER) and 575 GeV (MER), specifically for the F_L measurement. Studies have shown that these energies were the optimal choice [76]. At these energies, the ZEUS experiment determined F_L , see figure 8.1, covering the limited x and Q^2 ranges: $5 \times 10^{-4} < x < 0.007$ and $20 \text{ GeV}^2 < Q^2 < 130 \text{ GeV}^2$ [73].

The H1 collaboration has also measured F_L [77, 78, 79] in a wider kinematic range: $2.9 \times 10^{-5} < x < 0.01$ and $1.5 \text{ GeV}^2 < Q^2 < 800 \text{ GeV}^2$. The H1 collaboration

ZEUS

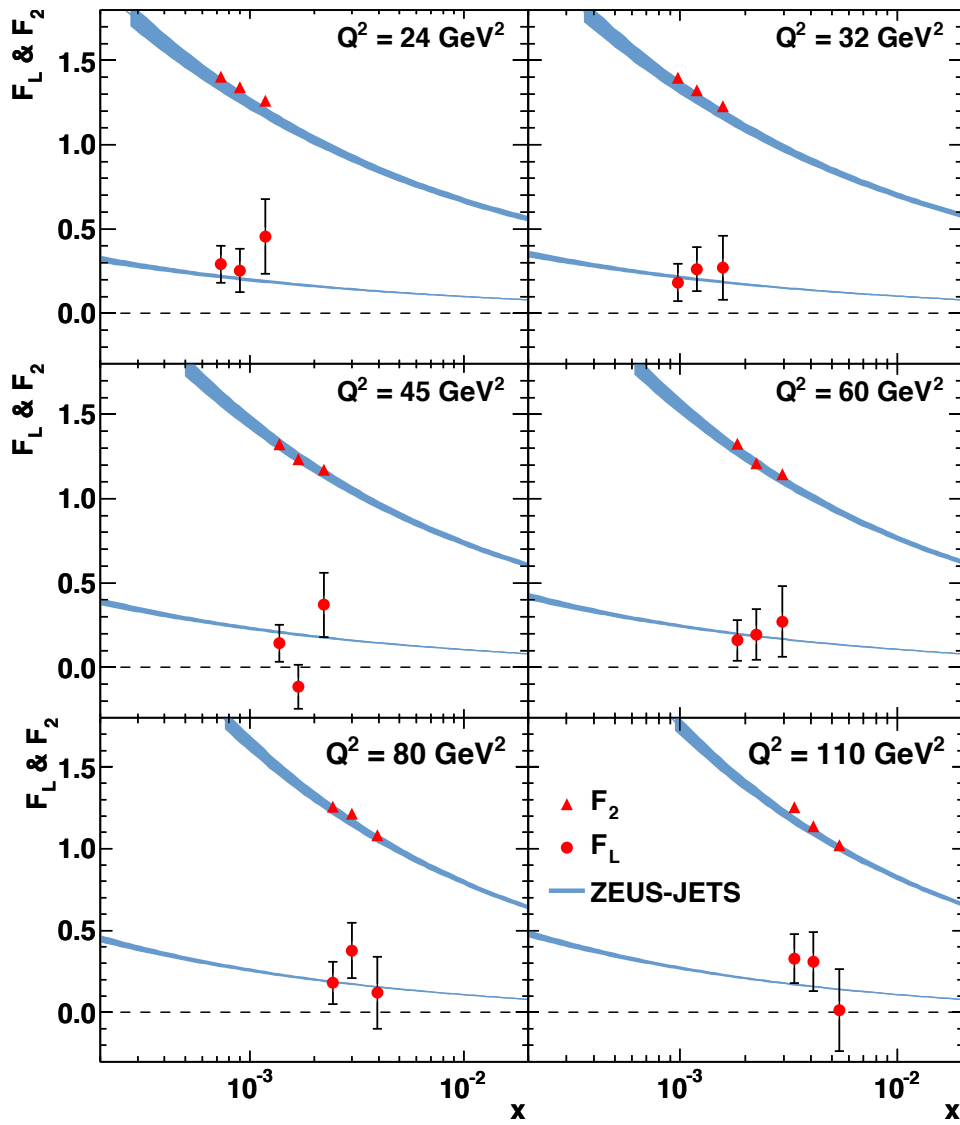


Figure 8.1: F_L and F_2 measured from the ZEUS experiment covering the kinematic range $5 \times 10^{-4} < x < 0.007$ and $20 \text{ GeV}^2 < Q^2 < 130 \text{ GeV}^2$. Results are compared with predictions from the ZEUS-JETS PDF. [73]

was able to extend the measurement to lower Q^2 because the H1 central tracking has a larger reach than the ZEUS Central Tracking Detector. The measurements of H1 and ZEUS have been combined into a single set of measurements, which is shown in figure 8.2. The shaded area in this plot highlights the region where both

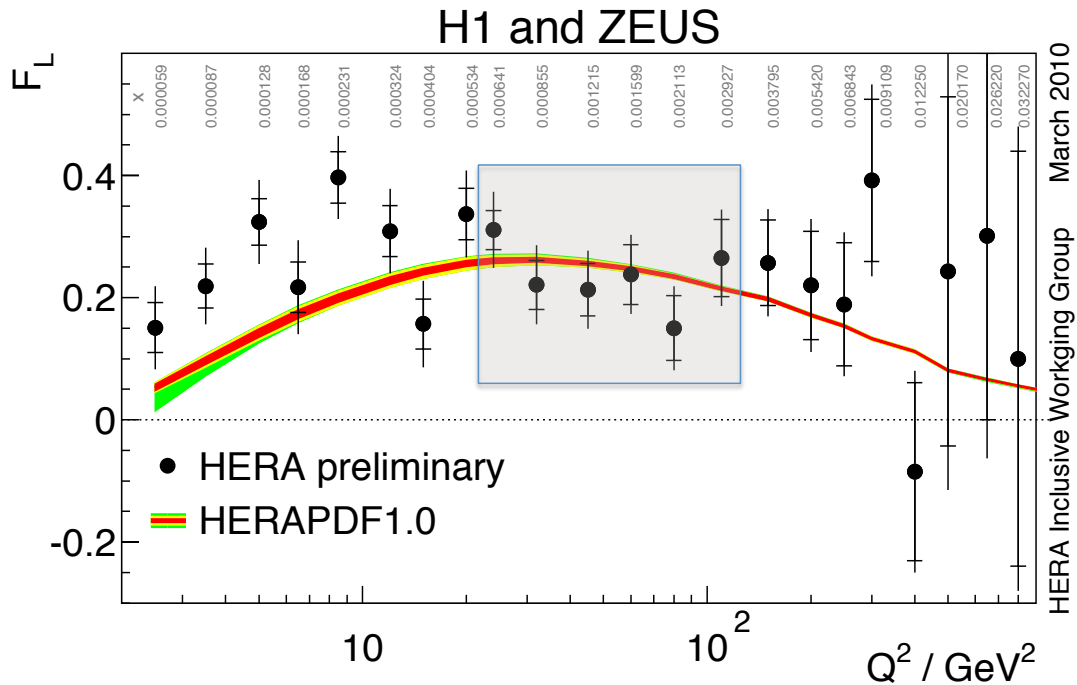


Figure 8.2: H1 and ZEUS combined measurement of F_L . The shaded region indicates regions where ZEUS has previously measured F_L . Results are compared with the HERAPDF1.0 PDF.

H1 and ZEUS have performed F_L measurements. Divergence from the theoretical predictions is observed at low- Q^2 , the reason for which is not well understood. A measurement from the ZEUS experiment, in this region, could greatly improve our understanding of F_L . Efforts are currently underway to extend the kinematic range of the ZEUS measurement. My own contributions to this effort are the subject of this chapter.

8.2 Experimental Procedure

8.2.1 Datasets

The F_L measurement outlined in this thesis uses data from all three HER, MER and LER running periods. Two samples were obtained for each of these periods, making six data samples in total. The first sample is the *nominal Z vertex* sample, which is defined in section 5.9.1 and requires that the Z vertex be reconstructed within the range $-30 < Z_{vtx} < 30$ cm. The second sample is called the *satellite vertex* sample because of the requirement that the event topology is consistent with the interaction occurring between the positive proton satellite and a nominal electron bunch. This sample is defined in section 5.9.2 with the notable requirement that the Z vertex be reconstructed in the range $30 < Z_{vtx} < 100$ cm. Using satellite vertex events it is possible to extend the measurable kinematic range to lower Q^2 . The reader is referred to figure 5.11 for a graphical representation of a satellite vertex event.

8.2.2 Measurement Technique

The reduced cross section for inclusive ep scattering is

$$\sigma_r(x, Q^2, y) = F_2(x, Q^2) - \frac{y^2}{Y_+} F_L(x, Q^2) \quad (8.1)$$

where $Y_+ = 1 + (1 - y)^2$. The F_L contribution can be isolated by measuring σ_r for the same x and Q^2 values while varying y . From the relation $Q^2 = sxy$, it is clear that this can be achieved only by varying the centre-of-mass energy, \sqrt{s} , which is defined as $s = 4E_e E_p$. The centre-of-mass energy can be reduced by lowering either the proton or the electron beam energies. Lowering the proton beam energy was

shown to be more favourable because it required only minimal changes to the trigger logic¹.

Equation 8.1 shows the relationship between the reduced cross section, σ_r , and the structure functions F_2 and F_L . F_L and F_2 are extracted simultaneously using a Rosenbluth plot [80]. The same σ_r is measured at each centre-of-mass energy and plotted against y^2/Y_+ . In a Rosenbluth plot, F_L becomes the slope of the line fitted to the points,

$$F_L(x, Q^2) = -\partial\sigma_r(x, Q^2, y)/\partial(y^2/Y_+) \quad (8.2)$$

where F_2 is simply the y -intercept of the said line,

$$F_2(x, Q^2) = \sigma_r(x, Q^2, y = 0). \quad (8.3)$$

The precision of this procedure depends on the lever arm, or the ability to measure the largest possible range in y^2/Y_+ .

Running HERA at $E_p = 460$ GeV, the lowest possible energy, while maintaining an adequate luminosity, helps maximize the y range. The high- y region is also subject to significant radiative corrections. A detailed study of radiative corrections to DIS (see chapter 6) demonstrated that this process is well described by MC predictions. Furthermore, a MC study (see section 4.2.1) shows that, after applying the $E - p_z > 42$ GeV cut, the radiative correction is less than 10% with no strong dependence on y .

¹ The second level trigger uses the total sum of $E - p_z$ to perform its selection. If the electron beam energy were to be lowered, the total sum of $E - p_z$ would no longer be centred around 55 GeV.

8.2.3 Improvements to Previous Measurement

Prior to this thesis, the ZEUS collaboration has already published a F_L measurement using the nominal Z vertex and data from the HER, MER and LER running periods [73]. The previous ZEUS measurement was limited to the region $20 < Q^2 < 130 \text{ GeV}^2$. This measurement aims to extend the Q^2 range of the nominal measurement to lower Q^2 and to use events in the satellite vertex to extend to even lower Q^2 . A substantial effort has been directed to the extension of the F_L measurement. Focus has been directed to improving several aspects of the event reconstruction, including:

- An extensive data reprocessing, which included a more accurate description for the alignment of the micro vertex detector.
- A new map of the RCAL energy scale was developed. This includes the most recent inactive material maps and provides new scaling factors for each RCAL cell.
- The Z vertex distribution in the MC has undergone non-biased reweighting, much like the one described in section 5.1.5.
- A detailed study of radiative corrections has been performed in chapter 6 of this thesis. Insights from this study allow for an extension to higher- y values.

8.2.4 Cross Section Extraction

The cross section is extracted according to the equation as in section 7.2.5.

$$\sigma_r(y, Q^2) = \frac{N_{data} - N_{MC}^{Bkg}}{N_{MC}^{DIS}} \sigma_r^{theory}(y, Q^2) \quad (8.4)$$

where N_{MC}^{Bkg} is the background term and contains all the contributions from background processes, like photoproduction and QEDC. The theoretical cross section is calculated using the ZEUS-JETS parameterisation of the proton PDF.

As before, the bin sizes were chosen so that every bin will have roughly equal statistics. The purity, efficiency and acceptance indicators are used to check the quality of the bin. The acceptance for the nominal LER analysis is shown in figure 8.3 for both the nominal and shifted vertex analyses. From this figure we see that the satellite ver-

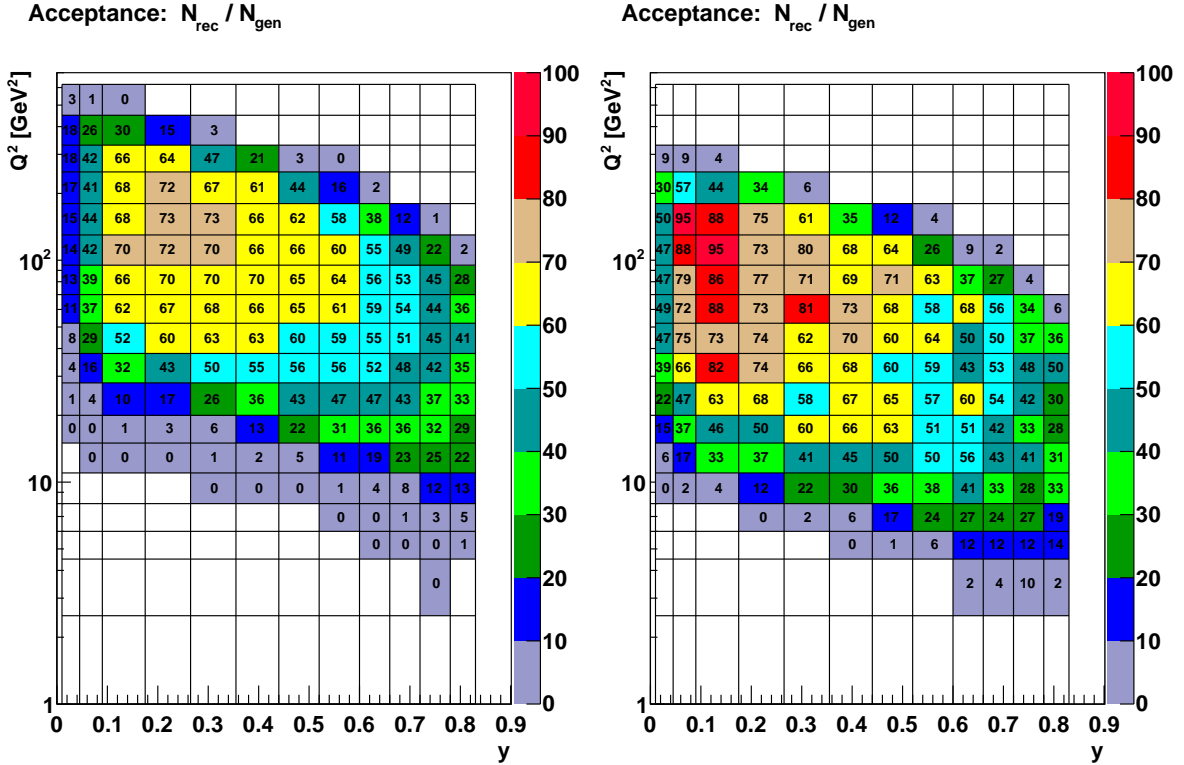


Figure 8.3: The acceptance of events in the (y, Q^2) plane, in percent, for the LER nominal (left) and satellite (right) analyses.

tex analysis has a higher acceptance at lower Q^2 than the nominal analyses. With the satellite vertex analysis, it is possible to measure down to $Q^2 > 2.5$ GeV². The purity, efficiency and acceptance are shown for all data samples in Appendix C.1.1.

8.3 Results

8.3.1 Reduced Cross Sections

The reduced cross section, σ_r , is measured for multiple beam energies and is shown in figure 8.4 for the nominal vertex data and figure 8.5 for the satellite vertex data. Cross sections measured in bins with acceptances below 20% and purities below 30% are not displayed.

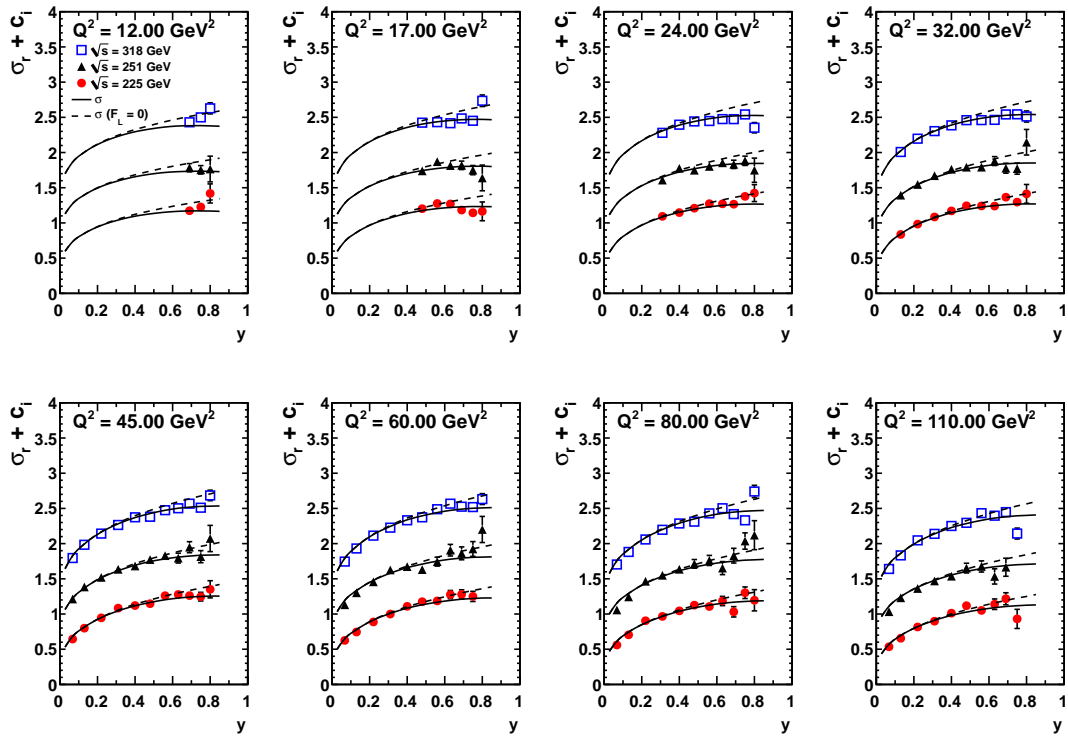


Figure 8.4: The reduced cross section for the nominal vertex HER, MER and LER data samples. The HER and MER data points are shifted by an arbitrary value for clarity. Only statistical errors are shown.

As of now, the nominal vertex measurement and the satellite vertex measurement have been treated independently. However, in the overlapping regions it is beneficial

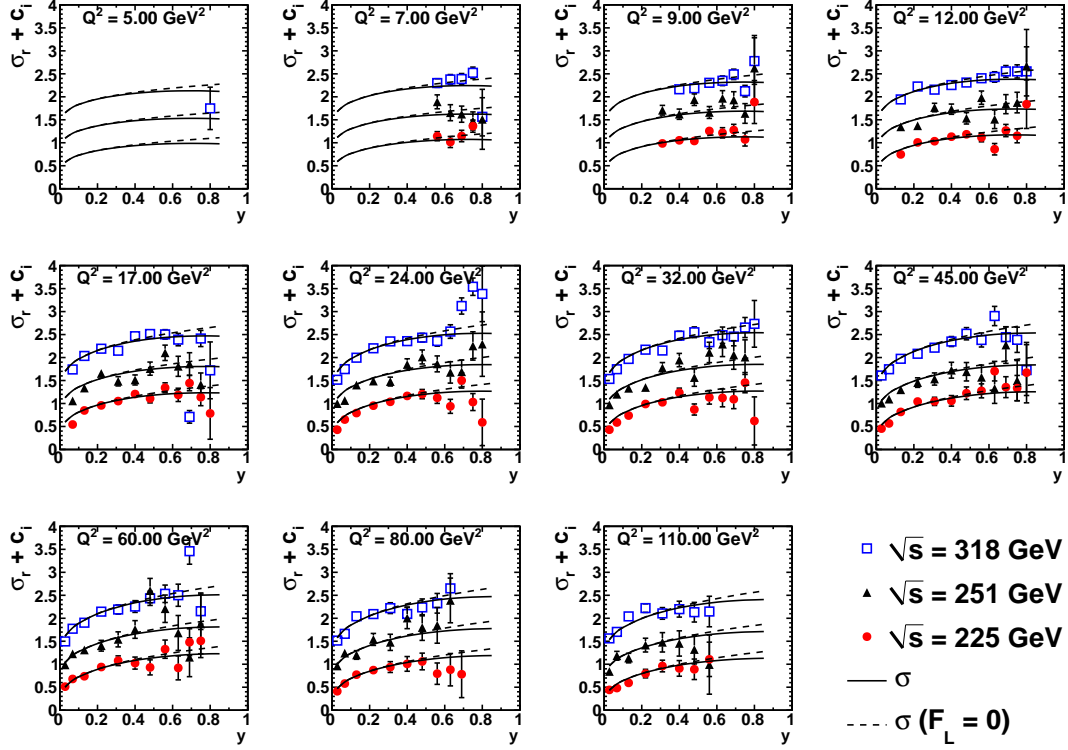


Figure 8.5: The reduced cross section for the satellite vertex HER, MER and LER data samples. The HER and MER data points are shifted by an arbitrary value for clarity. Only statistical errors are shown.

to combine the two measurements by taking a weighted average,

$$\sigma_{comb} = \left[\frac{\sigma_{nom}}{\delta_{nom}^2} + \frac{\sigma_{sat}}{\delta_{sat}^2} \right] / \left[\frac{1}{\delta_{nom}^2} + \frac{1}{\delta_{sat}^2} \right] \quad (8.5)$$

where the σ_{nom} and σ_{sat} are the measured cross sections for the nominal and satellite vertex samples respectively and δ represents the corresponding statistical uncertainties. The combined cross sections are displayed in figure 8.6 for the HER, MER and LER samples. The cross section values are given in tables C.1 - C.3.

These results are compared with ZEUS-JETS PDF predictions. The dashed lines in figure 8.6 show the predicted cross sections when σ_r is assumed to have no contributions from F_L . In the medium Q^2 range ($17 \text{ GeV}^2 \leq Q^2 \leq 32 \text{ GeV}^2$), a clear

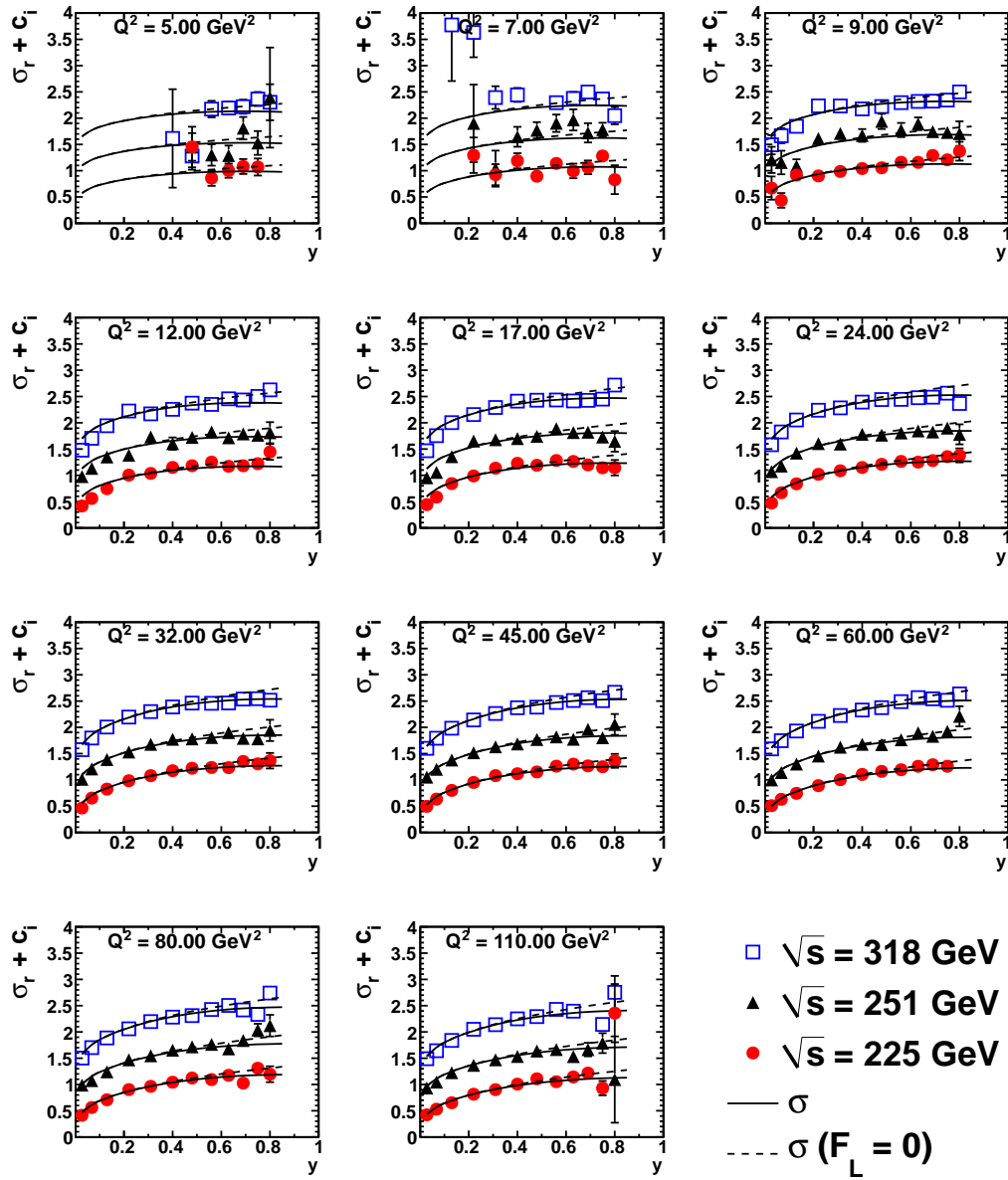


Figure 8.6: The combined reduced cross section for HER, MER and LER data samples. The HER and MER data points are shifted by an arbitrary value for clarity. Only statistical errors are shown.

preference for data to follow the solid line is observed. In other bins, no strong conclusion can be made.

8.3.2 F_L Measurement

For the reduced cross sections displayed above, binning was chosen such that the HER, MER and LER samples had the same bins in (y, Q^2) plane. For the F_L measurement, the binning has been redefined such that the HER, MER and LER share a common binning in the (x, Q^2) plane.

The cross sections are re-evaluated using the new binning. By representing the reduced cross sections as points in a $(\sigma, y/Y_+)$ plane (e.g. using the so-called ‘‘Rosenbluth Plot’’ representation [80]), a linear relation can be written as:

$$\sigma_r = F_2 - F_L \frac{y^2}{Y_+}. \quad (8.6)$$

From equation 8.6 it is clear that F_L is the slope of the line while F_2 is given by the y -intercept. An example of such a plot using nominal vertex data and for $Q^2 = 32 \text{ GeV}^2$ is shown in figure 8.7. In this plot, each point represents a reduced cross section

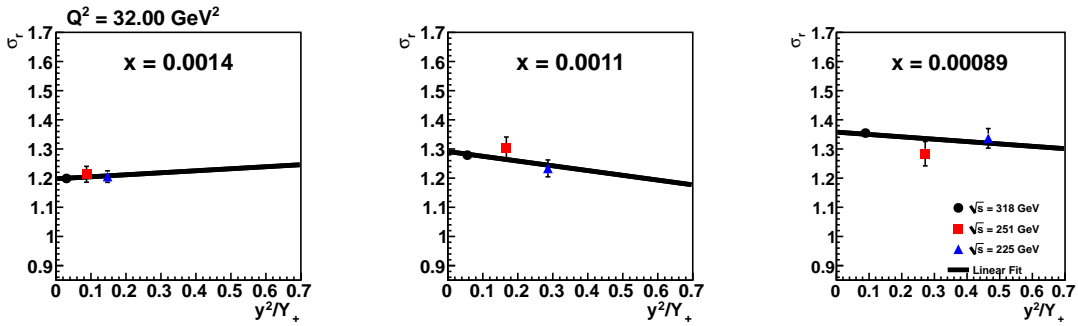


Figure 8.7: Rosenbluth plots for $Q^2 = 32 \text{ GeV}^2$ and three bins of x for nominal vertex data.

measured at a different centre-of-mass energy. A linear fitting routine is used to determine F_L and F_2 .

These measurements are displayed in figure 8.8 for the nominal vertex samples, figure 8.9 for the satellite vertex samples and figure 8.10 for the combined nominal and satellite vertex samples. The extracted F_L and F_2 values are compared with the ZEUS-JETS PDF and the measured values for the combined measurement are displayed in table C.4.

The complete set of Rosenbluth plots for the nominal and satellite vertex combined measurements are displayed in Appendix C.2. From the Rosenbluth plots it can be noted that the fit is primarily constrained by the HER and LER samples and that the MER sample shows a tendency to deviate from the linear fit. This could result from the lower statistics in the MER sample.

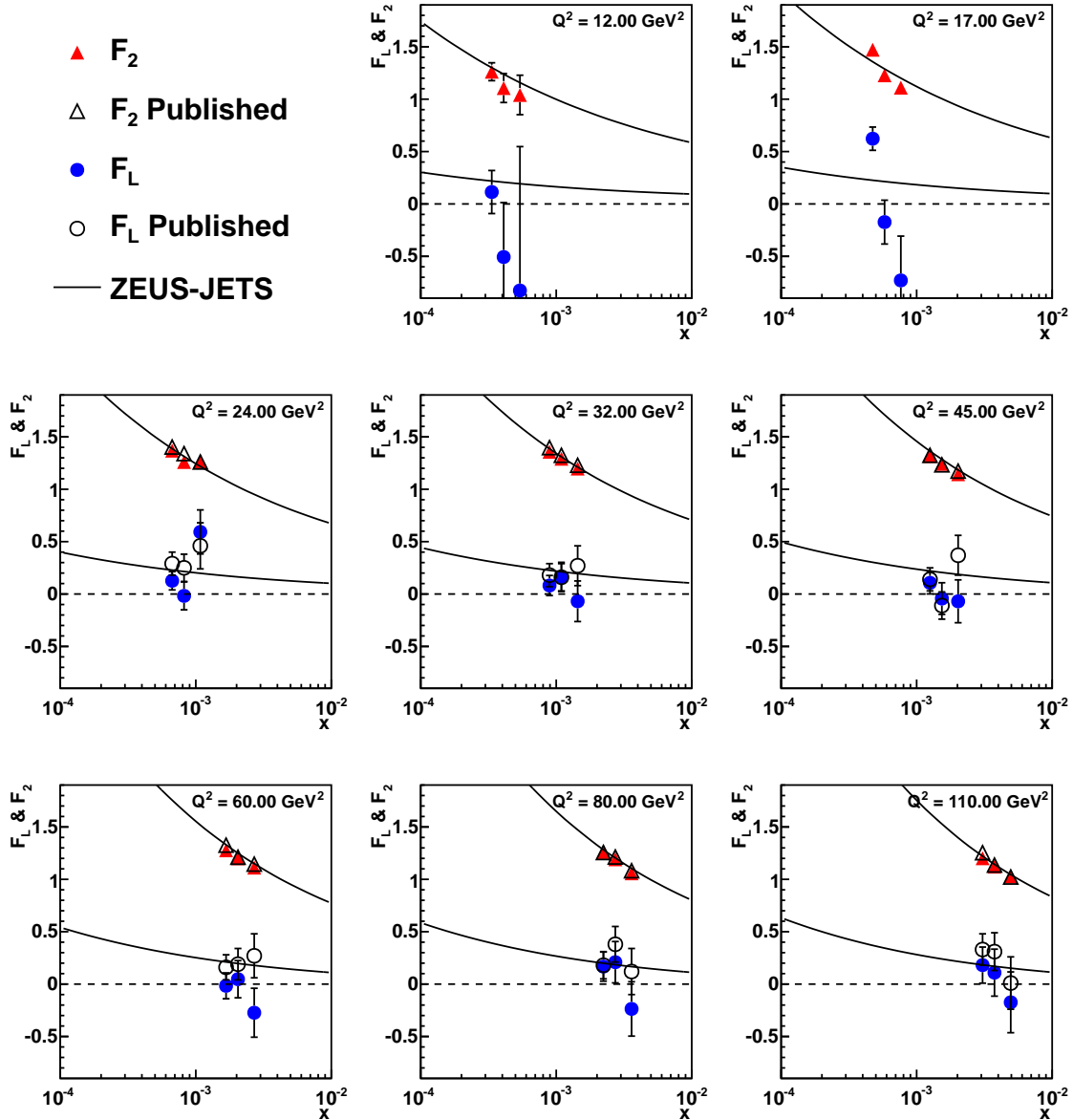


Figure 8.8: F_L and F_2 using the nominal vertex data samples. Results are compared with the ZEUS-JETS parameterization of the proton PDF. Statistical errors are shown and in some cases are smaller than the data points. For comparison the previously published results [73] are shown.

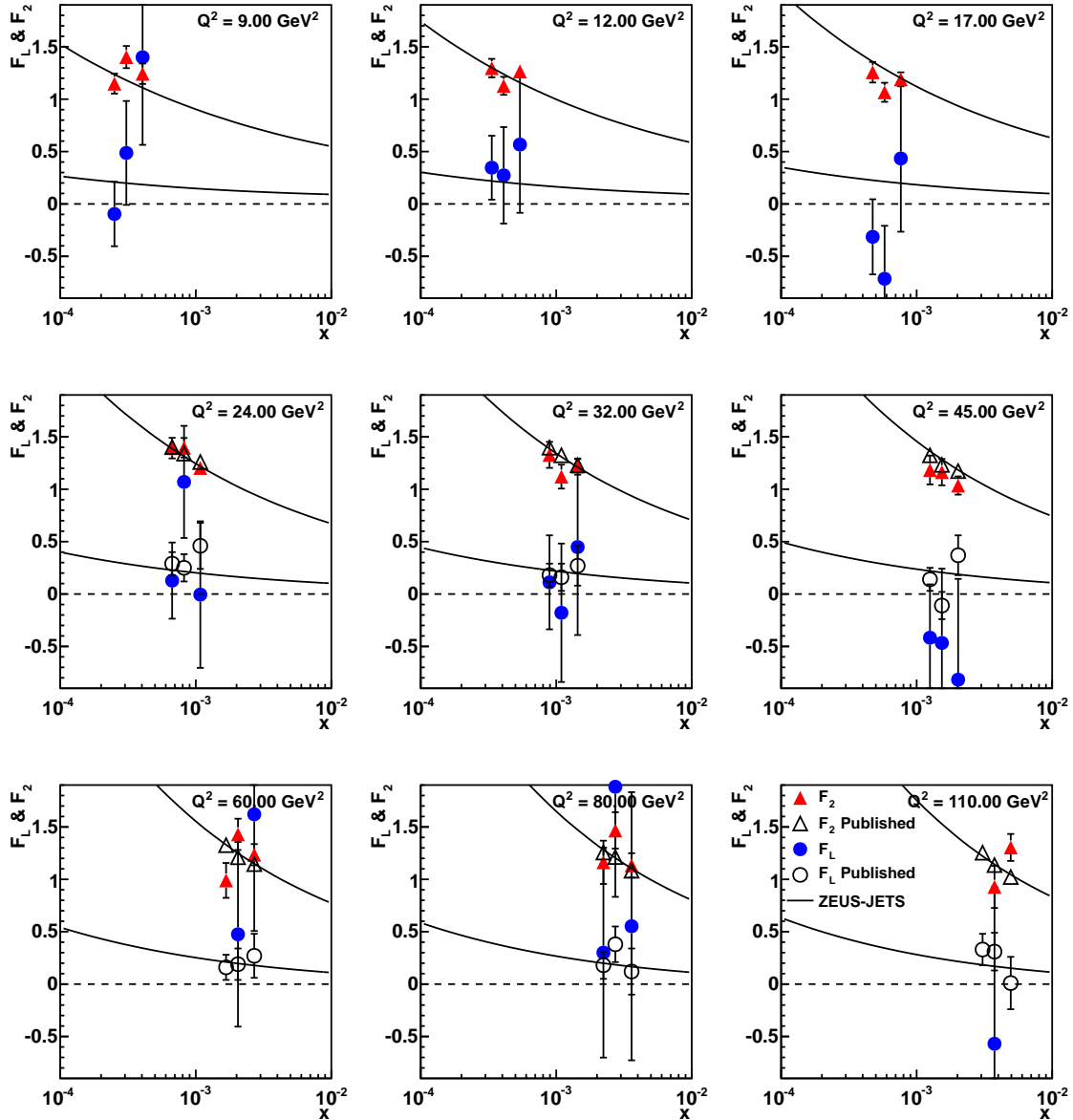


Figure 8.9: F_L and F_2 using the satellite vertex data samples. Results are compared with the ZEUS-JETS parameterization of the proton PDF. Statistical errors are shown and in some cases are smaller than the data points. For comparison the previously published results [73] are shown.

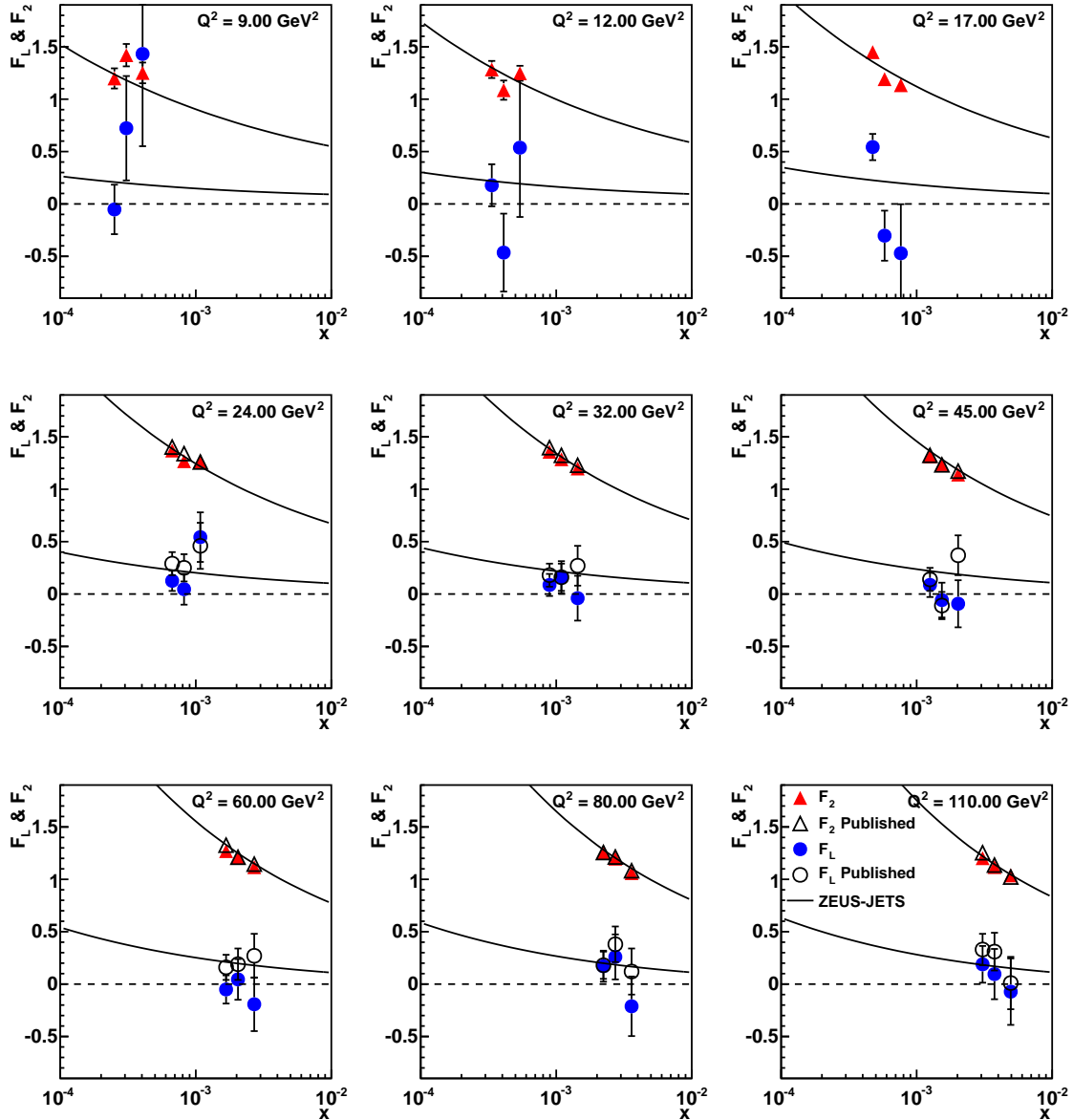


Figure 8.10: F_L and F_2 for the combined nominal and satellite vertex data samples. Results are compared with the ZEUS-JETS parameterization of the proton PDF. Statistical errors are shown and in some cases are smaller than the data points. For comparison the previously published results [73] are shown.

CHAPTER 9

Discussions

9.1 Radiative Events

The larger part of this thesis was devoted to studies of initial state radiation (ISR). Monte Carlo (MC) studies (see section 4.2.1) have shown that ISR, although it can be heavily suppressed by cutting on $E - p_z$, leads to corrections as large as 50% at y 0.8.

Two of the three analyses studied in this thesis involve ISR (see chapters 6 and 7), a discussion of these results will be given in this section.

9.1.1 Verification of the Radiative Correction

Unlike corrections resulting from other backgrounds, such as photoproduction or QED-Compton (QEDC), radiative corrections are next-to-leading order (NLO) corrections to the DIS cross section. **HERACLES** calculates these NLO contributions and adjusts the kinematics of the leading order interaction [70]. Without radiative corrections, one would expect poor agreement between data and Monte Carlo (MC). A measured differential cross section consists of a “Born” component and a “radiative” component, this is represented by equation 6.1. Factorization theory (see section 2.5.1) defines the F_2 structure function as the convolution of a Parton Distribution Function (PDF) term and a hard scattering term. In this asymptotically free

region, the hard scattering term can be calculated using perturbation theory, while the PDF must be determined from measurements. Measurements in regions subject to high radiative corrections will be subject to high uncertainties. Currently, experimentalists rely on HERACLES, however, until this thesis, ZEUS has never verified it experimentally. A measurement of the radiative DIS cross section was presented in chapter 6. This measurement utilized a new calibration and simulation of the far luminosity system detectors. This measurement would not have been possible without these newly developed tools.

This is the first measurement of the radiative correction at ZEUS. There are several reasons that this quantity has not previously been measured. Some of which are listed below:

- The primary function of the PCAL was to count Bethe-Heitler (BH) photons. This counting rate was used in the luminosity calculation. The PCAL detector was never properly calibrated and has never been relied on for energy measurements. Until the PCAL was calibrated (work from section 5.5 in this thesis), we were unaware that it could be used for energy measurements.
- The PCAL produces a non-linear response due to the $4.2X_0$ of inactive graphite placed in front of it (see figure 3.12). Aerogel Cherenkov detectors (AERO) were imbedded at two locations inside the inactive material. Combining the energy measurements from the AERO and the PCAL (PCAL+AERO), provides a more precise and linear response than the PCAL alone. This is demonstrated in figure 5.9.

- A GEANT simulation failed at describing the light collection in the two aerogel detectors and was subsequently abandoned. Furthermore, the luminosity system was never included in MOZART, the global ZEUS detector MC simulation framework.
- The contribution from bremsstrahlung overlays was thought to overwhelm the ISR signal. It was not known, until attempted, whether or not a ISR signal could be extracted.

9.1.2 Discussion of Results

The ISR cross section measurement was displayed in figure 6.19 and consistency with theoretical values was observed for both $E-p_z$ and PCAL methods. The two methods agree within 10% for the HER dataset and 6% for the ISR dataset, which is well within the uncertainty bands for every bin. This result has undergone a goodness-of-fit significance test which returned $\chi^2/ndf = 18.16/27$ corresponding to a 89.8% confidence level that the data is well described by the theoretical distribution.

The systematic studies performed in chapter 6, demonstrate that the $E-p_z$ method is somewhat more stable. The tables of values for both the $E-p_z$ method and the PCAL method are given in section B.1.1 and section B.1.2 respectively. Both of these results are missing an estimate for the systematic uncertainty on the BH subtraction. Since both methods have a different BH subtraction procedure, one method can be used to estimate this systematic uncertainty for the other. The more stable approach, the $E-p_z$ method, was chosen for the default method. The differences between the two methods ranged between 0.6% and 25% but averaged to about 11.5%. This error was added in quadrature to the previously calculated systematic uncertainties. The resulting ISR cross section is shown in figure 9.1. Once again, data and MC have

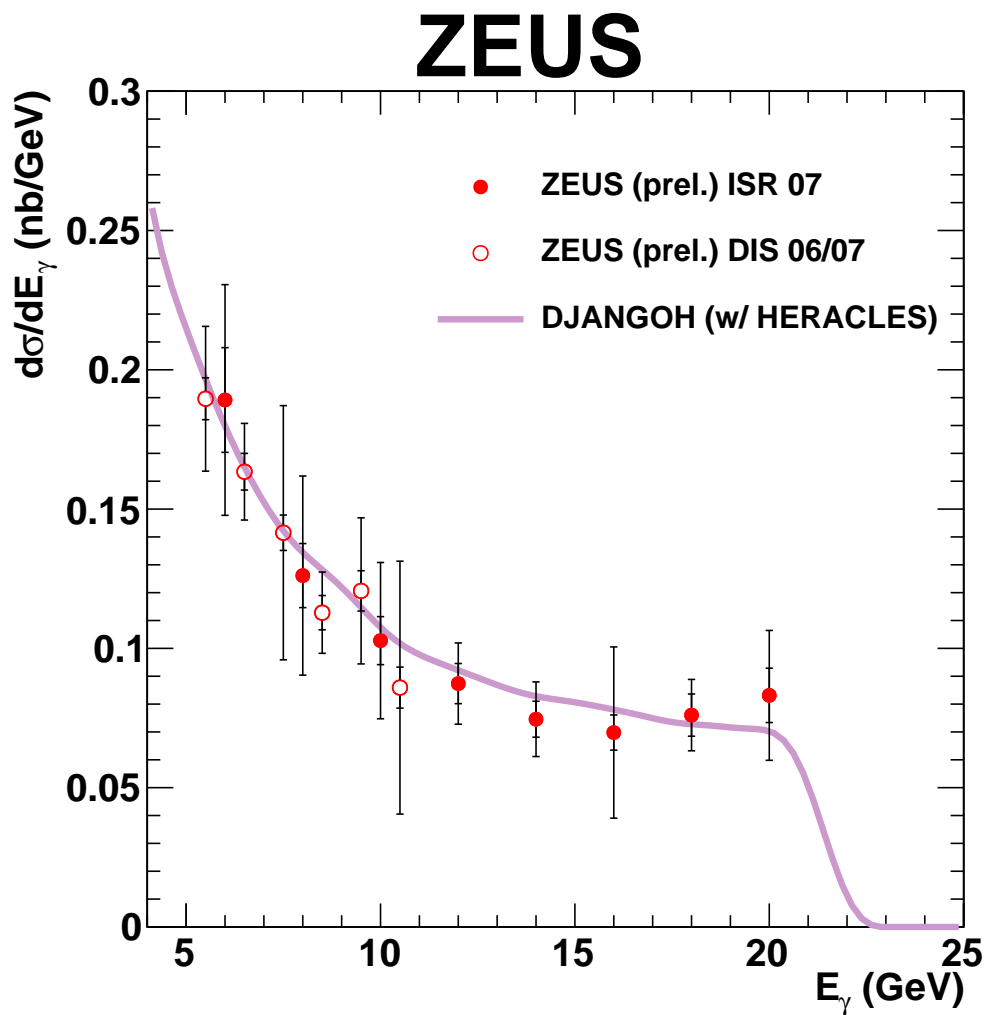


Figure 9.1: The ISR cross section, both statistical and systematic errors are shown.

undergone a goodness-of-fit test. This result has a $\chi^2/ndf = 2.44/13$ corresponding to a 99.93% confidence level.

Results from this analysis cannot be directly compared with the H1 analysis (see figure 6.1), since the two measurements do not share an identical phase space.

9.1.3 Measurement of the DIS reduced Cross section using Tagged-ISR Events

ISR provides a unique opportunity to extend the kinematically accessible region of DIS measurements at ZEUS. Using the PCAL+AERO measurement and simulation, it was shown that it is possible to tag ISR events and to subsequently reconstruct the kinematics of that event taking into consideration the energy carried by the ISR photon. This approach was used in chapter 7 to reconstruct events down to $Q^2 = 3.0 \text{ GeV}^2$.

A high BH background contributed to large systematic uncertainties and low purities in this measurement. Some bins exhibited systematic uncertainties over 100%. For y values less than 0.35, systematic uncertainties were generally below 10% and purities were above 35%. Properly reconstructed ISR events will tend to migrate from higher- y to lower- y and this feature was generally seen in this measurement. Table B.5 and B.6 display the reduced cross sections, along with the number of data and background events. From these values, and from the purity plots in figure B.12, it is clear very few ISR events remain in the high- y region after reconstructing and the background contribution overwhelms (and in some cases is larger than) the ISR contribution.

This analysis was done to check the performance of the PCAL+AERO simulation and calibration and to check the feasibility of a F_L measurement with ISR. These new tools have so far been very successful at describing the data, this is evident from the measurement of the ISR cross section and the low- Q^2 DIS reduced cross section.

9.1.4 The Longitudinal Structure Function with ISR

Theoretically, it is possible to measure the longitudinal structure function using radiative events as a means to reduce the center-of-mass energy [81]. This has previously been tried with ZEUS using the HERA-I data [69]. This measurement was statistically limited and consistent with $F_L = 0$. This attempt is shown in figure 9.2. For this thesis, this route was avoided. Efforts were focused on improving and ex-

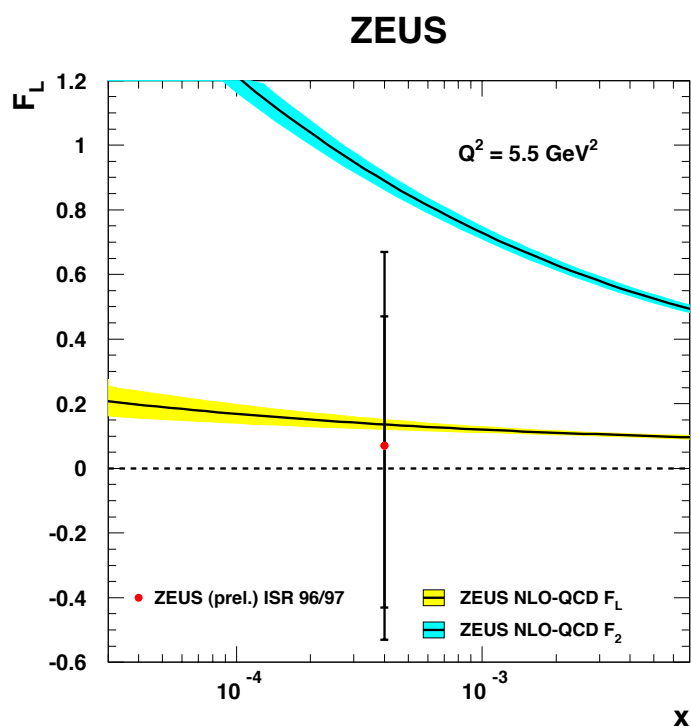


Figure 9.2: A measurement of the longitudinal structure function, F_L , from radiative events using 1996/1997 data [69].

tending the F_L extracted from the proton reduced energy beam. The ISR analyses play a significant role in this measurement as well. The radiative correction measured in chapter 6 is essential for understanding measurements in high- y or low- x regions. Furthermore, the cross sections measured in chapter 7 overlap, in kinematic space,

with the HER nominal and satellite vertex measurements. This overlap can lead to a reduction of the correlated systematics or at least a consistency check.

To perform a measurement of F_L with ISR would require much more statistics than used for this analysis. Some theoretical publications predict that this can be achieved with 200 pb^{-1} [81]. ZEUS has accumulated almost 0.5 fb^{-1} , which is sufficient to perform this measurement. However, to utilize these statistics, the PCAL+AERO simulation must be tuned for each individual running period and the BH overlay contribution would have to be suitably treated.

9.1.5 Opportunities for New Studies

With the PCAL+AERO calibration and simulation there are possibilities for new studies. This section will briefly identify some of the measurements possible with these new components.

Measurement of the total Photon-Proton Cross Section

Photon-proton interactions are known to occur at HERA. These processes are collectively known as photoproduction and are described by the process $e^+p \rightarrow e^+\gamma p \rightarrow e^+X$, where γ is an almost real photon and is used to probe the proton. These events have $Q^2 \lesssim 10^{-3} \text{ GeV}^2$ and are produced in abundance, as can be seen from the $\frac{1}{Q^4}$ dependence of the DIS cross section (see equation 2.19). The published measurement of the energy dependence of the photon-proton cross section utilizes the PCAL+AERO assembly in conjunction with the TAG6 for vetoing bremsstrahlung overlay events and for determining the fraction of good events removed resulting from the veto. A photon energy distribution is shown in figure 9.3, this result marks the first time the PCAL+AERO assembly has been used in a publication [42].

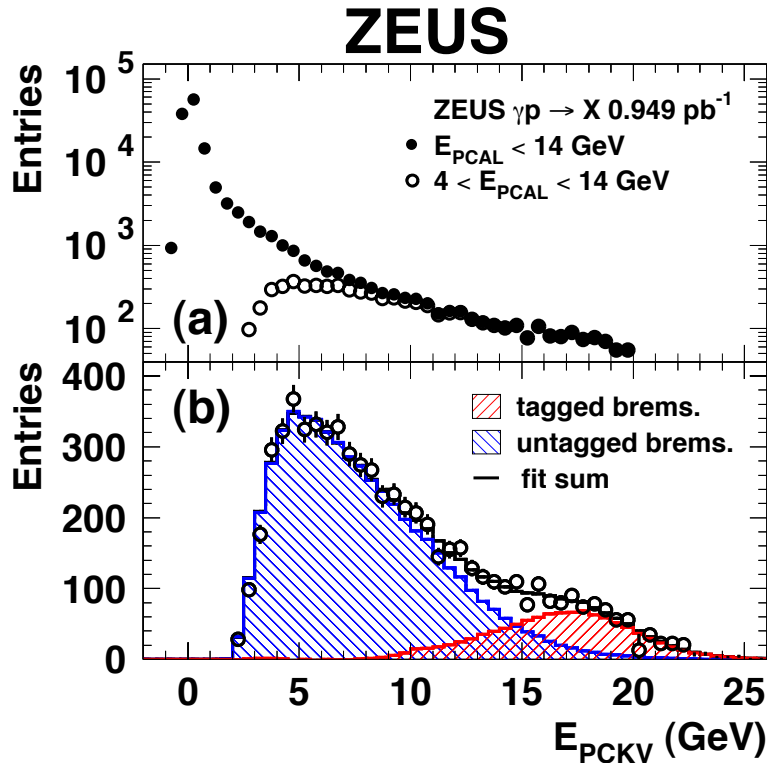


Figure 9.3: The energy spectrum of photons in the PCAL+AERO. This result demonstrates the success of the PCAL+AERO assembly to describe bremsstrahlung events.

The PCAL+AERO assembly combined with the TAG6 may be used to veto bremsstrahlung events and to better classify photoproduction events.

Determination of the PCAL Acceptance for Luminosity Measurements

The PCAL+AERO simulation can be used to determine the acceptance of photons in the luminosity system. The luminosity measurement relies on an accurate description of the aperture and the number of events which convert to e^+e^- pairs upon exiting the HERA vacuum system. These values are tuned into the PCAL+AERO simulation and variations on these parameters can be used to determine the systematic uncertainties involved in the luminosity measurement.

9.2 F_L

These measurements mark the first time that F_L has been measured in the region $Q^2 < 20 \text{ GeV}^2$ by the ZEUS experiment. The measurements presented in chapter 8 are still in development. Discrepancies in the measured F_L values, exist between the published values and those presented in this thesis. Most of the observed fluctuations lay within one standard deviation of the published values. Nevertheless, these discrepancies are currently the subject of intense investigation.

The longitudinal structure function is directly related to the gluon Parton Distribution Function (PDF), $g(x)$. Of all the PDFs accessible to HERA, $g(x)$ has the largest uncertainty. The F_L measurement was a major achievement for the ZEUS physics programme and will help provide better constraints on $g(x)$. The first measurement of F_L performed by ZEUS was in the range $20 < Q^2 < 130 \text{ GeV}^2$ [73]. As can be seen from figure 8.2, deviations from the HERAPDF1.0 set are observed at low- Q^2 , a region previously inaccessible at ZEUS. Events measured in the satellite vertex and improvements in the event reconstruction have allowed us to perform measurement in the low- Q^2 region. The measurement extension goes as low as $Q^2 = 8.0 \text{ GeV}^2$. Below that value, statistics, acceptances and bin purities are insufficient to perform a reliable measurement of F_L . However, reduced cross section measurements have been performed down to $Q^2 = 4.5 \text{ GeV}^2$, but only in a limited y region.

The effects on the $g(x)$ PDF will only become clear once the measurement is complete and the results are implemented into the PDF sets.

CHAPTER 10

Conclusions

In this thesis the radiative contribution to deep inelastic scattering has been measured with an accuracy of typically better than 10%. This is the first time that this measurement has been performed at the ZEUS experiment. This measurement improves our understanding of the radiative correction, which can have large effects on the over all deep inelastic scattering cross section. Regions with high electron inelasticities (y) are known to be heavily affected by radiative corrections. Monte Carlo studies estimate that in the highest- y region this correction can reach above 250%. Knowing that the radiative processes predicted by HERACLES is correct can help reduce uncertainties on measurements at high- y and helps to extend the structure function measurements to this region.

In chapter 8 of this thesis, measurements of the reduced cross section, σ_r , and of the longitudinal structure function, F_L , and of F_2 were reported. These measurements were made in a Q^2 region not easily accessible to the ZEUS detector and they provide a crucial test of perturbative QCD. Measurements show consistency with theoretical predictions, nevertheless their impact will not be known until they are included into the global Parton Distribution Function (PDF) fits. The PDFs determined from HERA are an indispensable input for other experiments like the LHC. Improved precision on the PDFs, especially the gluon PDF, $g(x)$, will help to reduce the experimental errors at the new LHC collider experiments, which have the potential to discover new physics within and beyond the Standard Model of particle physics.

APPENDIX A

Control Distributions

A.1 Control Distributions

The control distributions for all datasets used in this thesis are shown in this section. These distributions compare measured data to fully reconstructed Monte Carlo for several key quantities including: electron energy, electron scattering angle, $E - p_z$ and the interaction Z vertex. Each control distribution corresponds to a different event sample. A summary of the samples used in this thesis is given in table 5.2.

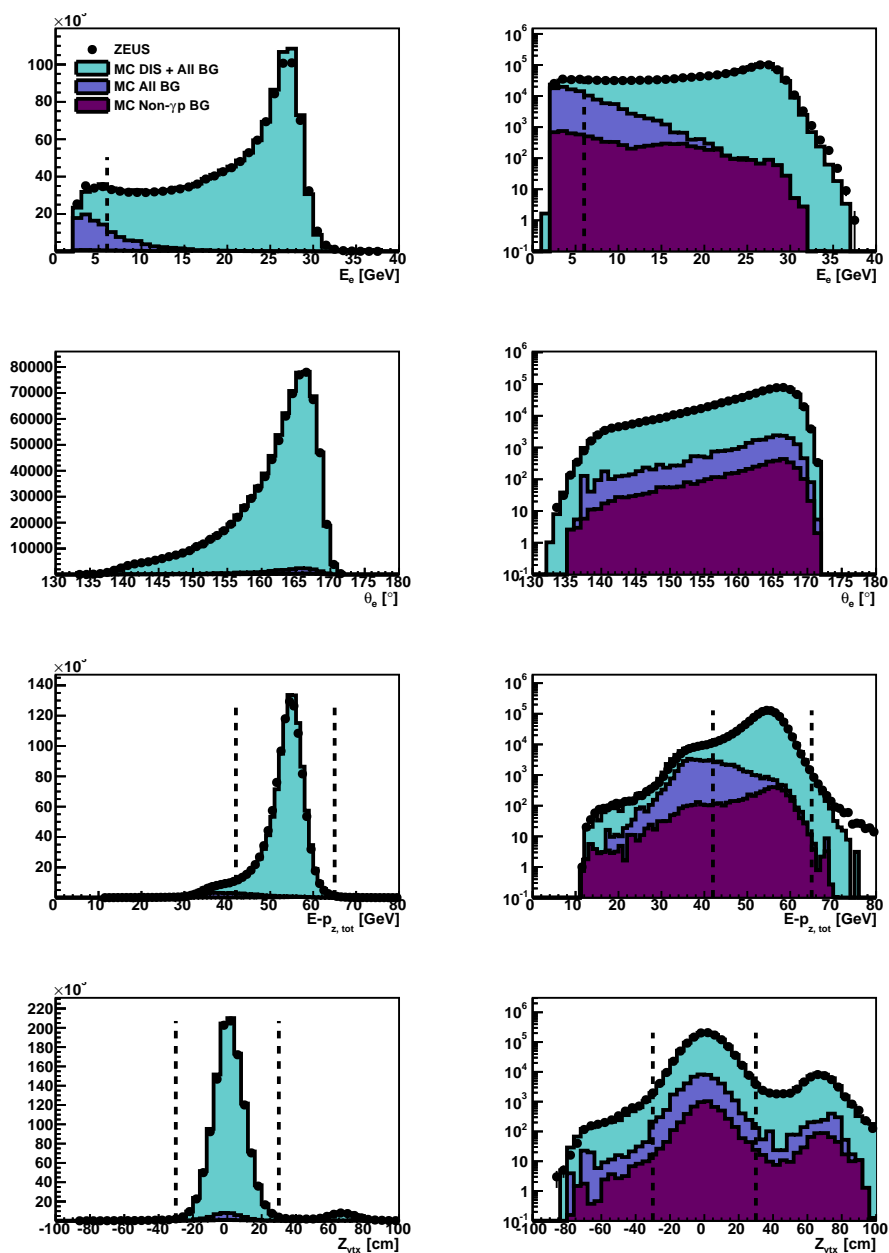


Figure A.1: HER Control distributions for four different detector quantities, ordered from top to bottom; electron energy (E_e'), electron scattering angle (θ_e'), $E - p_z$ (δ) and the Z vertex, presented in both linear (left) and log scales (right). The broken vertical line represents the position of the actual selection cut. The background is from photoproduction and QEDC.

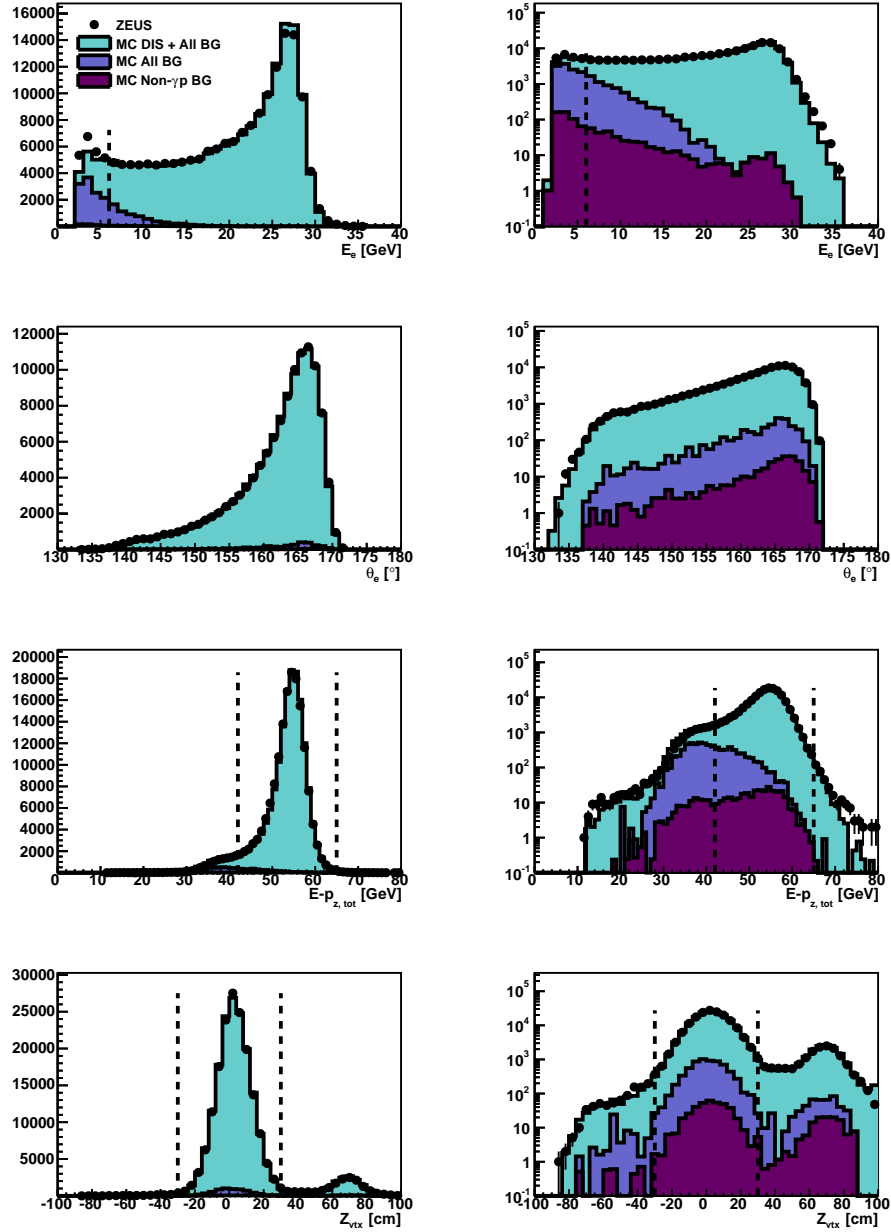


Figure A.2: MER Control distributions for four different detector quantities, ordered from top to bottom; electron energy (E_e), electron scattering angle (θ_e), $E - p_z$ (δ) and the Z vertex, presented in both linear (left) and log scales (right). The broken vertical line represents the position of the cut.

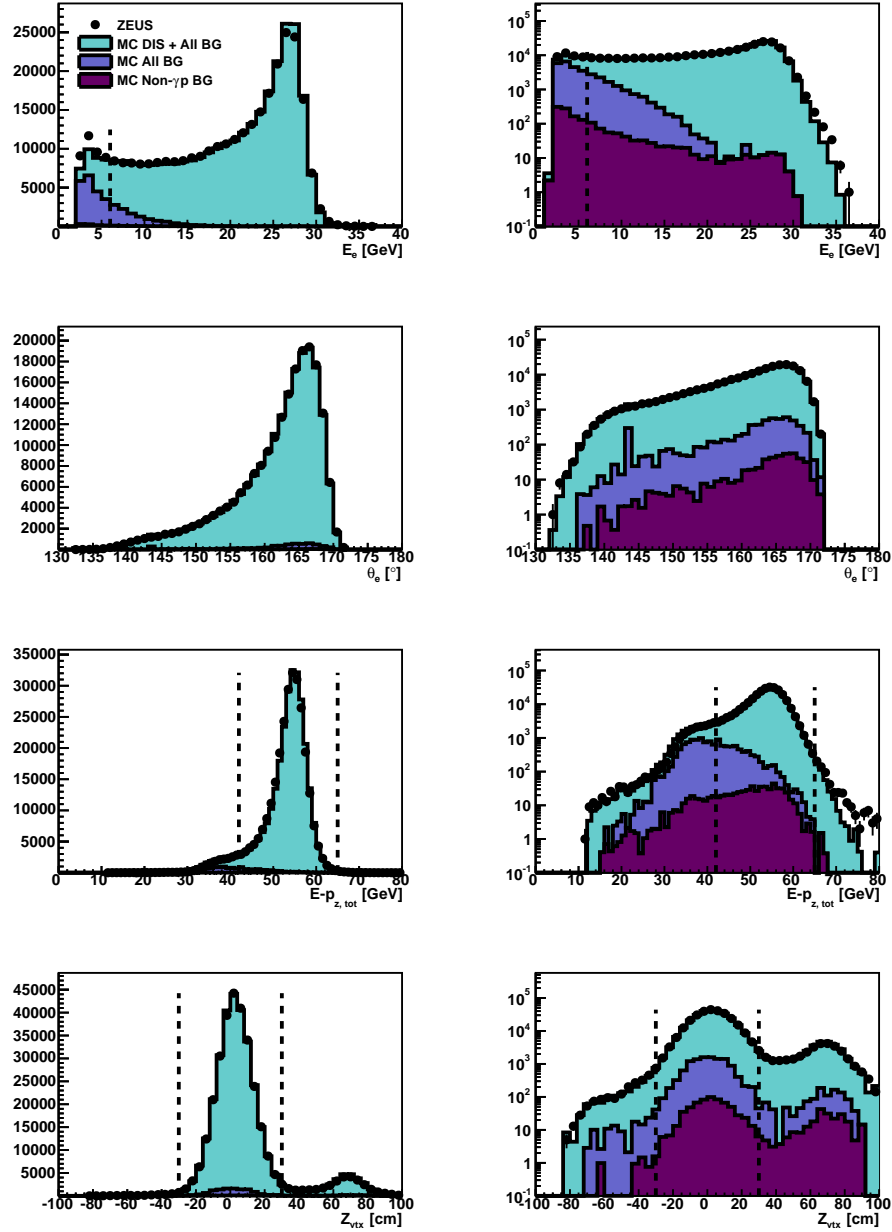


Figure A.3: LER Control distributions for four different detector quantities, ordered from top to bottom; electron energy (E_e'), electron scattering angle (θ_e'), $E - p_z$ (δ) and the Z vertex, presented in both linear (left) and log scales (right). The broken vertical line represents the position of the cut.

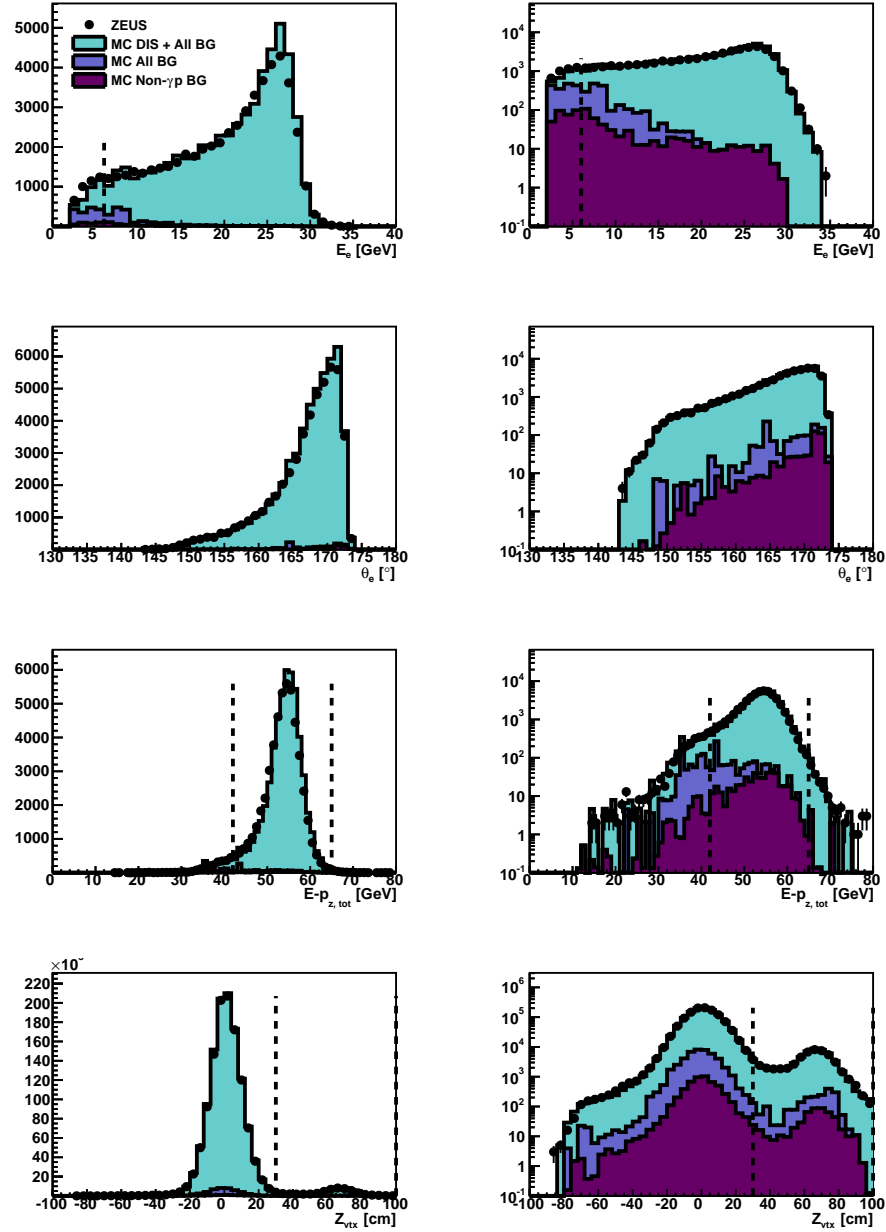


Figure A.4: Satellite Z_{vtx} HER Control distributions for four different detector quantities, ordered from top to bottom; electron energy (E'_e), electron scattering angle (θ'_e), $E - p_z$ (δ) and the Z vertex, presented in both linear (left) and log scales (right). The broken vertical line represents the position of the cut.

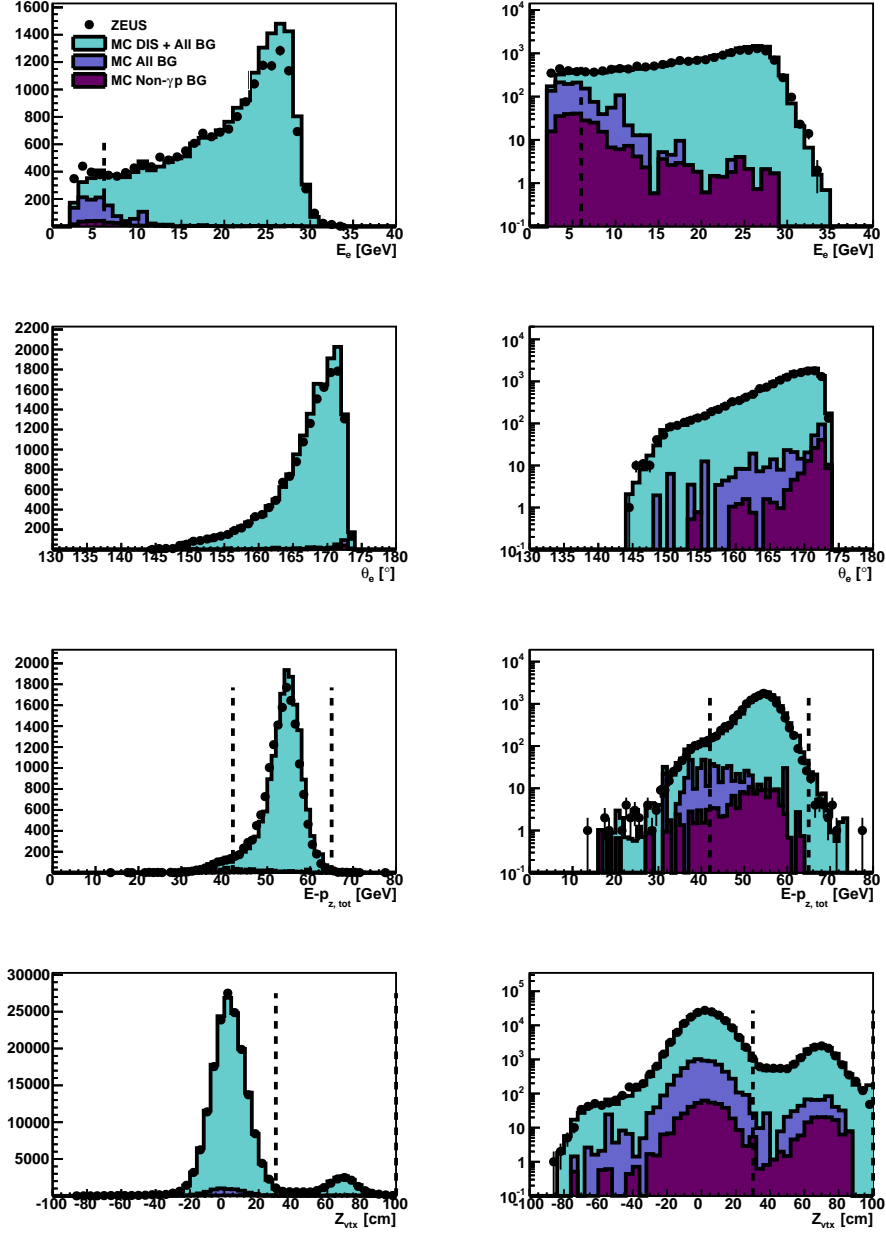


Figure A.5: Satellite Z_{vtx} MER Control distributions for four different detector quantities, ordered from top to bottom; electron energy (E_e), electron scattering angle (θ_e), $E - p_z$ (δ) and the Z vertex, presented in both linear (left) and log scales (right). The broken vertical line represents the position of the cut.

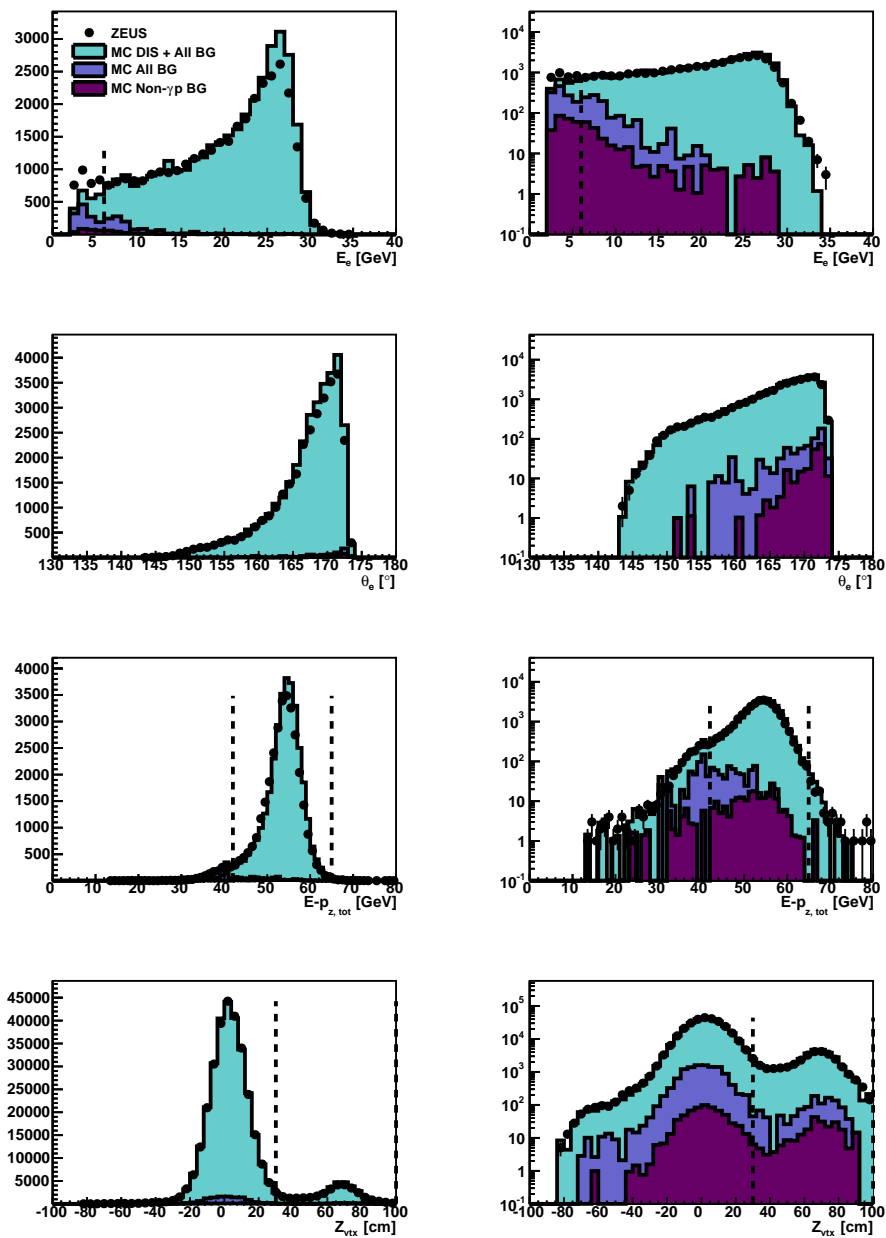


Figure A.6: Satellite Z_{vtx} LER Control distributions for four different detector quantities, ordered from top to bottom; electron energy (E'_e), electron scattering angle (θ'_e), $E - p_z$ (δ) and the Z vertex, presented in both linear (left) and log scales (right). The broken vertical line represents the position of the cut.

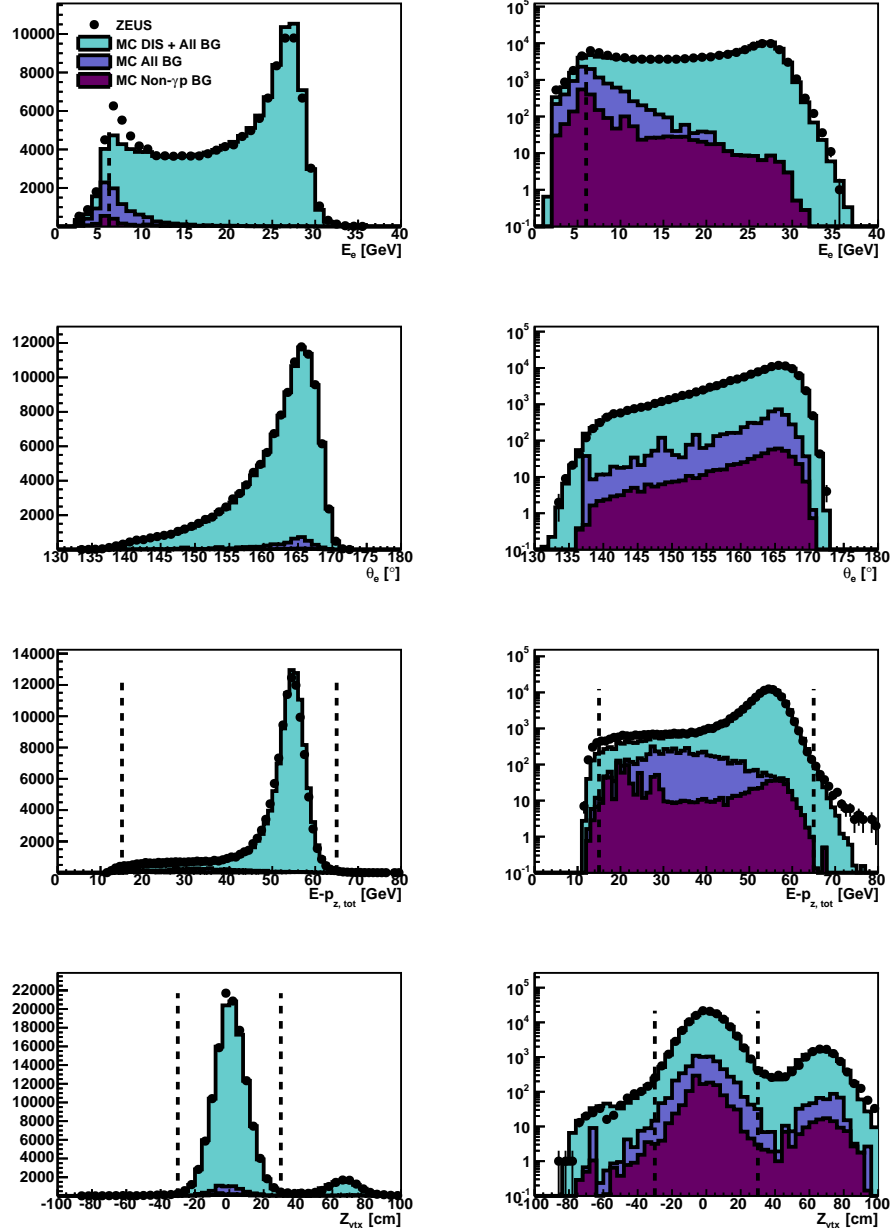


Figure A.7: ISR Control distributions for four different detector quantities, ordered from top to bottom; electron energy (E_e'), electron scattering angle (θ_e'), $E - p_z$ (δ) and the Z vertex, presented in both linear (left) and log scales (right). The broken vertical line represents the position of the cut.

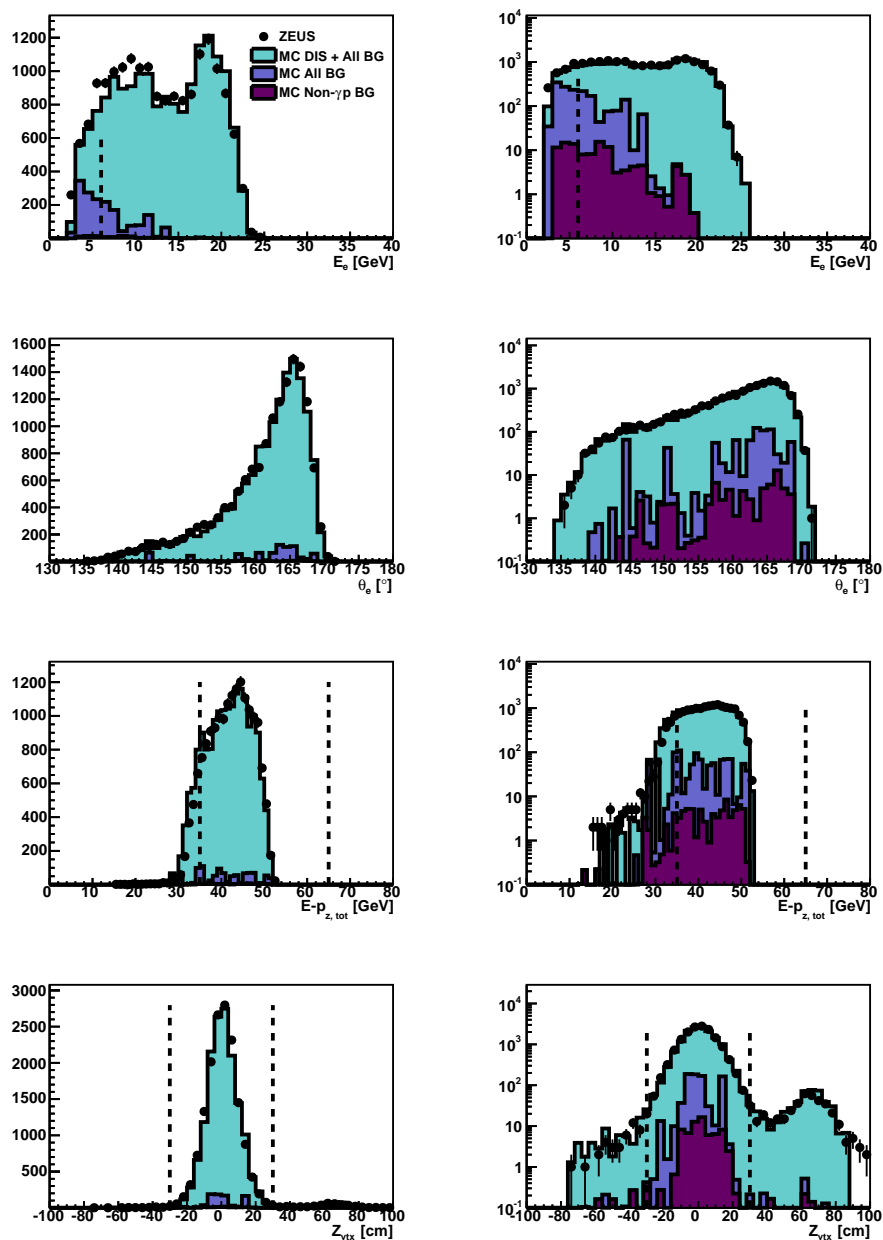


Figure A.8: ISR-Tagged Sample for the HER running period. Control distributions for four different detector quantities, ordered from top to bottom; electron energy (E'_e), electron scattering angle (θ'_e), $E - p_z$ (δ) and the Z vertex, presented in both linear (left) and log scales (right). The broken vertical line represents the position of the cut.

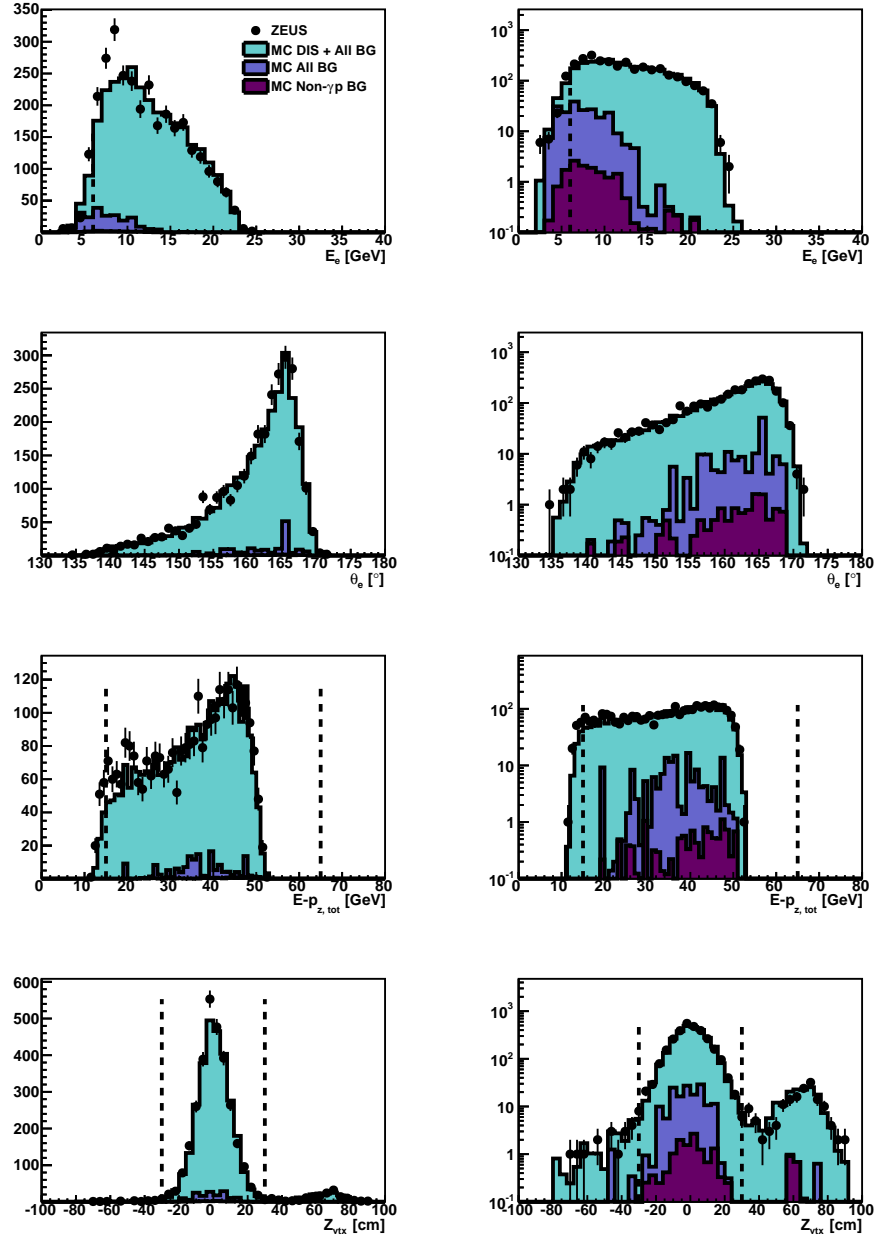


Figure A.9: ISR-Tagged Sample for the ISR running period. Control distributions for four different detector quantities, ordered from top to bottom; electron energy (E'_e), electron scattering angle (θ'_e), $E - p_z$ (δ) and the Z vertex, presented in both linear (left) and log scales (right). The broken vertical line represents the position of the cut.

APPENDIX B

Radiative Events

B.1 Values for the ISR Cross Section

In chapter 6 the ISR cross section was measured using two different approaches. These methods have been referred to throughout this thesis as the $E - p_z$ method and the PCAL method. Sections B.1.1 and B.1.2 present the measured values of each data point for both the $E - p_z$ method and the PCAL method respectively.

In chapter 7 an event sample with a tagged ISR photon was used to reconstruct the event kinematics and measure the reduced deep inelastic scattering cross section. The table of values for this measurement is presented in section B.2.

B.1.1 ISR Cross Section Measurement with the $E - p_z$ Method

Tables B.3 and B.4 present the measured cross section values, along with the statistical and systematic errors for all the data points shown in figures 6.12 (a) and 6.12 (b).

E_γ (GeV)	$d\sigma/dE_\gamma$ (nb/GeV)	$\delta_{stat}(\%)$	$\delta_{sys}(\%)$
5.5	0.190 ± 0.014	3.963	3.599
6.5	0.163 ± 0.013	4.028	3.688
7.5	0.142 ± 0.014	4.490	5.325
8.5	0.113 ± 0.013	5.460	6.112
9.5	0.121 ± 0.019	5.993	9.422
10.5	0.086 ± 0.013	8.570	6.298

Table B.1: Values for the ISR cross section, $d\sigma/dE_\gamma$, for the HER dataset, obtained using the $E - p_z$ method. δ_{stat} and δ_{sys} are the statistical and systematic errors respectively. Values correspond to figure 6.12 (a).

E_γ (GeV)	$d\sigma/dE_\gamma$ (nb/GeV)	$\delta_{stat}(\%)$	$\delta_{sys}(\%)$
6.0	0.189 ± 0.029	9.932	5.462
8.0	0.126 ± 0.016	9.116	3.348
10.0	0.103 ± 0.013	8.386	3.880
12.0	0.087 ± 0.011	8.248	4.246
14.0	0.075 ± 0.009	8.651	3.629
16.0	0.070 ± 0.009	9.040	3.936
18.0	0.076 ± 0.012	9.960	5.214
20.0	0.083 ± 0.018	11.735	9.822

Table B.2: Values for the ISR cross section, $d\sigma/dE_\gamma$, for the ISR dataset, obtained using the $E - p_z$ method. δ_{stat} and δ_{sys} are the statistical and systematic errors respectively. Values correspond to figure 6.12 (b).

B.1.2 ISR Cross Section Measurement with the PCAL Method

Tables B.3 and B.4 present the measured cross section values, along with the statistical and systematic error for all the data points shown in figures 6.18 (a) and 6.18 (b) respectively.

E_γ (GeV)	$d\sigma/dE_\gamma$ (nb/GeV)	$\delta_{stat}(\%)$	$\delta_{sys}(\%)$
5.5	0.199 ± 0.028	2.037	11.827
6.5	0.159 ± 0.019	2.220	9.414
7.5	0.117 ± 0.013	2.442	8.508
8.5	0.114 ± 0.014	2.716	9.248
9.5	0.114 ± 0.017	3.105	11.732
10.5	0.111 ± 0.015	3.476	10.277

Table B.3: Values for the ISR cross section, $d\sigma/dE_\gamma$, for the HER dataset, obtained using the PCAL method. δ_{stat} and δ_{sys} are the statistical and systematic errors respectively. Values correspond to figure 6.18 (a).

E_γ (GeV)	$d\sigma/dE_\gamma$ (nb/GeV)	$\delta_{stat}(\%)$	$\delta_{sys}(\%)$
6.0	0.178 ± 0.036	4.577	15.869
8.0	0.110 ± 0.018	5.073	11.519
10.0	0.090 ± 0.014	5.405	9.916
12.0	0.091 ± 0.012	5.748	7.008
14.0	0.078 ± 0.015	5.902	13.414
16.0	0.053 ± 0.015	6.352	21.944
18.0	0.075 ± 0.017	7.005	15.202
20.0	0.078 ± 0.019	8.103	16.201

Table B.4: Values for the ISR cross section, $d\sigma/dE_\gamma$, for the HER dataset, obtained using the PCAL method. δ_{stat} and δ_{sys} are the statistical and systematic errors respectively. Values correspond to figure 6.18 (b).

B.2 Cross Sections for the ISR-Tagged Sample

The ISR-tagged sample is defined in section 5.9.4. The reduced cross section for events where the ISR photon was tagged and reconstructed was displayed in section 7.3. The table of values corresponding to this measurement are displayed in tables B.5 and B.6 for the HER and ISR datasets respectively. In figures 7.4 and 7.5, bins with systematic uncertainties larger than 25% were suppressed, these bins are included in the tables below.

In section B.2.1 the figures show the difference from the standard measurement for an applied positive and negative variation. Figures B.1 - B.5 display for the HER dataset and figures B.6 - B.11 show the ISR dataset.

Q^2 (GeV ²)	y	N_{data}	N_{MC}^{Bkg}	σ_r	$\delta_{stat}(\%)$	$\delta_{sys}(\%)$
8.50	0.05	45	1	0.97 ± 0.29	22.81	7.07
8.50	0.22	425	180	0.99 ± 0.28	11.74	16.84
8.50	0.48	1267	998	1.25 ± 1.04	18.70	64.88
15.50	0.05	713	22	0.74 ± 0.06	5.35	2.18
15.50	0.22	1514	490	1.18 ± 0.14	5.38	6.79
15.50	0.48	1788	1400	1.08 ± 0.48	15.21	29.30
24.00	0.05	757	30	0.77 ± 0.07	5.31	4.23
24.00	0.22	872	317	0.95 ± 0.12	7.27	5.79
24.00	0.48	756	547	1.36 ± 0.50	18.54	18.56
32.00	0.05	613	29	0.73 ± 0.08	5.90	5.19
32.00	0.22	642	148	1.15 ± 0.12	7.19	3.09
32.00	0.48	467	358	1.11 ± 0.61	27.63	27.14
45.00	0.05	477	28	0.64 ± 0.06	6.65	3.39
45.00	0.22	505	129	1.04 ± 0.12	8.28	2.83
45.00	0.48	342	262	1.27 ± 0.68	32.52	20.72

Table B.5: Values for the reduced cross section, σ_r , measured from the ISR-tagged sample using the HER Dataset. N_{data} , N_{MC}^{Bkg} , δ_{stat} and δ_{sys} are the number of events in the data, number of background events expected, the statistical error and systematic error respectively. Values correspond to figure 7.4.

Q^2 (GeV ²)	y	N_{data}	N_{MC}^{Bkg}	σ_r	$\delta_{stat}(\%)$	$\delta_{sys}(\%)$
4.25	0.05	149	4	0.90 ± 0.17	12.86	5.67
4.25	0.22	94	39	1.02 ± 0.47	25.27	20.98
4.25	0.48	18	15	1.77 ± 10.47	178.50	411.44
8.50	0.05	216	2	0.84 ± 0.18	9.89	11.89
8.50	0.22	179	67	1.11 ± 0.42	17.02	20.94
8.50	0.48	130	105	0.94 ± 1.85	64.69	131.33
15.50	0.05	236	5	0.65 ± 0.13	8.98	10.42
15.50	0.22	241	70	1.13 ± 0.27	12.74	10.71
15.50	0.48	158	163	-0.14 ± 0.34	343.93	109.81
24.00	0.05	151	6	0.73 ± 0.15	11.74	9.13
24.00	0.22	117	40	0.96 ± 0.26	19.13	7.58
24.00	0.48	93	59	1.94 ± 1.24	41.82	22.19
32.00	0.05	115	4	0.74 ± 0.16	13.47	8.80
32.00	0.22	90	18	1.24 ± 0.28	18.87	3.48
32.00	0.48	52	40	1.09 ± 1.36	84.85	39.86
45.00	0.05	77	3	0.61 ± 0.14	16.04	7.43
45.00	0.22	65	15	1.10 ± 0.32	22.56	6.46
45.00	0.48	40	28	1.72 ± 1.84	77.69	29.42

Table B.6: Values for the reduced cross section, σ_r , measured from the ISR-tagged sample using the ISR Dataset. N_{data} , N_{MC}^{Bkg} , δ_{stat} and δ_{sys} are the number of events in the data, number of background events expected, the statistical error and systematic error respectively. Values correspond to figure 7.5.

B.2.1 Systematics

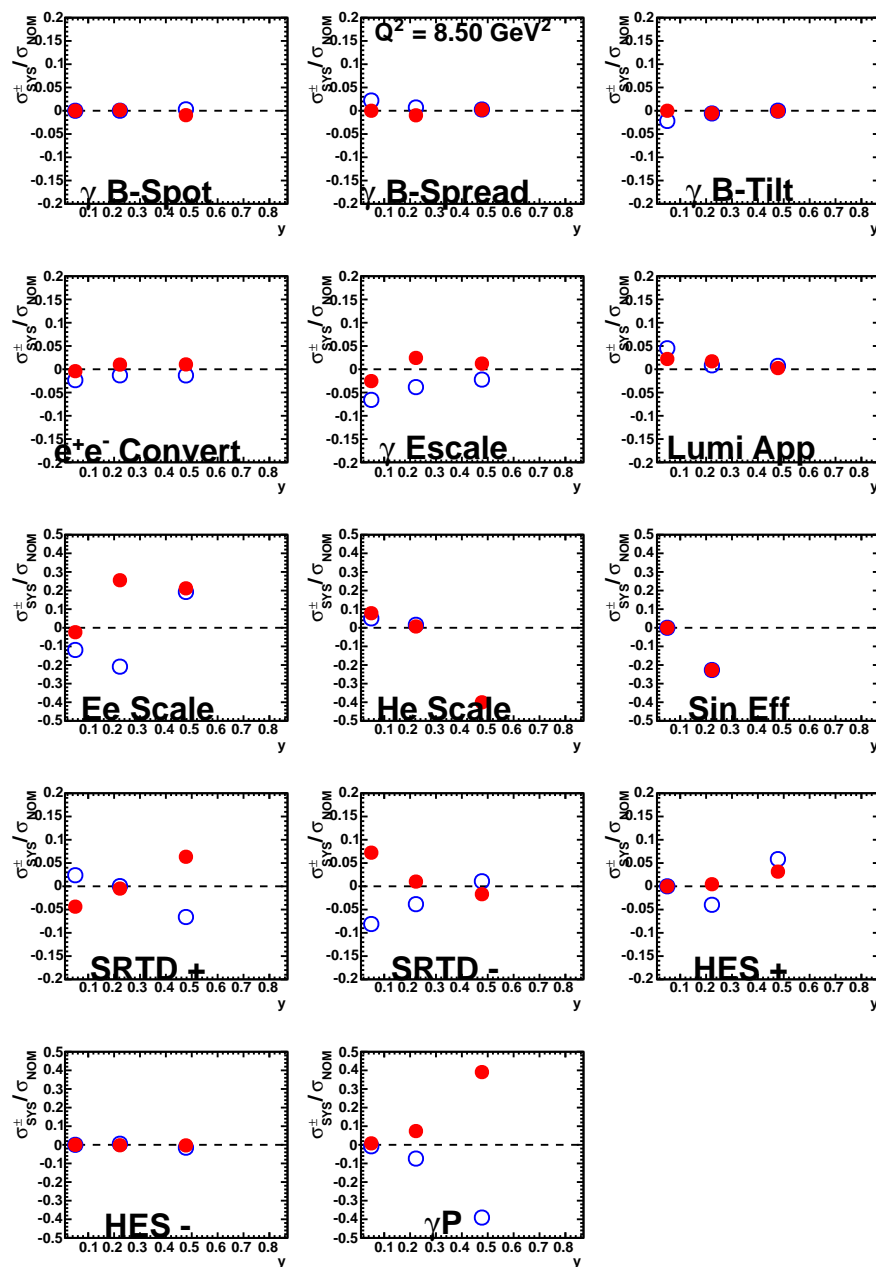


Figure B.1: A visual representation of the systematic variations applied to the reduced cross section, σ_r , measured with ISR-tagged events from the HER dataset. The text in the figure (bottom) corresponds to table 6.1 and the open (closed) red (blue) circles correspond to a positive(negative) variation applied to the central value. Results are for $Q^2 = 8.5 \text{ GeV}^2$.

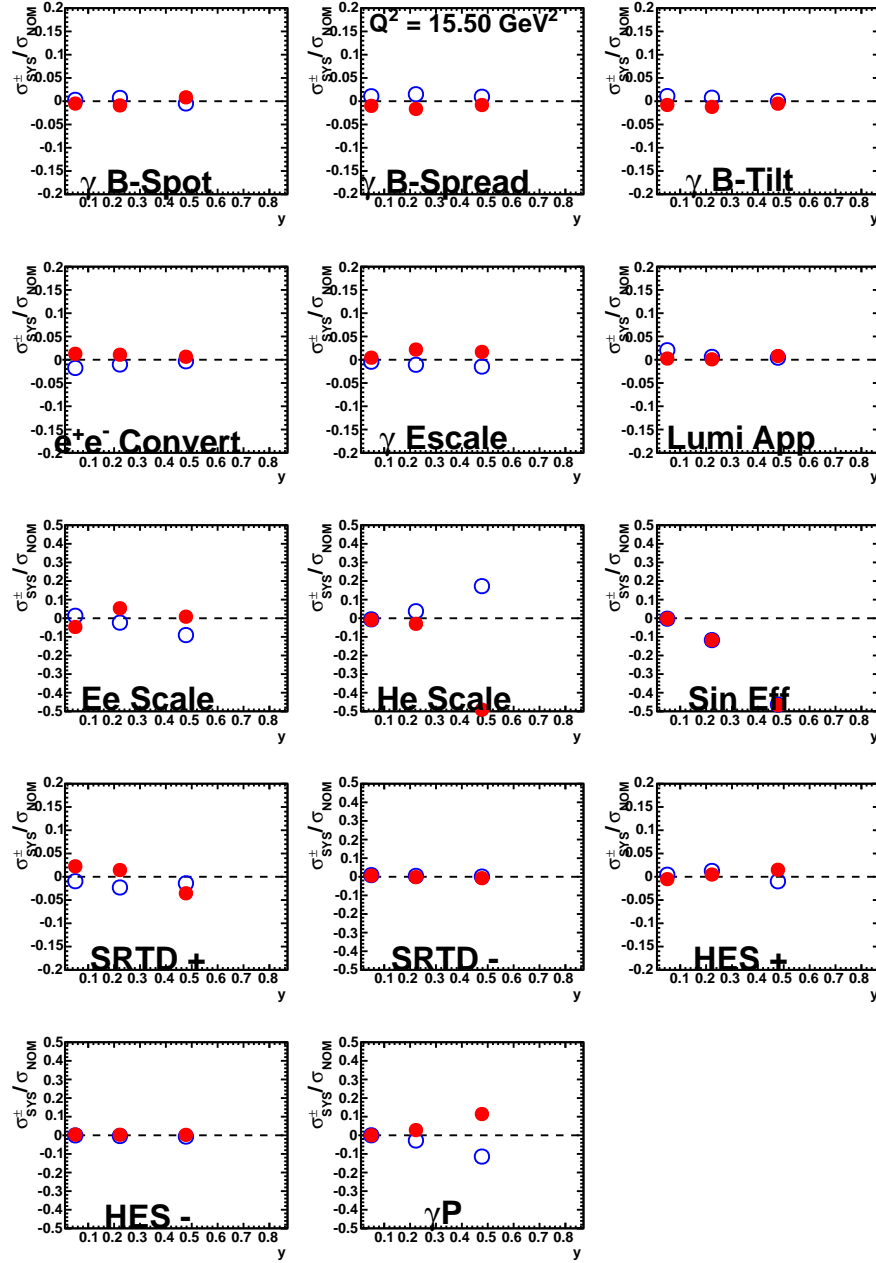


Figure B.2: A visual representation of the systematic variations applied to the reduced cross section, σ_r , measured with ISR-tagged events from the HER dataset. The text in the figure (bottom) corresponds to table 6.1 and the open (closed) red (blue) circles correspond to a positive(negative) variation applied to the central value. Results are for $Q^2 = 15.5 \text{ GeV}^2$.

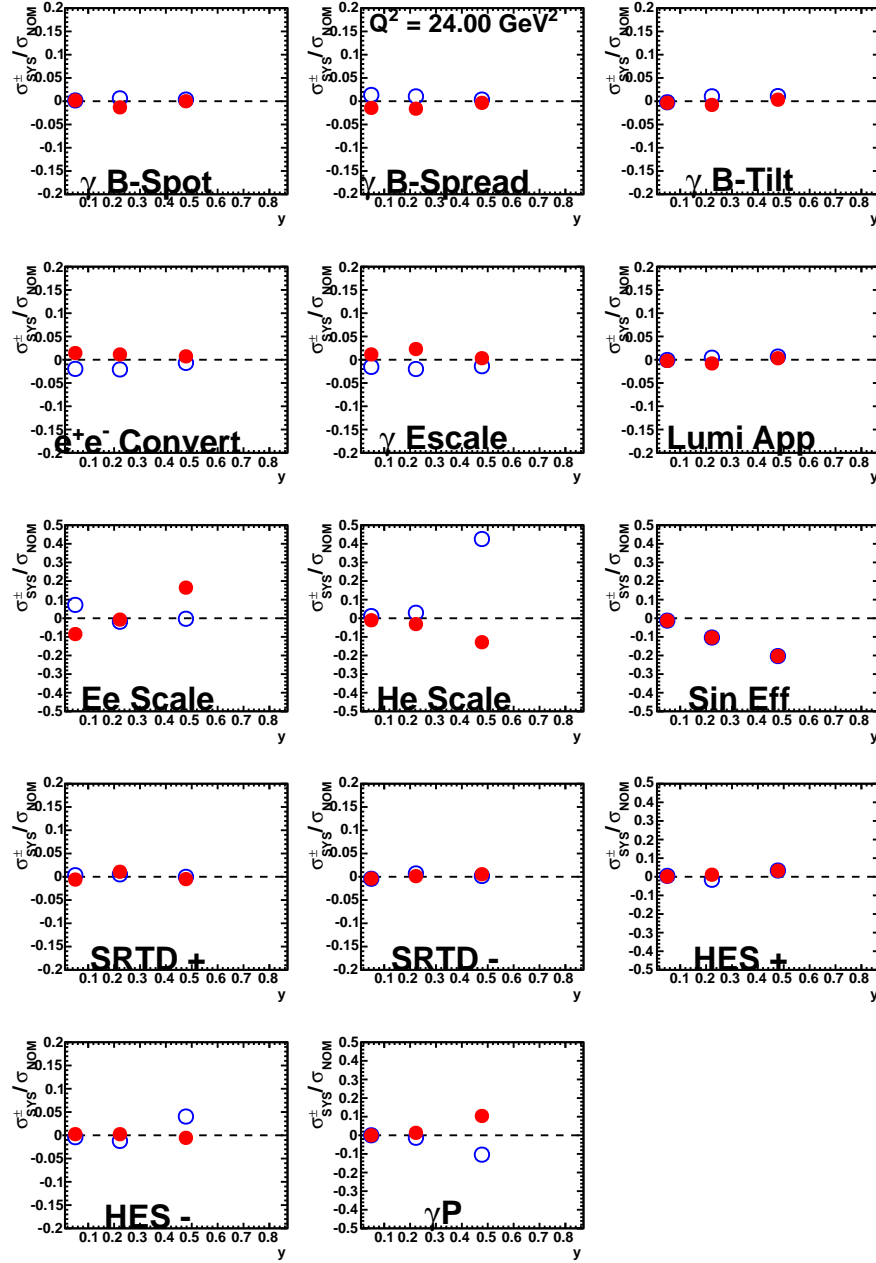


Figure B.3: A visual representation of the systematic variations applied to the reduced cross section, σ_r , measured with ISR-tagged events from the HER dataset. The text in the figure (bottom) corresponds to table 6.1 and the open (closed) red (blue) circles correspond to a positive(negative) variation applied to the central value. Results are for $Q^2 = 24.0 \text{ GeV}^2$.

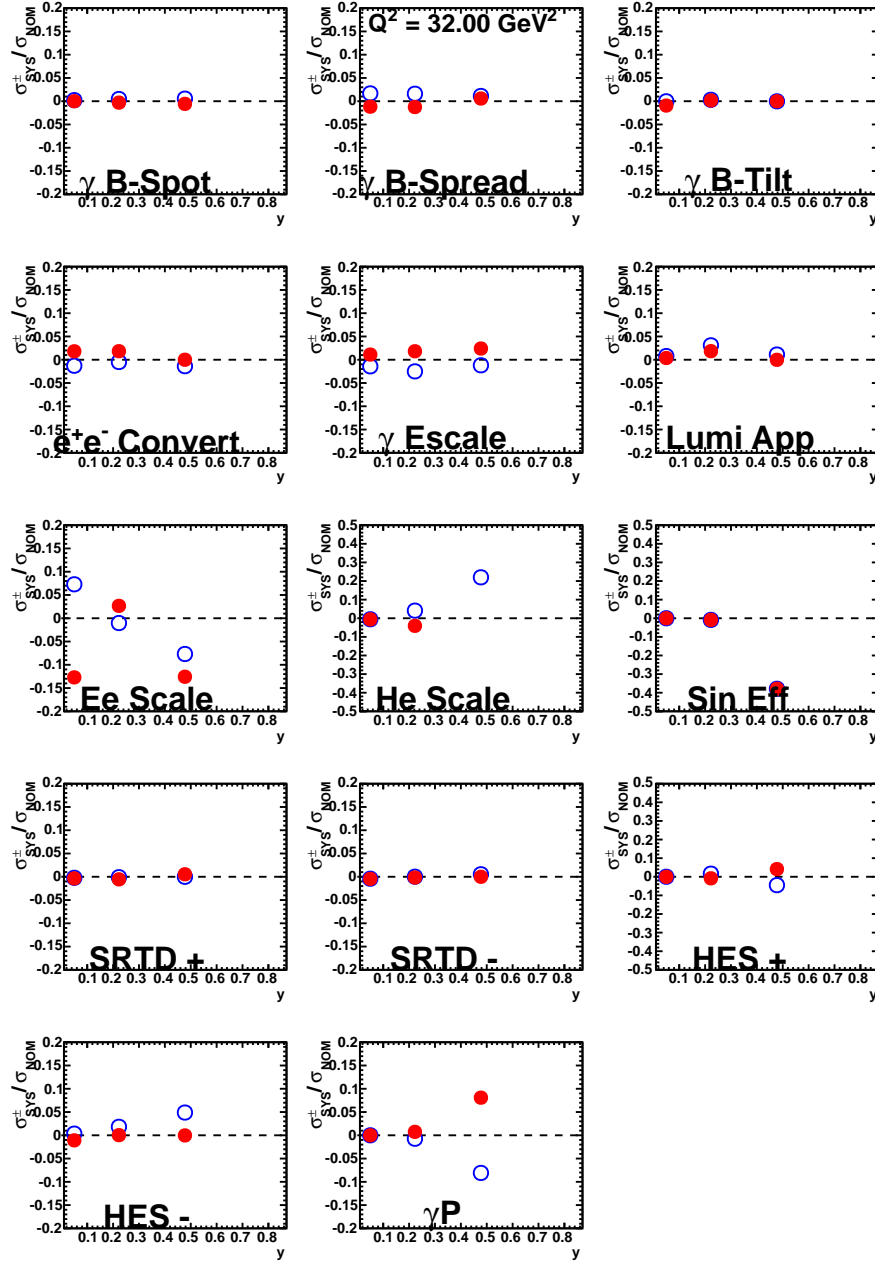


Figure B.4: A visual representation of the systematic variations applied to the reduced cross section, σ_r , measured with ISR-tagged events from the HER dataset. The text in the figure (bottom) corresponds to table 6.1 and the open (closed) red (blue) circles correspond to a positive(negative) variation applied to the central value. Results are for $Q^2 = 32.0 \text{ GeV}^2$.

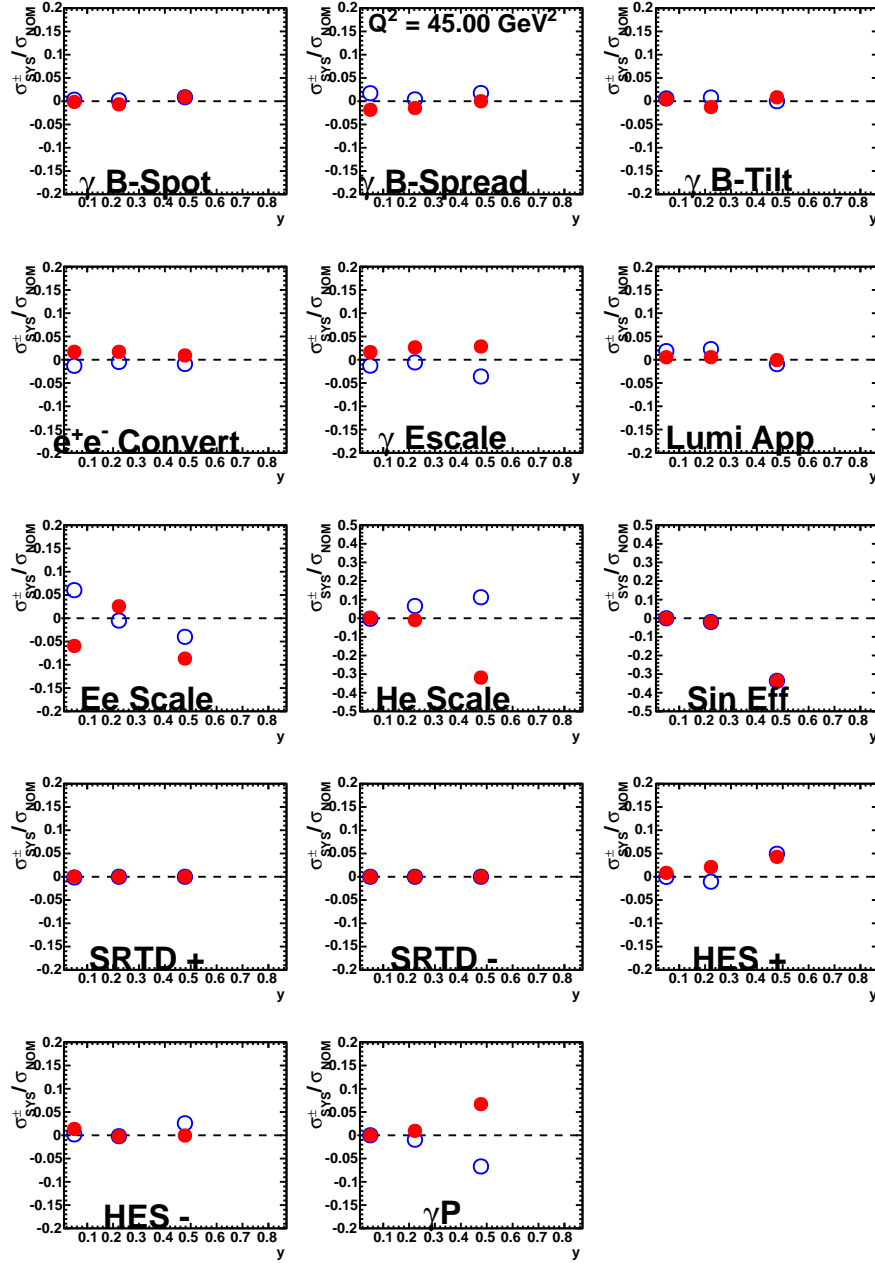


Figure B.5: A visual representation of the systematic variations applied to the reduced cross section, σ_r , measured with ISR-tagged events from the HER dataset. The text in the figure (bottom) corresponds to table 6.1 and the open (closed) red (blue) circles correspond to a positive(negative) variation applied to the central value. Results are for $Q^2 = 45.0 \text{ GeV}^2$.

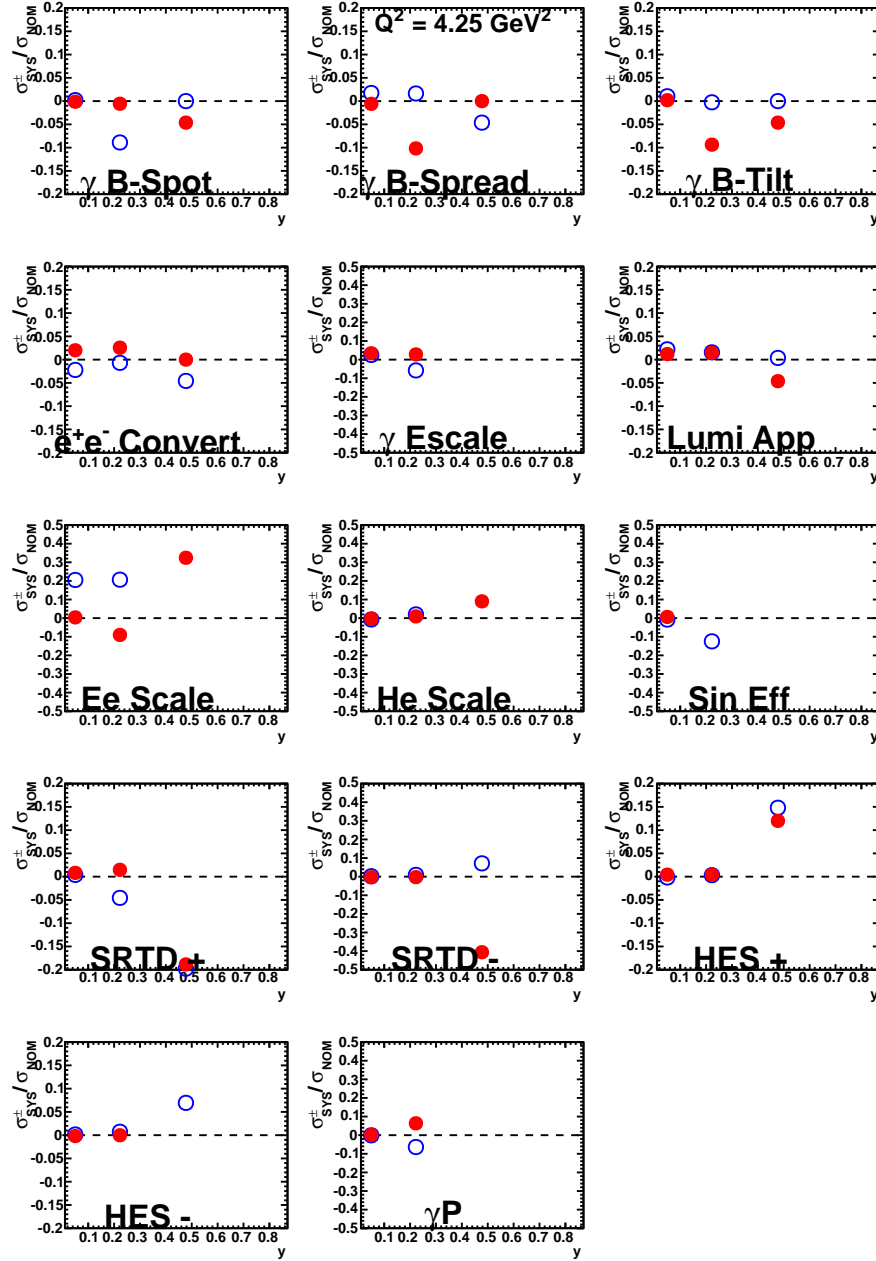


Figure B.6: A visual representation of the systematic variations applied to the reduced cross section, σ_r , measured with ISR-tagged events from the ISR dataset. The text in the figure (bottom) corresponds to table 6.1 and the open (closed) red (blue) circles correspond to a positive(negative) variation applied to the central value. Results are for $Q^2 = 4.25 \text{ GeV}^2$.

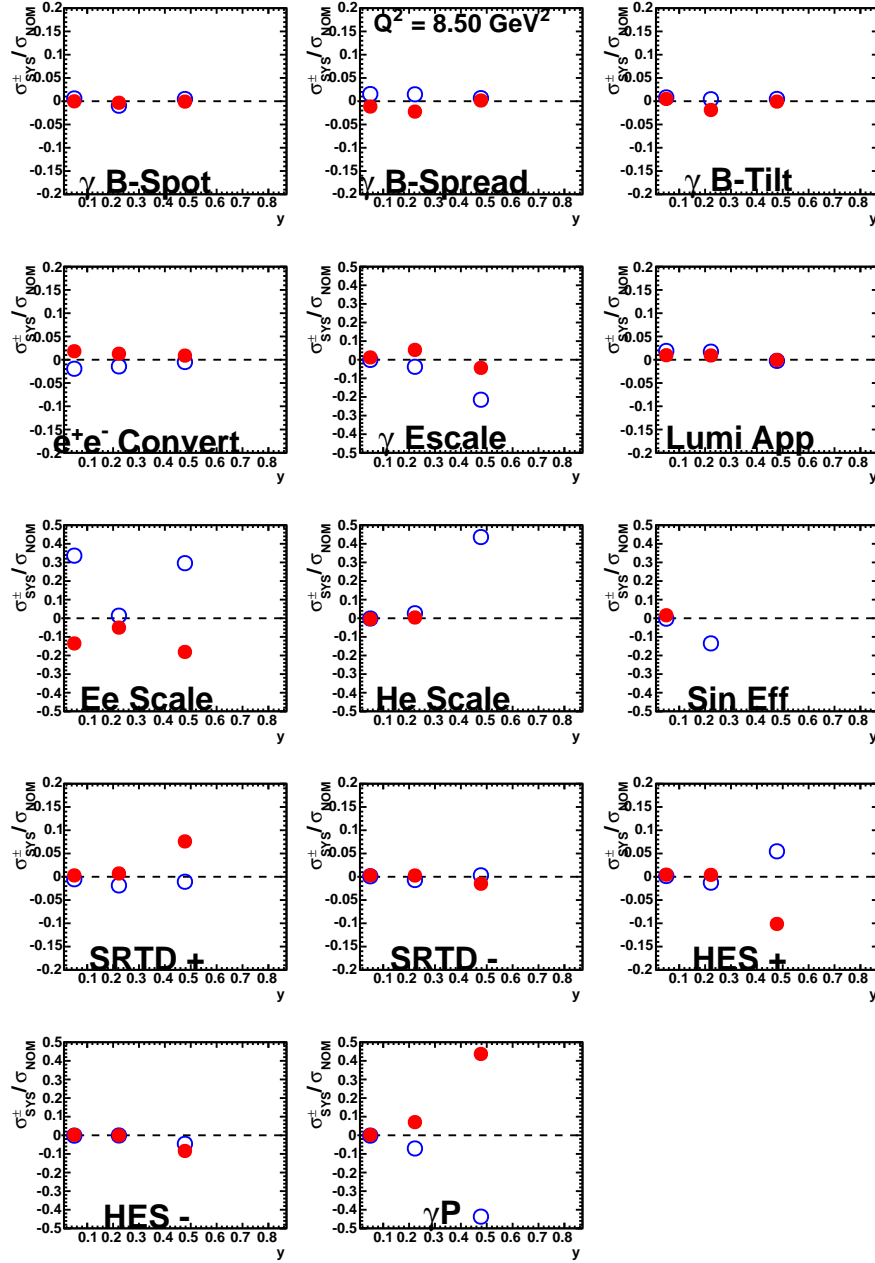


Figure B.7: A visual representation of the systematic variations applied to the reduced cross section, σ_r , measured with ISR-tagged events from the ISR dataset. The text in the figure (bottom) corresponds to table 6.1 and the open (closed) red (blue) circles correspond to a positive(negative) variation applied to the central value. Results are for $Q^2 = 8.5 \text{ GeV}^2$.

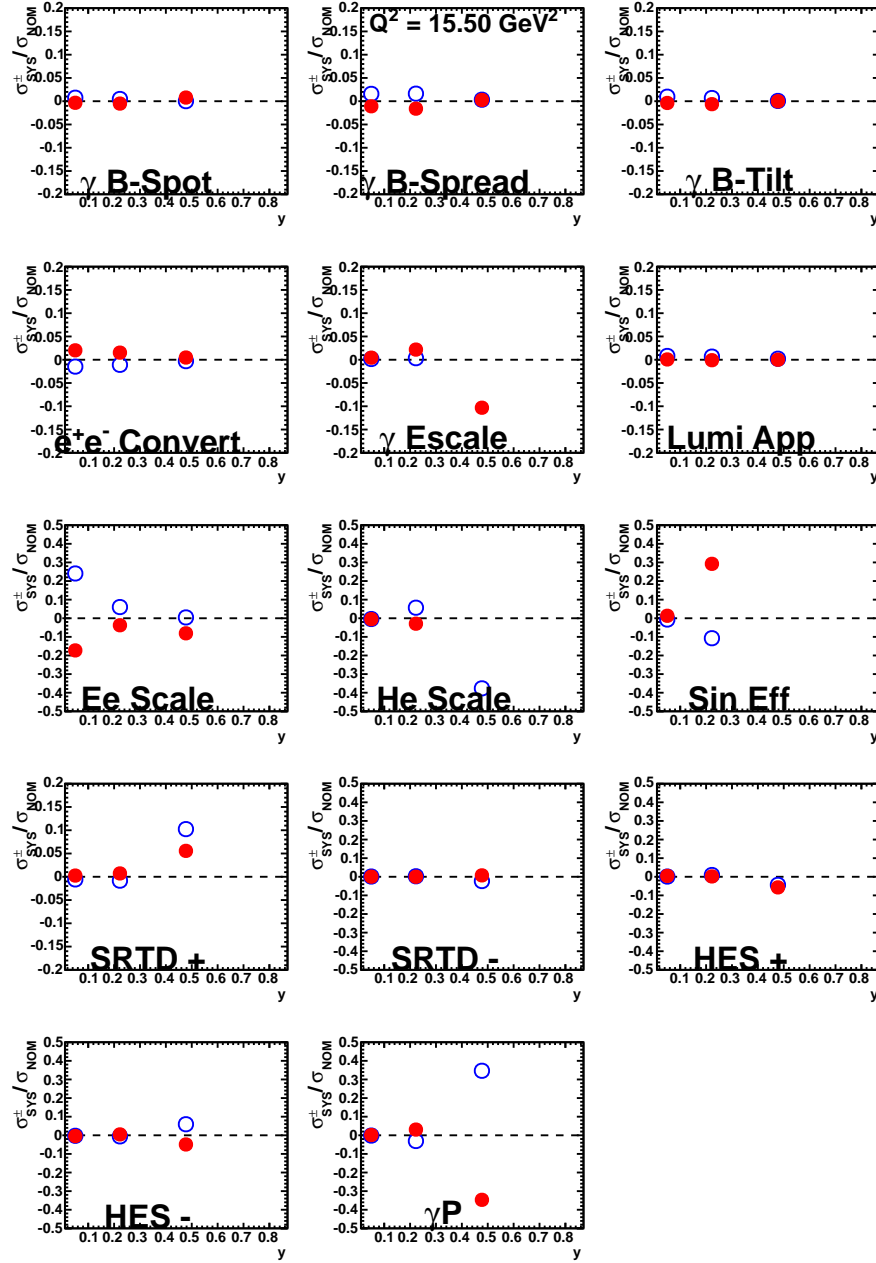


Figure B.8: A visual representation of the systematic variations applied to the reduced cross section, σ_r , measured with ISR-tagged events from the ISR dataset. The text in the figure (bottom) corresponds to table 6.1 and the open (closed) red (blue) circles correspond to a positive(negative) variation applied to the central value. Results are for $Q^2 = 15.5 \text{ GeV}^2$.

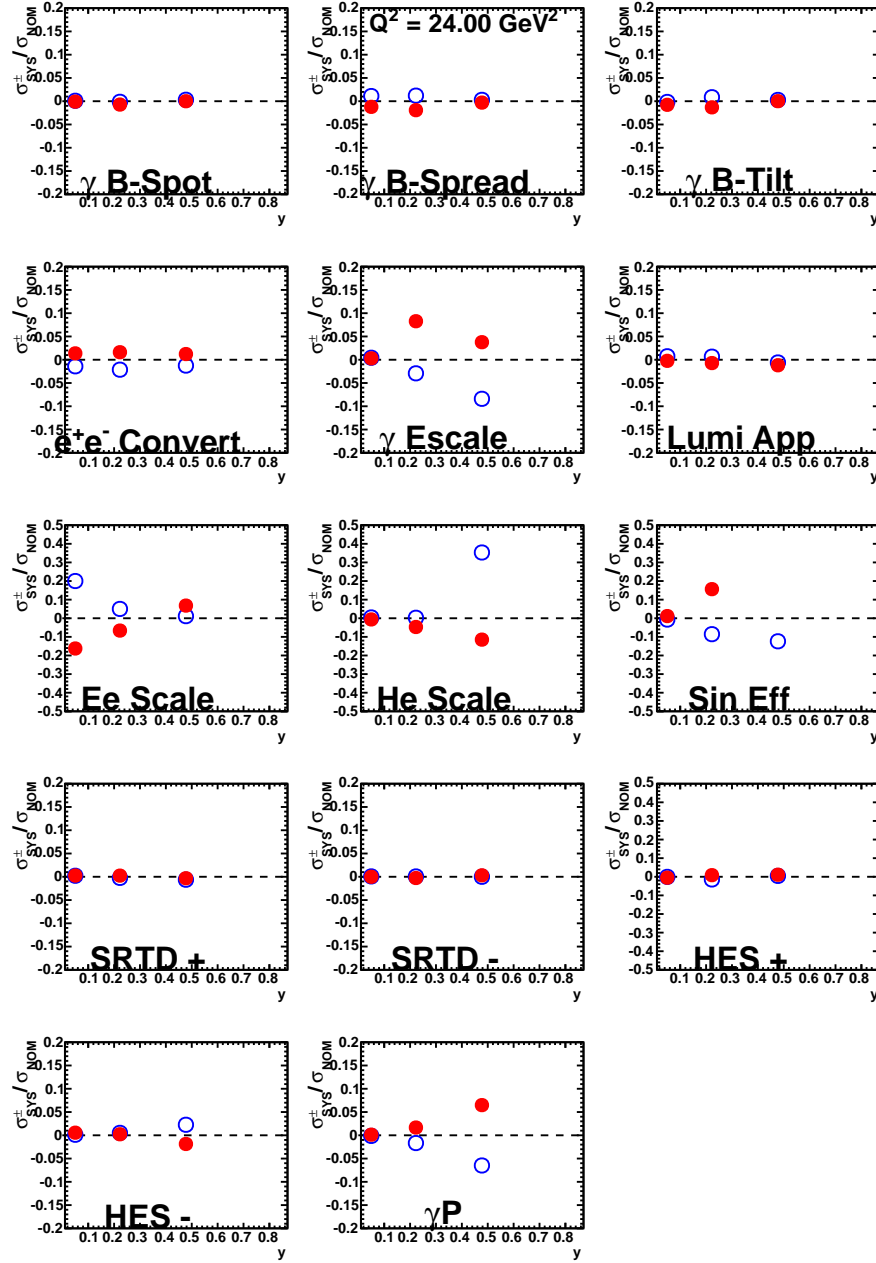


Figure B.9: A visual representation of the systematic variations applied to the reduced cross section, σ_r , measured with ISR-tagged events from the ISR dataset. The text in the figure (bottom) corresponds to table 6.1 and the open (closed) red (blue) circles correspond to a positive(negative) variation applied to the central value. Results are for $Q^2 = 24.0 \text{ GeV}^2$.

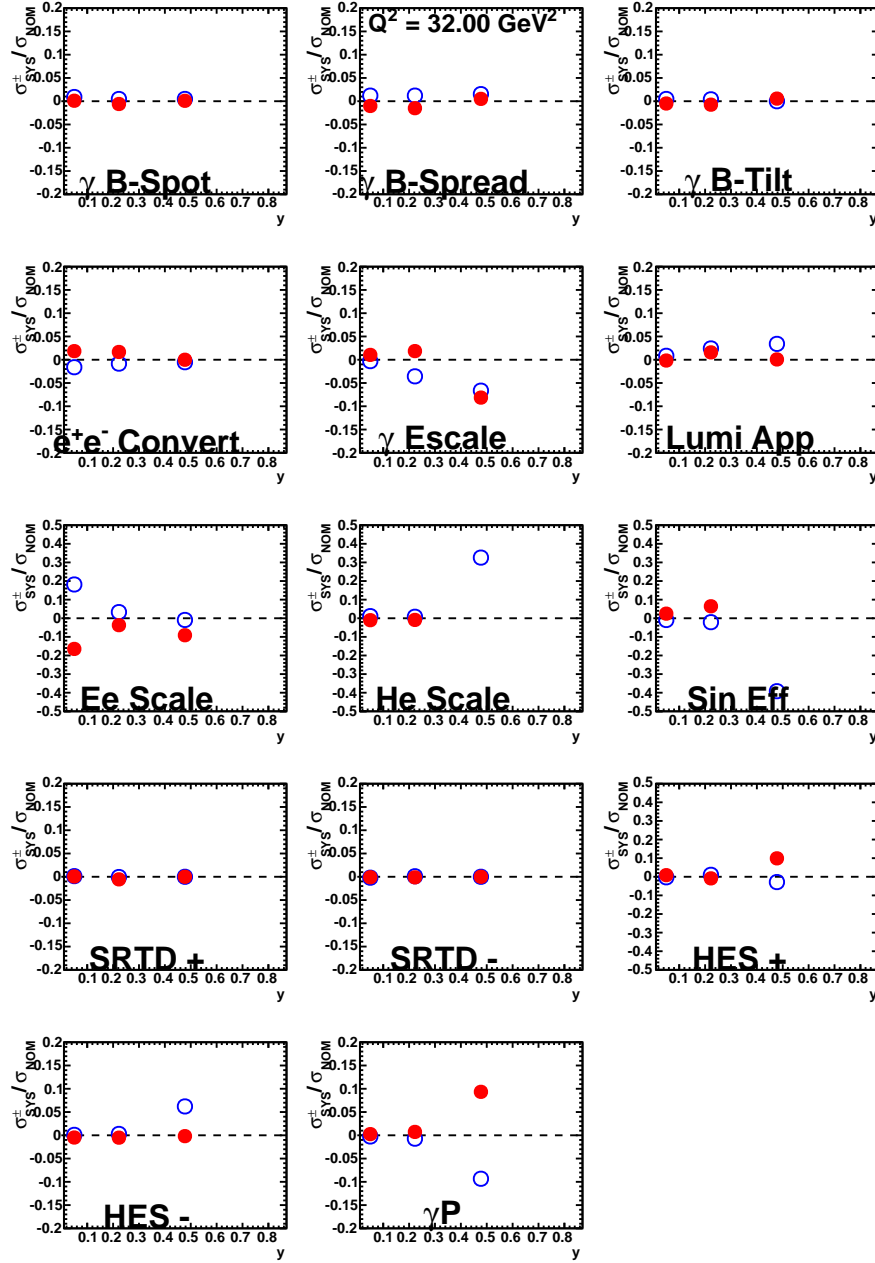


Figure B.10: A visual representation of the systematic variations applied to the reduced cross section, σ_r , measured with ISR-tagged events from the ISR dataset. The text in the figure (bottom) corresponds to table 6.1 and the open (closed) red (blue) circles correspond to a positive(negative) variation applied to the central value. Results are for $Q^2 = 32.0 \text{ GeV}^2$.

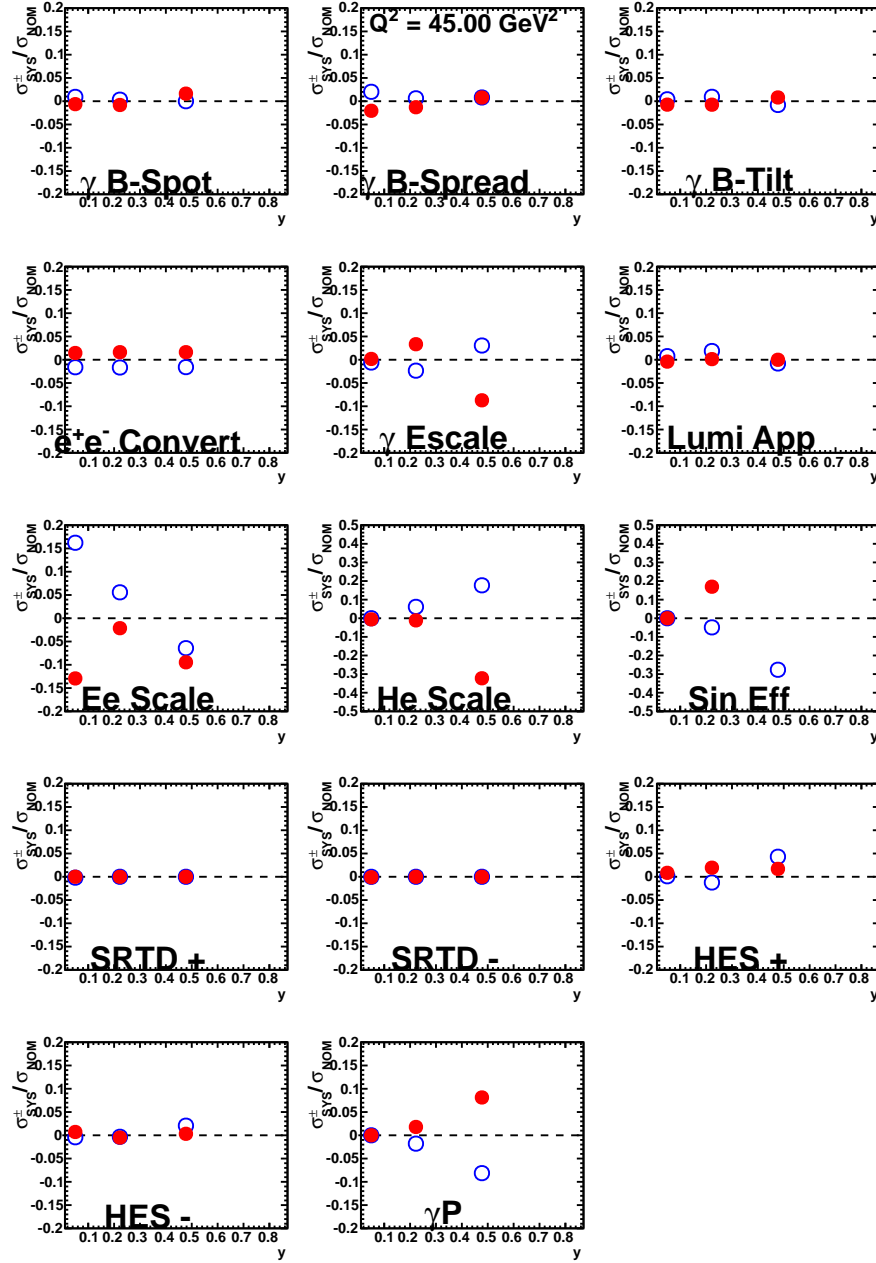


Figure B.11: A visual representation of the systematic variations applied to the reduced cross section, σ_r , measured with ISR-tagged events from the ISR dataset. The text in the figure (bottom) corresponds to table 6.1 and the open (closed) red (blue) circles correspond to a positive(negative) variation applied to the central value. Results are $Q^2 = 45.0 \text{ GeV}^2$.

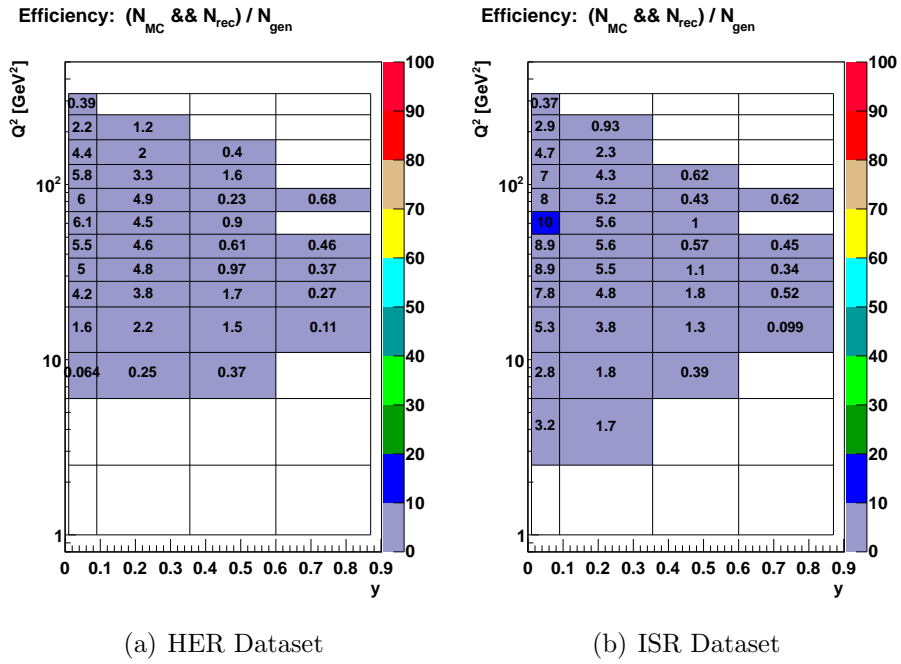


Figure B.13: The Efficiency of the bins determined from a Monte Carlo study. The bin values and the colour scale (right) is given in percent (%).

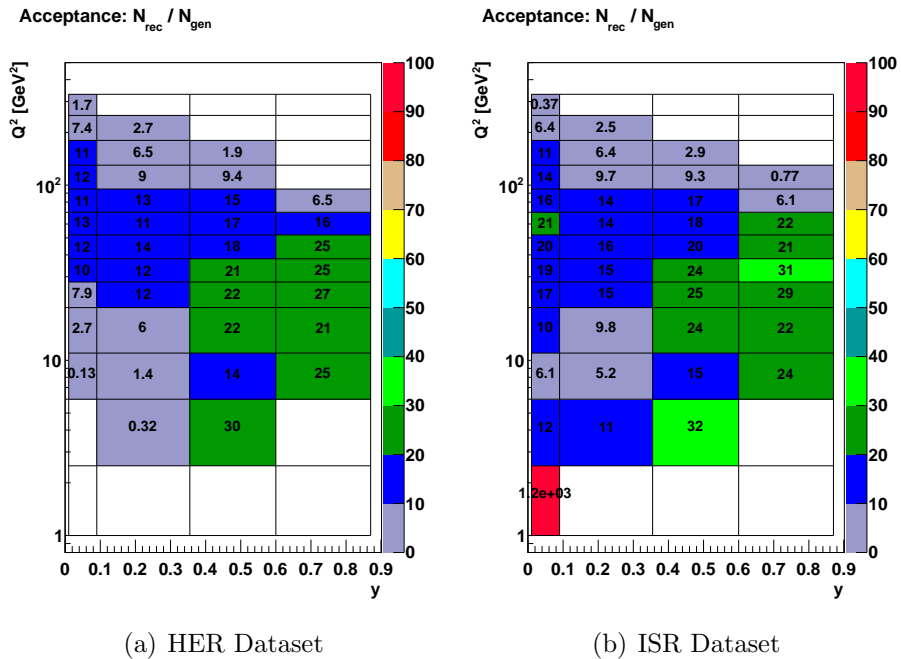


Figure B.14: The detector acceptance from a Monte Carlo study. The bin values and the colour scale (right) is given in percent (%).

APPENDIX C

F_L Measurement

C.1 F_L Measurement

The longitudinal structure function, F_L , was measured in chapter 8. This chapter presents the table of values for the combined nominal and satellite vertex reduced cross section measurements along with their corresponding F_L and F_2 measurements.

In section C.1.1 the purities, efficiencies and acceptances for the nominal and satellite vertex samples are displayed separately.

While the Rosenbluth plots used to fit each F_L and F_2 measurement in the combined cross sections are shown in section C.2.

Q^2 (GeV ²)	y	x	σ_r HER	δ_{stat} (%)
5	0.63	$7.83 \cdot 10^{-5}$	1.1935	10.40
5	0.69	$7.14 \cdot 10^{-5}$	1.2187	10.94
5	0.75	$6.57 \cdot 10^{-5}$	1.3649	9.76
5	0.80	$6.16 \cdot 10^{-5}$	1.3027	26.35
7	0.56	$1.23 \cdot 10^{-4}$	1.2948	7.83
7	0.63	$1.10 \cdot 10^{-4}$	1.3760	8.96
7	0.69	$1.00 \cdot 10^{-4}$	1.4982	7.01
7	0.75	$9.20 \cdot 10^{-5}$	1.3653	4.41
7	0.80	$8.63 \cdot 10^{-5}$	1.0480	15.69
9	0.31	$2.86 \cdot 10^{-4}$	1.2321	5.92
9	0.40	$2.22 \cdot 10^{-4}$	1.1765	6.60
9	0.48	$1.85 \cdot 10^{-4}$	1.2215	7.17
9	0.56	$1.58 \cdot 10^{-4}$	1.2955	6.13
9	0.63	$1.41 \cdot 10^{-4}$	1.3184	4.44
9	0.69	$1.29 \cdot 10^{-4}$	1.3240	3.01
9	0.75	$1.18 \cdot 10^{-4}$	1.3447	2.33
9	0.80	$1.11 \cdot 10^{-4}$	1.4995	6.67
12	0.13	$9.10 \cdot 10^{-4}$	0.9436	4.43
12	0.22	$5.38 \cdot 10^{-4}$	1.2238	4.43
12	0.31	$3.82 \cdot 10^{-4}$	1.1697	5.77
12	0.40	$2.96 \cdot 10^{-4}$	1.2558	5.24
12	0.48	$2.46 \cdot 10^{-4}$	1.3736	3.42
12	0.56	$2.11 \cdot 10^{-4}$	1.3493	2.40
12	0.63	$1.88 \cdot 10^{-4}$	1.4564	2.08
12	0.69	$1.71 \cdot 10^{-4}$	1.4344	1.91
12	0.75	$1.58 \cdot 10^{-4}$	1.5011	1.83
12	0.80	$1.48 \cdot 10^{-4}$	1.6261	5.22
17	0.03	$6.10 \cdot 10^{-3}$	0.4675	10.68
17	0.07	$2.48 \cdot 10^{-3}$	0.7541	6.44
17	0.13	$1.29 \cdot 10^{-3}$	1.0024	4.24
17	0.22	$7.62 \cdot 10^{-4}$	1.1560	3.82
17	0.31	$5.41 \cdot 10^{-4}$	1.2908	2.74
17	0.40	$4.19 \cdot 10^{-4}$	1.4117	2.00
17	0.48	$3.49 \cdot 10^{-4}$	1.4294	1.73
17	0.56	$2.99 \cdot 10^{-4}$	1.4339	1.57
17	0.63	$2.66 \cdot 10^{-4}$	1.4155	1.81
17	0.69	$2.43 \cdot 10^{-4}$	1.4267	1.91
17	0.75	$2.23 \cdot 10^{-4}$	1.4502	2.05
17	0.80	$2.10 \cdot 10^{-4}$	1.7178	5.10
24	0.03	$8.61 \cdot 10^{-3}$	0.5818	5.49
24	0.07	$3.51 \cdot 10^{-3}$	0.8253	3.00
24	0.13	$1.82 \cdot 10^{-3}$	1.0533	1.57
24	0.22	$1.08 \cdot 10^{-3}$	1.2387	1.32
24	0.31	$7.63 \cdot 10^{-4}$	1.2834	1.27
24	0.40	$5.92 \cdot 10^{-4}$	1.3937	1.23
24	0.48	$4.93 \cdot 10^{-4}$	1.4415	1.25
24	0.56	$4.23 \cdot 10^{-4}$	1.4455	1.34
24	0.63	$3.76 \cdot 10^{-4}$	1.4769	1.66
24	0.69	$3.43 \cdot 10^{-4}$	1.4872	1.82
24	0.75	$3.16 \cdot 10^{-4}$	1.5633	1.94
24	0.80	$2.96 \cdot 10^{-4}$	1.3672	5.67
32	0.03	$1.15 \cdot 10^{-2}$	0.5749	2.98
32	0.07	$4.67 \cdot 10^{-3}$	0.7966	1.69
32	0.13	$2.43 \cdot 10^{-3}$	1.0057	1.01
32	0.22	$1.43 \cdot 10^{-3}$	1.1957	1.01
32	0.31	$1.02 \cdot 10^{-3}$	1.3001	1.08
32	0.40	$7.89 \cdot 10^{-4}$	1.3883	1.20
32	0.48	$6.57 \cdot 10^{-4}$	1.4617	1.34
32	0.56	$5.63 \cdot 10^{-4}$	1.4575	1.53
32	0.63	$5.01 \cdot 10^{-4}$	1.4644	1.99
32	0.69	$4.57 \cdot 10^{-4}$	1.5391	2.10
32	0.75	$4.21 \cdot 10^{-4}$	1.5454	2.34
32	0.80	$3.94 \cdot 10^{-4}$	1.5170	5.59
45	0.03	$1.61 \cdot 10^{-2}$	0.6005	2.17
45	0.07	$6.57 \cdot 10^{-3}$	0.7929	1.34
45	0.13	$3.41 \cdot 10^{-3}$	0.9833	0.90
45	0.22	$2.02 \cdot 10^{-3}$	1.1407	1.00
45	0.31	$1.43 \cdot 10^{-3}$	1.2636	1.13
45	0.40	$1.11 \cdot 10^{-3}$	1.3733	1.31
45	0.48	$9.24 \cdot 10^{-4}$	1.3847	1.57
45	0.56	$7.92 \cdot 10^{-4}$	1.4730	1.70
45	0.63	$7.04 \cdot 10^{-4}$	1.5105	2.15
45	0.69	$6.43 \cdot 10^{-4}$	1.5647	2.34
45	0.75	$5.92 \cdot 10^{-4}$	1.5079	2.64
45	0.80	$5.55 \cdot 10^{-4}$	1.6674	4.75
60	0.03	$2.15 \cdot 10^{-2}$	0.5901	2.25
60	0.07	$8.76 \cdot 10^{-3}$	0.7462	1.50
60	0.13	$4.55 \cdot 10^{-3}$	0.9302	1.03
60	0.22	$2.69 \cdot 10^{-3}$	1.1143	1.15
60	0.31	$1.91 \cdot 10^{-3}$	1.2257	1.34
60	0.40	$1.48 \cdot 10^{-3}$	1.3297	1.56
60	0.48	$1.23 \cdot 10^{-3}$	1.3749	1.82
60	0.56	$1.06 \cdot 10^{-3}$	1.4896	1.95
60	0.63	$9.39 \cdot 10^{-4}$	1.5660	2.45
60	0.69	$8.57 \cdot 10^{-4}$	1.5427	2.75
60	0.75	$7.89 \cdot 10^{-4}$	1.5148	3.05
60	0.80	$7.39 \cdot 10^{-4}$	1.6326	4.81
80	0.03	$2.87 \cdot 10^{-2}$	0.5031	2.88
80	0.07	$1.17 \cdot 10^{-2}$	0.7017	1.75
80	0.13	$6.07 \cdot 10^{-3}$	0.8861	1.19
80	0.22	$3.59 \cdot 10^{-3}$	1.0597	1.32
80	0.31	$2.54 \cdot 10^{-3}$	1.1970	1.51
80	0.40	$1.97 \cdot 10^{-3}$	1.2823	1.80
80	0.48	$1.64 \cdot 10^{-3}$	1.3107	2.14
80	0.56	$1.41 \cdot 10^{-3}$	1.4276	2.28
80	0.63	$1.25 \cdot 10^{-3}$	1.5048	2.81
80	0.69	$1.14 \cdot 10^{-3}$	1.4189	3.29
80	0.75	$1.05 \cdot 10^{-3}$	1.3310	3.78
110	0.03	$3.94 \cdot 10^{-2}$	0.4904	3.17
110	0.07	$1.61 \cdot 10^{-2}$	0.6425	2.07
110	0.13	$8.34 \cdot 10^{-3}$	0.8384	1.37
110	0.22	$4.93 \cdot 10^{-3}$	1.0506	1.50
110	0.31	$3.50 \cdot 10^{-3}$	1.1380	1.79
110	0.40	$2.71 \cdot 10^{-3}$	1.2495	2.06
110	0.48	$2.26 \cdot 10^{-3}$	1.2923	2.45
110	0.56	$1.94 \cdot 10^{-3}$	1.4295	2.57
110	0.63	$1.72 \cdot 10^{-3}$	1.3967	3.36

Table C.1: The reduced cross section, σ_r , values for the HER dataset for the nominal and satellite vertex combined measurement. Also shown is the statistical error δ_{stat} . This table of values corresponds to figure 8.6

Q^2 (GeV ²)	y	x	σ_r MER	δ_{stat} (%)
5	0.69	$1.14 \cdot 10^{-4}$	1.3094	16.32
5	0.75	$1.05 \cdot 10^{-4}$	1.0277	22.03
5	0.80	$9.86 \cdot 10^{-5}$	-0.2708	351.69
7	0.56	$1.97 \cdot 10^{-4}$	1.4033	11.79
7	0.63	$1.75 \cdot 10^{-4}$	1.4673	13.70
7	0.69	$1.60 \cdot 10^{-4}$	1.2205	15.00
7	0.75	$1.47 \cdot 10^{-4}$	1.2822	10.16
7	0.80	$1.38 \cdot 10^{-4}$	-0.6182	53.17
9	0.40	$3.55 \cdot 10^{-4}$	1.1712	10.38
9	0.48	$2.96 \cdot 10^{-4}$	1.4390	10.09
9	0.56	$2.54 \cdot 10^{-4}$	1.2747	10.55
9	0.63	$2.25 \cdot 10^{-4}$	1.3936	8.69
9	0.69	$2.06 \cdot 10^{-4}$	1.2442	7.26
9	0.75	$1.89 \cdot 10^{-4}$	1.2282	6.22
9	0.80	$1.77 \cdot 10^{-4}$	1.2056	19.41
12	0.13	$1.46 \cdot 10^{-3}$	0.8491	7.42
12	0.22	$8.61 \cdot 10^{-4}$	0.8821	9.11
12	0.31	$6.11 \cdot 10^{-4}$	1.2297	8.67
12	0.40	$4.73 \cdot 10^{-4}$	1.1031	10.59
12	0.48	$3.94 \cdot 10^{-4}$	1.2213	7.77
12	0.56	$3.38 \cdot 10^{-4}$	1.3253	5.47
12	0.63	$3.00 \cdot 10^{-4}$	1.2143	5.71
12	0.69	$2.74 \cdot 10^{-4}$	1.2884	5.11
12	0.75	$2.52 \cdot 10^{-4}$	1.2623	5.30
12	0.80	$2.37 \cdot 10^{-4}$	1.3105	15.36
17	0.03	$9.75 \cdot 10^{-3}$	0.4529	16.66
17	0.07	$3.97 \cdot 10^{-3}$	0.5554	14.75
17	0.13	$2.06 \cdot 10^{-3}$	0.8549	8.09
17	0.22	$1.22 \cdot 10^{-3}$	1.1521	6.72
17	0.31	$8.65 \cdot 10^{-4}$	1.1778	6.07
17	0.40	$6.70 \cdot 10^{-4}$	1.1992	5.22
17	0.48	$5.59 \cdot 10^{-4}$	1.2413	4.56
17	0.56	$4.79 \cdot 10^{-4}$	1.3876	3.85
17	0.63	$4.26 \cdot 10^{-4}$	1.3142	4.60
17	0.69	$3.89 \cdot 10^{-4}$	1.3205	5.03
17	0.75	$3.58 \cdot 10^{-4}$	1.2289	5.93
17	0.80	$3.35 \cdot 10^{-4}$	1.1392	17.19
24	0.03	$1.38 \cdot 10^{-2}$	0.5701	10.27
24	0.07	$5.61 \cdot 10^{-3}$	0.6758	7.37
24	0.13	$2.91 \cdot 10^{-3}$	0.9227	3.82
24	0.22	$1.72 \cdot 10^{-3}$	1.1035	3.30
24	0.31	$1.22 \cdot 10^{-3}$	1.0947	3.45
24	0.40	$9.47 \cdot 10^{-4}$	1.2808	3.14
24	0.48	$7.89 \cdot 10^{-4}$	1.2644	3.37
24	0.56	$6.76 \cdot 10^{-4}$	1.3061	3.61
24	0.63	$6.01 \cdot 10^{-4}$	1.3449	4.40
24	0.69	$5.49 \cdot 10^{-4}$	1.3249	4.91
24	0.75	$5.05 \cdot 10^{-4}$	1.3987	5.18
24	0.80	$4.73 \cdot 10^{-4}$	1.2795	14.90
32	0.03	$1.84 \cdot 10^{-2}$	0.5115	7.53
32	0.07	$7.48 \cdot 10^{-3}$	0.7085	4.37
32	0.13	$3.88 \cdot 10^{-3}$	0.8875	2.72
32	0.22	$2.29 \cdot 10^{-3}$	1.0311	2.76
32	0.31	$1.63 \cdot 10^{-3}$	1.1774	2.85
32	0.40	$1.26 \cdot 10^{-3}$	1.2733	3.18
32	0.48	$1.05 \cdot 10^{-3}$	1.2806	3.62
32	0.56	$9.01 \cdot 10^{-4}$	1.3065	4.09
32	0.63	$8.01 \cdot 10^{-4}$	1.4003	4.97
32	0.69	$7.32 \cdot 10^{-4}$	1.2906	6.02
32	0.75	$6.73 \cdot 10^{-4}$	1.2813	6.78
32	0.80	$6.31 \cdot 10^{-4}$	1.4418	14.02
45	0.03	$2.58 \cdot 10^{-2}$	0.5522	5.69
45	0.07	$1.05 \cdot 10^{-2}$	0.7017	3.64
45	0.13	$5.46 \cdot 10^{-3}$	0.8787	2.38
45	0.22	$3.23 \cdot 10^{-3}$	1.0169	2.65
45	0.31	$2.29 \cdot 10^{-3}$	1.1298	3.01
45	0.40	$1.77 \cdot 10^{-3}$	1.1846	3.64
45	0.48	$1.48 \cdot 10^{-3}$	1.2688	4.11
45	0.56	$1.27 \cdot 10^{-3}$	1.3188	4.45
45	0.63	$1.13 \cdot 10^{-3}$	1.2735	6.02
45	0.69	$1.03 \cdot 10^{-3}$	1.4614	5.85
45	0.75	$9.47 \cdot 10^{-4}$	1.3030	7.19
45	0.80	$8.87 \cdot 10^{-4}$	1.5727	12.66
60	0.03	$3.44 \cdot 10^{-2}$	0.4993	6.51
60	0.07	$1.40 \cdot 10^{-2}$	0.6403	4.27
60	0.13	$7.28 \cdot 10^{-3}$	0.8019	2.85
60	0.22	$4.30 \cdot 10^{-3}$	0.9543	3.18
60	0.31	$3.05 \cdot 10^{-3}$	1.1221	3.46
60	0.40	$2.37 \cdot 10^{-3}$	1.1773	4.20
60	0.48	$1.97 \cdot 10^{-3}$	1.1716	5.18
60	0.56	$1.69 \cdot 10^{-3}$	1.2637	5.47
60	0.63	$1.50 \cdot 10^{-3}$	1.3965	6.48
60	0.69	$1.37 \cdot 10^{-3}$	1.3300	7.56
60	0.75	$1.26 \cdot 10^{-3}$	1.4232	7.91
60	0.80	$1.18 \cdot 10^{-3}$	1.7009	11.26
80	0.03	$4.59 \cdot 10^{-2}$	0.4880	7.11
80	0.07	$1.87 \cdot 10^{-2}$	0.5739	5.19
80	0.13	$9.71 \cdot 10^{-3}$	0.7407	3.39
80	0.22	$5.74 \cdot 10^{-3}$	0.9688	3.43
80	0.31	$4.07 \cdot 10^{-3}$	1.0465	4.16
80	0.40	$3.16 \cdot 10^{-3}$	1.1530	4.86
80	0.48	$2.63 \cdot 10^{-3}$	1.2166	5.56
80	0.56	$2.25 \cdot 10^{-3}$	1.2639	6.15
80	0.63	$2.00 \cdot 10^{-3}$	1.1779	8.56
80	0.69	$1.83 \cdot 10^{-3}$	1.3373	8.23
80	0.75	$1.68 \cdot 10^{-3}$	1.5368	7.76
110	0.03	$6.31 \cdot 10^{-2}$	0.4329	8.76
110	0.07	$2.57 \cdot 10^{-2}$	0.5454	5.92
110	0.13	$1.33 \cdot 10^{-2}$	0.7251	3.84
110	0.22	$7.89 \cdot 10^{-3}$	0.8649	4.31
110	0.31	$5.60 \cdot 10^{-3}$	0.9699	4.89
110	0.40	$4.34 \cdot 10^{-3}$	1.0337	5.87
110	0.48	$3.62 \cdot 10^{-3}$	1.1368	6.67
110	0.56	$3.10 \cdot 10^{-3}$	1.1653	7.23
110	0.63	$2.75 \cdot 10^{-3}$	1.0338	10.83

Table C.2: The reduced cross section, σ_r , values for the MER dataset for the nominal and satellite vertex combined measurement. Also shown is the statistical error δ_{stat} . This table of values corresponds to figure 8.6

Q^2 (GeV ²)	y	x	σ_r LER	δ_{stat} (%)
5	0.69	$1.43 \cdot 10^{-4}$	1.0799	13.14
5	0.75	$1.31 \cdot 10^{-4}$	1.0704	15.18
5	0.80	$1.23 \cdot 10^{-4}$	-1.0998	47.74
7	0.56	$2.46 \cdot 10^{-4}$	1.1384	9.58
7	0.63	$2.19 \cdot 10^{-4}$	0.9956	13.93
7	0.69	$2.00 \cdot 10^{-4}$	1.0642	12.21
7	0.75	$1.84 \cdot 10^{-4}$	1.2805	7.47
7	0.80	$1.73 \cdot 10^{-4}$	0.8291	33.08
9	0.40	$4.44 \cdot 10^{-4}$	1.0413	7.65
9	0.48	$3.70 \cdot 10^{-4}$	1.0555	9.03
9	0.56	$3.17 \cdot 10^{-4}$	1.1603	8.31
9	0.63	$2.82 \cdot 10^{-4}$	1.1584	7.45
9	0.69	$2.57 \cdot 10^{-4}$	1.2901	5.07
9	0.75	$2.37 \cdot 10^{-4}$	1.2073	4.56
9	0.80	$2.22 \cdot 10^{-4}$	1.3712	13.07
12	0.13	$1.82 \cdot 10^{-3}$	0.7452	5.65
12	0.22	$1.08 \cdot 10^{-3}$	1.0031	5.57
12	0.31	$7.63 \cdot 10^{-4}$	1.0359	7.06
12	0.40	$5.92 \cdot 10^{-4}$	1.1502	6.79
12	0.48	$4.93 \cdot 10^{-4}$	1.1819	5.68
12	0.56	$4.23 \cdot 10^{-4}$	1.2508	4.10
12	0.63	$3.76 \cdot 10^{-4}$	1.1722	4.33
12	0.69	$3.43 \cdot 10^{-4}$	1.1817	4.01
12	0.75	$3.16 \cdot 10^{-4}$	1.2210	3.89
12	0.80	$2.96 \cdot 10^{-4}$	1.4448	10.44
17	0.03	$1.22 \cdot 10^{-2}$	0.4424	11.15
17	0.07	$4.97 \cdot 10^{-3}$	0.5845	8.72
17	0.13	$2.58 \cdot 10^{-3}$	0.8418	5.50
17	0.22	$1.52 \cdot 10^{-3}$	0.9873	5.46
17	0.31	$1.08 \cdot 10^{-3}$	1.1360	4.39
17	0.40	$8.38 \cdot 10^{-4}$	1.2280	3.66
17	0.48	$6.98 \cdot 10^{-4}$	1.1909	3.43
17	0.56	$5.99 \cdot 10^{-4}$	1.2819	2.98
17	0.63	$5.32 \cdot 10^{-4}$	1.2638	3.53
17	0.69	$4.86 \cdot 10^{-4}$	1.1985	3.88
17	0.75	$4.47 \cdot 10^{-4}$	1.1431	4.48
17	0.80	$4.19 \cdot 10^{-4}$	1.1442	12.86
24	0.03	$1.72 \cdot 10^{-2}$	0.4720	8.70
24	0.07	$7.01 \cdot 10^{-3}$	0.6677	5.22
24	0.13	$3.64 \cdot 10^{-3}$	0.8377	3.01
24	0.22	$2.15 \cdot 10^{-3}$	1.0188	2.58
24	0.31	$1.53 \cdot 10^{-3}$	1.0867	2.50
24	0.40	$1.18 \cdot 10^{-3}$	1.1487	2.53
24	0.48	$9.86 \cdot 10^{-4}$	1.2089	2.58
24	0.56	$8.45 \cdot 10^{-4}$	1.2648	2.62
24	0.63	$7.51 \cdot 10^{-4}$	1.2517	3.36
24	0.69	$6.86 \cdot 10^{-4}$	1.2804	3.67
24	0.75	$6.31 \cdot 10^{-4}$	1.3556	3.89
24	0.80	$5.92 \cdot 10^{-4}$	1.3789	9.63

Q^2 (GeV ²)	y	x	σ_r LER	δ_{stat} (%)
32	0.03	$2.29 \cdot 10^{-2}$	0.4644	6.02
32	0.07	$9.35 \cdot 10^{-3}$	0.6537	3.43
32	0.13	$4.85 \cdot 10^{-3}$	0.8247	2.09
32	0.22	$2.87 \cdot 10^{-3}$	0.9835	2.07
32	0.31	$2.04 \cdot 10^{-3}$	1.0805	2.22
32	0.40	$1.58 \cdot 10^{-3}$	1.1746	2.42
32	0.48	$1.31 \cdot 10^{-3}$	1.2218	2.72
32	0.56	$1.13 \cdot 10^{-3}$	1.2358	3.05
32	0.63	$1.00 \cdot 10^{-3}$	1.2335	3.99
32	0.69	$9.15 \cdot 10^{-4}$	1.3509	4.00
32	0.75	$8.41 \cdot 10^{-4}$	1.3054	4.75
32	0.80	$7.89 \cdot 10^{-4}$	1.3646	10.85
45	0.03	$3.23 \cdot 10^{-2}$	0.4966	4.58
45	0.07	$1.31 \cdot 10^{-2}$	0.6347	2.91
45	0.13	$6.83 \cdot 10^{-3}$	0.8002	1.88
45	0.22	$4.03 \cdot 10^{-3}$	0.9515	2.04
45	0.31	$2.86 \cdot 10^{-3}$	1.0815	2.23
45	0.40	$2.22 \cdot 10^{-3}$	1.1171	2.73
45	0.48	$1.85 \cdot 10^{-3}$	1.1511	3.22
45	0.56	$1.58 \cdot 10^{-3}$	1.2613	3.36
45	0.63	$1.41 \cdot 10^{-3}$	1.2997	4.25
45	0.69	$1.29 \cdot 10^{-3}$	1.2667	4.84
45	0.75	$1.18 \cdot 10^{-3}$	1.2508	5.42
45	0.80	$1.11 \cdot 10^{-3}$	1.3618	9.73
60	0.03	$4.30 \cdot 10^{-2}$	0.5099	4.59
60	0.07	$1.75 \cdot 10^{-2}$	0.6306	3.05
60	0.13	$9.10 \cdot 10^{-3}$	0.7440	2.22
60	0.22	$5.38 \cdot 10^{-3}$	0.8907	2.44
60	0.31	$3.82 \cdot 10^{-3}$	1.0035	2.78
60	0.40	$2.96 \cdot 10^{-3}$	1.1042	3.18
60	0.48	$2.46 \cdot 10^{-3}$	1.1624	3.64
60	0.56	$2.11 \cdot 10^{-3}$	1.1931	4.16
60	0.63	$1.88 \cdot 10^{-3}$	1.2589	5.12
60	0.69	$1.71 \cdot 10^{-3}$	1.2883	5.52
60	0.75	$1.58 \cdot 10^{-3}$	1.2597	6.26
60	0.80	$1.48 \cdot 10^{-3}$	-0.5790	20.50
80	0.03	$5.74 \cdot 10^{-2}$	0.4135	6.18
80	0.07	$2.34 \cdot 10^{-2}$	0.5615	3.79
80	0.13	$1.21 \cdot 10^{-2}$	0.7091	2.52
80	0.22	$7.17 \cdot 10^{-3}$	0.9025	2.60
80	0.31	$5.09 \cdot 10^{-3}$	0.9645	3.17
80	0.40	$3.94 \cdot 10^{-3}$	1.0431	3.73
80	0.48	$3.29 \cdot 10^{-3}$	1.1226	4.26
80	0.56	$2.82 \cdot 10^{-3}$	1.0930	5.03
80	0.63	$2.50 \cdot 10^{-3}$	1.1748	6.09
80	0.69	$2.29 \cdot 10^{-3}$	1.0259	7.64
80	0.75	$2.10 \cdot 10^{-3}$	1.3023	6.54
110	0.03	$7.89 \cdot 10^{-2}$	0.4225	6.52
110	0.07	$3.21 \cdot 10^{-2}$	0.5298	4.38
110	0.13	$1.67 \cdot 10^{-2}$	0.6523	2.97
110	0.22	$9.86 \cdot 10^{-3}$	0.8146	3.22
110	0.31	$7.00 \cdot 10^{-3}$	0.9016	3.82
110	0.40	$5.42 \cdot 10^{-3}$	1.0068	4.34
110	0.48	$4.52 \cdot 10^{-3}$	1.1080	4.73
110	0.56	$3.87 \cdot 10^{-3}$	1.0524	5.84
110	0.63	$3.44 \cdot 10^{-3}$	1.1435	6.84

Table C.3: The reduced cross section, σ_r , values for the LER dataset for the nominal and satellite vertex combined measurement. Also shown is the statistical error δ_{stat} . This table of values corresponds to figure 8.6

Q^2 GeV	x	F_L	F_2
9	$2.51 \cdot 10^{-4}$	-0.05 ± 0.24	1.198 ± 0.096
9	$3.07 \cdot 10^{-4}$	0.72 ± 0.50	1.420 ± 0.107
9	$4.05 \cdot 10^{-4}$	1.43 ± 0.88	1.251 ± 0.099
12	$3.34 \cdot 10^{-4}$	0.18 ± 0.20	1.284 ± 0.082
12	$4.09 \cdot 10^{-4}$	-0.46 ± 0.37	1.086 ± 0.092
12	$5.40 \cdot 10^{-4}$	0.54 ± 0.66	1.247 ± 0.072
17	$4.74 \cdot 10^{-4}$	0.54 ± 0.13	1.449 ± 0.042
17	$5.80 \cdot 10^{-4}$	-0.30 ± 0.24	1.191 ± 0.054
17	$7.65 \cdot 10^{-4}$	-0.47 ± 0.47	1.134 ± 0.056
24	$6.69 \cdot 10^{-4}$	0.13 ± 0.10	1.370 ± 0.024
24	$8.19 \cdot 10^{-4}$	0.05 ± 0.15	1.268 ± 0.025
24	$1.08 \cdot 10^{-3}$	0.54 ± 0.24	1.260 ± 0.022
32	$8.92 \cdot 10^{-4}$	0.09 ± 0.11	1.358 ± 0.023
32	$1.09 \cdot 10^{-3}$	0.16 ± 0.15	1.287 ± 0.022
32	$1.44 \cdot 10^{-3}$	-0.04 ± 0.21	1.199 ± 0.017
45	$1.25 \cdot 10^{-3}$	0.09 ± 0.12	1.313 ± 0.024
45	$1.54 \cdot 10^{-3}$	-0.06 ± 0.17	1.241 ± 0.022
45	$2.02 \cdot 10^{-3}$	-0.09 ± 0.22	1.140 ± 0.016
60	$1.67 \cdot 10^{-3}$	-0.05 ± 0.13	1.270 ± 0.028
60	$2.05 \cdot 10^{-3}$	0.04 ± 0.19	1.206 ± 0.026
60	$2.70 \cdot 10^{-3}$	-0.19 ± 0.26	1.116 ± 0.019
80	$2.23 \cdot 10^{-3}$	0.17 ± 0.15	1.258 ± 0.031
80	$2.73 \cdot 10^{-3}$	0.26 ± 0.21	1.198 ± 0.028
80	$3.60 \cdot 10^{-3}$	-0.21 ± 0.28	1.059 ± 0.020
110	$3.07 \cdot 10^{-3}$	0.19 ± 0.18	1.202 ± 0.036
110	$3.75 \cdot 10^{-3}$	0.10 ± 0.24	1.117 ± 0.032
110	$4.95 \cdot 10^{-3}$	-0.07 ± 0.32	1.038 ± 0.023

Table C.4: The measured values of F_L and F_2 for the combined nominal and satellite vertex analysis. The quoted errors are statistical. Values correspond to figure 8.10.

C.1.1 Purities, Efficiencies and Acceptances

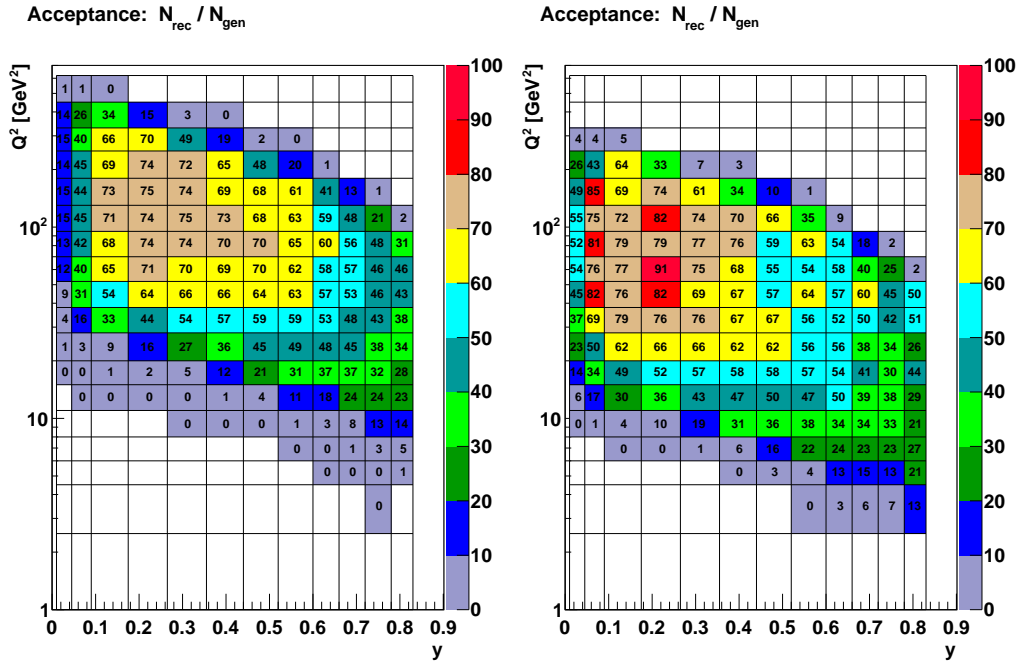


Figure C.1: The acceptance for the nominal (left) and satellite (right) Z -vertex samples from a Monte Carlo study for the HER dataset.

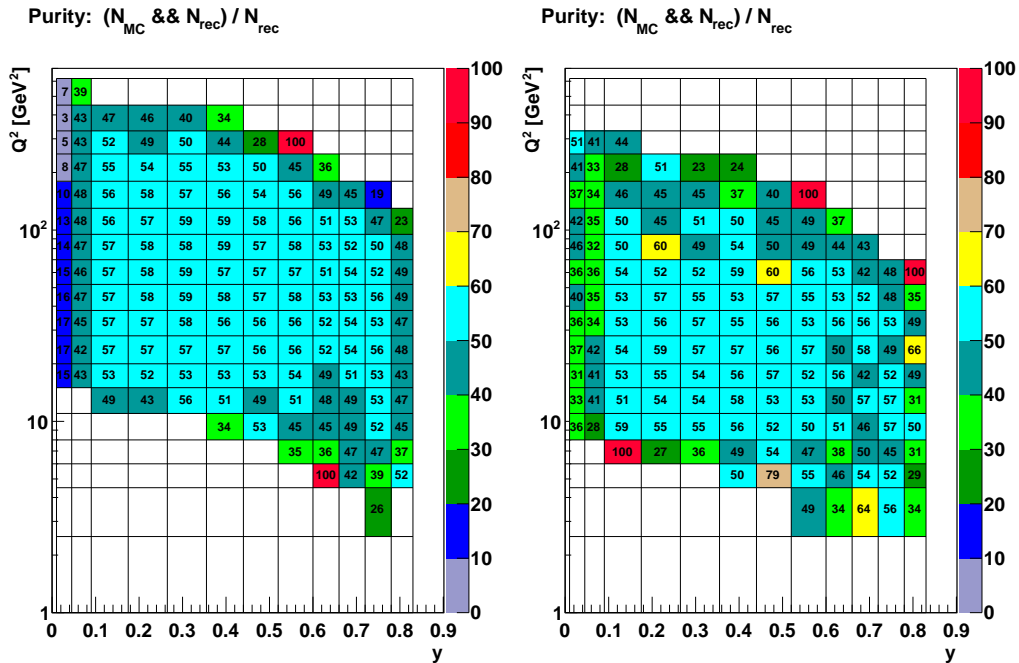


Figure C.2: The purity for the nominal (left) and satellite (right) Z -vertex samples from a Monte Carlo study for the HER dataset.

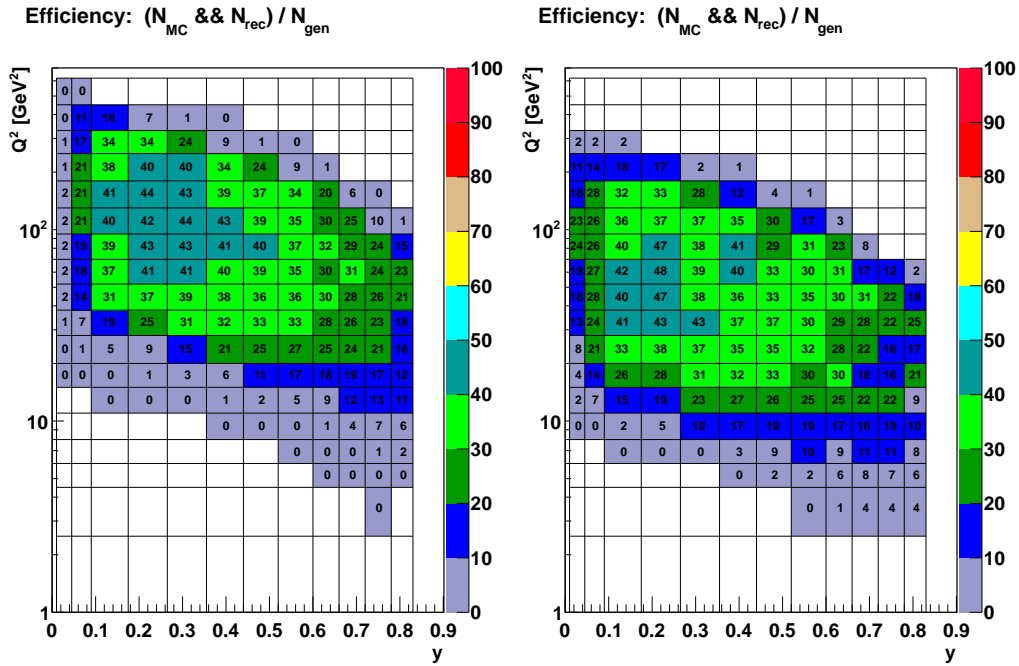


Figure C.3: The efficiency for the nominal (left) and satellite (right) Z -vertex samples from a Monte Carlo study for the HER dataset.

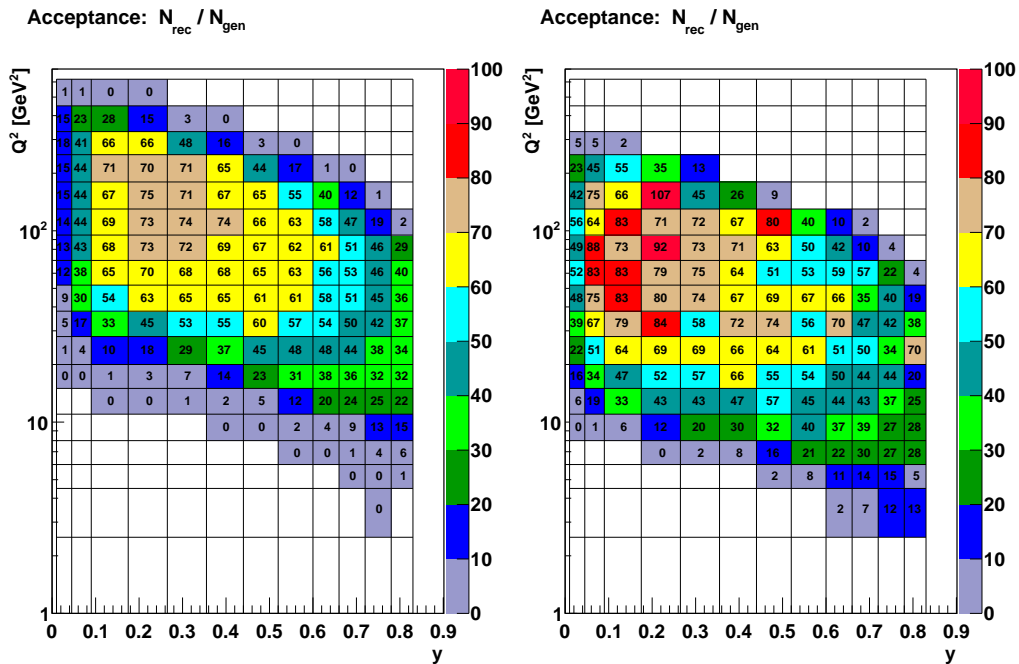


Figure C.4: The acceptance for the nominal (left) and satellite (right) Z -vertex samples from a Monte Carlo study for the MER dataset.

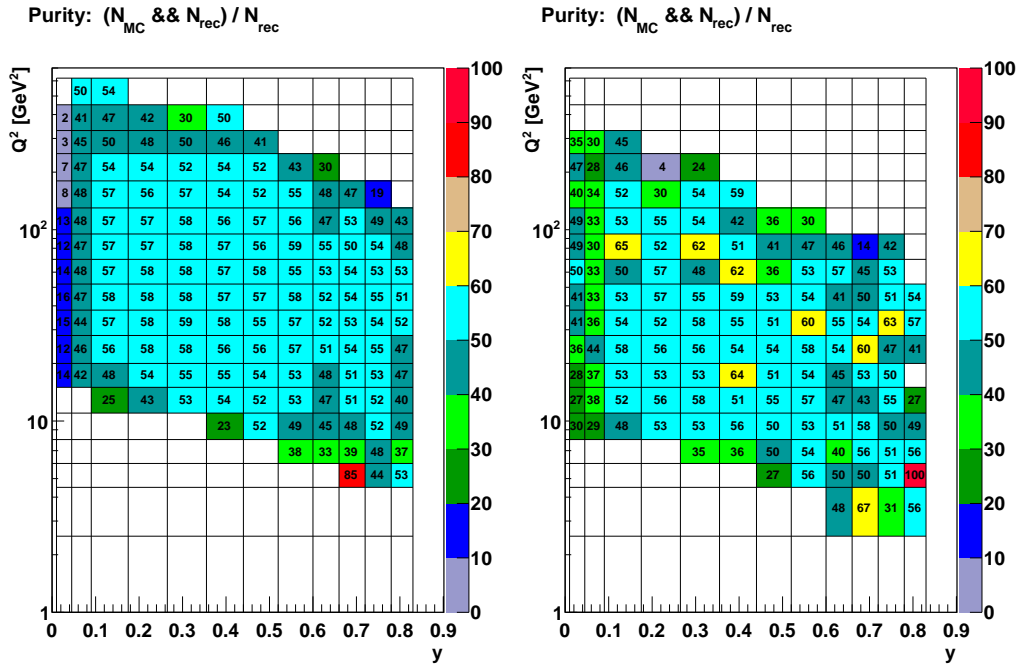


Figure C.5: The purity for the nominal (left) and satellite (right) Z -vertex samples from a Monte Carlo study for the MER dataset.

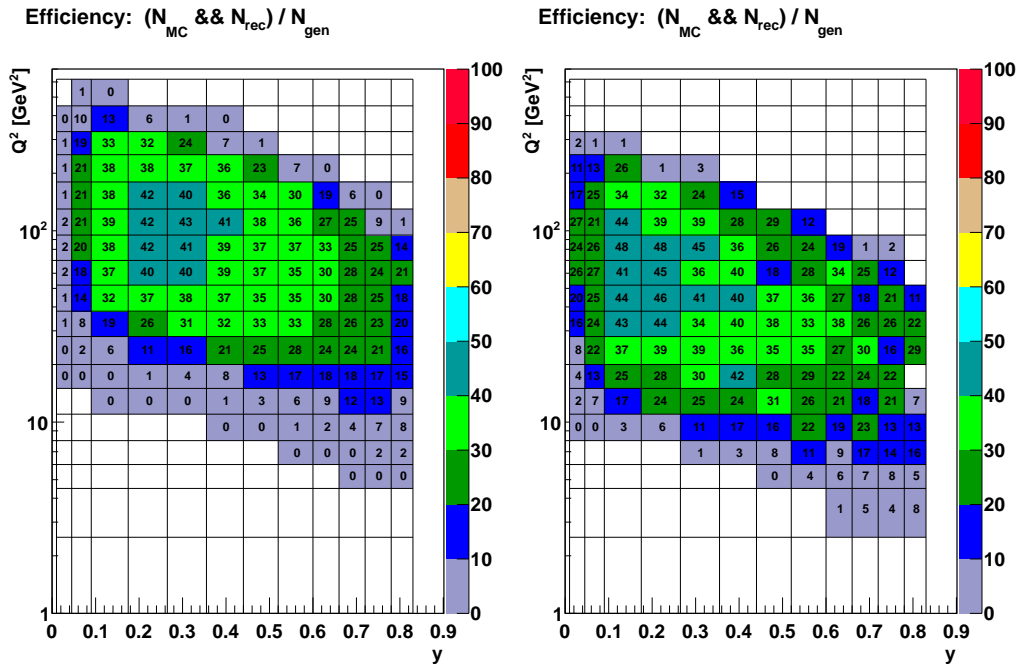


Figure C.6: The efficiency for the nominal (left) and satellite (right) Z -vertex samples from a Monte Carlo study for the MER dataset.

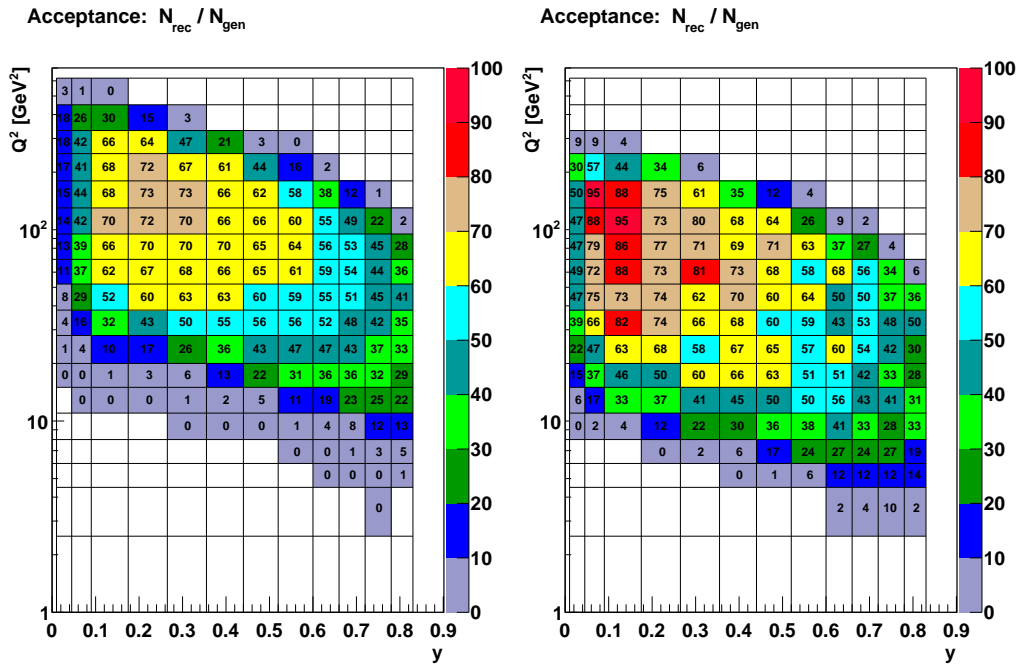


Figure C.7: The acceptance for the nominal (left) and satellite (right) Z -vertex samples from a Monte Carlo study for the LER dataset.

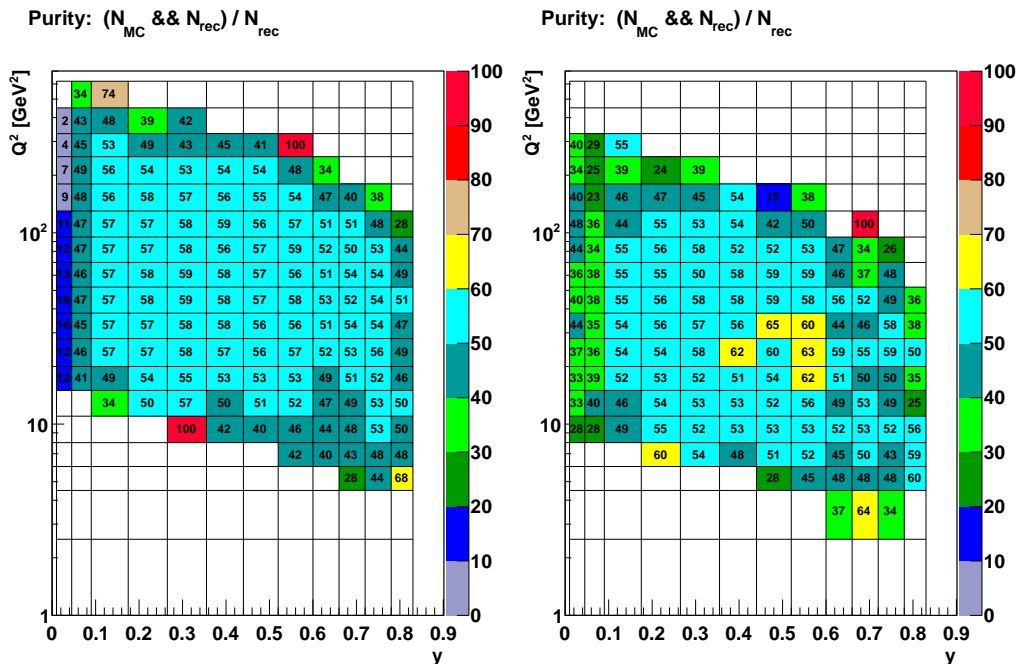


Figure C.8: The purity for the nominal (left) and satellite (right) Z -vertex samples from a Monte Carlo study for the LER dataset.

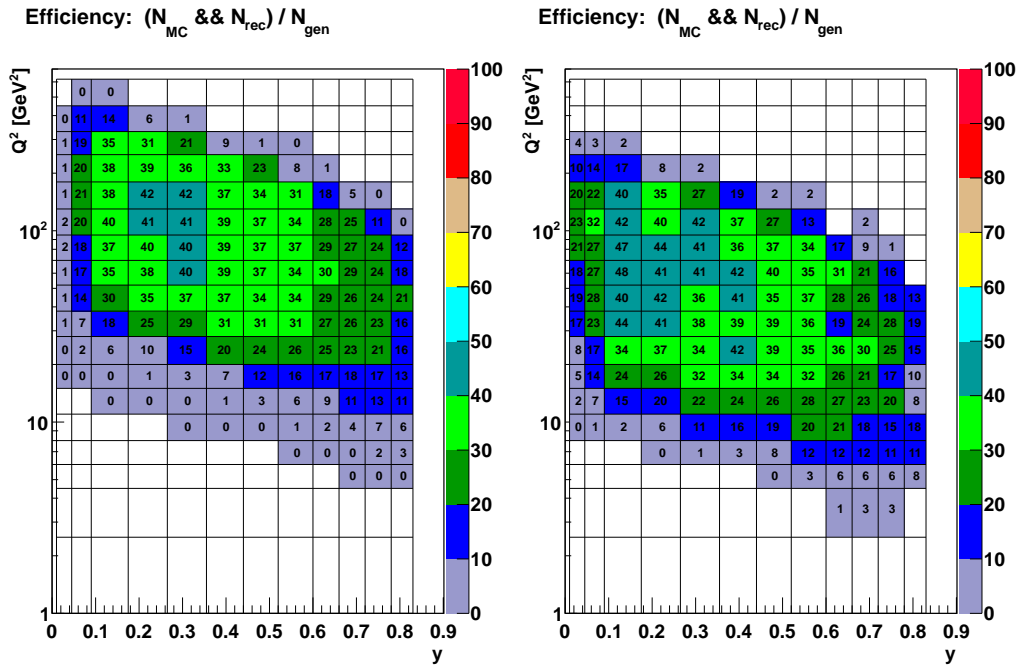


Figure C.9: The efficiency for the nominal (left) and satellite (right) Z -vertex samples from a Monte Carlo study for the LER dataset.

C.2 Rosenbluth Plots

C.2.1 Combined Nominal and Satellite Vertex

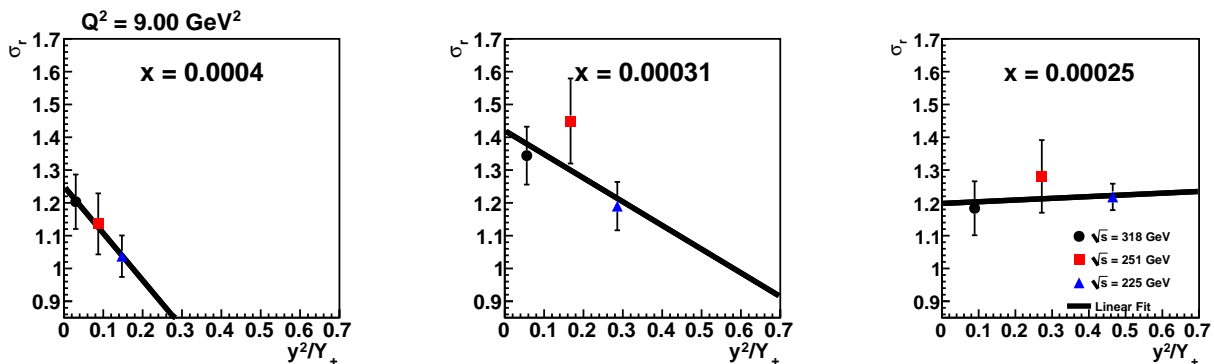


Figure C.10: Rosenbluth plots for $Q^2 = 9 \text{ GeV}^2$ and three bins of x for the combined nominal and satellite vertex data.

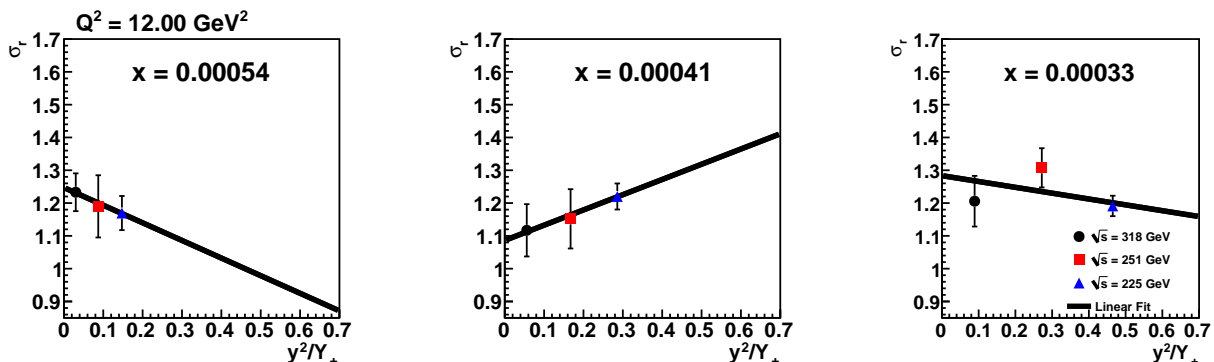


Figure C.11: Rosenbluth plots for $Q^2 = 12 \text{ GeV}^2$ and three bins of x for the combined nominal and satellite vertex data.

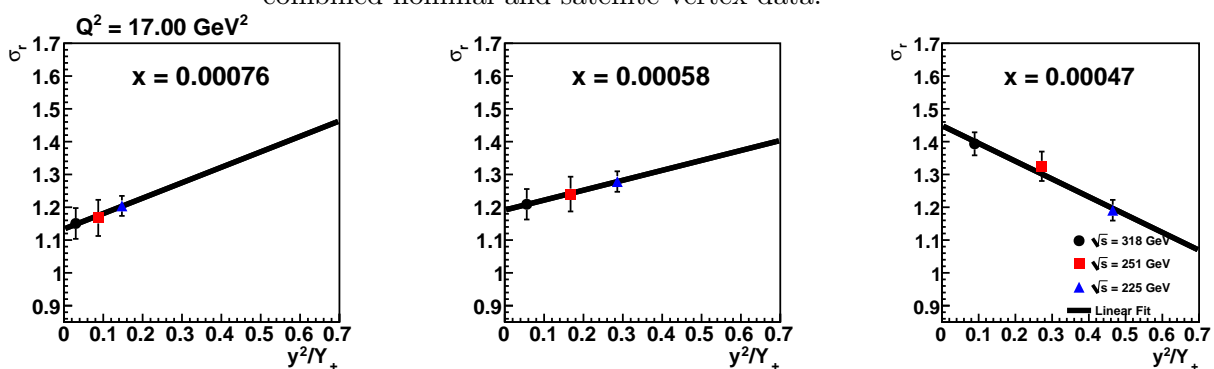


Figure C.12: Rosenbluth plots for $Q^2 = 17 \text{ GeV}^2$ and three bins of x for the combined nominal and satellite vertex data.

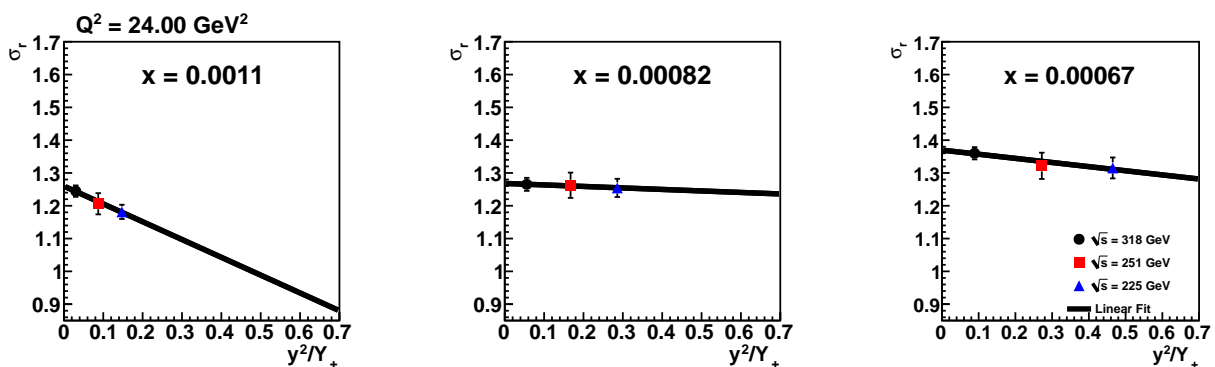


Figure C.13: Rosenbluth plots for $Q^2 = 24 \text{ GeV}^2$ and three bins of x for the combined nominal and satellite vertex data.

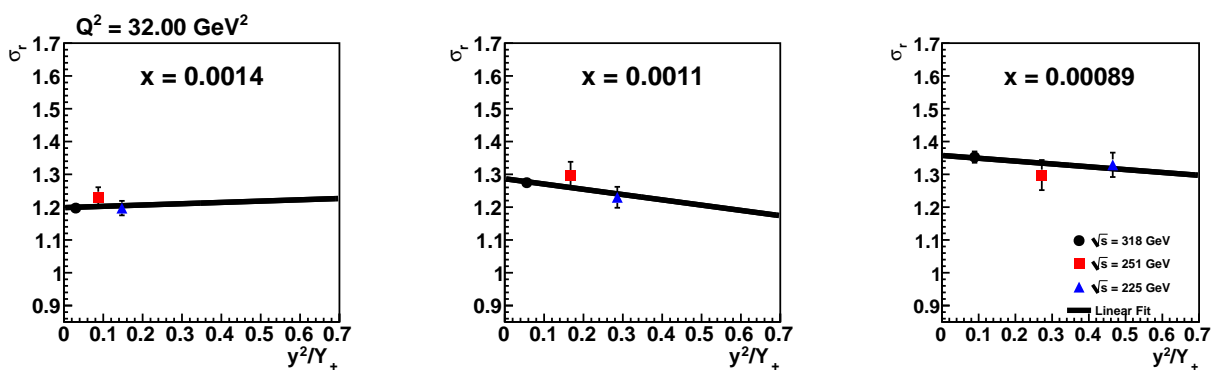


Figure C.14: Rosenbluth plots for $Q^2 = 32 \text{ GeV}^2$ and three bins of x for the combined nominal and satellite vertex data.

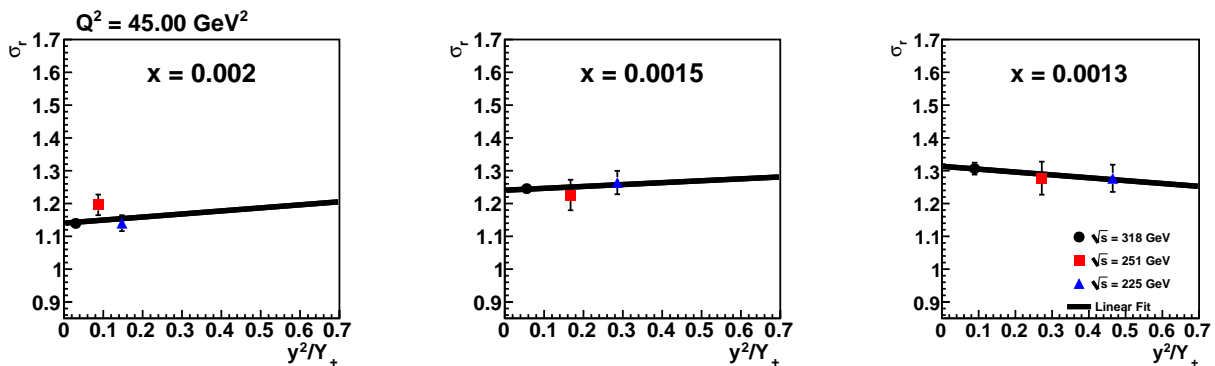


Figure C.15: Rosenbluth plots for $Q^2 = 45 \text{ GeV}^2$ and three bins of x for the combined nominal and satellite vertex data.

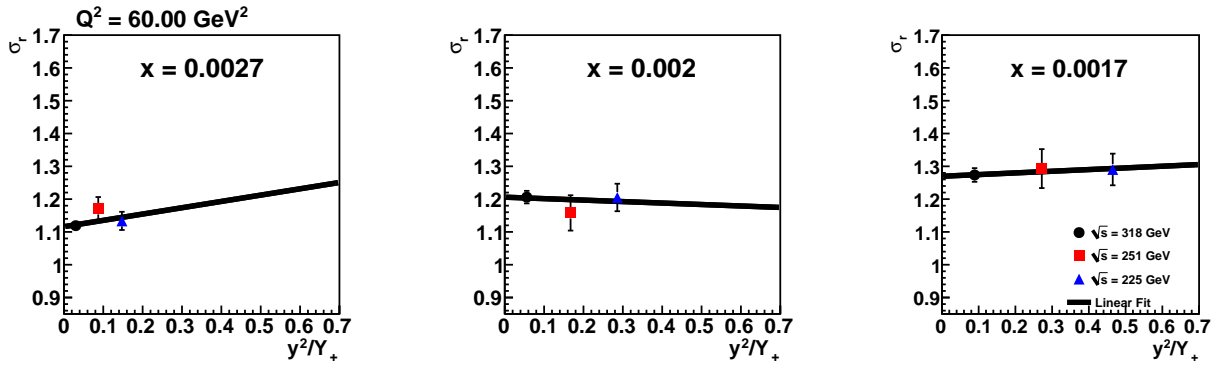


Figure C.16: Rosenbluth plots for $Q^2 = 60 \text{ GeV}^2$ and three bins of x for the combined nominal and satellite vertex data.

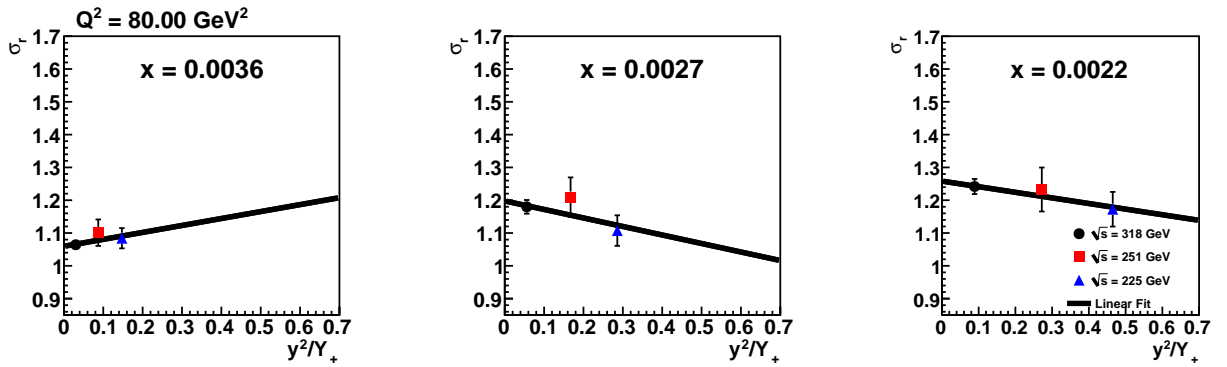


Figure C.17: Rosenbluth plots for $Q^2 = 80 \text{ GeV}^2$ and three bins of x for the combined nominal and satellite vertex data.

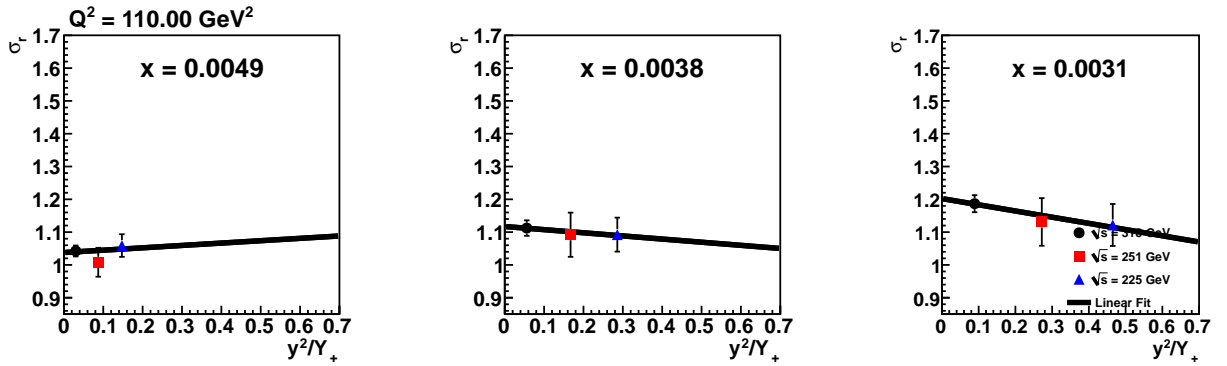


Figure C.18: Rosenbluth plots for $Q^2 = 110 \text{ GeV}^2$ and three bins of x for the combined nominal and satellite vertex data.

APPENDIX D

Glossary of Abbreviations

AERO	-	Aerogel Cherenkov Detector
BCAL	-	Barrel Calorimeter
BH	-	Bethe-Heitler
CTD	-	Central Tracking Detector
CTEQ	-	Coordinated Theoretical-Experimental Project on QCD
DGLAP	-	Dokshitzer, Gribov, Lipatov, Altarelli and Parisi
DIS	-	Deep Inelastic Scattering
FCAL	-	Forward Calorimeter
FLT	-	First Level Trigger
HER	-	High Energy Running period
HERA	-	Hadron-Electron Ring Accelerator
HES	-	Hadron-Electron Separator
ISR	-	Initial State Radiation
KP	-	Kinematic Peak
LER	-	Low Energy Running period
MC	-	Monte Carlo
MER	-	Medium Energy Running period
NLO	-	Next to Leading Order
MVD	-	Micro Vertex Detector
PCAL	-	Photon Calorimeter
PDF	-	Parton Distribution Function
QCD	-	Quantum Chromodynamics
QED	-	Quantum Electrodynamics
QPM	-	Quark Parton Model
RCAL	-	Rear Calorimeter
SPEC	-	Luminosity Spectrometer
SLT	-	Second Level Trigger
SRTD	-	Small Angle Rear Tracking Detector
TAG6	-	6-Meter Tagger
TLT	-	Third Level Trigger

REFERENCES

- [1] D. J. Griffiths, *Introduction to Elementary Particles* (John Wiley & Sons, Inc., 1987).
- [2] Wikipedia, *List of particles — Wikipedia, The Free Encyclopedia*, http://en.wikipedia.org/w/index.php?title=List_of_particles&oldid=403386200 (2010), [Online; accessed 4-January-2011].
- [3] G. Sterman *et al.*, *Handbook of perturbative QCD*, Rev. Mod. Phys. **67**(1), 157 (1995).
- [4] K. Nakamura and Others (Particle Data Group), J. Phys. G **37** (2010).
- [5] H. Abramowicz and A. Caldwell, *HERA collider physics*, Rev. Mod. Phys. **71**(5), 1275 (1999).
- [6] H. Frauenfelder, E. Henley, and A. Garcia, *Subatomic physics* (Prentice-Hall, 1974).
- [7] C. Burgess and G. Moore, *The Standard Model: a Primer* (Cambridge University Press, UK, 2007).
- [8] M. Peskin and D. Schroeder, *An Introduction to Quantum Field Theory* (Westview Press, 1995).
- [9] R. Roberts, *The Structure of the Proton* (Cambridge University Press, 1993).
- [10] R. Devenish and A. Cooper-Sarkar, *Deep Inelastic Scattering* (Oxford University Press, UK, 2004).
- [11] Y. L. Dokshitzer, Sov. Phys. JETP **46**, 641 (1977).
- [12] V. Gribov and L. Lipatov, Sov. J. Nucl. Phys **15**, 438 (1972).
- [13] V. Gribov and L. Lipatov, Sov. J. Nucl. Phys **15**, 675 (1972).
- [14] G. Altarelli and G. Parisi, Nucl. Phys **B 126**, 298 (1977).
- [15] J. Kretzschmar, *Proton Structure Measurements and the HERAPDF fit*, Arxiv preprint arXiv:0906.1108 (2009).

- [16] S. Chekanov *et al.* (ZEUS Collaboration), *An NLO QCD analysis of inclusive cross-section and jet-production data from the ZEUS experiment*, Eur. Phys. J. C **42**(1), 1 (2005).
- [17] H. Lai *et al.* (CTEQ Collaboration), *Global QCD Analysis of Parton Structure of the Nucleon: CTEQ5 Parton Distributions*, Eur. Phys. J. C **12** (2000).
- [18] A. Martin *et al.*, *Parton distributions for the LHC*, Eur. Phys. J. C **63**(2), 189 (2009).
- [19] H. Plathow-Besch, *PDFLIB: a library of all available parton density functions of the nucleon, the pion and the photon and the corresponding α_s calculations*, Comp. Phys. Comm. **75**(3), 396 (1993).
- [20] N. Tuning, *Proton Structure Functions at HERA*, Ph.D. thesis, University of Amsterdam (2001).
- [21] G. Wolf, *The Kinematics of Deep Inelastic Scattering in the Presence of Initial State Radiation*, Arxiv preprint hep-ex/9704006 (1997).
- [22] H. Anlauf, A. Arbuzov, and E. Kuraev, *QED corrections to DIS with a tagged photon at HERA*, Arxiv preprint hep-ph/9907248 (1999).
- [23] R. Gerger, A. Bornheim, and E. Hilger, *Measurement of the Proton Structure Function F_2 using ISR Events from 1995 Data (unpublished)*, ZEUS Note 98-034 (1998).
- [24] HERA, *Proposal for a Large Electron-Proton Colliding Beam Facility at DESY*, DESY **81**(10) (1981).
- [25] M. Minty, *Summary Of Recent High Luminosity Experiments After The HERA-II Luminosity Upgrade And Future Prospects*, DESY, HERA **03-25** (2003).
- [26] U. Holm *et al.* (ZEUS Collaboration), *The ZEUS Detector - Status Report (unpublished)*, <http://www-zeus.desy.de/bluebook/bluebook.html> (1993).
- [27] A. Garfagnini, *The ZEUS microvertex detector*, Nucl. Instrum. Methods A **435**(1-2), 34 (1999).
- [28] C. Coldewey, *The ZEUS microvertex detector*, Nucl. Instrum. Methods A **447**, 44 (2000).
- [29] T. Haas, *The ZEUS microvertex detector*, Nucl. Instrum. Methods A **549**(1-3), 37 (2005).
- [30] B. Foster *et al.*, *The Design and construction of the ZEUS central tracking detector*, Nucl. Instrum. Methods A **338**(2-3), 254 (1994).

- [31] B. Foster *et al.*, *The performance of the ZEUS central tracking detector z-by-timing electronics in a transputer based data acquisition system*, Nucl. Phys. B **32**, 181 (1993).
- [32] C. Liu, *Neutral Strangeness Production with the ZEUS Detector at HERA*, Ph.D. thesis, McGill University (2007).
- [33] A. Caldwell *et al.*, *Design and implementation of a high precision readout system for the ZEUS calorimeter*, Nucl. Instrum. Methods A **321**(1-2), 356 (1992).
- [34] I. Gregor, in *Nuclear Science Symposium Conference Record, 2007. NSS'07. IEEE* (IEEE, 2007), vol. 1, pp. 249–253.
- [35] A. Bernstein *et al.*, *Beam tests of the ZEUS barrel calorimeter*, Nucl. Instrum. Methods A **336**(1-2), 23 (1993), ISSN 0168-9002.
- [36] A. Bamberger *et al.*, *The small angle rear tracking detector of ZEUS*, Nucl. Instrum. Methods A **401**(1), 63 (1997).
- [37] I. Ambats *et al.*, *Studies of hardon-electron separators for the ZEUS barrel calorimeter*, Nucl. Instrum. Methods A **368**(2), 364 (1996).
- [38] P. Göttlicher, in *Proceedings of the Tenth International Conference on Calorimetry in Particle Physics: Pasadena, California, USA, 25-29 March 2002* (World Scientific Pub Co Inc, 2002), p. 296.
- [39] T. Danielson, *A Measurement of Multijet Production in Low- x_{Bj} Neutral Current Deep Inelastic Scattering with ZEUS at HERA*, Ph.D. thesis, University of Wisconsin - Madison (2007).
- [40] W. Smith *et al.*, *The ZEUS calorimeter first level trigger*, Nucl. Instrum. Methods A **355**(2-3), 278 (1995), ISSN 0168-9002.
- [41] H. Bethe and W. Heitler, *On the stopping of fast particles and on the creation of positive electrons*, Proceedings of the Royal Society of London. Series A, Containing Papers of a Mathematical and Physical Character **146**(856), 83 (1934).
- [42] H. Abramowicz *et al.* (ZEUS Collaboration), *Measurement of the energy dependence of the total photon-proton cross section at HERA*, Phys. Lett. B **697**(3), 184 (2011).
- [43] M. Helbich *et al.*, *The spectrometer system for measuring ZEUS luminosity at HERA*, Nucl. Instrum. Methods A **565**(2), 572 (2006).
- [44] J. Chwastowski *et al.*, *Aerogel Cherenkov detectors for the luminosity measurement at HERA*, Nucl. Instrum. Methods A **504**(1-3), 222 (2003).

- [45] H. Spiesberger, *HERACLES and DJANGO: Event Generation for ep, Interactions at HERA Including Radiative Processes* (1998).
- [46] G. Corcella, I. Knowles, G. Marchesini, S. Moretti, K. Odagiri, P. Richardson, M. Seymour, and B. Webber, *HERWIG 6: An event generator for hadron emission reactions with interfering gluons (including supersymmetric processes)*, J. HEP **2001**, 010 (2001).
- [47] T. Sjöstrand, S. Mrenna, and P. Skands, *PYTHIA 6.4 physics and manual*, J. HEP **2006**, 026 (2006).
- [48] T. Hass, *Generating Monte Carlo Events with MOZART (unpublished)*, ZEUS Note 92-021 (1992).
- [49] R. Brun and F. Carminati, *GEANT detector description and simulation tool*, CERN Program Library Long Writeup W **5013** (1993).
- [50] L. Lönnblad, *Ariadne version 4—A program for simulation of QDC cascades implementing the colour dipole model*, Computer Physics Communications **71**(1-2), 15 (1992).
- [51] G. Gustafson, *Dual description of a confined colour field*, Physics Letters B **175**(4), 453 (1986).
- [52] T. Sjöstrand, *High-energy-physics event generation with PYTHIA 5.7 and JETSET 7.4*, Comp. Phys. Comm. **82**, 74 (1994).
- [53] H. Spiesberger, *Monte Carlo treatment of radiative corrections at HERA*, Nucl. Phys. B **29**(1), 221 (1992).
- [54] B. Andersson *et al.*, *Parton fragmentation and string dynamics*, Physics Reports **97**, 31 (1983).
- [55] R. Brun and F. Rademakers, *ROOT—An object oriented data analysis framework*, Nucl. Instrum. Methods A **389**(1-2), 81 (1997).
- [56] D. Vladimir, *Revision to 2006/07 e+ Luminosity Measurement* (2011), unpublished internal ZEUS presentation.
- [57] S. Paganis, *A Luminosity Spectrometer for the Zeus Experiment at HERA*, Arxiv preprint hep-ex/0011080 (2000).
- [58] H. Abramowicz, A. Caldwell, and R. Sinkus, *Neural network based electron identification in the ZEUS calorimeter*, Nucl. Instrum. Methods A **365**(2-3), 508 (1995).
- [59] J. Grosse-Knetter, *Corrections for the Hadronic Final State(unpublished)*, ZEUS Note 98-031 (1998).

- [60] N. Tuning, *ZUFOS: Hadronic final state reconstruction with calorimeter, tracking and backslash correction (unpublished)*, ZEUS Note 01-021 (2001).
- [61] G. Hartner, *VCTRAK Briefing: Program and Math (unpublished)*, ZEUS Note 98-058 (1998).
- [62] K. Oliver *et al.*, *A Minimum Bias Z vertex Distribution for 2005-2006 eP Interactions at ZEUS(unpublished)*, ZEUS Note 07-008 (2007).
- [63] S. Shimizu, *Measurement of the Proton Longitudinal Structure Function F_L at HERA*, Ph.D. thesis, University of Tokyo (2009).
- [64] A. Blondel and F. Jacquet, *Detection of the charged current event*, DESY 79-48 (1979).
- [65] T. Abe, *Comp. Phys. Comm.* **136** (2001).
- [66] H. Spiesberger *et al.*, in *Proc. of the 1991 HERA Physics Workshop* (1991), p. 798.
- [67] M. W. Krasny, in *Proc. of the 1991 HERA Physics Workshop* (1991), p. 850.
- [68] L. Favart, S. Schlenstedt, and H. Spiesberger, *Summary and outlook of WG70: Radiative effects*, Prepared for Workshop on Monte Carlo Generators for HERA Physics (Plenary Starting Meeting) (1998).
- [69] J. Scott, *First Direct Measurement of FL using ISR Events in Deep Inelastic Scattering at HERA*, Ph.D. thesis, University of Bristol (2000).
- [70] H. Spiesberger, A. Kwiatkowski, and H. Moehring, *HERACLES. An Event Generator for ep Interactions at HERA Including Radiative Processes* (1996).
- [71] T. Ahmed *et al.* (H1 Collaboration), *Experimental study of hard photon radiation processes at HERA*, *Z. Phys* **66**(4), 529 (1995).
- [72] P. K. Sinervo, in *Proceedings of the Conference on Statistical Problems in Particle Physics, Astrophysics, and Cosmology (PhyStat2003)* (2003), pp. 8–11.
- [73] S. Chekanov *et al.* (ZEUS Collaboration), *Measurement of the longitudinal proton structure function at HERA*, *Phys. Lett. B* **682**(1), 8 (2009).
- [74] M. Derrick *et al.* (ZEUS Collaboration), *Measurement of the Proton Structure Function F_2 at low x and low Q^2 at HERA*, *Z. Phys* **C69**, 607 (1996).
- [75] S. Chekanov *et al.* (ZEUS Collaboration), *Measurement of the neutral current cross section and F_2 structure function for deep inelastic ep scattering at HERA*, *The European Physical Journal C* **21**(3), 443 (2001).

- [76] E. Lohrmann, *Choice of Proton Energy in FL Measurements (unpublished)*, ZEUS Note 06-003 (2006).
- [77] C. Adloff (H1 Collaboration), *Determination of the Longitudinal Proton Structure Function F_L at Low x* , Arxiv preprint hep-ex/9611017 (1996).
- [78] F. D. Aaron *et al.* (H1 Collaboration), *Measurement of the proton structure function $F_L(x, Q^2)$ at low x* , Phys. Lett. B **665**(4), 139 (2008).
- [79] F. D. Aaron *et al.* (H1 Collaboration), *Measurement of the Inclusive ep^\pm Scattering Cross Section at High Inelasticity y and of the Structure Function F_L* , DESY (10-228) (2010).
- [80] M. Rosenbluth, *High energy elastic scattering of electrons on protons*, Phys. Rev. **79**(4), 615 (1950).
- [81] M. Krasny, W. Placzek, and H. Spiesberger, *Determination of the longitudinal structure function at HERA from radiative events*, Z. Phys **53**(4), 687 (1992).